THÈSE

En vue de l'obtention du

DOCTORAT DE L'UNIVERSITÉ DE TOULOUSE

Délivré par : *l'Université Toulouse 3 Paul Sabatier (UT3 Paul Sabatier)*

Présentée et soutenue le *30/09/2016* **par :**

Peter R. Wiecha

Linear and Nonlinear Optical Properties of High Refractive Index Dielectric Nanostructures

---

JURY

Dr. Nicolas BONOD	CNRS, Institut Fresnel, Marseille
Prof. Rémi CARMINATI	ESPCI, Paris-Tech, Institut Langevin, Paris
Prof. Gérard COLAS DES FRANCS	Université de Bourgogne, ICB, Dijon
Dr. Bernhard URBASZEK	CNRS, LPCNO, INSA, Toulouse
Prof. Adnen MLAYAH	Université Paul Sabatier, CEMES, Toulouse
Dr. Aurélie LECESTRE	CNRS, LAAS, INP, Toulouse

École doctorale et spécialité :

SDM : Nano-physique, nano-composants, nano-mesures - COP 00

Unité de Recherche :

Centre d'Elaboration de Matériaux et d'Etudes Structurales (UPR 8011)

Directeur(s) de Thèse :

Prof. Vincent PAILLARD et *Dr. Arnaud ARBOUET*

Rapporteurs :

Dr. Nicolas BONOD et *Prof. Rémi CARMINATI*

typeset with XeLaTeX

Acknowledgements

Initially, I want to thank the French education ministry "ministère de l'éducation nationale, de l'enseignement supérieur et de la recherche" for granting me funding for my PhD thesis. I also thank the directors of the CEMES, Dr. Alain Claverie, et depuis fin 2015 Dr. Etienne Snoeck, for the opportunity to work in the laboratory and for ensuring a most pleasant working atmosphere.

Then, first of all, I thank my co-supervisor Prof. Vincent Paillard who was always available for any kind of concerns and countless interesting discussions. Thanks to Vincent, the last three years were not only fruitful in terms of scientific productivity but also very enriching in a human way. Thank you for your support in truly every respect.

Since typesetting is a strictly sequential matter, I unfortunately have to decide on an order in this acknowledgement. However, I would equally like to thank my second co-supervisor Dr. Arnaud Arbouet. I am grateful for the opportunity to work on his "FEMTO" setup and for his trust when I started tinkering around with all the expensive equipment. I want to express my special gratitude also for the permanent availability concerning any kind of discussions – either scientific or personal related – for many inspiring ideas, the establishing of many contacts with other researchers and for his priceless efforts in helping me with job applications.

I would also very much like to thank Dr. Christian Girard for his countless stimulating ideas and explanations and particularly for his friendly and very motivating support. Thank you also for your availability and for unhesitatingly sharing valuable pieces of code.

Furthermore, thank you Dr. Aurélien Cuche, for letting me participate in the interesting aluminum thermo-plasmonics project and for very helpful hints concerning optical setups and alignment.

My thankfulness goes also to Dr. Guilhem Larrieu and Dr. Aurélie Lecestre from LAAS/CNRS in Toulouse, who fabricated the beautiful silicon nano-structures by electron-beam lithography. Thank you for the patience and perseverance to do several iterations of fabrication in order to obtain the best possible samples.

In the hope to not forget too many persons, I want to thank furthermore

- Prof. Gerard Colas des Francs for his help and explanations on simulations by the Green Dyadic Method. Particularly I want to express my gratitude for sharing his 2D GDM code.
- Prof. Otto Muskens from Southampton for the fruitful collaboration on several projects with plasmonic antennas
- Dr. Thierry Baron from LTM-CNRS in Grenoble for the VLS grown SiNWs.
- Dr. Frank Fournel from CEA/LETI in Grenoble for the SOQ and SOI substrates.
- Dr. Houssem Kallel for many precious explanations in the first months of my thesis.
- Prof. Adnen Mlayah for his support and many interesting discussions.
- Leo for the fruitful cooperation and funny nights in Toulouse
- Gonzague for letting me use the sample preparation room including the microscope and for entertaining company in the lab when we were trying SHG from liquid crystals

- Robin, Philippe, Luis and Giuseppe for assisting me with the scanning electron microscope.
- Victor for a precious piece of SOI substrate.
- My m'bares Alessandro and Giuseppe, who taught me about south Italian culture and language and eventually became my Sicilian family. Thanks to you it was never boring in the office.
- Chloé for convincing me to run the PhD student association for one year, and
- Delphine and Audrey for managing this association with me. I won't forget sitting on the back row of Delphine's car, petrified by her intrepid driving style!
- And finally Thomas, Nico and Aurélie for taking over the burden of this association.
- All the other PhD students of the CEMES for making the last three years so pleasant.

I would absolutely mention the legions of open source developers from around the world who, in their vast majority, voluntarily create powerful software environments, which are not subject to any proprietary restrictions. Some selected examples are the GNU project, the Latex project or the Python software foundation including libraries such as numpy/scipy and matplotlib.

Finally I would like to thank my friends for providing the urgently required distraction from work. Thank you David, Manu, Holger, Andisepp, my friends from the Kauferinger Chaos-Trupp (your visit in Toulouse will remain unforgotten), Johannes, Simon, Anna, Sören, Marie, Markus, Floflo, Irene and all the others, I unforgivably have forgotten at this point.

At last I want to thank my family for their support – not only over the last couple of years. I want to thank my Dad for proof-reading the French parts of this thesis. And I deeply thank in particular Cristina for her patience during the last months, and our sons Simon and Oscar, who often had to wait until late at night for my return from work, for their cheering, carefree happiness.

Contents

Abstract

Nano-photonic structures offer a highly interesting platform to enhance light-matter interaction on a nanometer scale. Recently, high-index dielectric structures have gained increasing attention as possible low-loss alternatives to plasmonic nano-antennas made from noble metals. Furthermore, since non-linear effects offer many unique functionalities like the coherent up-conversion of photons, including the generation of harmonics, many efforts are being made to exploit such phenomena in nano-photonics. In this thesis, an analysis is presented on nonlinear optical effects in individual dielectric structures, specifically in silicon nanowires (SiNWs). Nanowires develop strong optical resonances in the visible and infrared spectral range. In this context, strong enhancement of the optical near-field together with a large surface to volume ratio support the appearance of nonlinear effects. We show that, compared to bulk Si, a two orders of magnitude increase in second harmonic generation (SHG) is feasible and furthermore unravel different polarization and size-dependent contributions at the origin of the SHG. Numerical simulations are carried out to reaffirm these experimental findings for which a numerical technique is presented to describe nonlinear effects on the basis of the Green Dyadic Method (GDM). In the last part of the thesis, the GDM is used together with evolutionary optimization (EO) algorithms to tailor and optimize optical properties of photonic nano-structures. We eventually fabricate samples, based on EO design, and successfully verify the predictions of the optimization algorithm. It turns out that EO is an extremely versatile tool and has a tremendous potential for many kinds of further applications in nano-optics.

Résumé

La nano-optique est un vaste domaine permettant d'étudier et d'exalter l'interaction lumière-matière à l'échelle nanométrique. Ce domaine couvre notamment la plasmonique, mais depuis quelques années, un effort est porté sur les nanostructures diélectriques à fort indice de réfraction (typiquement des semiconducteurs comme le silicium). Des effets similaires aux nanoparticules plasmoniques peuvent être obtenus, tels un comportement d'antenne et l'exaltation de phénomènes non linéaires (génération d'harmoniques), avec l'avantage de faibles pertes. Dans cette thèse, une analyse des propriétés optiques linéaires et non linéaires de nanostructures individuelles. Une première partie est dédiée aux nanofils de silicium qui supportent de fortes résonances optiques dont le nombre et la gamme spectrale, du proche UV au proche IR, sont fonction de leur diamètre. Dans ces conditions, l'exaltation du champ proche optique et un rapport surface sur volume élevé favorisent l'apparition de processus non linéaires. Ainsi la génération de seconde harmonique (SHG) par rapport au silicium massif est augmentée de deux ordres de grandeur. En outre, différentes contributions à l'origine de la SHG peuvent être adressées individuellement en fonction de la polarisation du laser d'excitation et de la taille des nanofils. Les résultats expérimentaux sont confrontés à des simulations numériques (méthode dyadique de Green, GDM), qui permettent d'identifier les différentes contributions. Dans une seconde partie, la méthode dyadique de Green est couplée à des algorithme évolutionnistes (EO) pour la conception et l'optimisation de propriétés optiques choisies de nanostructures semiconductrices ou métalliques, par exemple diffusion résonnante de différentes longueurs d'ondes pour différentes polarisations. Des échantillons de nanostructures de silicium, réalisés à partir des résultats de l'EO, vérifient avec succès les prédictions de l'algorithme d'optimisation, démontrant l'énorme potentiel de l'EO pour de nombreuses applications en nanophotonique requérant une optimisation simultanée de différents paramètres.

Chapter 1

Introduction and Motivation

1.1 Nano-Optics

Nano-optics is a field which is increasingly drawing attention of researchers worldwide. In general, nano-optics is the research field on effects of light-matter interaction occurring at subwavelength dimensions – thus at the nanometer scale for visible and near-infrared light. Usually, all phenomena can be described by classical electrodynamics, *i.e.* by the set of Maxwell's equations [1]. In this chapter we give an overview of different material systems and of the current research progress on photonic nano-structures and their applications. A comparison between plasmonic structures and high-index dielectric antennas motivates more profound investigations on the latter material system. Finally we give a brief review on nonlinear effects in nano-optics.

1.1.1 Plasmonics

One of the main driving forces in nano-optics is the field of plasmonics [2, 3]. Interaction of electromagnetic waves with metals can launch collective oscillations of free electrons from the conduction band. The dielectric constant of metals is negative (see Fig. 1.1b), leading to an imaginary wavevector. Fields are therefore evanescent and confined within a small region at the surface, called "skin-depth" [4]. In consequence, collection oscillations of the electrons propagate along the surface and are called surface plasmon polaritons (SPP) [5–8]. In small metal particles, the propagation of SPPs is hindered due to the spatial confinement and localized modes appear, so-called localized surface plasmon (LSP) resonances (see Fig. 1.1a). For an extensive introduction on plasmonics, we refer the reader to reference [2]. These confined plasmon oscillations allow to squeeze light into tiny volumes of subwavelength size, far below the diffraction limit and yield extremely high local field enhancements [9]. In the visible spectral range this results in characteristic sizes of several tenths to a few hundreds of nanometers. Such plasmonic particles are often referred to as "optical antennas" [10–13].

A multitude of designs for such antennas have been proposed for various purposes. It is for example possible to obtain spectrally well defined resonances which may be used for color-filtering and -rendering or printing at the diffraction limit [14–19] or, on the other hand, to create broadband antennas [20]. Other designs allow either polarization-sensitivity or -insensitivity [16, 21, 22] and polarization conversion [23, 24]. Furthermore it is possible to create interferences between modes resulting in Fano-like resonances [25] or enhancement of higher multipolar radiative transitions that would usually be too weak for observation [26]. Also chiral responses can be tailored to react sensitive to left- or right-circular polarized light [27–29]. Another example is strong directivity in the scattered angular intensity distribution that can

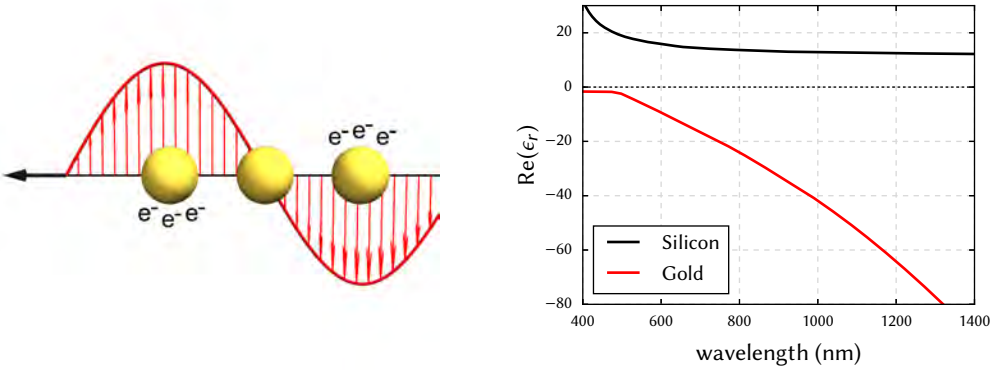

(a) Localized Plasmon

(b) Dispersion of Silicon and Gold

Figure 1.1: (a) sketch of localized surface plasmons in gold nanospheres induced by an electromagnetic field and (b) real part of the relative permittivity of gold and silicon.

for example be achieved with antenna arrangements similar to radio-frequency antennas [30–35]. Also forward/backward anisotropic scattering can be obtained [36] and even the possibility of wavelength-dependent switching of directionality has been reported [37]. Larger two-dimensional antennas pronounce higher order spatial modes with complex, tailorable field distributions that can be resolved for example using two-photon luminescence (TPL) [38–41] or electron energy loss spectroscopy (EELS) techniques [42]. Acoustic vibrations can be optically excited in nano-antennas, that have been used as nano-sources for hypersound generation [43, 44].

Applications range from signal processing [45, 46] over surface enhanced spectroscopies where strong plasmonic field enhancements are exploited to boost signals from few or even single molecules, from weak fluorescent transitions or from molecular vibrations [20, 47–49] to biomedical applications in which plasmonic particles are used as nano-biosensors for specific biomolecules [50], as biomarkers [51, 52] or for local thermal treatment [53, 54] and drug delivery [55]. Sharp resonances can be used for tuning [56] and sensing [57, 58] in optomechanical plasmonic resonators.

1.1.2 Photonic Particles from High-Index Dielectric Materials

The main focus of this work will be put on another type of photonic nanostructures, namely high-refractive index dielectric nanoparticles. Usually, the latter materials comprise semiconductors such as germanium or silicon (Si refractive index in the visible $n \approx 3.5$ - 4). The decisive difference to plasmonics is the lack of free carriers. This results in a positive real part of the dielectric function (see Fig. 1.1b) which means that light can actually propagate inside the material. Under electric fields, the material is polarized due to a displacement of the *bound* carriers relative to their lattice atoms and this polarization is proportional to the dielectric contrast with the environment (see also appendix 6.4.4).

In the past several years, many functionalities of plasmonic systems have been made accessi-

ble also from high-index dielectric nanostructures – with the advantage of very low absorptive losses [59, 60].

1.1.2.1 Individual Structures

In the early 2000's, the possibility to use horizontal silicon nanowires (SiNWs) as antennas for visible light was first exploited in the context of enhanced absorption [61] and Raman spectroscopy [62]. By simply changing the diameter, optical resonances can be tuned all over the UV and visible spectrum up to the infrared [63, 64]. An optical darkfield microscopy image of different large NWs is shown in Fig. 1.2a, where the size-dependent redshift of the resonance wavelength is clearly visible. It was then shown, that also the material composition is a convenient parameter for tuning the resonance positions [65]. In nanowires, these resonances are strongly polarization dependent, as is their nearfield distribution [66], a property that can be used for polarization filters [67] or to obtain spectrally enhanced and strongly polarized photoluminescence from direct bandgap semiconductor NWs [68]. A multitude of structures has been studied in the meantime, such as low aspect ratio [69, 70] and vertical nanowires [71], nanospheres [72], nanodiscs [73], hollow nanocylinders [74] coupled dimers [75–77] or even complex bio-inspired structures [78]. Also heterostructures composed of mixed materials have been investigated [79]. For example the absorption efficiency of NWs could be increased significantly by using amorphous-/crystalline-Si [80] or Ge/Si core/shell structures [81].

Similar functionalities as with plasmonic antennas have been realized on the high-index dielectrics platform. Guiding light for all-optical signal processing is a commercially established application of silicon nanostructures [82, 83] and efforts are being made to couple other dielectric materials to the CMOS platform [84]. Nanowires are also used to guide single photons or entangled photon pairs e.g. for quantum computing [85]. Apart from wave-guiding, numerous other possible applications exist. The possibility to obtain well defined optical resonances in high-index nanowires can be used to create single-NW lasers [86] and achieve mode-filtered lasing from such individual NWs [87]. Recently an optical diode for circularly polarized light has been proposed [88] which is a step towards all-optical logical elements. It is also possible to create forwards/backwards selective uni-directional scattering [89–92] or even scattering towards arbitrary angles [93] by taking advantage of interferences between degenerate resonance modes. The aforementioned possibility to tune the resonance wavelengths is similarly flexible as in plasmonic antennas and is supposed to be very valuable for solar cell applications [94–97]. It has been also shown, that high-index dielectric nano antennas can be used as alternatives to metal particles in surface enhanced fluorescence spectroscopy (SEF) and surface enhanced Raman spectroscopy (SERS) [98]. While field-enhancement is several times lower compared to metal antennas, larger field volumes and by far lower losses may compensate this drawback in many applications [99].

1.1.2.2 Dielectric Metamaterials

When individual nano-structures are put together and are arranged orderly on large areas, such surfaces can have very surprising macroscopic optical properties – that, very importantly, are tailorable to individual needs. Such so-called *metasurfaces* or *metamaterials* [100] are often made of plasmonic elements [101], but here we will focus on an introduction to all-dielectric metamaterials [102, 103].

In direct analogy to the optical properties of individual nanostructures, metasurfaces with spectrally well defined resonances can be designed. In this way, optical band-pass filters [104], full-color holograms [105], highly absorptive surfaces [106], polarization converters [107] or, by putting the individual dielectric elements on a flexible substrate, mechanically tunable metamaterials [108] have been created. By tuning spectrally the ratio of forward and backward scattering, metasurfaces with particularly high reflectance [109–111] or transmittance [112] have been reported, as well as metasurfaces designed for ultra-fast optically induced transparency [113]. The ability to spatially tune the phase of an incident beam allows wavefront shaping, polarization control e.g. for radially polarized beam generation or focusing from planar structures [114, 115]. A generalized Brewster effect can be obtained from surfaces composed of silicon nanospheres which has been used for the tailoring of directional scattering [116]. Directionality has also been used to vertically couple light from a waveguide to free space, which opens perspectives for applications in optical signal processing [117]. Even materials can be designed that allow optical cloaking, i.e invisibility of small objects [118] (for details on cloaking, see [119] or [120]).

1.1.2.3 Beyond Optics

High-index dielectric nanostructures are also promising for possible multi-purpose applications. For instance thermal rectification in telescopic Si NWs – which basically represent diodes for heat transport – has been demonstrated recently for NWs with diameters $\approx 10\,\mathrm{nm}$ [121]. Thermoelectric properties could be enhanced in dielectric metamaterials by artificially increasing the ratio of electric over heat conductivity [122]. Another research group used resistance hysteresis in silicon nanowires with encoded abrupt doping-profiles to implement non-volatile memory [123]. Such effects could be exploited simultaneously to the unique optical properties of dielectric nanoparticles with manifold imaginable applications.

1.1.3 High-Index Dielectric vs. Plasmonic Nanostructures

In the preceding introduction, we focused mainly on the similarities of plasmonic and dielectric materials. Let us now compare the differences between them in some more detail in order to expose advantages and drawbacks of the two material systems.

1.1.3.1 Fabrication

We will start with some words on the fabrication of nanostructures. Plasmonic structures consist of metals, usually gold, silver or aluminum. They are either evaporated on a substrate with a subsequent lithographic step and lift-off [124] or chemically synthesized [125–128]. Colloidal particles have been orderly arranged with DNA origami templates [129] or larger chemically synthesized crystalline flakes can be very rapidly structured by interferometric lithography [130]. The first approach suffers from the relatively poor and often polycrystalline quality of evaporated metals whereas the mono-crystalline metal nanoparticles from the latter technique usually cannot be up-scaled to obtain large-area substrates.

High-index dielectric materials can also be evaporated or sputtered with the same drawbacks that hold for the metal case. Silicon nanowires can be grown by vapor-liquid-solid (VLS) epitaxy, which is a technique that can be easily up-scaled. A key advantage of the VLS-method is that it allows a very accurate definition of the size and aspect ratio of a large quantity of simultaneously

(a) Darkfield Image of Silicon NWs

(b) Magnetic Resonances: Au vs. Si

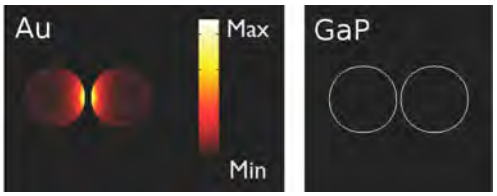

(c) Heat Dissipation: Au vs. GaP

Figure 1.2: (a): Darkfield image of 5 µm long SOI-etched silicon nanowires with widths from 30 nm at the left to 400 nm at the right. (b) sketch of magnetic field generation in metal split-ring resonators (left) and dielectric nanospheres (right), reprinted from Kuznetsov et al. [72]. Copyright (2012) CC BY. (c) comparison of heat dissipation in gold (left) and gallium phosphide dimers (right), adapted with permission from Albella et al. [75]. Copyright (2014) American Chemical Society.

grown nanowires [131]. In particular for silicon, another common approach is the lithographic definition of structures on the crystalline silicon layer on a silicon-on-insulator (SOI) substrate [132, 133]. A key advantage in this context is the almost perfect control of structure definitions thanks to the compatibility to state-of-the art CMOS technology procedures.

1.1.3.2 Losses

A major disadvantage of plasmonic nanostructures for field enhanced spectroscopy are the significant losses associated to the large imaginary part of the dielectric permittivity in metals. These losses are responsible for significant heat generation in the particles which can be lethal for fragile biomolecules. If the emitters survive the heating, their weak signals might be directly re-absorbed by the lossy metal particle, neutralizing the effect of enhanced emission. Although high-index dielectrics yield significantly lower field enhancements, the associated losses are even by several orders of magnitude smaller (see also Fig. 1.3). For structures of comparable field enhancements, the difference in temperature gradients between plasmonic and dielectric particles can reach several 100 °C [75, 99] (see Fig. 1.2c).

The very low losses are a key advantage of dielectric materials when it comes to spectroscopy applications. However, the dissipation in plasmonic antennas can be used for localized heat generation at a nanometer scale [134] which on the other hand is not possible with dielectric nanostructures.

1.1.3.3 Electric Field Enhancement

Field enhanced spectroscopy is one of the main applications for plasmonic particles. High field enhancements are necessary in order to boost the weak signals from few or even single molecules. Field enhancement in the vicinity of high-index semiconductor nanoparticles is essentially proportional to the dielectric contrast between the particle ($\epsilon_{r,1}$) and its environment ($\epsilon_{r,0}$). This is a result of the continuity conditions for fields across dielectric interfaces (see appendix A.1)

$$E_{\parallel,0} = E_{\parallel,1} \qquad \epsilon_{r,0}\, E_{\perp,0} = \epsilon_{r,1}\, E_{\perp,1}. \tag{1.1}$$

The normal component of the electric field close to the particle is enhanced by the ratio of the permittivities and possibly further amplified due to the presence of resonant modes. For many semiconductors, strong field enhancement in the order of $\approx$ 100-fold amplification of the field intensities are possible ($\epsilon_r > 10$), where resonant optical modes further increase the effect [66, 76, 98] (see Fig. 1.3). Also a tightly focused excitation can increase the field enhancement and lower the effective volume of high field concentration [135]. The enhancement factors are nevertheless significantly lower than in plasmonics, where three orders of magnitude in intensity enhancement can easily be achieved [75]. While in plasmonics generally the strongest nearfields can be obtained, dielectric particles offer larger volumes of field enhancement [98], which, under circumstances, can be advantageous. The range of the strongest field enhancement is in the order of $\approx$ 1 nm for plasmonic antennas and $\approx$ 10 nm in dielectric nano-particles. This is in particular advantageous when it comes to the fabrication of nano-particles featuring such small gaps. Reported gain in fluorescence rate using dielectric particles range from values $\approx$ 5 [136] to $\approx$ 35 [98].

1.1.3.4 Magnetic Field Enhancement

Another noteworthy difference are strong magnetic resonances in dielectric nanoparticles, which are hard to obtain in plasmonic antennas [72, 137–140]. Magnetic dipolar resonances in dielectric dimers can yield an $\approx$ 100-fold increase of magnetic field intensities at visible frequencies [76], similarly strong as the electric field enhancement. In plasmonics, comparable performances are achievable only with complex asymmetric particle arrangements [141] or in the infrared using split-ring resonators [142] (see also Fig. 1.2b). The performance of magnetic field enhancement generally suffers from strong losses in plasmonic particles in the visible spectral range [72].

The magnetic resonances in dielectric nanoantennas can be used to tailor the magnetic local density of states [143]. Furthermore they can lead to behavior similar to magnetic media in actually non-magnetic ($\mu_r = 1$) media. Because the magnetic resonances can be tuned to be of comparable strength with the electric resonances, the so-called Kerker-condition ($\mu_r = \epsilon_r$, [144]) can be fulfilled even in dielectric media where clearly $\mu_r \neq \epsilon_r$, leading to strongly directional scattering [89, 91, 145–147].

Apart from the visible spectral range, strong magnetic fields have been demonstrated in high-index dielectric particles also for GHz [148] and THz frequencies [149].

1.1.3.5 Scattering

Finally, despite very strong field enhancements, scattering to the farfield from plasmonic antennas is limited [150] and often outperformed by their dielectric counterparts [75], as demonstrated

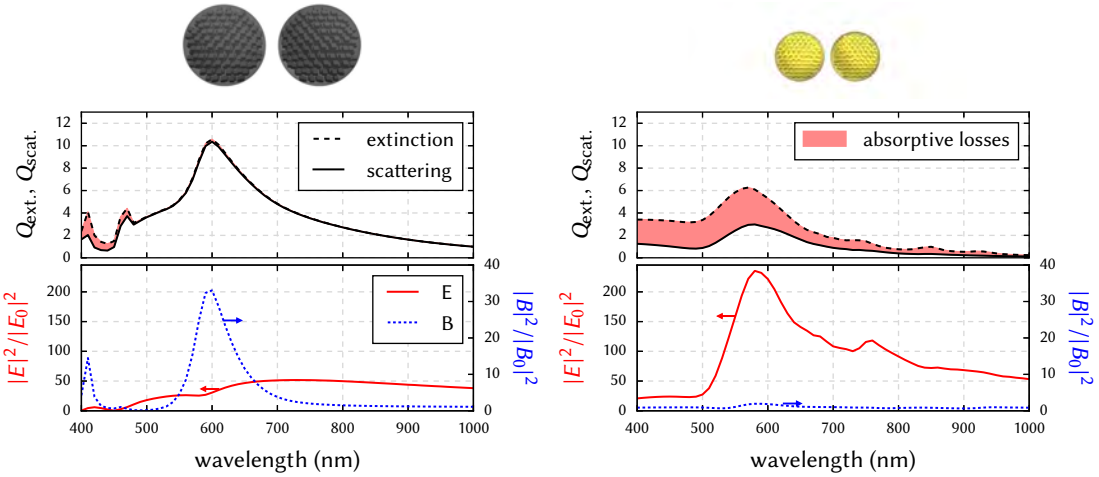

(a) $R = 80\,\text{nm}$ Silicon Dimer (b) $R = 40\,\text{nm}$ Gold Dimer

Figure 1.3: Extinction and scattering efficiency spectra (top) as well as nearfield enhancement (bottom: **E**-field: red, **B**-field: blue) in the gap of (a) a dimer of two silicon spheres with radius $R = 80\,\text{nm}$ and (b) a gold dimer with $R = 40\,\text{nm}$. Gap is $R/4$ in both cases. Sizes were chosen to obtain resonances around $\lambda = 600\,\text{nm}$. Incident planewave polarized along dimer axis. Dimers are placed in vacuum. A sketch of the model and numerical mesh used in the simulations for the gold and silicon dimers is shown above the plots.

by the numerical simulations comparing the scattering efficiencies from gold and silicon dimers, shown in Fig. 1.3. In summary, dielectric antennas may be equal or even favorable alternatives to plasmonic systems, dependent on the targeted application.

1.1.4 Hybrid Plasmonic-Dielectric Nanostructures

In many regards, the plasmonic and dielectric platforms offer complementary properties. It is therefore not surprising, that efforts are being made to bring together both systems into hybrid plasmonic-dielectric nanostructures and combine their mutual advantages.

High-index particles have been used for example as "sensors" for plasmons, coupling propagating SPPs on metal surfaces to the farfield [151]. Inversely, metal particles were incorporated in dielectric waveguides to filter frequencies in the waveguide transmission around the plasmonic particles' resonance [152]. In different works, the coupling between plasmonic particles and dielectric nanowires was used to circumvent the polarization-anisotropy in scattering from semiconductor nanowires [153, 154]. In this context, metal/dielectric nanospheres were proposed as "super-scatterers" with remarkably high scattering efficiencies due to superposition of multiple resonances [155] or inversely "super-absorbers" were designed by decorating silicon nanowires with plasmonic gold particles [156]. In quantum dot doped NWs, lasing from sub diffraction-limit mode-volumes was realized by coupling to SPPs [157]. Plasmonic antennas were employed to boost photoluminescence from III-V semiconductor nanostructures via strong field enhancement [158]. Hybrid waveguides were suggested that offer spectrally broad high power transmissions and could be promising for scanning-tip microscopy applications like SNOM in order to guide light to few square-nanometer small sample areas [159]. Concepts to

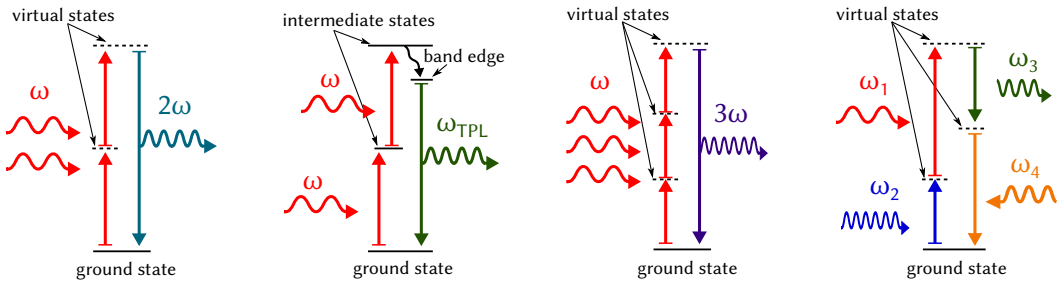

(a) SHG (b) TPL (c) THG (d) FWM

Figure 1.4: Schemes illustrating (a) second harmonic generation, (b) two photon induced photoluminescence, (c) third harmonic generation and (d) one possible interaction diagram of four-wave mixing.

improve directional emission have also been proposed on the basis of hybrid plasmonics. Compared to an all-metal design [30], enhanced directivity could be achieved using a metal antenna as driving element and a low-loss dielectric antenna as director [160]. In a similar work the significantly lower losses have been pointed out, using a dielectric component to reduce re-absorption [161]. Also, difficulties associated with the weak optical magnetism of plasmonic particles can be avoided using mixed metal-dielectric structures [162]. This might be an important concept if strong magnetic fields are desired in the vicinity of metal structures. Finally, promising applications can also be found in photovoltaics. For example, patterned metal-films with embedded silicon nano-pillars showed drastically increased absorption compared to non-patterned films, while the low electrical resistance of the metal film was maintained [163].

1.2 Nonlinear Effects

All properties and applications of nano-photonic particles described above were based on a linear optical response. If the amplitude of the exciting electromagnetic field is high enough, *nonlinear* optical effects occur, that can offer a large range of unique functionalities beyond linear optics. Probably the most popular nonlinear optical effect is harmonics generation [164]. Among this, the most prominent examples are second harmonic (SHG, illustrated in Fig. 1.4a) and third harmonic generation (THG, Fig. 1.4c): Two (or three) photons of a fundamental wavelength λ_0 are coherently up-converted (i.e. the process happens instantaneously, there are no intermediate states) to a single photon with $\lambda_{\mathrm{SHG}} = \lambda_0/2$ (or $\lambda_{\mathrm{THG}} = \lambda_0/3$). Apart from harmonics generation, other widely exploited nonlinear phenomena are: Sum- and difference-frequency generation (not shown), four-wave mixing (FWM, Fig. 1.4d) used for example in optical parametric oscillators and amplifiers [165, 166], or two photon induced photoluminescence (TPL, see Fig. 1.4b), which is an incoherent conversion of two incident photons to one photon of shorter wavelength (with $\lambda_0 > \lambda_{\mathrm{TPL}} > \lambda_0/2$), involving intermediate states with finite lifetimes [167, 168].

The link between nonlinear optics and nano-antennas is the need of high field amplitudes in the former and the possibility to strongly enhance electric fields in the latter. Therefore nano-photonic structures seem ideal candidates to evoke nonlinear effects and increasing interest is

being put on nonlinear nano-optics. In this section, we give an overview on current research and on applications of nonlinear effects in nanometric plasmonic and dielectric systems.

1.2.1 Nonlinear Plasmonics

Following the outline of the previous section, we will start with some brief examples of current research on nonlinear effects in plasmonics.

In gold, which is a centrosymmetric crystal, second order nonlinear effects such as SHG vanish in the dipolar approximation [169]. Nevertheless, by breaking the symmetry at the level of the nano-structure design, significant SHG can be obtained from gold plasmonic antennas [170]. It turned out, that SHG can even be further enhanced using multi-resonant antennas with modes at λ_0 and $\lambda_0/2$ [171–175], but the efficiency of propagation of SHG to the farfield remains crucially dependent on microscopic symmetries [176, 177]. It has been shown, that by using a control beam at $\lambda_0/2$, the directionality and scattering efficiency of SHG can be controlled [178]. Furthermore, size dependent polarization effects occur in SHG from nanoparticles, that arise from different physical processes at the origin of the nonlinear radiation [179, 180]. Equally to SHG, also THG can be heavily enhanced in resonant plasmonic antennas [181]. Other nonlinear effects like sum- or difference-frequency generation and four-wave mixing can also be enhanced [182, 183]. Apart from enhancement of nonlinear processes, the incoherent character of two photon luminescence can be used to image spatial mode distributions in larger two-dimensional plasmonic resonators [38, 39, 184, 185]. A more extensive overview on nonlinear plasmonics can be found in reviews on this topic, e.g. by Kauranen and Zayats [186] or by Butet et al. [187].

Despite all recent progresses in nonlinear plasmonics it has been shown that the efficiency of nonlinear processes in metal nano-particles is inherently limited, mainly due to dissipation processes [188].

1.2.2 Nonlinear Effects in Dielectric Nanostructures

Because of lower losses and other advantages like compatibility to CMOS technology (for silicon), high-index dielectric structures may also be promising alternatives to nonlinear plasmonics. Particularly nonlinear photonics on the silicon platform are subject of current research, with the goal of implementing all-optical signal processing in Si-based microelectronic devices [189]. Third-order nonlinear effects are very promising in this context, because of the inherently high $\chi^{(3)}$ of silicon. This allows enhanced third harmonic generation with factors of up to 10^5 compared to bulk Si using photonic crystals [190] or dielectric nano-antennas [191–194]. Harmonic light can be produced, intense enough to be visible with the bare human eye [195].

1.2.2.1 SHG from Non-Centrosymmetric Materials

Despite the great prospects of third order effects, they can be experimentally inconvenient because the fundamental frequency has to be chosen in the infrared in order to obtain a response in the visible. Therefore, second order effects and in particular second harmonic generation (SHG) are subject of current research. In this context, dielectrics with a non-centrosymmetric crystal offer a great advantage over plasmonics, because SHG can be generated from the bulk crystal itself.

Strong second harmonic light could be for example generated from subwavelength small AlGaAs cylinders and was found to be enhanced by magnetic Mie resonances [196]. Using this strong SHG in nonlinear farfield-microscopy was used to reveal the spatial patterning of hybrid guided- / Mie-modes (see also [69]) in GaAs nanowires [197]. Control on properties of nonlinear effects has also been reported. For example the directionality of the (strongly enhanced) SHG from ZnTe NWs [198] or AlGaAs nanodiscs [199] can be controlled by means of the incident beam polarization and the particle's aspect ratio. Also the polarization of the SH light in the farfield could be controlled by modal engineering in GaP nanopillars [200].

1.2.2.2 SHG from Centrosymmetric Materials

Elemental silicon is among the experimentally most convenient materials. Unfortunately, like all elemental crystals with face-centered cubic (fcc) lattice, bulk Si has an inversion symmetry and therefore doesn't support second order nonlinear effects in the dipolar approximation.

Nevertheless, second order nonlinear effects and particularly SHG is still of interest in centrosymmetric nano-particles. Due to a breaking of the inversion symmetry at interfaces and with large surface-to-volume ratios in small particles, the effective nonlinear susceptibility is actually non-zero. Furthermore, field-gradients can arise due to tight focusing or resonant optical modes, that also break the symmetry locally and support a second-order nonlinear response. Therefore, a lot of theoretical work has been done for SHG from nanoparticles of centrosymmetric materials [201–206]. Experimentally, enhancement of SHG has been reported for example from SiNW arrays ($> \times 50$ compared to bulk) [207]. Also Si photonic crystals can enhance SHG and THG significantly, even under cw excitation sufficiently strong fields could be obtained to generate measurable second harmonic light. Radiation patterns confirmed in these experiments, that THG is indeed generated within the bulk, while SHG is a surface effect [195]. As SHG requires a breaking of the symmetry at some point, strained dielectric slabs have been studied in this context as well. And indeed, a good enhancement of SHG from strained silicon [208, 209] or germanium waveguides [210] was found. However, it has been recently reported that the influence of strain on the bulk second order susceptibility of silicon had been overestimated earlier [211].

1.2.3 Hybrid Plasmonic/Dielectric Structures

Also in nonlinear nano-optics, attempts are being made to combine advantages of plasmonics and high-index dielectrics. A tremendous increase of THG by a factor of 10^6 could be achieved by coupling indium-tin-oxide (ITO) to the enhanced nearfield of a plasmonic antenna [212]. In an other work, the efficiency of FWM (Fig. 1.4d) could be increased using a hybrid silicon/plasmonic waveguide [213].

1.2.4 Applications

Probably the best motivation for further investigations on nonlinear properties are the manifold possible applications of nonlinear optical effects in nano-structures. The fact that SHG from centrosymmetric crystals is a surface effect is widely exploited for macroscopic surface characterization [214–218]. But also on a nanometer scale, characteristic surface signatures can be obtained from SHG spectroscopy. The surface second harmonic light from gallium-nitride (GaN) nanowires for example contains a signature of the surface orientation [219] or aluminum grain

boundary interfaces can be analyzed by SHG microscopy [220]. Nonlinear optical effects are also widely used in signal processing based on silicon photonics [189]. As an example, a passive optical modulator was realized thanks to a strain-induced increase in nonlinearity by one order of magnitude in silicon waveguides [221]. Also ultrafast all-optical switching can be obtained in silicon nano-structures, making use of a spectral shift of the magnetic dipole resonance caused by two-photon absorption [222]. Apart from quantum computing, where a lot of effort is put in both linear [223–225] and nonlinear [226] optical techniques, optical computing might also be done in a more classical way, basing on optical switching. An optical transistor would require some nonlinear optical phenomena in order to achieve a switching behavior. Such a device has been proposed as early as 1976 by Jain and Pratt Jr. [227] who suggested that a refractive-index perturbation induced by a "base" beam could be used to nonlinearly control the intensity of SHG from the device by a variation of the phase-matching condition. In this device, the equivalent to the collector would be the fundamental incident beam and the emitted SHG would correspond to a transistor's emitter. More recently, a polarization controlled logical element was proposed using TPL from plasmonic nanostructures supporting higher-order spatial modes [40].

Equivalently to surface second harmonic generation, SHG is highly sensitive to small changes of the nano-particle geometry, which has been proposed to be exploited for far-field measurements of few nanometer small distances using a kind of optical "nano-ruler" [228]. Infrared-excited SHG from dielectric GaP nanoparticles has been proposed as femtosecond nanometer light source at visible frequencies for applications related to bio-imaging [200]. In such nano-probes, engineering of the geometry allows to shape the modes and thereby the harmonic nearfield as well as its polarization state. In the context of nano-scale localized sensing, it has been shown that a nonlinear response can offer about one order of magnitude higher sensitivity to changes in the refractive index compared to linear optical refractive index sensing [229]. An other work-group used cadmium-sulfide (CdS) NWs as nanometer scale optical correlators which opens perspectives for on-chip ultrafast optical technologies [230]. Finally, nonlinear effects can be used in bio-medical applications. SiNWs were used as biomarkers and excited with an infrared fs-laser. The detected THG provides not only the biomarkers' positions but also information on their orientation due to anisotropic THG as a result from the high aspect ratio of the NWs [231].

1.3 Scope of this Work

The focus in this work will be put on nonlinear effects in dielectric structures, in particular in silicon nanowires. In the first part (page 13 and following), the fundamental electro-dynamical theory will be introduced and an introduction to nonlinear optical effects will be given. We will give an overview on the Green dyadic method (GDM), a technique for the numerical modeling of the response of nano-objects to an excitation by electromagnetic fields. In this context, also for nonlinear optical effects a numerical description will be presented and discussed (page 39 and following).

In the second part (page 55 and following), a thorough study of the optical behavior of silicon nanowires (SiNWs) in the visible spectral range will be performed. At first, the linear optical properties will be discussed. Subsequently the nonlinear optical response will be subject of an experimental and theoretical analysis. Finally, second harmonic generation (SHG) will be examined in detail and we will find, that the origin of the frequency doubling in SiNWs depends on the polarization of the fundamental field as well as on the size of the nanowires, which opens

interesting perspectives for further studies of surface SHG from nanowires or for applications which require control of the harmonic emission.

In the last part (page 89 and following), we will discuss the more technological problem of nanostructure design. As described above, optical properties of photonic nanostructures can be tailored to specific needs. For this, usually some reference design is chosen by intuitive considerations. By a systematic analysis of the system, the desired properties are maximized subsequently. However, finding optimum geometries for a given problem is not trivial, and often trade-offs have to be made. We therefore tackle the problem in an inverse way: After defining the desired optical properties, a corresponding geometry is searched using evolutionary optimization algorithms. We show, that using a thorough definition of the problem and structure model, this technique can be used for the optimization and automatic design of photonic nanostructures with regards to various optical properties. To demonstrate the approach, we apply evolutionary optimization on silicon nanostructures to obtain maximum SHG as well as on plasmonic nanoantennas for directional scattering. At last, we employ an even more general *multi-objective* evolutionary algorithm in order to simultaneously maximize scattering at two target wavelengths in multi-resonant dielectric nano-scatterers. The optimized structures are finally fabricated by electron-beam lithography and the predictions of the experiment are verified experimentally.

Chapter 2

Modeling Optical Effects at the Nanoscale

When James Clark Maxwell worked out his groundbreaking equations in the 1860s [1], he noticed that they naturally describe a fundamental property of electromagnetic fields: The ability to propagate as waves at the speed of light – even in vacuum, independent of any carrying medium. Electromagnetic waves in a range of wavelengths from the ultraviolet to the far infrared (some 10 nm to several 10 µm) are usually referred to as *light*, including the visible light from around 400 nm to 700 nm. The description of effects from the interaction of light with subwavelength small particles will be the scope of this chapter.

2.1 Definition of the Problem

Generally, the goal of nano-optical problems is to find the electric (and / or magnetic) fields in a particular nanostructure under external excitation, like illustrated in figure 2.1a. The nanostructure is usually placed in a homogeneous environment and often lies on top of a substrate. The external excitation is usually realized by a laser beam. Other possible fundamental fields such as electron beam excitation [232] are outside the scope of this work but can be treated formally equal to "classical" electromagnetic fields [233].

The response of a nanoparticle to an illumination is obtained by resolving Maxwell's equations for the given system. In the first part of this chapter we will introduce the fundamental electrodynamical theory. We then present a volume integral approach for the numerical resolution of Maxwell's equations based on Green's dyadic functions. In the last part we give an introduction to nonlinear optics and present an extension of the numerical model for the description of Second Harmonic Generation.

2.2 Electrodynamics

2.2.1 Maxwell's Equations

All kind of electromagnetic phenomena are entirely explained by the four *Maxwell's equations* which write (in SI units):

$$\mathrm{div}\mathbf{D} = \rho \tag{2.1a}$$

$$\mathrm{rot}\mathbf{E} = -\frac{\partial \mathbf{B}}{\partial t} \tag{2.1b}$$

$$\mathrm{div}\mathbf{B} = 0 \tag{2.1c}$$

$$\mathrm{rot}\mathbf{H} = \frac{\partial \mathbf{D}}{\partial t} + \mathbf{j} \tag{2.1d}$$

with the current density $\mathbf{j}$, the charge density ρ, the electric field $\mathbf{E}$ and electric displacement $\mathbf{D}$ as well as the magnetic field $\mathbf{B}$ and the magnetizing field $\mathbf{H}$. All above fields are functions of space ($\mathbf{r}$) and time (t). Interaction of matter with light is described by solutions for the electromagnetic fields that fulfill Maxwell's equations for the considered system. Most commonly, the electric displacement is related to the electric field using the electric polarization density $\mathbf{P}$

$$\mathbf{D} = \epsilon_0 \mathbf{E} + \mathbf{P} \tag{2.2}$$

and the magnetizing field to the magnetic field using the magnetization density $\mathbf{M}$

$$\mathbf{H} = \frac{1}{\mu_0}\mathbf{B} - \mathbf{M} \tag{2.3}$$

The response of material to fields is represented by this electric polarization and magnetization (see figure 2.1a). They are defined as the electric dipole moment $\mathrm{d}\mathbf{p}$ and the magnetic moment $\mathrm{d}\mathbf{m}$ per volume element $\mathrm{d}V$, respectively (for details, see e.g. [234, chapter 4.1 and 6.1]):

$$\mathbf{P} = \frac{\mathrm{d}\mathbf{p}}{\mathrm{d}V} = \epsilon_0 \chi \, \mathbf{E} \tag{2.4a}$$

$$\mathbf{M} = \frac{\mathrm{d}\mathbf{m}}{\mathrm{d}V} = \chi_\mathrm{m} \, \mathbf{H} \tag{2.4b}$$

Like the fields, both the polarization and the magnetization are functions of space and time. The right-hand side terms are first-order Taylor expansions of $\mathbf{P}$ and $\mathbf{M}$ as function of the electric and magnetizing fields, respectively. These linear approximations are valid only for linear materials. We will see in section 2.4, that we can describe non-linear effects by introducing higher-order terms to the equations for the polarization and magnetization.

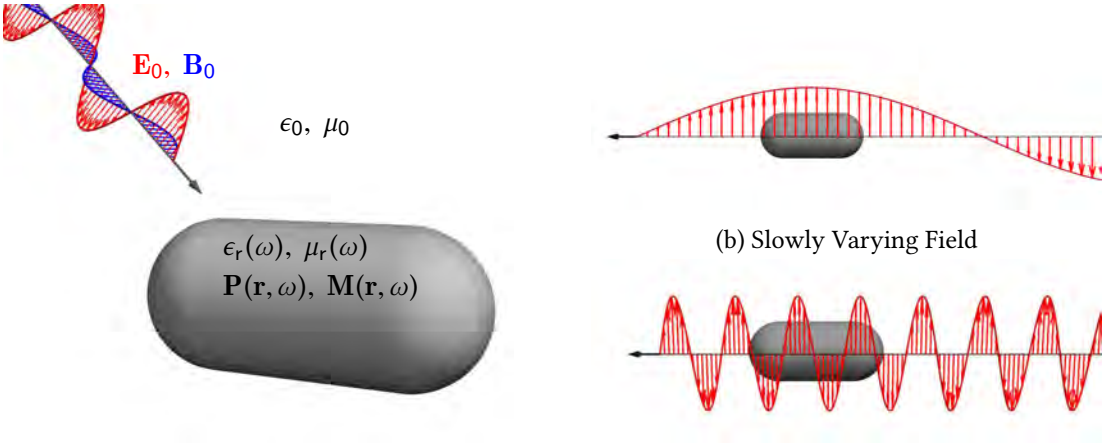

(a) Nano-Object in Vacuum

(b) Slowly Varying Field

(c) Rapidly Varying Field

Figure 2.1: (a) shows an arbitrary object placed in vacuum made of a material characterized by ϵ_r and μ_r. Its response to incident electromagnetic fields $\mathbf{E}_0$, $\mathbf{B}_0$ can be described by the polarization $\mathbf{P}$ and the magnetization $\mathbf{M}$. In (b) a nano-object which is small compared to the wavelength is shown, whereas in (c) a particle is shown with large size compared to the wavelength.

2.2.2 Dielectric Permittivity

The above equations together with eq. (2.2) and (2.3) yield the so called constitutive relations [235, chapter 2.3]

$$\mathbf{D} = \epsilon_0 \epsilon_r \, \mathbf{E} \tag{2.5a}$$

$$\mathbf{B} = \mu_0 \mu_r \, \mathbf{H} \tag{2.5b}$$

with $\chi = \epsilon_r - 1$ and $\chi_\mathrm{m} = \mu_r - 1$. ϵ_r and μ_r are the relative dielectric permittivity and magnetic permeability, respectively. They are defined as the ratios of the material's permittivity and permeability relative to the vacuum values ϵ_0 and μ_0.

For simplicity, we will consider in the following only non-magnetic media, i.e. we assume $\mu_r = 1$ and consequently $\mathbf{M} = 0$.

The dielectric permittivity describes the wavelength dependent response of a material to electromagnetic fields. All interplaying physical effects are phenomenologically combined in this material constant. The refractive index is linked to ϵ_r and μ_r by

$$n = \sqrt{\epsilon_r \mu_r} = \sqrt{\epsilon_r} \quad \text{(non-magnetic media)} \tag{2.6}$$

Note that ϵ_r is complex in our notation, the imaginary part is responsible for energy dissipation. For details see for example [235, chapter 2.6].

In the following, we will give a brief comparison of the dielectric behavior of metals and dielectrics.

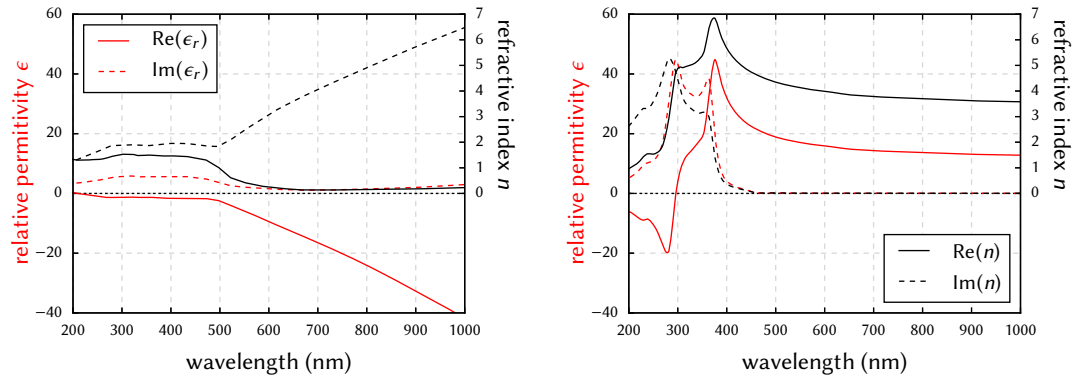

(a) Gold (b) Silicon

Figure 2.2: Dispersion of gold (a) and silicon (b). The permittivity is drawn in red, the refractive index in black color. The respective real parts are shown with solid, imaginary parts with dashed lines.

2.2.2.1 Metals

In metals, an impinging electromagnetic wave induces collective oscillations of the conduction electrons, so-called surface plasmon polaritons (SPP) [5]. Because of electromagnetic screening due to the free carriers at visible frequencies, those oscillations are bound to a small volume at the surface of the metal, characterized by the *skin-depth* [4] (see eq. (2.10)). The screening effect is described by a negative real part of the dielectric permittivity, leading to purely evanescent fields inside metals. The collective electron oscillations can be driven to a resonance at the so-called plasma frequency ω_p.

The permittivity of gold (from [236]) is shown as an example in Fig. 2.2a. The non-zero $\mathrm{Im}(\epsilon_r)$ is responsible for thermal dissipation. As consequence of this, together with the negative real part of ϵ_r, the imaginary part of the refractive index n is much larger than its real part. This generally reflects the fact that electromagnetic waves are strongly damped inside the metal.

The relative permittivity of metals can be roughly approximated by the Drude model [237]. Following the notation of Johnson and Christy [236], the permittivity can be written using a Lorentzian oscillator model

$$\epsilon_r(\omega) = \frac{\omega_\mathrm{p}^2}{\omega_\mathrm{p}^2 - \omega^2 - \mathrm{i}\omega/\tau_e} \tag{2.7}$$

with the electron relaxation time τ_e and the plasma frequency ω_p [238, chapter 1]

$$\tau_e = \frac{m\sigma}{N_e e^2}, \qquad \omega_\mathrm{p} = \sqrt{\frac{N_e e^2}{\epsilon_0 m}} \tag{2.8}$$

where ϵ_0 is the vacuum permittivity, σ the Drude conductivity, N_e the electron number density, e the electron charge and m its effective mass. For frequencies sufficiently far below the plasmon resonance at ω_p, this is a reasonable approximation.

2.2.2.2 Dielectrics

In dielectrics, the absence of free charge carriers results in an entirely different dispersion relation. Dielectrics respond to electric fields by a local displacement of bound charges relative to the lattice atoms. No screening takes place and electromagnetic fields can propagate inside the medium. Therefore, the relative permittivity is positive in dielectrics.

In Fig. 2.2b, the dispersion of silicon (from [239]) is shown as an example. If the photon energy is lower than the direct band gap (in Si at around 370 nm), the dielectric constant is mainly real and positive valued. The refractive index is also almost purely real and very high – between 3 and 4 throughout the visible and infrared. In consequence silicon absorbs very little compared to metals. If the photon energy is higher than the direct bandgap, free carriers can be excited and the dielectric permittivity is not necessarily positive anymore. This can be seen in the silicon dispersion below $\lambda \approx 370\,\mathrm{nm}$

Generally, the dispersion of dielectrics can also be described by an oscillator model, formally equal to equation (2.7). For silicon, very accurate dispersion models for the visible spectral range exist, using multiple oscillators [240, 241].

2.2.3 Quasistatic Approximation

Before we elaborate a way to obtain general solutions of Maxwell's equations, let's consider a particular case of light-matter interaction. In structures whose dimensions are much smaller than the wavelength, thus $d \ll \lambda_0$, effects induced by a varying field amplitude along a structure (so-called *retardation*) can usually be neglected. Such a situation is shown in figure 2.1b. The electric field over the whole particle is regarded as totally in phase. This is referred to as the *quasistatic approximation*, in which the displacement current $\partial\mathbf{D}/\partial t$ is neglected and equation (2.1d) simplifies to

$$\mathrm{rot}\mathbf{H} \approx \mathbf{j} \tag{2.9}$$

which is known as Ampere's law.

For metal nanoparticles, the field decays exponentially from the surface towards the bulk core. In this case, the quasistatic approximation requires the further condition that the size of the nanoparticle is small compared to the skin depth [4]

$$d_{\mathrm{skin}} = \frac{\lambda_0}{2\pi}\sqrt{\frac{\epsilon_0 + \epsilon_r}{\epsilon_0^2}} \tag{2.10}$$

which is given here for a particle of permittivity ϵ_r placed in vacuum. For metal structures significantly smaller than d_{skin}, the internal field can be considered homogeneous over the nanoparticle and proportional to the external field.

Many theoretical models in nano-optics are based on this approximation. A prominent example is the so called *Rayleigh scattering*, scattering from very small subwavelength particles in the quasistatic limit [242]. Rayleigh scattering is responsible for the blue color of the sky. As we will see in more detail in section 2.4, also second harmonic generation from dielectric nanoparticles can be analytically described by making simplifications like the assumption of quasistatic fields [202, 243].

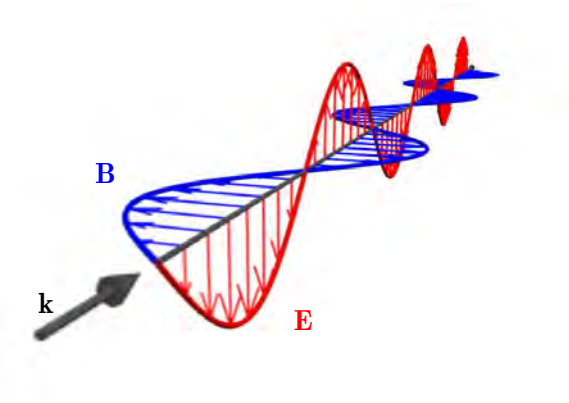

Figure 2.3: Sketch of a monochromatic electromagnetic wave.

2.2.4 Problems Including Retardation Effects

The quasistatic approximation can only be applied on particles whose size is significantly smaller than the wavelength of the incident light. For particles large compared to the wavelength like the one illustrated in figure 2.1c, retardation effects occur and Maxwell's equations must be solved rigorously in order to describe the resulting phenomena.

2.2.4.1 Time Harmonic Fields in Phasor Representation

We will see that it is of enormous practical advantage to consider monochromatic fields. This is not such a restriction as it might occur in the first place because the use of harmonic waves as *ansatz* for the solution of Maxwell's equations can subsequently be generalized to arbitrarily time-dependent fields by a superposition of harmonic fields and inverse Fourier transformation. In the following, we will therefore express all fields using complex exponentials:

$$\mathbf{E}(\mathbf{r},t) = \hat{\mathbf{E}}_0(\mathbf{r})\,\mathrm{e}^{\mathrm{i}(-\omega t+\varphi)} \tag{2.11}$$

with the amplitude $\hat{\mathbf{E}}_0$, the wavevector $\mathbf{k}_0$, the angular frequency ω and a phase φ. As we treat harmonic oscillations, the angular frequency is a convenient way to express the wavelength λ and writes:

$$\omega = \frac{2\pi c}{\lambda} = k_0 c \tag{2.12}$$

with the wavenumber $k_0 = |\mathbf{k}_0|$ and the speed of light c

$$c = \frac{1}{\sqrt{\epsilon_0 \mu_0}} \tag{2.13}$$

It is possible to separate the phase φ from the argument of the exponential in eq. (2.11) and include it in the complex amplitude:

$$\mathbf{E}(\mathbf{r},t) = \hat{\mathbf{E}}_0(\mathbf{r})\,\mathrm{e}^{-\mathrm{i}\omega t}\,\mathrm{e}^{\mathrm{i}\varphi} = \mathbf{E}_0(\mathbf{r})\,\mathrm{e}^{-\mathrm{i}\omega t} \tag{2.14}$$

The amplitude $\mathbf{E}_0(\mathbf{r}) = \hat{\mathbf{E}}_0(\mathbf{r})\,\mathrm{e}^{\mathrm{i}\varphi}$ is called a *phasor* or, more literally, a *complex amplitude*. The imaginary part of $\mathbf{E}_0$ contains the total phase information which is given by the angle in the

complex plane

$$\varphi(\mathbf{r}) = \text{atan2}\Big(\text{Im}\left(\mathbf{E}_0(\mathbf{r})\right), \text{Re}\left(\mathbf{E}_0(\mathbf{r})\right)\Big). \tag{2.15}$$

φ is also a function of space. The real part of the complex field $\mathbf{E}(\mathbf{r}, t)$ represents the *physical* amplitude of the electric field at time t. We note that it is possible to sum, substract or differentiate phasors without limiting the generality.

The above expressions hold equally for the magnetic field of electromagnetic waves.

2.2.4.2 Wave Equation

The time-harmonicity of the fields can now be used to explicitly perform the differentiation $\partial/\partial t$ in equations (2.1) which leads to the macroscopic, Fourier transformed Maxwell's equations (compare with [235, chapter 2.4]):

$$\text{div}\mathbf{D}(\mathbf{r}, \omega) = \rho(\mathbf{r}, \omega) \tag{2.16a}$$
$$\text{rot}\mathbf{E}(\mathbf{r}, \omega) = \text{i}\omega\mathbf{B}(\mathbf{r}, \omega) \tag{2.16b}$$
$$\text{div}\mathbf{B}(\mathbf{r}, \omega) = 0 \tag{2.16c}$$
$$\text{rot}\mathbf{H}(\mathbf{r}, \omega) = -\text{i}\omega\mathbf{D}(\mathbf{r}, \omega) + \mathbf{j}(\mathbf{r}, \omega) \tag{2.16d}$$

Maxwell's equations represent a coupled system of linear, partial differential equations. They can be decoupled by applying the vectorial curl operator ($\text{rot}\mathbf{A} = \nabla \times \mathbf{A}$) on equation (2.16b) and substituting with eq. (2.16d). By then making use of the relations between the electric field and the displacement and between magnetizing field and magnetization (Eqs. (2.2) and (2.3)), we obtain

$$\begin{aligned} \text{rot}(\text{rot}\mathbf{E}) &= \text{i}\omega\,\text{rot}\mathbf{B} \\ &= \text{i}\omega\mu_0\Big(\text{rot}(\mathbf{H} + \mathbf{M})\Big) \\ &= \text{i}\omega\mu_0(-\text{i}\omega\mathbf{D} + \mathbf{j}) \\ &= \text{i}\omega\mu_0(-\text{i}\omega\epsilon_0\epsilon_r\mathbf{E} + \mathbf{j}) \\ &= \epsilon_r\frac{\omega^2}{c^2}\mathbf{E} + \text{i}\omega\mu_0\mathbf{j} \end{aligned} \tag{2.17}$$

We consider non-magnetic media and therefore $\mathbf{M} = 0$. Using the identity

$$\nabla \times (\nabla \times \mathbf{A}) = \nabla(\nabla\mathbf{A}) - \Delta\mathbf{A} \tag{2.18}$$

and

$$\mathbf{D} = \epsilon_0\mathbf{E} + \mathbf{P} \quad \Rightarrow \quad \text{div}\mathbf{D} = \epsilon_0\text{div}\mathbf{E} + \text{div}\mathbf{P} = 0 \tag{2.19}$$

we find

$$\epsilon_r\frac{\omega^2}{c^2}\mathbf{E} + \Delta\mathbf{E} = \frac{-1}{\epsilon_0\epsilon_r}\nabla(\text{div}\mathbf{P}) - \text{i}\omega\mu_0\mathbf{j}. \tag{2.20}$$

Eq. (2.19) means that we consider only media with vanishing free charge density ($\rho_\text{f} = 0 \rightarrow \rho = \rho_\text{b}$[1]), in order to be able to make some further simplifications[2].

[1] ρ_b is the *bound* charge density where by definition holds $\rho_\text{b} = -\text{div}\mathbf{P}$, see for example [234, chapter 4.2.1]

[2] The reason why the simplification of a dielectric constant works also in the case of metals where free carriers seem to exist is because the dielectric function is based on the *macroscopic* Maxwell's equations (Eqs. (2.17)). When

With the speed of light $c^2 = (\epsilon_0\mu_0)^{-1}$ and the wavenumber inside the non-magnetic medium $k = \sqrt{\epsilon_r}\, k_0 = \sqrt{\epsilon_r}\, \omega c^{-1}$ this becomes

$$(\Delta + k^2)\mathbf{E} = \frac{-1}{\epsilon_0\epsilon_r}\nabla\nabla\mathbf{P} - \mathrm{i}\omega\mu_0\mathbf{j}. \tag{2.21}$$

In linear materials, dipolar approximations of the bound charge density $\rho_\mathrm{b}(\mathbf{r}, \omega)$ and the current density $\mathbf{j}(\mathbf{r}, \omega)$ can be developed by means of the electric polarization (2.4a)

$$\rho_\mathrm{b} = -\nabla\mathbf{P} \tag{2.22}$$

$$\mathbf{j} = \frac{\partial}{\partial t}\mathbf{P} = -\mathrm{i}\omega\,\mathbf{P}. \tag{2.23}$$

While the latter relation is evident because we are assuming time-harmonic fields, Eq. (2.22) can be easily derived from the definition of the electric polarization density (see for example [234, chapter 4.2.1]).

Inserting (2.23) in equation (2.21) (we included Eq. (2.22) in our derivation already using Eq. (2.19)) eventually brings us to the wave equation for the electric field:

$$(\Delta + k^2)\mathbf{E} = -\frac{1}{\epsilon_0\epsilon_r}\nabla\nabla\mathbf{P} + \omega^2\mu_0\mathbf{P} \tag{2.24}$$

$$\boxed{(\Delta + k^2)\mathbf{E} = -\frac{1}{\epsilon_0\epsilon_r}\left(k^2 + \nabla\nabla\right)\mathbf{P}.} \tag{2.25}$$

We want to point out, that this equation is formally identical to the mechanical wave equation describing for example an oscillating string [234, chapter 9.1]. In the case of the electromagnetic wave equation, the speed of the propagation is the speed of light c which eq. (2.25) contains implicitly through the wavenumber k. Furthermore the waveequation is found to be a more general form of Poissons' equation in electrostatics, which it becomes in the static case, i.e. when $k = 0$ [244].

While we will limit our considerations to non-magnetic media, we point out as a final note that an analogous wave equation can be found likewise for the magnetic field (see for example [234, chapter 9.2]).

2.2.5 Green's Functions

In order to solve an inhomogeneous linear partial differential equation like the wave equation, the concept of *Green's functions* is a versatile tool. At first we want to illustrate the basic idea. For this we start with a differential equation

$$LA(x) = g(x) \tag{2.26}$$

integrating the macroscopic system, free charge carriers only exist if the metal is actually charged. If this is not the case, a dielectric function can indeed be used to describe the metal's optical properties including plasmonic effects.

where L is an arbitrary linear differential operator and $g(x)$ the inhomogeneity of the differential equation. It would be pleasant to obtain something like an inverse of the differential operator L in order to write $A(x) = L^{-1}g(x)$. Unfortunately, the operator L can in general not be inverted[1]. The principle idea is therefore to search an operator G for which holds

$$LG = 1 \tag{2.27}$$

If it is possible to find such an operator G, we obtain also a particular solution of eq. (2.26):

$$LA(x) = (LG)g(x) = L(Gg(x)) \qquad \Rightarrow \qquad A(x) = Gg(x) \tag{2.28}$$

Instead of searching an operator G for the inhomogeneity "1" as we did in eq. (2.27) for our demonstration, it turns out to be of more general use to consider a point-source-like inhomogeneity defined by a Dirac delta function $\delta(x - x')$

$$LG(x, x') = \delta(x - x') \tag{2.29}$$

Note that in general, the *Green's function* G defined by eq. (2.29) is not only dependent on the parameter of the differential equation (here x), but also on the position of the inhomogeneity x'. Multiplication with the original inhomogeneity and integration of eq. (2.29) leads to

$$\begin{aligned} \int LG(x, x')g(x)\mathrm{d}x &= \int \delta(x - x')g(x)\mathrm{d}x \\ &= g(x) \\ &= LA(x) \end{aligned} \tag{2.30}$$

Making use of the linearity of L we finally have:

$$A(x) = \int G(x, x')g(x)\mathrm{d}x \tag{2.31}$$

Thus we solved the differential equation for arbitrary inhomogeneities $g(x)$, provided that G can be found from eq. (2.29). Note that we assumed here that L can be pulled out of the integral in eq. (2.30).

2.2.6 Green's Function for the Electromagnetic Wave Equation

Let's write again the wave equation for the electric field (eq. (2.25))

$$(\Delta + k^2)\mathbf{E} = -\frac{1}{\epsilon_0\epsilon_r}\left(k^2 + \nabla\nabla\right)\mathbf{P} \tag{2.32}$$

By assuming time-harmonic fields, we could eliminate the time-derivatives in Maxwell's equations which rendered eq. (2.32) to the form of a Helmholtz equation:

$$(\Delta + k^2)\, A(x) = g(x) \tag{2.33}$$

[1] or the Method of Green's functions is simply much easier to employ or yields a more general solution

As depicted in section 2.2.5, the associated Green's function G_0 is defined by considering a Dirac function as inhomogeneity:

$$(\Delta + k^2)\, G_0(x, x') = \delta(x - x'). \tag{2.34}$$

From this definition, G_0 is found to be

$$G_0(\mathbf{r}, \mathbf{r}') = \frac{1}{4\pi} \cdot \frac{\mathrm{e}^{\pm \mathrm{i}k\,|\mathbf{r}-\mathbf{r}'|}}{|\mathbf{r} - \mathbf{r}'|} = \frac{\mathrm{e}^{\pm \mathrm{i}kR}}{4\pi R}. \tag{2.35}$$

In the latter equation, we replaced the parameter x by the distance $R = |\mathbf{R}| = |\mathbf{r} - \mathbf{r}'|$ between source point $\mathbf{r}'$ and observation position $\mathbf{r}$. For a detailed derivation of eq. (2.35) see for example [244, chapter 6.4] or [245, chapter 1.2].

The scalar Green's Function for the wave equation (equation (2.35)) corresponds to an incoming (minus sign) or outgoing (plus sign) spherical wave. After equation (2.31), solutions of the wave equation can be written as an integral over this scalar Green's function. This is equivalent to a superposition of spherical waves and thus identical to the Huygens-Fresnel principle.

2.2.7 Dyadic Green's Function

An electric dipole oscillating in X direction will in general induce an electric field with x, y and z components. As a consequence, the scalar Green's function (eq (2.35)) is not fully sufficient to develop solutions of the wave equation. We therefore need to extend the scalar Green's function to a notation that corresponds to the vectorial character of the fields. Following [235, chapter 2.10], we can define a Green's function for each component of the electric field

$$(\Delta + k^2)\, \mathbf{G}_x(\mathbf{r}, \mathbf{r}', \omega) = \mathbf{n}_x \cdot \delta(\mathbf{r} - \mathbf{r}') \tag{2.36}$$

where $\mathbf{G}_x$ is a vector composed of scalar Green's Functions and $\mathbf{n}_x$ is the unit vector in X direction. By doing the same for the Y and Z direction and the according components of the electric polarization, we can write

$$(\Delta + k^2)\, \mathbf{G}_{\mathrm{dyad}}(\mathbf{r}, \mathbf{r}', \omega) = \mathbf{I} \cdot \delta(\mathbf{r} - \mathbf{r}') \tag{2.37}$$

with the unit tensor $\mathbf{I}$. $\mathbf{G}_{\mathrm{dyad}}$ (in bold type) is a tensor with 3×3 components (because we are dealing with three-dimensional fields) and is called a *Green Dyad*, *Green tensor* or *Dyadic Green's function*. Dyadic Green's functions are a tight notation for N N-dimensional Green's functions.

In the following, we will define the Dyadic Green's function slightly differently. The concept however is identical to the here presented description.

2.3 Green Dyadic Method

After having presented the theoretical basis of electrodynamics and a short introduction to Green's formalism in the previous section, we now want to explicitly solve the wave equation for an arbitrary object placed in a homogeneous environment. For simplicity, we continue considering monochromatic (i.e. time-harmonic) waves propagating in linear, isotropic, homogeneous and non-magnetic media.

We will start with the derivation of the "Lippmann-Schwinger equation", which defines the self-consistent problem associated to the depicted configuration. We will develop the explicit form of Green's Dyad for a homogeneous environment and will subsequently present a method for the numerical resolution of the optical Lippmann-Schwinger equation. The generic term for the resolution of the wave equation by means of Green Dyadic functions is, for obvious reasons, *Green Dyadic Method*.

2.3.1 Lippmann-Schwinger Equation

By defining two operators (following the way of proceeding of Girard [246])

$$\mathcal{A} = \Delta + k^2 \qquad \mathcal{B} = -\frac{1}{\epsilon_r}\left(k^2 + \nabla\nabla\right) \tag{2.38}$$

we can write the wave equation for the electric field (eq. (2.25)) in a more compact form

$$\mathcal{A}\,\mathbf{E}(\mathbf{r},\omega) = \frac{1}{\epsilon_0}\,\mathcal{B}\cdot\mathbf{P}. \tag{2.39}$$

We now apply the concept of Green's functions (see section 2.2.5)

$$\mathcal{A}\,\mathbf{G}_0(\mathbf{r},\mathbf{r}',\omega) = \frac{1}{\epsilon_0}\,\mathcal{B}\,\delta(\mathbf{r}-\mathbf{r}'). \tag{2.40}$$

We formally make use of the invertibility of the Laplacian [247, vol. 3, "elliptic operators"] and write

$$\mathbf{G}_0(\mathbf{r},\mathbf{r}',\omega) = \frac{1}{\epsilon_0}\,\mathcal{A}^{-1}\,\mathcal{B}\,\delta(\mathbf{r}-\mathbf{r}'). \tag{2.41}$$

By comparing the latter with the particular solution of equation (2.39), we get

$$\begin{aligned}\mathbf{E}_\mathrm{p}(\mathbf{r},\omega) &= \frac{1}{\epsilon_0}\,\mathcal{A}^{-1}\,\mathcal{B}\cdot\mathbf{P}\\ &= \frac{1}{\epsilon_0}\,\mathcal{A}^{-1}\int \mathcal{B}\cdot\mathbf{P}(\mathbf{r}',\omega)\delta(\mathbf{r}-\mathbf{r}')\mathrm{d}\mathbf{r}'\\ &= \frac{1}{\epsilon_0}\int \mathbf{G}_0(\mathbf{r},\mathbf{r}',\omega)\cdot\mathbf{P}(\mathbf{r}',\omega)\mathrm{d}\mathbf{r}'.\end{aligned} \tag{2.42}$$

For the general solution of the electric field, we have to add the solution $\mathbf{E}_0$ of the homogeneous wave equation (in absence of any polarizing material, i.e. with finite electric susceptibility). Usually this will be the incident field – or in other words, the exciting field. We get

$$\mathbf{E}(\mathbf{r},\omega) = \mathbf{E}_0(\mathbf{r},\omega) + \frac{1}{\epsilon_0}\int \mathbf{G}_0(\mathbf{r},\mathbf{r}',\omega)\cdot\mathbf{P}(\mathbf{r}',\omega)\mathrm{d}\mathbf{r}'. \tag{2.43}$$

This equation signifies a remarkable result: Provided we have an expression for $\mathbf{G}_0$ we now know the emitted electric field at every position in space for arbitrary polarization densities.

If we recall the linear approximation $\mathbf{P} = \epsilon_0\chi\mathbf{E}$ of the polarization as function of the electric

field which we introduced in section 2.2.1, we can finally write for linear media

$$\boxed{\mathbf{E}(\mathbf{r},\omega) = \mathbf{E}_0(\mathbf{r},\omega) + \int \mathbf{G}_0(\mathbf{r},\mathbf{r}',\omega)\cdot\chi\mathbf{E}(\mathbf{r}',\omega)\mathrm{d}\mathbf{r}'} \tag{2.44}$$

where the integration is performed over the "source region", which is the volume where material exists with an electric susceptibility other than that of vacuum, i.e. $\chi \neq 0$. Equation (2.44) is the vectorial *Lippmann-Schwinger equation* for the electric field – a widely used equation in quantum mechanical scattering theory[1]. Quantum mechanics shares many formal ideas with optics – as one example, we remind of the close relation between particle wave functions and electromagnetic waves – so this analogy does not surprise too much.

We note that in a homogeneous and isotropic environment, the electric susceptibility of by themselves (piecewise) isotropic and homogeneous objects placed in this environment can be generalized very easily using their relative electric permittivities

$$\chi_{\text{rel.}}(\mathbf{r},\omega) = \begin{cases} \epsilon_{r,\text{mat.}}(\mathbf{r},\omega) - \epsilon_{r,\text{env.}}(\omega) & \text{for } \mathbf{r} \text{ inside the object(s)} \\ 0 & \text{for } \mathbf{r} \text{ in the environment} \end{cases}$$

2.3.2 Field Susceptibility for a Homogeneous Environment

For the explicit solution of the Lippmann-Schwinger equation (2.44), we need to find an analytical expression for the Dyadic Green's function

$$\mathbf{G}_0(\mathbf{r},\mathbf{r}',\omega) = \frac{1}{\epsilon_0}\,\mathcal{A}^{-1}\,\mathcal{B}\,\delta(\mathbf{r}-\mathbf{r}'). \tag{2.45}$$

With the scalar Green's function G_0 defined by the Helmholtz equation (see section 2.2.6)

$$\mathcal{A}\cdot G_0(\mathbf{r},\mathbf{r}',\omega) = \delta(\mathbf{r}-\mathbf{r}') \tag{2.46}$$

we can write

$$G_0(\mathbf{r},\mathbf{r}',\omega) = \mathcal{A}^{-1}\,\delta(\mathbf{r}-\mathbf{r}'). \tag{2.47}$$

Multiplication with $\mathcal{B}$ yields

$$\begin{aligned} \mathcal{B}\cdot G_0(\mathbf{r},\mathbf{r}',\omega) &= \mathcal{B}\cdot\mathcal{A}^{-1}\,\delta(\mathbf{r}-\mathbf{r}') \\ &= \mathcal{A}^{-1}\cdot\mathcal{B}\,\delta(\mathbf{r}-\mathbf{r}') \end{aligned} \tag{2.48}$$

where we used the commutability of partial differentiation of continuous functions in the last step [248, chapter 1.13].

Comparison with eq. (2.41) and using the outgoing variant of the scalar Green's function (plus sign in eq. (2.35)) leads us to the relation between the scalar and the Dyadic Green's function and

[1] To be precise: Quantum mechanics uses it's scalar counterpart, describing probability densities for particle positions

with that to the explicit form of the latter

$$\begin{aligned}\mathbf{G}_0(\mathbf{r},\mathbf{r}',\omega) &= \frac{1}{\epsilon_0}\,\mathcal{B}\cdot G_0(\mathbf{r},\mathbf{r}',\omega)\\ &= \frac{1}{\epsilon_0}\,\mathcal{B}\cdot\frac{\mathrm{e}^{+\mathrm{i}kR}}{4\pi R}\\ &= \frac{1}{4\pi\epsilon_0\epsilon_r}\Big(-k^2\mathbf{T}_1(\mathbf{R}) - ik\mathbf{T}_2(\mathbf{R}) + \mathbf{T}_3(\mathbf{R})\Big)\mathrm{e}^{\mathrm{i}kR}\end{aligned} \tag{2.49}$$

where we used again the abbreviations $\mathbf{R} = \mathbf{r} - \mathbf{r}'$ and $R = |\mathbf{R}|$. In analogy to related literature [246, 249, 250], we introduced the three tensors

$$\mathbf{T}_1(\mathbf{R}) = \frac{\mathbf{RR} - \mathbf{I}R^2}{R^3} \tag{2.50}$$

$$\mathbf{T}_2(\mathbf{R}) = \frac{3\mathbf{RR} - \mathbf{I}R^2}{R^4} \tag{2.51}$$

$$\mathbf{T}_3(\mathbf{R}) = \frac{3\mathbf{RR} - \mathbf{I}R^2}{R^5} \tag{2.52}$$

where $\mathbf{RR}$ is the tensor-dot-product of the two vectors. Note that $\mathbf{T}_1$ describes farfield effects while $\mathbf{T}_2$ and $\mathbf{T}_3$ account for the nearfield with ($\mathbf{T}_2$) and without retardation ($\mathbf{T}_3$ – quasistatic approximation, see section 2.2.3).

The Green's Dyad $\mathbf{G}_0$ is also referred to as the *field susceptibility*, because it can be seen as a generalization of the electric susceptibility. If we multiply $\mathbf{G}_0(\mathbf{r},\mathbf{r}',\omega)$ with a dipole $\mathbf{p}$ at $\mathbf{r}'$ the result is the field at position $\mathbf{r}$, emitted by this dipole. This is also why $\mathbf{G}_0$ is furthermore called a *propagator* – it mathematically propagates the electric field of a source into free space.

2.3.2.1 Objects in Multi-Layer Environments

The above derived field susceptibility $\mathbf{G}_0$ describes polarizing material in a homogeneous environment. One of the main advantages of Green's Dyadic Method is the possibility to easily add analytically solvable constraints to the observation system like for example a substrate (such as illustrated in fig. 2.4). For doing so, we can make use of the required linearity[1] of $\mathbf{G}_0$ and simply add the Green's Dyadic function describing the influence of additional boundaries like a substrate

$$\mathbf{G}_{\text{tot.}} = \mathbf{G}_0 + \mathbf{G}_{\text{substrate}} \tag{2.53}$$

Such a surface Dyad can be found for instance using the method of mirror charges. For details and descriptions of efficient computational methods, we refer to the works of Cai and Yu [251] or Paulus et al. [252] where also a generalization to multi-layered systems is presented.

2.3.2.2 Periodic Structures

In the same manner like multi-layered environments, periodically repeated structures can be treated: By including a Bloch periodicity in the *Ansatz* for the electric field, a Dyadic Green's function can be derived that correctly accounts for interference effects from a two-dimensional

[1] in terms of Physics, the linearity of an operator describes the superposition principle

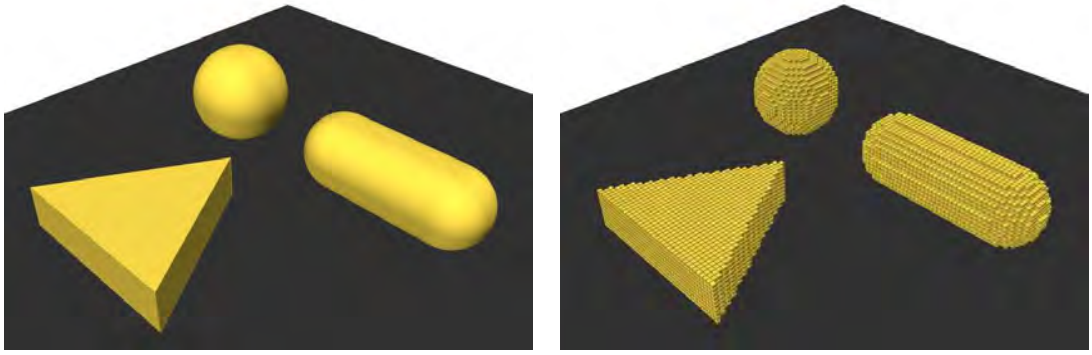

(a) Arbitrary Nanostructure (b) Cubic Volume Discretization

Figure 2.4: (b) shows a cubic volume discretization of an arbitrary nanostructure, illustrated in (a), which is composed of multiple elements lying on a substrate.

array made of an elementary computation cell [253–256]. The GDM is therefore also a powerful tool in the design and simulation of metasurfaces.

2.3.2.3 Two-Dimensional Problems

Using appropriate Green's functions, also two-dimensional problems can easily be treated, i.e. infinitely long structures with arbitrary cross-sections [257, 258]. This technique is useful as a mode solver for waveguides [259]. Also particles with very high aspect-ratios like silicon nanowires can be approximated using the GDM-2D technique with very rapid convergence. This will be used later in this thesis.

2.3.3 Volume Discretization

For arbitrarily shaped objects, the integral in the Lippmann-Schwinger equation (2.44) can generally not be solved analytically. In the following we describe a numerical approach for its solution which requires the transition from the integral to a sum over finite size volume elements (see also [246]):

$$\mathbf{E}(\mathbf{r}_i,\omega) = \mathbf{E}_0(\mathbf{r}_i,\omega) + \chi(\omega)\sum_{j=1}^{N}\mathbf{G}_{\text{tot.}}(\mathbf{r}_i,\mathbf{r}_j,\omega)\cdot\mathbf{E}(\mathbf{r}_j,\omega)\cdot V_{\text{cell}} \tag{2.54}$$

where we discretized the nano-object using N cubic volume elements as illustrated in figure 2.4, with side length d and thus $V_{\text{cell}} = d^3$. For reasons of clarity the dependency on the frequency ω will be omitted in the following. We can rewrite eq. (2.54) as follows

$$\begin{aligned}\mathbf{E}_0(\mathbf{r}_i) &= \mathbf{E}(\mathbf{r}_i) - \chi\sum_{j=1}^{N}\mathbf{G}_{\text{tot.}}(\mathbf{r}_i,\mathbf{r}_j)\cdot\mathbf{E}(\mathbf{r}_j)\cdot V_{\text{cell}} \\ &= \sum_{j=1}^{N}\Big(\delta_{ij}\mathbf{I} - \chi V_{\text{cell}}\cdot\mathbf{G}_{\text{tot.}}(\mathbf{r}_i,\mathbf{r}_j)\Big)\cdot\mathbf{E}(\mathbf{r}_j)\end{aligned} \tag{2.55}$$

where δ_{ij} is the Kronecker delta and $\mathbf{I}$ the Cartesian unitary tensor.

Let us now define two $3N$-dimensional vectors containing the ensemble of all electric field vectors in the discretized nano-object

$$\mathbf{E}_{0,\text{obj.}} = \Big(E_{0,x}(\mathbf{r}_1), E_{0,y}(\mathbf{r}_1), E_{0,z}(\mathbf{r}_1), \qquad E_{0,x}(\mathbf{r}_2), \ \ldots, \quad \ldots, \ E_{0,z}(\mathbf{r}_N)\Big) \tag{2.56}$$

$$\mathbf{E}_{\text{obj.}} = \Big(E_{x}(\mathbf{r}_1), E_{y}(\mathbf{r}_1), E_{z}(\mathbf{r}_1), \qquad E_{x}(\mathbf{r}_2), \ \ldots, \quad \ldots, \ E_{z}(\mathbf{r}_N)\Big). \tag{2.57}$$

Together with the $3N \times 3N$ matrix $\mathbf{M}$ composed of 3×3 sub-matrices

$$\mathbf{M}_{ij} = \delta_{ij}\mathbf{I} - \chi V_{\text{cell}} \mathbf{G}_{\text{tot.}}(\mathbf{r}_i, \mathbf{r}_j) \tag{2.58}$$

we obtain a coupled system of $3N$ linear equations

$$\mathbf{E}_{0,\text{obj.}} = \mathbf{M} \cdot \mathbf{E}_{\text{obj.}} \,. \tag{2.59}$$

If we are able to determine the inverse of the matrix $\mathbf{M}$ defined by eq. (2.58), we can calculate the field $\mathbf{E}$ inside the structure for all possible incident fields $\mathbf{E}_0$ (at frequency ω) by means of a simple matrix-vector multiplication:

$$\boxed{\mathbf{E}_{\text{obj.}} = \mathbf{M}^{-1} \cdot \mathbf{E}_{0,\text{obj.}} \,.} \tag{2.60}$$

In the following, we will use the symbol $\mathbf{K}$ for the inverse matrix

$$\mathbf{K}(\omega) = \mathbf{M}^{-1}(\omega) \tag{2.61}$$

which we will call the *generalized field propagator* as introduced by Martin et al. [260].

Finally, with equation (2.44), we can use the field susceptibility with the field inside the particle in order to calculate the total electric field at any point outside the nanostructure.

2.3.3.1 Renormalization of Greens Dyadic Function

When integrating the source region, we integrate scalar Green's functions of the form of spherical waves

$$f(\mathbf{r}, \mathbf{r}') = \frac{\mathrm{e}^{ik\,|\mathbf{r}-\mathbf{r}'|}}{|\mathbf{r}-\mathbf{r}'|}. \tag{2.62}$$

Obviously, this function diverges if $\mathbf{r} = \mathbf{r}'$, which occurs when the field of a point dipole $\mathbf{p}\delta(\mathbf{r}-\mathbf{r}')$ is being evaluated at the dipole's position $\mathbf{r}'$. As a consequence, in order to remove this singularity we need to apply a regularization scheme when integrating the polarization distribution in equation (2.43) over the volume of its extension [261]. For a three dimensional cubic mesh, a simple renormalization rule for the free-space Green's Dyad is found [262, section 4.3]

$$\mathbf{G}_0^{\text{cube}}(\mathbf{r}_i, \mathbf{r}_i) = \frac{-1}{3\epsilon_{r,\text{env}} d^3}\mathbf{I}. \tag{2.63}$$

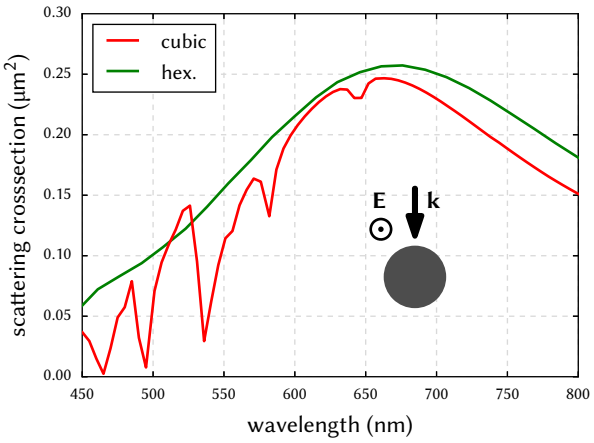

(a) Scattering Spectra of SiNW

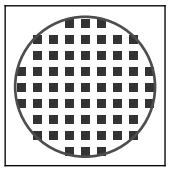

(b) Cubic Mesh

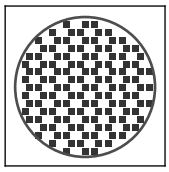

(c) Hexagonal Mesh

Figure 2.5: (a) shows the calculated scattering spectra of a silicon nanowire discretized using cubic and hexagonal meshes. The meshes are shown in (b) and (c) perpendicular to the long axis of the wire.

A hexagonal compact mesh in 3D can be regularized analogously using [250, section 3.1]

$$\mathbf{G}_0^{\text{hex}}(\mathbf{r}_i, \mathbf{r}_i) = \frac{-\sqrt{2}}{3\epsilon_{r,\text{env}} d^3}\mathbf{I} \tag{2.64}$$

with d the stepsize of the volume discretization. While a cubic cell has a volume of $V_{\text{cell}} = d^3$, in the hexagonal compact case, the volume of a cell equals $V_{\text{cell}} = d^3/\sqrt{2}$ and also must be accordingly adapted in Eq. (2.58). Because it treats the field of a dipole at the location of the dipole itself, the sub-matrix $\mathbf{M}_{ii}$ is also called "self-term".

The choice of an appropriate mesh can be crucial for the convergence of the method. When curved structures like wires of circular section are modeled, a hexagonal mesh should usually be preferred. On the other hand, for structures with flat surfaces and normal angles cubic meshing yields better results. Figure 2.5a shows a pathological comparison of scattering spectra for a plane-wave excited silicon nanowire of diameter $D = 60\,\text{nm}$, discretized using cubic and hexagonal meshing with equal nominal stepsize (8 nm). Cross-sections of the wire structure models are shown in figures 2.5b and 2.5c.

We note that a regularization method for finite tetrahedral volume elements of variable size and shape has been proposed by Kottmann and Martin [257].

2.3.3.2 Paraxial Fields

We now have developed a mathematical scheme to solve the wave-equation for time-harmonic, monochromatic fields. For any incident field – which is what corresponds to the homogeneous solution $\mathbf{E}_0(\mathbf{r}, t)$ of the wave-equation – we are able to calculate the electric field distribution inside an arbitrary nano-particle. In order to entirely simulate optical effects in nanoscale structures we need to describe the incident electric field.

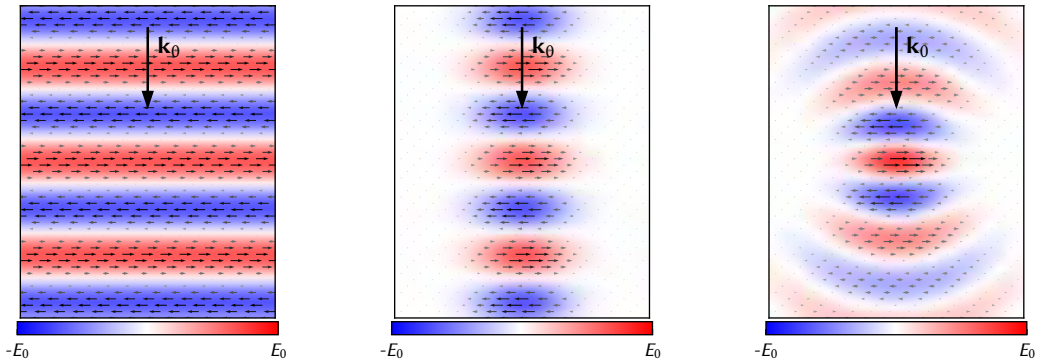

(a) Plane Wave (b) Focused Plane Wave (c) Paraxial Gaussian

Figure 2.6: Real parts of different paraxial fields (field directions indicated by small black arrows). The focal point of (b) and (c) is in the center of the plots. X-direction is the horizontal axis along which the light is linearly polarized. The vertical direction corresponds to the Z-axis with incidence along $-Z$.

In addition to monochromaticity and time harmonicity, it is often convenient in numerical simulations to consider fields that propagate uniformly in one single direction only. Such fields are called *paraxial*.

Plane Wave The probably most simple representative is a plane wave, i.e. a wave that has uniform fields on all planes perpendicular to its propagation vector $\mathbf{k}_0$, as shown in figure 2.6b. Using a complex amplitude (see Eq. (2.14)), it writes:

$$\mathbf{E}_0(\mathbf{r}, t) = \mathbf{E}_0 \, \mathrm{e}^{\mathrm{i}(\mathbf{k}_0 \mathbf{r} - \omega t)} \tag{2.65}$$

Plane waves have interesting physical properties which makes them also particularly convenient for calculations. If we insert equation (2.65) in Maxwell's equation for the curl of the electric field (Eq. (2.1b)) it follows that

$$\mathbf{B}_0 = \frac{k_0}{\omega} \left(\frac{\mathbf{k}_0}{k_0} \times \mathbf{E}_0 \right) \tag{2.66}$$

which means

$$|\mathbf{B}_0| = \frac{1}{c} |\mathbf{E}_0|. \tag{2.67}$$

Plane waves waves are obviously *transverse* with $\mathbf{E} \perp \mathbf{B} \perp \mathbf{k}_0$ as illustrated in figure 2.3 and a relation between their amplitudes exists. This is a good approximation in the far-field, at large distances from any discontinuities (like polarizable particles) of the homogeneous environment.

Also, in many cases the assumption of plane waves for the incident light on a nano-particle is a sufficiently good approximation. Unfocused light from a source located far from the observation position can be usually described using plane waves. This may be for example sunlight on the surface of the earth or light focused by a microscope, where the focal spot is large compared to the examined sample.

However, in situations where the focal spot becomes smaller than the observed area, plane-waves are often no longer adequate to describe the illumination. This is the case for example when doing raster-scan experiments with a tightly focused beam on larger nanoparticles (see section 2.3.3.4).

Focused Plane Wave A plane wave with a Gaussian intensity profile may often be sufficient to model effects introduced by focusing optics, as illustrated in figure 2.6b. A focused plane wave in Z-direction ($\mathbf{k}_0 \parallel \mathbf{e}_z$) has the form

$$\mathbf{E}_0(\mathbf{r}, t) = \mathbf{E}_0 \, \mathrm{e}^{\mathrm{i}(\mathbf{k}_0 \mathbf{r} - \omega t)} \cdot \exp\left(\frac{(x - x_0)^2 + (y - y_0)^2}{2w_{\text{spot}}^2}\right) \tag{2.68}$$

where w_{spot} is the width of the focused beam and the focal axis is at (x_0, y_0). The full width at half maximum (FWHM) can be calculated from w_{spot} using

$$w_{\text{FWHM}} = w_{\text{spot}} \cdot 2\sqrt{2 \ln 2}. \tag{2.69}$$

This is in many cases a good approximation for modeling experiments with focused beams.

Paraxial Gaussian Beam Often, lasers are used as sources of monochromatic, coherent light with high intensity. Light emitted from a laser-cavity is however not propagating like a plane wave, but rather as a Gaussian beam (see figure 2.6c). As the intensity profile differs significantly from the focused planewave, the use of a model for Gaussian beams may become necessary – particularly in larger objects, where the curved intensity profile of such a beam induces important field gradients along the propagation direction. A popular approximation to a real Gaussian beam is the so-called *paraxial approximation*, where all $\mathbf{k}$-vectors are parallel to one single propagation direction. It can be calculated using the following formula (propagation along Z-axis)

$$\mathbf{E}_0(\mathbf{r}, t) = \mathbf{E}_0 \frac{w_0}{w(z)} \exp\left(\frac{-r^2}{w(z)^2}\right) \exp\left(-\mathrm{i}\left(\omega t + k\left(z + \frac{r^2}{2R(z)}\right) - \zeta(z)\right)\right) \tag{2.70}$$

with the beam width or "waist" w_0 and the squared distance to the beam axis $r^2 = \Delta x^2 + \Delta y^2$. Δx, Δy are the distances to the beam axis in X and Y direction, respectively. In equation (2.70) we introduced furthermore the z-dependent beam waist

$$w(z) = w_0 \sqrt{1 + \left(\frac{z\lambda}{\pi w_0^2}\right)^2} \tag{2.71}$$

the radius of curvature

$$R(z) = z\left(1 + \left(\frac{\pi w_0^2}{z\lambda}\right)^2\right) \tag{2.72}$$

and the *Gouy phase*

$$\zeta(z) = \arctan\left(\frac{z\lambda}{\pi w_0^2}\right) \tag{2.73}$$

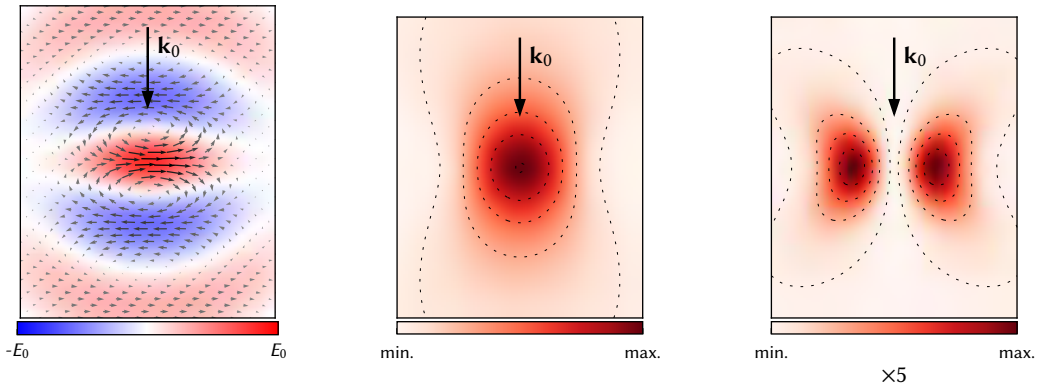

(a) Real Part of Amplitude (b) Total Intensity (c) Longitudinal Intensity

Figure 2.7: div**E** corrected field of a linear polarized tightly focused Gaussian beam. Field directions are indicated by small black arrows. In (b) and (c) time-averaged intensities are shown to illustrate where the value of the longitudinal field component (i.e. along the propagation direction) is largest. Linear scale between contour lines. Focal point in the center of the plots. X-direction is the horizontal axis along which the light is linearly polarized. The vertical direction corresponds to the Z-axis with incidence along $-Z$.

which is a result of the shorter path along the curvature close to the waist, compared to the path a plane wave would travel by continuing on a straight line [263].

Finally we note that, as the name suggests, the wavevectors of all paraxial fields are always parallel to one specific direction (we generally consider propagation along the Z direction). Effects that rely on the presence of **k**-vectors in multiple directions can therefore not be described by a paraxial field. Examples where this approximation may break down are coupling to guided modes with focused fields [264] or the rigorous description of scattering occurring in dark-field microscopy [265].

2.3.3.3 Tight Focus Correction of the Paraxial Gaussian

Under strong focus, i.e. with large beam curvatures $1/R(z)$ close to the focal point, the paraxial approximation of a Gaussian beam becomes inaccurate. In particular in the focal region, Maxwell's equation div$\mathbf{E} = 0$ (assuming no free charges) is not being satisfied any longer and a correction is required. Assuming a field propagating along the Z-direction (and therefore $E_{0,z} = 0$ in the paraxial approximation), we get by integration of eq. (2.16a)

$$E_{0,z} = -\int \left(\frac{\partial E_{0,x}}{\partial x} + \frac{\partial E_{0,y}}{\partial y} \right) \mathrm{d}z. \tag{2.74}$$

With the definition of the paraxial Gaussian field we find

$$E_{0,z}(x,y,z) = \frac{-2\mathrm{i}}{kw(z)^2} \cdot \left(\Delta x \, E_{0,x} + \Delta y \, E_{0,y} \right). \tag{2.75}$$

Here, Δx and Δy are the distances to the beam's propagation axis in X and Y direction. This equation can easily be adapted for arbitrary $\mathbf{k}$-vectors. In figure 2.7a-b, the real part and the total intensity of the corrected Gaussian field are plotted. Fig. 2.7c shows the intensity of the correction term, thus of the field components along the axial $\mathbf{k}$-vector. For tight focusing (NA 0.8 in the shown example), the correction term can approach around $5 - 10\%$ of the total field amplitude.

For more details on the description of focused electromagnetic fields, see [235, chapter 3].

2.3.3.4 Raster-Scan Simulations

Once the generalized propagator $\mathbf{K}$ is known, we can calculate the response of the system to arbitrary (monochromatic) exciting fields by means of a simple matrix-vector multiplication. This can be used to do raster-scan simulations at low numerical cost, by moving a focused incident beam step-by-step over the nano-object, while calculating and eventually post-processing the field at each position [185] (see also section 3.3.3.2).

2.3.4 Resolution of the Inversion Problem

We saw in the previous section that the electromagnetic response of a nano-particle of arbitrary shape can be calculated by inversion of the matrix $\mathbf{M}$, defined in Eq. (2.58). This inversion can be performed with standard numerical methods like LU-decomposition. An extensive explanation of LU-decomposition and details on its implementation can be found for example in [266, chapter 2.3]. We use the LU-implementation in the "SuperLU" library for direct inversion of $\mathbf{M}$ [267, 268]. Another possibility to calculate the inverse for the particular case of the GDM is to use a sequence of Dyson's equations [260]. A detailed description of the latter algorithm can be found in [249, chapter 2.4]. An advantage of the Dyson's sequence is its very good parallelization capability, superior to parallelized LU-decomposition. However, LU inversion has a better single-core performance (see Fig. 2.8b).

2.3.4.1 Conjugate Gradients

If we have a closer look at the matrix $\mathbf{M}$, we can make an interesting observation: While $\mathbf{M}$ is not exactly sparse[1], most of the entries have significantly smaller absolute values than very few large matrix elements. In Fig. 2.8a we show plots of the population of matrix $\mathbf{M}$ for some selected nano-structures. These population plots work as illustrated in the following examples:

$$\begin{bmatrix} 1 & 0 & 0 \\ 0 & 1 & 0 \\ 0 & 0 & 1 \end{bmatrix} = \quad \begin{bmatrix} 2 & 1 & 0 \\ 1 & 2 & 1 \\ 0 & 1 & 2 \end{bmatrix} = \quad \begin{bmatrix} 1 & 2 & 3 \\ 4 & 5 & 6 \\ 7 & 8 & 9 \end{bmatrix} = \quad . \tag{2.76}$$

$\mathbf{M}$ contains also phase-information and is therefore complex, hence we use the absolute values of the matrix elements for the population patterns. In addition, the maximum of the color-code in Fig. 2.8a is clipped to 10 % of the maximum absolute value in the matrix to increase the contrast. Clearly, the matrices contain very few entries with values of more than some % of the overall maximum and yet > 60 % of all elements are generally non-zero.

[1] A sparse matrix consists of mostly zeros and very few non-zero entries

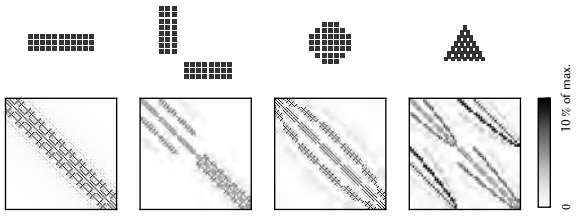

(a) Population Patterns of $\mathbf{M}$ for Some Structures

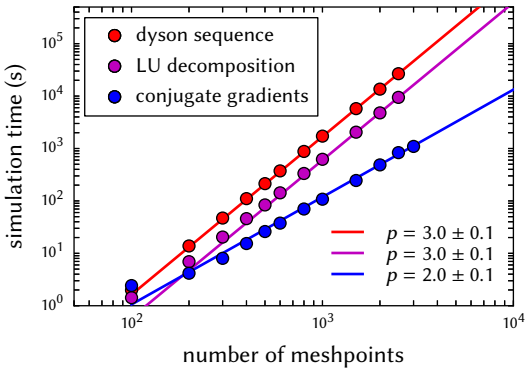

(b) Timing for Dyson / LU / CG

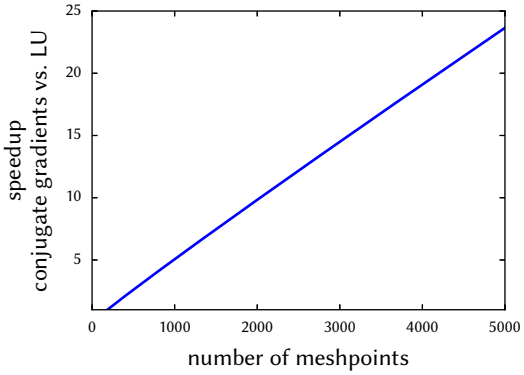

(c) Speedup CG vs. LU

Figure 2.8: In (a), population patterns of matrices $\mathbf{M}$ are shown at $\lambda = 1\,\mu\text{m}$ for a selection of structures (stepsize 10 nm, same scale for all sketches). The structures are one layer of mesh-points high, in order to keep the number of matrix-elements low. White corresponds to an absolute value of 0, black to $\geq 10\,\%$ of the matrix's largest element. (b) shows timings of nanowire-simulations for spectra with 30 wavelengths as a function of the number of meshpoints. Dyson's sequence, LU-decomposition and conjugate gradients are compared and fitted by a power-law (resulting power given on the bottom right). (c) shows the speedup when comparing conjugate gradients to LU-decomposition as a function of meshpoints.

It turns out, that such matrices are good candidates for iterative solving using so-called "Krylow-subspace methods". The most popular algorithm of this class is the conjugate gradients (CG) method and its derivations like biconjugate gradients (for non-symmetric problems) or complex CG [269]. A detailed description of the method can be found in [266, chapter 2.7]. The main idea of these iterative methods is, that the inverse of the matrix is in many cases not actually required. For simulations that massively make use of the generalized propagator (like raster-scan simulations), the CG technique is therefore not the method of choice. It may be on the other hand an advantageous approach, if we search a solution for $\mathbf{E}$ that satisfies

$$\mathbf{M} \cdot \mathbf{E} = \mathbf{E}_0 \tag{2.77}$$

for one single incident field $\mathbf{E}_0$. During the CG-iterations, matrix-vector multiplications $\mathbf{M} \cdot \mathbf{x}$ are performed following a minimization scheme in which $\mathbf{M} \cdot \mathbf{x}$ converges eventually to $\mathbf{E}_0$. Theoretically, for a $N \times N$ matrix CG converge to the exact solution after N iterations and each

iteration itself has a computational cost $\propto N^2$. In reality, the convergence is often very rapid in the beginning, and a solution with sufficient precision can be obtained after very few iterations, yielding a total computational cost $\propto N^2$ instead of a N^3 scaling for exact inversion for example with LU-decomposition. Indeed, we find a N^3-scaling for complete inversion by LU or Dyson's sequence and a N^2 dependence when using conjugate gradients (Fig. 2.8b). Particularly for larger numbers of meshpoints, this can result in a significant speedup, as shown in Fig. 2.8c.

2.3.4.2 Preconditioning

The speed of the convergence of conjugate gradients is crucially dependent on the condition of the matrix $\mathbf{M}$ and generally can be massively improved by doing a *preconditioning* step before starting the actual iterative scheme. Let's assume, $\mathbf{A}$ of the equation system

$$\mathbf{A} \cdot \mathbf{x} = \mathbf{b} \tag{2.78}$$

would be the identity matrix $\mathbf{I}$. Then CG would have converged within the first iteration. A possible approach for preconditioning is therefore to reshape the problem using a matrix $\mathbf{P}$

$$\mathbf{A} \cdot (\mathbf{P} \cdot \hat{\mathbf{x}}) = \mathbf{b}. \tag{2.79}$$

If $\mathbf{P}$ is a close approximation to $\mathbf{A}^{-1}$, $\mathbf{AP}$ will be close to the identity $\mathbf{I}$ and the system would converge very quickly under conjugate gradients iterations. Eq. (2.79) is called a right-preconditioned system. Consequently, a good preconditioner for our problem is a close approximation to the inverse of $\mathbf{M}$. Several algorithms exist to search pseudo-inverse matrices for preconditioning. A very popular one is the *incomplete* LU-decomposition (ILU) [270] that scales with N^2 and which we use also in our implementation within the Green Dyadic method.

2.3.4.3 Recycling of the Preconditioner

When calculating spectra using the GDM, the electric field in a particle is calculated for a large number of closely spaced wavelengths, at each of which the matrix $\mathbf{M}$ is (incompletely) inverted. Most often, the electric field distribution changes only marginally for slightly different wavelengths and so does the matrix $\mathbf{M}$. Unfortunately, a *very similar* matrix is of little use for exact calculations, but we have seen in the preceding section that an *approximation* to the exact inverse $\mathbf{M}^{-1}$ can be a good preconditioner $\mathbf{P}$ for CG.

When calculating dense spectra (i.e. many points on the wavelength axis), we can use this fact and significantly accelerate the calculation with conjugate gradients by recycling the preconditioner matrix until a certain lower limit for the speedup factor is reached. In other words, we will be using the same $\mathbf{P}$ repeatedly for several consecutive wavelengths and only if the acceleration is below a speed-up limit, a new preconditioner is calculated and subsequently re-used for the following wavelengths. In Fig. 2.9a the timing for the calculation of each wavelength is shown for the case of recycling (blue) and re-calculation (red line) of the preconditioner matrix. In the "recycling" case (re-calculation threshold was a minimum speedup-factor of 2), we see that the preconditioner is only calculated a total of 6 times for a spectrum of 100 wavelengths. Particularly at lower frequencies, the electric field seems to change little and the preconditioner remains a good approximation to $\mathbf{M}^{-1}$ over a large spectral range (only one recalculation between

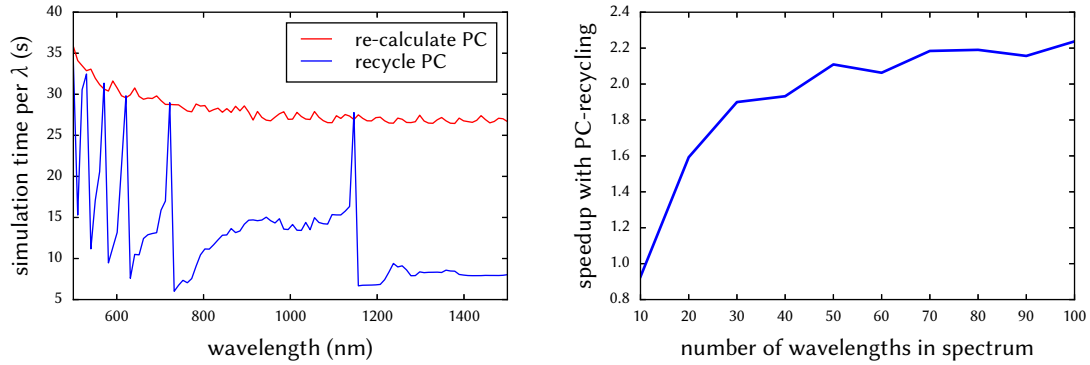

(a) Timing for CG PC-Recycling

(b) Speedup CG PC-Recycling

Figure 2.9: (a) shows timings per wavelength for a CG-GDM simulation of a silicon nanowire with a step-size of 10 nm and 50 nm diameter, consisting of $\approx$ 2000 dipoles. The preconditioner was either calculated for each wavelength (red) or recycled for multiple wavelengths until the resulting speedup dropped below a factor of 2. In (b) the total speedup for the calculation of the whole spectrum is plotted against the number of wavelengths in the spectrum.

$\approx$ 750 nm and 1500 nm). As shown in Fig. 2.9b, this technique can divide the total calculation time by more then 2.

Another possible application when preconditioner recycling may be beneficial is in series of simulations with many very similar or slowly transformed nano-structures like antennas of gradually increasing size.

2.3.5 Comparison to other Numerical Methods

Other methods than the GDM can be used for solving electrodynamical problems in nano-optics. A widely used frequency domain solver is for example the open source software DDSCAT [271], which implements a frequency domain technique formally equal to the GDM presented above, called the discrete dipole approximation (DDA). However, there exist two main differences to GDM as employed throughout this work: First, the renormalization problem is circumvented by setting the self-terms to zero and including the corresponding contributions using a physical polarizability for each dipole, corresponding to the mesh geometry. Second, in the DDSCAT implementation of DDA, the matrix $\mathbf{M}_{\mathrm{DDSCAT}}$ is not stored in memory. The resolution of Eq. (2.59) is done by conjugate gradients where the elements $M_{\mathrm{DDSCAT},ij}$ are computed in-time during the calculation of the vector-matrix products $\mathbf{M}_{\mathrm{DDSCAT}} \cdot \mathbf{x}$. To speed up the process, an FFT-scheme to decrease the cost of these matrix-vector multiplications is used [272]. A drawback is that without storing $\mathbf{M}$, efficient preconditioning is very difficult. Convergence of the DDSCAT conjugate gradient iterative scheme is therefore relatively slow and only given for very fine discretization meshes, further slowing down the procedure due to large sizes of the coupled dipole matrix $\mathbf{M}_{\mathrm{DDSCAT}}$.

Maxwell's equations can be reformulated as a set of surface-integral equations. It is therefore possible to develop a similar formalism as the above explained volume integral method in which only the surfaces of a nanostructure are discretized instead of the volume [273]. A great

advantage of this so-called boundary element method (BEM) is the smaller amount of discretization cells, which however is only valid if the fields inside the structure are not required. With MNPBEM a free BEM-implementation exists, developed by Hohenester and Trügler [274].

Another very popular technique for electrodynamical simulations is the finite-difference time-domain (FDTD) method. As the name suggests, the calculation is performed in the time domain, which means that Maxwell's equations are iteratively evolved by small steps in time. An incoming wave travels time-step by time-step along the region of interest and when the pulse has passed or turn-on effects fully decayed (for plane wave illumination), the actual numerical measurement is performed. The obvious disadvantage is the additional dimension (time), that needs to be discretized. In particular for 3D problems, this usually leads to far higher computational costs compared to frequency domain simulations. A further disadvantage is that no tabulated permittivity data can be used which makes many dispersive media like metals difficult to be treated. The dispersion has to be taken from analytical models or the permittivity set constant. On the other hand, using short and therefore spectrally broad pulses, a whole spectrum can be obtained in a single simulation run. Frequency domain techniques require each wavelength to be calculated separately. A powerful open source implementation that comes with a rich toolbox is the software "MEEP" [275]. For a general introduction on finite differences methods, see for example [266, chapter 17]. A review on different numerical techniques in nanooptics, including benchmarks, can be found in ref. [276].

2.3.6 Post-Processing: Analysis of the GDM Results

Subsequent to the calculation of the excited field inside the structure, this information is usually further processed to obtain experimentally accessible physical quantities.

2.3.6.1 Electric Nearfield Outside the Nanostructure

With the field susceptibility (Eq. (2.43)), the field induced at any point $\mathbf{r}_{\text{outside}}$ at the exterior of the particle can be calculated from the electric polarization inside it:

$$\mathbf{E}(\mathbf{r}_{\text{outside}}) = \mathbf{E}_0(\mathbf{r}_{\text{outside}}) + \frac{1}{\epsilon_0} \sum_i^{N_{\text{cells}}} \mathbf{G}_0(\mathbf{r}_{\text{outside}}, \mathbf{r}_i) \cdot \chi V_{\text{cell}} \mathbf{E}(\mathbf{r}_i) \tag{2.80}$$

where the sum is carried out over all N meshpoints at positions $\mathbf{r}_i$.

At the example of a silicon dimer, nearfield maps 20 nm below the structure are shown for wavelengths at and off resonance in figure 2.10a.

Note that also scanning near-field optical microscopy (SNOM) signals can be calculated from GDM simulations. In this case, the presence of the scanning tip needs to be taken into account [277, 278].

2.3.6.2 Magnetic Nearfield

An oscillating dipole emits a propagating electromagnetic wave with an electric and a magnetic component. Consequently, also a magnetic nearfield is induced in the vicinity of electromagnetically excited media, even if the material is non-magnetic. After Faraday's induction law

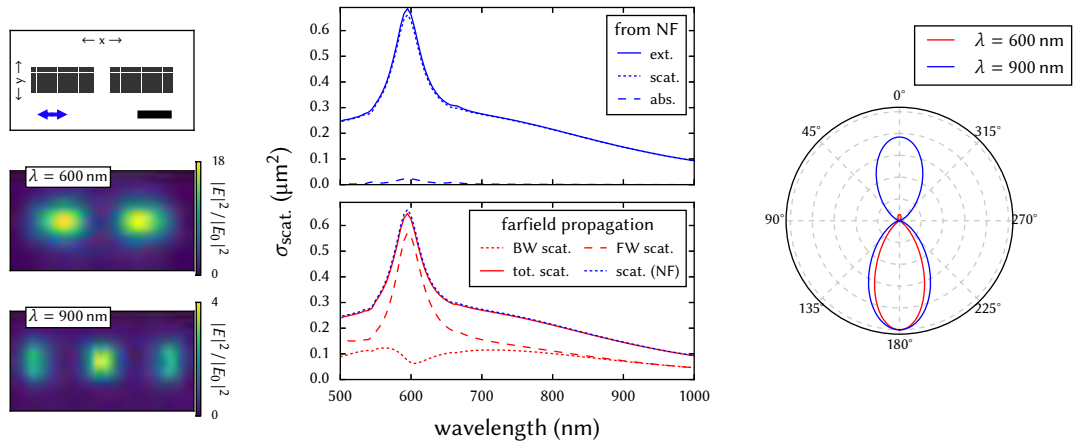

(a) Nearfield (b) Scattering Spectra (c) Radiation Pattern

Figure 2.10: In (a), the considered silicon dimer structure is shown (top, XY-Plane), where the incident polarization is indicated by a blue arrow and the scalebar is 100 nm. The center and bottom plot show nearfields at $\lambda = 600$ nm and $\lambda = 900$ nm, respectively. Calculated 20 nm below the structure. Corresponding extinction, scattering and absorption spectra are shown in (b), calculated from the nearfield (top) and by propagation to the farfield of the meshpoints as dipolar sources (bottom). The latter allows to distinguish directional scattering (forward (FW) and backward (BW) scattering is shown). (c) shows radiation patterns in the XZ-Plane of the scattering for incidence at $\lambda = 600$ nm and (red) $\lambda = 900$ nm (blue). Incident planewave from positive Z (0°), polarized along X.

from Maxwell's equations, the magnetic field can be obtained from the electric field in the nanoparticle (Eq. (2.16b)). For time-harmonic fields, we get

$$\mathbf{B}(\mathbf{r},\omega) = \frac{\nabla \times \mathbf{E}(\mathbf{r},\omega)}{\mathrm{i}\omega} \tag{2.81}$$

which can be solved numerically via finite differentiation (see e.g. Fig. 3.1).

Alternatively, a propagator $\mathbf{G}^{\mathrm{HE}}$ [279] can be used to obtain the magnetic field outside the source region. In this way it is possible to calculate nearfield maps or field enhancement spectra for the magnetic field (see for instance Fig. 1.3).

2.3.6.3 Extinction Spectra from the Nearfield in a Nanostructure

The linear response in the farfield can be characterized by the scattered and absorbed light, which in sum is called the "extinction". Usually these values are given as cross sections $\sigma_{\mathrm{scat.}}, \sigma_{\mathrm{abs.}}$ and $\sigma_{\mathrm{ext.}}$ which have the unit of an area. The extinction and scattering cross sections can be calculated from the nearfield in the discretized structure [280]

$$\sigma_{\mathrm{ext}} = \frac{2\pi n}{\lambda_0 \cdot |E_0|^2} \sum_{i=1}^{N_{\mathrm{cells}}} \mathrm{Im}\left(\mathbf{E}^*_{0,i} \cdot \mathbf{P}_i\right) \tag{2.82}$$

$$\sigma_{\text{abs}} = \frac{2\pi n}{\lambda_0 \cdot |E_0|^2} \sum_{i=1}^{N_{\text{cells}}} \left(\text{Im}\left(\mathbf{P_i} \cdot \mathbf{E}_i^*\right) - \frac{2}{3} k^3 |\mathbf{P}_i|^2 \right). \tag{2.83}$$

The scattering cross section finally is the difference of extinction and absorption

$$\sigma_{\text{scat}} = \sigma_{\text{ext}} - \sigma_{\text{abs}}. \tag{2.84}$$

$\mathbf{E}_i$ and $\mathbf{P}_i$ are the field and electric polarization at meshpoint i, respectively, induced by an excitation with a fundamental field $\mathbf{E}_{0,i}$. Complex conjugation is indicated with a superscript asterisk (*). Note that the prefactor of the above sums is $k/|E_0|^2$ with the wavenumber in the source region k.

The upper plot in figure 2.10b shows spectra for a planewave excited silicon dimer calculated from the nearfield.

2.3.6.4 Farfield Pattern of the Scattered Light

The complex electric field in the farfield radiated from an arbitrary polarization distribution can be calculated using a corresponding Greens Dyad $\mathbf{G}_{\text{ff}}$ (assuming a dipolar emission from each of the N meshpoints):

$$\mathbf{E}_{\text{ff}}(\mathbf{r}_j) = \sum_{i}^{N_{\text{cells}}} \mathbf{G}_{\text{ff}}(\mathbf{r}_i, \mathbf{r}_j) \cdot \mathbf{P}(\mathbf{r}_i) \tag{2.85}$$

Using the farfield term $\mathbf{T}_1$ (equation (2.50)) we can find the following Green's tensor for an oscillating dipole in vacuum (vacuum wavenumber k_0)

$$\begin{aligned} \mathbf{G}_{\text{ff,vac.}}(\mathbf{r}, \mathbf{r}_0, \omega) = \quad & k_0^2 \frac{\exp(\mathrm{i}k_0 R)}{R} \\ & \cdot \exp\Big(-\mathrm{i}k_0 \sin(\theta)\big(\cos(\varphi) \cdot x_0 + \sin(\varphi) \cdot y_0\big)\Big) \exp\Big(-\mathrm{i}k_0 \cos(\theta) \cdot z_0\Big) \\ & \cdot \begin{bmatrix} 1 - \sin^2(\theta)\cos^2(\varphi) & -\sin^2(\theta)\cos(\varphi)\sin(\varphi) & -\sin(\theta)\cos(\theta)\cos(\varphi) \\ -\sin^2(\theta)\cos(\varphi)\sin(\varphi) & 1 - \sin^2(\theta)\sin^2(\varphi) & -\sin(\theta)\cos(\theta)\sin(\varphi) \\ -\sin(\theta)\cos(\theta)\cos(\varphi) & -\sin(\theta)\cos(\theta)\sin(\varphi) & \sin^2(\theta) \end{bmatrix} \end{aligned} \tag{2.86}$$

where for convenience the observation point $\mathbf{r}$ in the farfield was transformed to spherical coordinates (θ, φ, R) while the location of the source dipole $\mathbf{r}$ is defined in Cartesian coordinates (dipole at (x_0, y_0, z_0)). Note that the presence of the illuminated nano-structure is fully taken into account also at the reemission, due to the self-consistent nature of the Green's formalism.

Also a substrate can again be included by means of an according Dyadic Green's function. An analytic approximation for a farfield-propagator to a layered system has been derived e.g. by Novotny [281]. Making use of the superposition principle, the radiation of single dipoles using the propagator Eq. (2.86) can be generalized to the total farfield radiation of an ensemble of N dipole-emitters, as shown in equation (2.85).

The farfield radiation pattern in the (XZ)-plane is shown in figure 2.10c for an incident planewave on the exemplary silicon dimer along the negative Z-direction. For $\lambda = 600\,\text{nm}$ (red), a strong anisotropic scattering in forward direction is observed, while off resonance ($\lambda = 900\,\text{nm}$, blue) the scattering is more or less uni-directional.

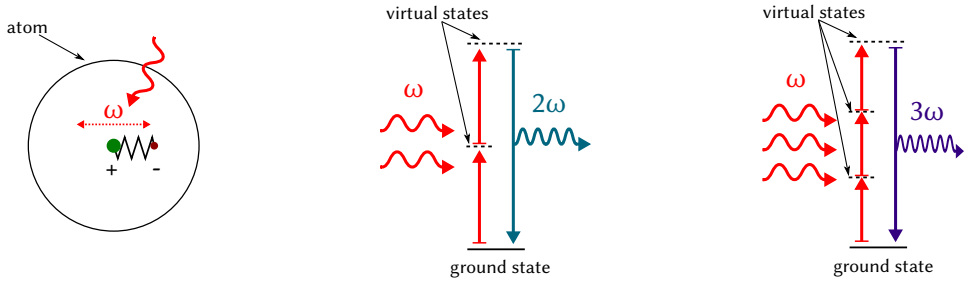

(a) Polarization of Medium (b) Scheme SHG (c) Scheme THG

Figure 2.11: In (a), the oscillation of an electron around its nucleus under electromagnetic excitation is illustrated. Sketches of SHG (b) and THG (c) are shown as examples of second and third order nonlinear processes, respectively.

A drawback of the calculation of the spectra from the nearfield-distribution as described in section 2.3.6.3 becomes obvious: These spectra do not contain any information about the directionality of the scattering. Let us assume we would try to measure scattering from the example silicon dimer in backscattering geometry. We would find a spectrum corresponding to the red dashed line ("BW scat.") in the lower plot of Fig. 2.10b, which differs significantly from the total scattering cross section (red solid line). Fortunately, information on directionality can be accessed using the farfield-propagator and we can calculate scattering spectra by re-propagating the electric polarization of the structure to the farfield at every wavelength of the spectrum. Hence, on the cost of additional computation time, the polarization of scattered light in the farfield and its directionality can be revealed.

2.4 Nonlinear Optics

Until now, we have dealt with linear optical phenomena, hence effects related to a response of matter to light that can be described in the context of the linear electric polarization as introduced in equation (2.4a).

In the following we will give a short introduction to the basic concepts of nonlinear optics and put a particular focus on Second Harmonic Generation (SHG) from surfaces. We will present a technique to describe SHG within the framework of the Green Dyadic method, which can easily be extended to other nonlinear processes.

For a detailed introduction to nonlinear optics, we refer for example to reference [282].

2.4.1 Expansion of the Electric Polarization

As long as the excitation fields are weak compared to the lattice potential of the media, optical phenomena can be explained by a linear response. We mentioned in section 2.2.1, that the electric polarization is the result of a Taylor expansion around $E = 0$, which is stopped after the first order term in the approximation of linear media. This resulted in the equation

$$P(t) \approx \epsilon_0 \chi E(t) \quad \left[+\mathcal{O}(E^2)\right] \tag{2.87}$$

For simplicity, scalar values are given. The linear electric susceptibility in isotropic, homogeneous media is the constant factor $\chi = \epsilon_r - 1$. It relates the electric polarization of the medium to the electric field. For non-isotropic media, the susceptibility χ is a tensor of rank 2, consisting of Fourier transforms from frequency to time-domain, if the medium is dispersive.

In the linear regime, the returning force acting on charges, oscillating around their nuclei at the frequency of illumination ω (see Fig. 2.11a), is a linear function of the charge displacement relative to the nucleus and thus described by a harmonic potential, as depicted in the plots on the left of Fig. 2.12. The nucleus, having a large mass compared to the electrons, is considered static. In reality, the potential is not harmonic (see examples in Fig. 2.12 center and right) and the linear approximation fails at sufficiently high photon rates. In consequence, if a medium is excited by an oscillating field of very high amplitude, the electron oscillations are becoming sensitive to the nonlinearity of the lattice potential and new phenomena occur. A comparison of driven oscillations in harmonic and anharmonic potentials is shown in figure 2.13a for different driving strengths: With increasing amplitude of the excitation field, the oscillation in an anharmonic potential is more and more deviating from an ideal harmonic oscillator. These deviations give rise to so-called *nonlinear* effects. They are usually classified according to the order of the nonlinearity in terms of the expansion of the electric polarization:

$$\begin{aligned} P_i(t) = \quad & \epsilon_0 \sum_j \chi^{(1)}_{ij}\, E_j(t) \\ & + \epsilon_0 \sum_{j,k} \chi^{(2)}_{ijk}\, E_j(t) E_k(t) \\ & + \epsilon_0 \sum_{j,k,l} \chi^{(3)}_{ijkl}\, E_j(t) E_k(t) E_l(t) \\ & + \dots \end{aligned} \tag{2.88}$$

which is often written in a compact form for the tensor products

$$\mathbf{P}_{\text{tot.}} = \underbrace{\epsilon_0 \chi^{(1)}\, \mathbf{E}}_{\text{Linear, } = \mathbf{P}^{(1)}} + \underbrace{\epsilon_0 \chi^{(2)}\, \mathbf{E}^2}_{\text{2. Order, } = \mathbf{P}^{(2)}} + \underbrace{\epsilon_0 \chi^{(3)}\, \mathbf{E}^3}_{\text{3. Order, } = \mathbf{P}^{(3)}} + \dots \tag{2.89}$$

The susceptibilities $\chi^{(n)}$ are tensors of rank $n+1$. For reasons of causality, in dispersive media they involve inverse Fourier transforms from frequency to time-domain to take account of the full electric field evolution before the observation time t.

2.4.1.1 Symmetric Potentials: Odd-Order Nonlinearities

Let us carry out some symmetry considerations at this point. The lattice potential in the bulk of a material has the same symmetry as the crystal lattice. It follows conclusively that media with an inversion-symmetric lattice like elemental fcc-semiconductors (e.g. silicon) have also a *symmetric* lattice potential as depicted in the center column of Fig. 2.12. For symmetry reasons, even-order terms of the electric polarization like $\mathbf{P}^{(2)}$ vanish in symmetric potentials:

$$\begin{aligned} -\mathbf{P}^{(2)} = \epsilon_0 \chi^{(2)} \left(-\mathbf{E}\right)^2 \quad &= \quad \epsilon_0 \chi^{(2)}\, \mathbf{E}^2 = \mathbf{P}^{(2)} \\ \Rightarrow \chi^{(2)} &\overset{!}{=} 0. \end{aligned} \tag{2.90}$$

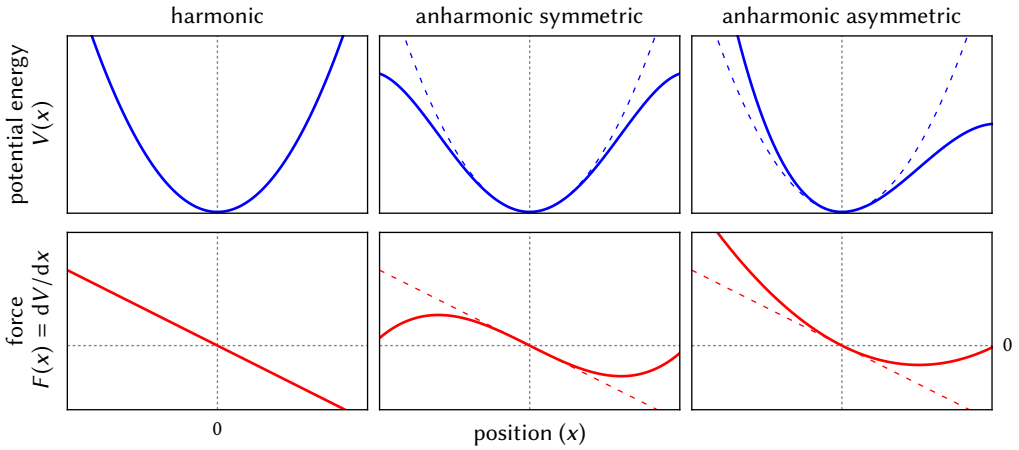

Figure 2.12: Harmonic (left), symmetric anharmonic (center), asymmetric anharmonic (right) potentials and corresponding restoring forces (bottom row), which become nonlinear functions of the position for anharmonic potentials. For comparison, the harmonic potential and the corresponding force are plotted as dashed lines in the plots of the asymmetric potentials.

In figure 2.13a the amplitude of an oscillation in a symmetric potential is shown as function of time (green line). The corresponding frequency-domain spectrum obtained by Fourier transformation is given in Fig. 2.13b. Like expected, the Fourier spectrum of an oscillation in a symmetric potential contains only odd-order harmonic frequencies, like for example the third harmonic (THG, depicted in Fig. 2.11c).

2.4.1.2 Asymmetric Potentials: Even-Order Nonlinearities

Even-order nonlinearities comprise effects explained by the terms $\mathbf{P}^{(2)}, \mathbf{P}^{(4)}, \ldots$ which include second harmonic generation (SHG, see Fig. 2.11b) or fourth harmonic generation. The constraint to odd-order nonlinear effects in symmetric anharmonic potentials is relaxed if the potential is not symmetric with respect to its energy-minimum (see Fig. 2.12, right). As shown in the lower plot of figure 2.13b, the Fourier spectrum of a driven oscillation in an asymmetric anharmonic potential does contain even-order harmonic frequencies. The corresponding time-domain data is shown in red in Fig. 2.13a. As a consequence, non-centrosymmetric crystals such as III-V semiconductors (GaAs, GaP, InP, ...) consisting of different atoms do support second order nonlinear effects. The nonlinear phenomena of lowest allowed order usually dominate the nonlinear response of the medium.

2.4.2 Second Harmonic Generation

In the following we will focus on second harmonic generation (SHG). SHG is the coherent upconversion of two photons of a fundamental frequency ω into one photon at twice the incident frequency $\omega_{\mathrm{SHG}} = 2\omega$ (i.e. half wavelength $\lambda_{\mathrm{SHG}} = \lambda/2$), as illustrated in figure 2.11b. As indicated in this sketch, there are no real electronic states involved, the absorption and reemission happen instantaneously.

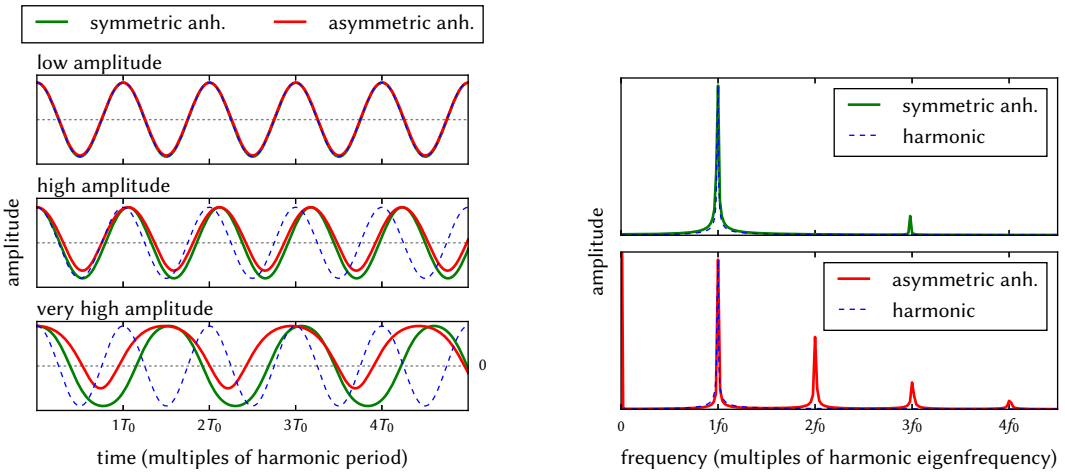

(a) Amplitude vs. Time

(b) Fourier Spectrum

Figure 2.13: (a) shows the amplitude over time for low (top), high (center) and very high (bottom) driving amplitudes. Oscillation in a symmetric (solid green) and an asymmetric (solid red) potential is compared to the case of a harmonic potential (dashed blue line). In (b), Fourier spectra corresponding to a driven oscillation in a symmetric (top) and an asymmetric (bottom) potential energy function are shown. Both are again compared to a harmonic oscillation (dashed blue line).

2.4.2.1 Phase-matching

Harmonic generation is a *coherent* nonlinear process which means that a fixed phase-relation between input and output photons exist. Due to this phase relation, SHG is usually inefficient because the phase between second harmonic light generated at different positions in the crystal lattice cause an overall destructive interference – the phase is determined by the fundamental field and therefore has a value of π at the harmonic wavelength. So-called *phase-matching* between the incident and the harmonic waves is required for efficient SHG from bulk crystals (see also [282, chapter 2]). Among other possible techniques, birefringence in crystals can be used to obtain a phase-condition for constructive SHG interference: The refractive index difference for light propagating at a certain angle with respect to the incident beam (usually along the ordinary and extraordinary axes) is exploited, which was the first successfully employed method for phase-matching [283].

When treating sub-wavelength small nanoparticles it is usually not necessary to consider phase-matching, because all harmonic generation processes occur in a very limited volume such that interference between the different source-positions has no great influence on the total emission.

2.4.2.2 Surface SHG

The most commonly used plasmonic particles, as well as many high refractive-index dielectric nano-structures are made from centrosymmetric materials (typical materials are e.g. gold or silver and silicon, respectively). We showed above that second-order effects in centrosymmetric crystals are forbidden as a result of symmetry.

To relax this constraint, locally the lattice symmetry can be broken for example by strain applied on one crystal direction [221, 284] or by strong field gradients [206]. Inversion symmetry is also broken at surfaces and interfaces where even-order nonlinear effects become possible. This *surface-SHG* has been first observed by Terhune et al. [285] very soon after the discovery of optical harmonic generation [164]. Because of its local origin at surfaces and interfaces, this form of SHG is often used for surface characterization [214, 215, 218, 220, 286–288] and has been subject of intense research ever since its discovery [289–292].

The second order surface susceptibility tensor has seven non-zero elements of which only three components are independent on isotropic surfaces ($C_{\infty,v}$-symmetry) [169]:

$$\begin{aligned} &\chi^{(2)}_{\perp\perp\perp} \\ &\chi^{(2)}_{\perp\parallel\parallel} \equiv \chi^{(2)}_{\perp\parallel_1\parallel_1} = \chi^{(2)}_{\perp\parallel_2\parallel_2} \\ &\chi^{(2)}_{\parallel\parallel\perp} \equiv \chi^{(2)}_{\parallel_1\parallel_1\perp} = \chi^{(2)}_{\parallel_2\parallel_2\perp} = \chi^{(2)}_{\parallel_1\perp\parallel_1} = \chi^{(2)}_{\parallel_2\perp\parallel_2} \end{aligned} \tag{2.91}$$

Subscripts $\parallel_1$ and $\parallel_2$ indicate two perpendicular directions tangential on the surface, $\perp$ the direction along the surface normal. The second order electric polarization of an isotropic surface then consists of three elements

$$\mathbf{P}^{(2)}_{\mathrm{sf}} = \mathbf{P}^{(2)}_{\perp\perp\perp} + \mathbf{P}^{(2)}_{\perp\parallel\parallel} + \mathbf{P}^{(2)}_{\parallel\parallel\perp} \tag{2.92}$$

that write

$$\mathbf{P}^{(2)}_{\perp\perp\perp} = \chi^{(2)}_{\perp\perp\perp}[E^2_\perp]\widehat{\mathbf{e}}_\perp \tag{2.93a}$$

$$\mathbf{P}^{(2)}_{\perp\parallel\parallel} = \chi^{(2)}_{\perp\parallel\parallel}[E^2_\parallel]\widehat{\mathbf{e}}_\perp \tag{2.93b}$$

$$\mathbf{P}^{(2)}_{\parallel\parallel\perp} = \chi^{(2)}_{\parallel\parallel\perp}[E_\parallel E_\perp]\widehat{\mathbf{e}}_\parallel. \tag{2.93c}$$

In the quasistatic approximation, the fundamental field inside a nano-structure (and at the surface) is considered constant and proportional to the exciting field. For very small particles compared to the incident field's wavelength, this approximation simplifies the problem and allows an analytical treatment of surface SHG [202]. Such theories have been developed for various problems like SHG from infinitely long, thin cylindrical nanowires [293, 294] or from small nano-spheres [201, 295]. In this context arrays of small nano-spheres [296] as well as individual nano-spheres [206] were investigated with extensions to tightly focused excitation. Further analytical work has been done, among others, on SHG from finite length cylindrical nanoparticles [204], metal tips [297] or small nanostructures of arbitrary shape [205].

Beyond the quasistatic approximation, extensions for the analytical Mie theory have been developed, e.g. for the case of SHG from infinitely long cylinders [298] or from metal spheres [299]. In figure 2.14, an example of second order nonlinear surface polarization is shown, calculated by Mie theory for a silicon nanowire of 100 nm diameter. Quiver-plots of the nonlinear polarization are compared to the fundamental electric field intensity inside the nanowire. A planewave is incident at normal angle from the top, polarized perpendicularly (2.14a, "TE") and parallel (2.14b, "TM") to the NW axis. While for TM illumination all terms except the $\mathbf{P}^{(2)}_{\perp\parallel\parallel}$ contribution vanish due to the cylindrical geometry, in the TE case all three contributions are generally non-zero (see

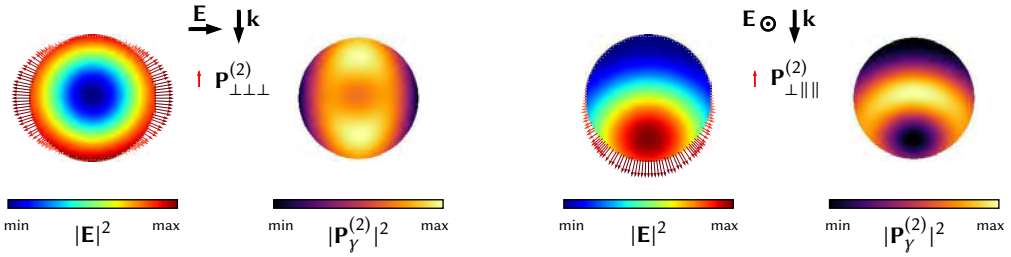

(a) TE Polarization

(b) TM Polarization

Figure 2.14: Crosssections of the fundamental field inside an infinitely long silicon nanowire (left colorplots), surface SHG (left vector-fields) and SHG γ-bulk contribution ($\nabla(\mathbf{E}^2)$, right colorplots) calculated from Mie theory. Diameter $D = 100\,\text{nm}$. Normal incidence with a polarization of the electric field perpendicular (a) and parallel (b) to the NW axis.

for details section 3.4.3). For TE excitation $\mathbf{P}^{(2)}_{\perp\perp\perp}$ is shown because in silicon $\chi^{(2)}_{\perp\perp\perp}$ is supposed to be the largest component of the second order susceptibility tensor [300].

Likewise, $\chi^{(2)}_{\perp\perp\perp}$ is the largest component of the second order susceptibility tensor in gold and silver [301, 302], hence $\mathbf{P}^{(2)}_{\perp\perp\perp}$ usually dominates the second harmonic generation process and often only this polarization component is taken into account [172, 174, 176]. If $\mathbf{P}^{(2)}_{\perp\perp\perp}$ is weak due to geometrical reasons, also other surface terms can contribute significantly to the overall second harmonic signal and need to be considered [195].

The above cited theoretical works treat objects of high symmetry with analytical descriptions. The general case of surface SHG from particles of arbitrary shape is most conveniently treated by numerical means. An approach using the GDM will be given later in this section.

2.4.2.3 Bulk Contributions to Surface-SHG

Although SHG is forbidden from the bulk of inversion symmetric crystals (see section 2.4.2.2), a second order polarization can occur from higher order terms like dipolar magnetic or quadrupolar electric components. The first non-vanishing order of these contributions, that can be expressed in terms of field gradients of the fundamental field, comprises four source terms [169, 290, 303]:

$$\mathbf{P}^{(2)}_{\text{sf,bulk}} = \mathbf{P}^{(2)}_{\gamma} + \mathbf{P}^{(2)}_{\beta} + \mathbf{P}^{(2)}_{\delta} + \mathbf{P}^{(2)}_{\zeta} \tag{2.94}$$

where

$$\mathbf{P}^{(2)}_{\gamma} = \gamma\ \nabla[\mathbf{E}^2] \tag{2.95a}$$
$$\mathbf{P}^{(2)}_{\beta} = \beta\ \mathbf{E}[\nabla \cdot \mathbf{E}] \tag{2.95b}$$
$$\mathbf{P}^{(2)}_{\delta} = \delta\ [\mathbf{E} \cdot \nabla]\mathbf{E} \tag{2.95c}$$
$$\mathbf{P}^{(2)}_{\zeta,i} = \zeta\ E_i \nabla_i E_i. \tag{2.95d}$$

Here, γ, β, δ and ζ are phenomenological susceptibility components that can be expressed in terms of $\chi^{(2)}$ elements [169, section 2.5]. In many cases, these bulk contributions can be neglected. For instance under planewave illumination in the quasistatic approximation, the fields

are constant and therefore $\mathbf{P}^{(2)}_{\text{sf,bulk}} = 0$. However, if resonant modes like LSP [2] or leaky mode resonances [304] exist, or if an incident beam is tightly focused onto the sample [206], field gradients arise and bulk contributions may become significant. It has been shown, that bulk contributions in centrosymmetric media can indeed become important enough to interfere with the local surface contributions to SHG [179, 302, 305, 306]. In this context, the so-called *non-separable* or *surface-like* γ-bulk contribution [169] can be written as a superposition of local surface contributions. However, employing suitable geometrical conditions allows to distinguish certain non-local bulk contributions from the local surface SHG using appropriate polarization selection rules [307].

2.4.3 SHG in the GDM

We will describe in the following how surface SHG from nano-particles can be calculated in the framework of the Green Dyadic method (see Sec. 2.3).

2.4.3.1 Second Harmonic Surface Nonlinear Polarization

The most significant contribution to SHG from centrosymmetric nano-structures is usually a local nonlinear polarization of the particle's surface (see above). In order to calculate surface SHG, the field inside the particle excited by the fundamental incident beam is determined in a first step using the GDM (explained in detail in the previous section).

Subsequently, the surface of the nano-structure has to be identified and a geometrical basis of one normal and two tangential unit-vectors has to be established at each point of the surface. In order to be applicable for particles of arbitrary shape, this can be done by counting the number of next neighbors N_{nn} of each meshpoint, either by a bruteforce method, or using sorting strategies like the so-called "kd-tree" technique [308]. The latter approach can improve the efficiency particularly in large systems with many meshpoints. An element of a cubic lattice is on the surface if, within the radius of one discretization step, it has less than the maximum possible $N_{\text{nn, bulk}} = 6$ neighbors on a three dimensional grid or $N_{\text{nn, bulk, 2D}} = 4$ on a two dimensional grid.

Once the surface meshpoints have been determined, unit vectors normal on the surface can be determined from the relative positions of the next neighbors. The unit-vectors pointing from each neighbor towards the surface element are added and the total vector is normalized, resulting in a perpendicular unit vector. This technique is illustrated in figure 2.15b (blue highlighted region). Using only the next neighbors limits the angles of surface vectors to multiples of $45\,^\circ$, which restricts the precision of the result particularly on curved surfaces. To improve the normal surface vectors on curved surfaces, a larger volume (2D: area) around the surface element can be used for the vector calculation. The green highlighted regions in figure 2.15 show an example, where all elements in a radius of $R_{\text{sf.-vec.}} = 3$ stepsizes were taken into account. The latter technique however may be disadvantageous at sharp angles between flat surfaces, where some smoothing of the edge will occur for large $R_{\text{sf.-vec.}}$. The choice of $R_{\text{sf.-vec.}}$ should therefore be some small value like $\approx 2-3$ stepsizes.

For a homogeneous and isotropic surface, the second order susceptibility components are identical for all tangential directions (Eq. (2.91)). The unitary tangential surface vectors can then be defined as two arbitrary orthogonal vectors, perpendicular to the normal surface vector $\widehat{\mathbf{e}}_\perp$.

$$\widehat{\mathbf{e}}_\perp \perp \widehat{\mathbf{e}}_{\parallel_1} \perp \widehat{\mathbf{e}}_{\parallel_2} \tag{2.96}$$

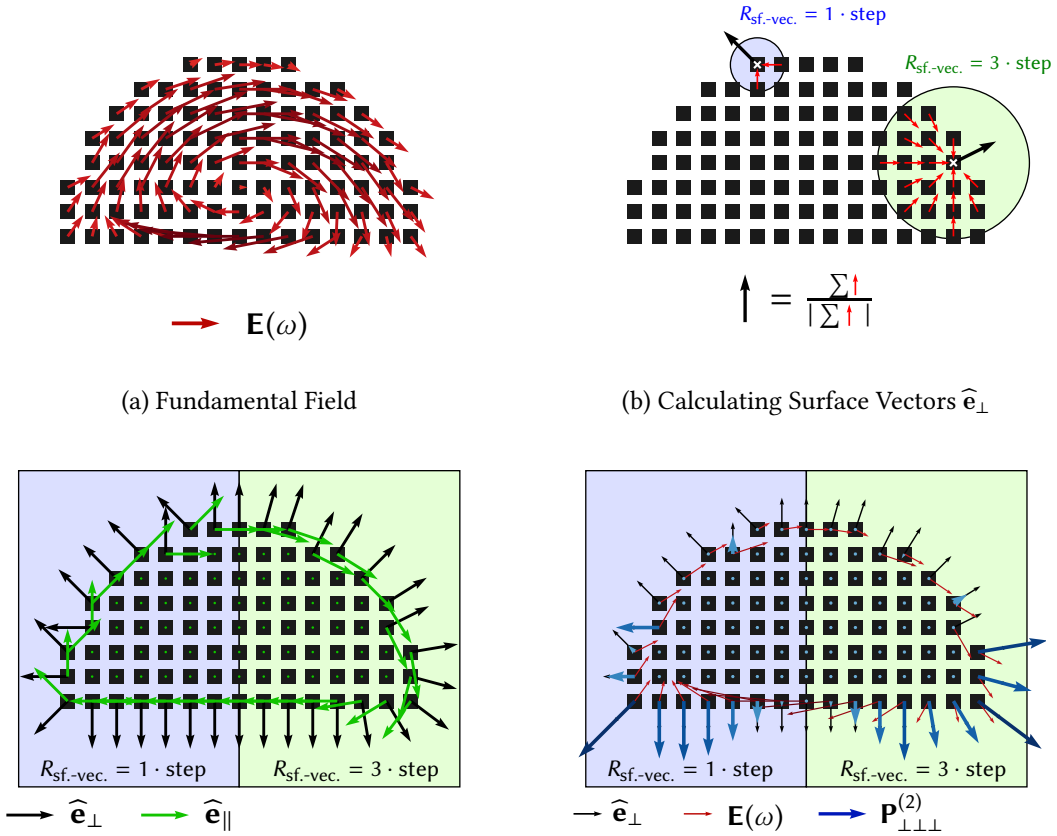

(a) Fundamental Field

(b) Calculating Surface Vectors $\widehat{\mathbf{e}}_{\perp}$

(c) Surface Vectors

(d) Nonlinear Surface Polarization

Figure 2.15: Numerical calculation of the surface-vectors and second order surface nonlinear polarization at the example of an infinitely long half-cylinder of radius $r_{\text{cyl}} = 150\,\text{nm}$. 2D sections in the XZ-plane are shown. The fundamental field ($\lambda = 800\,\text{nm}$) under excitation polarized along the horizontal axis is shown in (a). In (b), the procedure for calculating the surface-normal unit-vectors (black) is depicted using only next neighbors (blue circle) and using dipoles within a radius of $R_{\text{sf.-vec.}} = 3$ discretization steps (green circle). (c) shows the normal and tangential surface vectors obtained with $R_{\text{sf.-vec.}} = 1$ and $R_{\text{sf.-vec.}} = 3$ discretization steps (blue and green highlighted regions) and in (d) the final nonlinear polarization ($\mathbf{P}^{(2)}_{\perp\perp\perp}$) from the surface fields is shown.

For convenience, the projection of the electric field vector on the surface (at the considered surface position) can be taken

$$\mathbf{E}_{\parallel} = \mathbf{E} - \left(\mathbf{E} \cdot \widehat{\mathbf{e}}_{\perp}\right) \widehat{\mathbf{e}}_{\perp} \tag{2.97}$$

which reduces the problem to only two orthogonal vectors $\widehat{\mathbf{e}}_{\perp}$ and $\widehat{\mathbf{e}}_{\parallel}$ with

$$\widehat{\mathbf{e}}_{\parallel} = \frac{\mathbf{E}_{\parallel}}{|\mathbf{E}_{\parallel}|}. \tag{2.98}$$

Once $\widehat{\mathbf{e}}_{\perp}$ and $\widehat{\mathbf{e}}_{\parallel}$ are known, the nonlinear polarizations can be calculated by inserting them in equations (2.93), with

$$\begin{aligned} E_{\perp} &= \mathbf{E} \cdot \widehat{\mathbf{e}}_{\perp} \\ E_{\parallel} &= \mathbf{E} \cdot \widehat{\mathbf{e}}_{\parallel}. \end{aligned} \tag{2.99}$$

On the example of a coarsely discretized, two dimensional (infinitely long) half-cylinder of radius $r_{\text{cyl}} = 150\,\text{nm}$, parallel and perpendicular surface unit vectors are shown in Fig. 2.15c. The fundamental field in the structure for an excitation at $\lambda = 800\,\text{nm}$, polarized perpendicularly to the long axes, is shown in Fig. 2.15a. The surface field components as well as the nonlinear surface polarization $\mathbf{P}^{(2)}_{\perp\perp\perp}$ are shown in Fig. 2.15d.

2.4.3.2 Bulk Contributions to Surface SHG

In order to be applicable in the most general possible way, the bulk contributions to surface SHG – which arise from field gradients – are calculated numerically using finite differences derivatives. We use in particular *center-differentiation* [266, chapter 5.7]:

$$\begin{aligned} \frac{\partial f(x)}{\partial x} &= \lim_{\epsilon \to 0} \frac{f(x+\epsilon) - f(x-\epsilon)}{2\epsilon} \\ &\approx \frac{f(x+\Delta x) - f(x-\Delta x)}{2\Delta x} \end{aligned} \tag{2.100}$$

In the case of the GDM, Δx will usually be equal to the stepsize used for the discretization of the particle. Accordingly, this approximation will become worse for large discretization steps, in addition to the loss of precision already occurring at the calculation of the fundamental field.

As an example, intensity maps of $\mathbf{P}^{(2)}_{\gamma}$ for a silicon nanowire of diameter $D = 100\,\text{nm}$, calculated by numerical derivatives of fields from Mie theory, are shown in figure 2.14 (right plots).

2.4.3.3 Self-Consistent Nonlinear Polarization

In the following, the field due to the excitation at λ_0 will be referred to as the *fundamental* field, the field due to the second harmonic generation at $\lambda_0/2$ as the *harmonic* field. The nonlinear polarizations calculated following sections 2.4.3.1 and 2.4.3.2 take into account the optical properties of the particle only at the fundamental wavelength. A possible resonant response of the structure at the harmonic wavelength is not considered in the calculation, which may significantly boost or – in the case of an absorption-resonance – reduce the effective nonlinear effect. The presence of the structure should therefore be rigorously taken into account also at the harmonic field.

Approaches based on Green's Dyadic functions that consider the presence of the nanostructure at the harmonic field have been proposed in the modeling of nearfield microscopy [309–311]. We will describe a very similar formalism, utilizing the techniques introduced in section 2.3

So far, we calculate the fundamental field in the structure by solving the optical Lippmann-Schwinger equation (Eq. (2.44))

$$\mathbf{E}(\mathbf{r},\omega) = \mathbf{E}_0(\mathbf{r},\omega) + \int \mathbf{G}_0(\mathbf{r},\mathbf{r}',\omega)\cdot\chi\mathbf{E}(\mathbf{r}',\omega)\mathrm{d}\mathbf{r}' \tag{2.101}$$

From this linear response we calculated the nonlinear surface polarizations of centrosymmetric SHG. With their frequency dependencies they write

$$\begin{aligned}
\mathbf{P^{(2)}}_{\perp\perp\perp}(\mathbf{r},2\omega) &= \chi^{(2)}_{\perp\perp\perp}\left[E_\perp(\mathbf{r},\omega)^2\right]\widehat{\mathbf{e}}_\perp \\
\mathbf{P^{(2)}}_{\perp\parallel\parallel}(\mathbf{r},2\omega) &= \chi^{(2)}_{\perp\parallel\parallel}\left[E_\parallel(\mathbf{r},\omega)^2\right]\widehat{\mathbf{e}}_\perp \\
\mathbf{P^{(2)}}_{\parallel\parallel\perp}(\mathbf{r},2\omega) &= \chi^{(2)}_{\parallel\parallel\perp}\left[E_\parallel(\mathbf{r},\omega)E_\perp(\mathbf{r},\omega)\right]\widehat{\mathbf{e}}_\parallel
\end{aligned} \tag{2.102}$$

Note, that the bulk contributions to surface SHG with their expressions in Eqs. (2.95) can be treated in the same way as the local surface components.

To rigorously take into account the influence of the particle on the nonlinear field, we need to calculate the self-consistent field induced in the particle by the nonlinear polarization. In a first step we consider the nonlinear polarizations $\mathbf{P}^{(2)}(\mathbf{r},2\omega)$ as the source of an "effective incident field" at the harmonic frequency. We calculate the field within the nanostructure induced by the nonlinear polarization using the field susceptibility at the harmonic frequency (Eq. (2.43)). At the example of the $\chi^{(2)}_{\perp\perp\perp}$-contribution this yields

$$\mathbf{E}^{(2)}_{0,\perp\perp\perp}(\mathbf{r},2\omega) = \frac{1}{\epsilon_0}\int_V \mathbf{G}_0(\mathbf{r},\mathbf{r}',2\omega)\mathbf{P}^{(2)}_{\perp\perp\perp}(\mathbf{r},2\omega)\mathrm{d}\mathbf{r}' \tag{2.103}$$

with the field susceptibility tensor $\mathbf{G}_0$ at the *harmonic* frequency 2ω.

We assume that there is no external incident field $\mathbf{E}_0(2\omega)$ at the harmonic wavelength and hence $\mathbf{E}^{(2)}_{0,\perp\perp\perp}$ is the only driving field at 2ω. In a second step, we propagate the "effective incident field" inside the particle using the generalized propagator $\mathbf{K}$ (Eq. (2.60)) at the harmonic frequency:

$$\mathbf{E}^{(2)}_{\mathrm{sc},\perp\perp\perp}(\mathbf{r},2\omega) = \int_V \mathbf{K}(\mathbf{r},\mathbf{r}',2\omega)\mathbf{E}^{(2)}_{0,\perp\perp\perp}(\mathbf{r}',2\omega)\mathrm{d}\mathbf{r}'. \tag{2.104}$$

The subscript "sc" indicates self-consistent fields. Finally we obtain the *self-consistent nonlinear polarization* by a multiplication with the *linear* susceptibility at the harmonic frequency

$$\mathbf{P}^{(2)}_{\mathrm{sc},\perp\perp\perp}(\mathbf{r},2\omega) = \chi(2\omega)\cdot\mathbf{E}^{(2)}_{\mathrm{sc},\perp\perp\perp}(\mathbf{r},2\omega) \tag{2.105}$$

We see that the generalized propagator has to be calculated at both, the fundamental and the harmonic wavelength. As a consequence, self-consistent SHG is twice as expensive in terms of computational cost, compared to the calculation of only the non-linear polarization. A step-by-step illustration of SHG calculation is shown in figure 2.16.

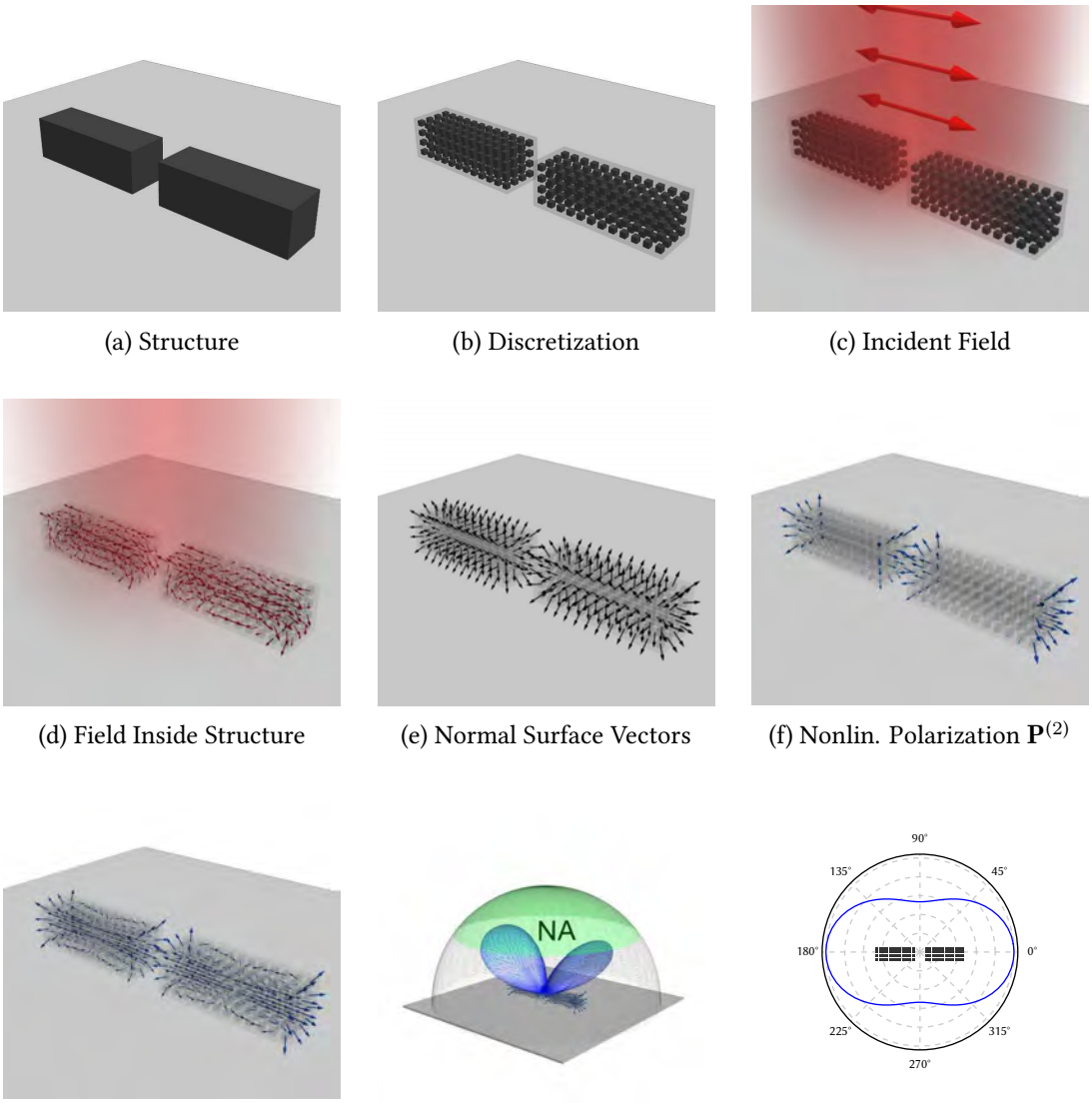

(a) Structure (b) Discretization (c) Incident Field

(d) Field Inside Structure (e) Normal Surface Vectors (f) Nonlin. Polarization $\mathbf{P}^{(2)}$

(g) Self-Consistent $\mathbf{P}^{(2)}_{\mathrm{sc}}$ (h) Farfield Propagation (i) Farfield Polarization

Figure 2.16: Illustration of the procedure for simulating SHG with the GDM at the example of a silicon dimer with dimensions $2\times 250\times 100\times 100\,\mathrm{nm}^3$ ($2\times L\times W\times H$) separated by a gap $G = 75\,\mathrm{nm}$. The investigated particle structure (a) is discretized (b) and the field induced by an incident beam is calculated using the GDM (c-d). From this linear response, the nonlinear surface polarization ($\mathbf{P}^{(2)}_{\perp\perp\perp}$ in the shown example) is calculated by first selecting the meshpoints at the particle's surface and determining the surface normal unit vectors (e). Using these, the nonlinear polarization is calculated from the fundamental field at the surface (f) and self-consistently propagated using the field susceptibility at the harmonic wavelength (g). Finally, the self-consistent nonlinear polarization can be propagated to the farfield (h) in order to calculated for example polar plots of the SHG (i) captured by a given numerical aperture (the green solid angle in (h) denotes NA 0.8). The inset in (i) shows a sketch of the dimer orientation with respect to the polar plot.

This approach can be easily adapted to other nonlinear processes. A third harmonic nonlinear polarization for example can be calculated directly from the fundamental field if a uniform $\chi^{(3)}$ tensor in the bulk can be assumed. Using non-uniform $\chi^{(n)}$ tensors would involve a slightly more complicated, yet straight-forward individual treatment of field-vector components. The self-consistent propagation can be done for other nonlinear processes exactly in the same way as shown above. The only prerequisite is that a nonlinear electric polarization can be approximated from the fundamental field.

As final remark we note that the components of the nonlinear susceptibility tensor $\chi^{(2)}$ are often not known and then set = 1. In this case an absolute comparison of the different contributions to SHG is prohibited.

2.4.4 Examples

In the last section of this chapter, we will give some examples of SHG from nanoparticles of centrosymmetric media, calculated with the technique described above. In the following we will refer to the "simple" nonlinear polarization if the self-consistent re-propagation of $\mathbf{P}^{(2)}$ has been omitted, in contrast to the "self-consistent SHG" calculated using $\mathbf{P}^{(2)}_{\mathrm{sc}}$.

2.4.4.1 Surface Vectors

In a first example, we compare the self-consistent SHG using $\mathbf{P}^{(2)}_{\mathrm{sc},\perp\perp\perp}$ from infinitely long silicon nanowires in vacuum of squared (Fig. 2.17b) and circular (Fig. 2.17a) cross sections. The diameters of $D_{\mathrm{squa.}} = 110\,\mathrm{nm}$ and $D_{\mathrm{cyl.}} = 140\,\mathrm{nm}$ are chosen such that under planewave excitation with $\lambda_0 = 800\,\mathrm{nm}$ and linear polarization along X ($\perp$ to the axis, transverse electric ["TE"]), a similar fundamental field distribution occurs in both geometries[1] (see red quiver plots (*i*) in Figs. 2.17). Stepsizes were $d = 6.7\,\mathrm{nm}$ and $d = 7.5\,\mathrm{nm}$ for the square and cylindrical wire, respectively. We calculated the normal surface vectors using different amounts of next neighbors (see Fig. 2.15): First neighbors (*ii*, calc. like blue area in Fig. 2.15b), first and diagonal neighbors (*iii*), up to second neighbors (*iv*) and meshpoints from a large area (11×11 neighbors) around the surface position. Farfield radiation patterns are shown below the nearfield plots for self-consistent (solid lines) and simple (from $\mathbf{P}^{(2)}_{\perp\perp\perp}$) SHG calculation (dashed lines). The structure is placed in the origin, illumination is incident from the top.

We can observe, that for flat surfaces (squared wire), the calculation of the surface vectors seems satisfactory already using only the closest meshpoints, limiting the vector directions to multiples of $45\,°$. If a large amount of neighbors is taken into account, artificial inclination of the vector close to the edges occurs, which impacts on the farfield radiation pattern. Therefore, in the case of flat surfaces, not too large amounts of neighbors should be taken for surface SHG calculation. On the other hand, in geometries which imply round surfaces, this conditions seems to reverse: The first-neighbor surface polarization is visually noncontinuous and results in significant backward-SHG. In all other cases (also in the squared wire), mainly forward-SHG is obtained, which has also been reported for plasmonic nano-particles [312]. We conclude that at round surfaces it is important to approximate the surface normal by a higher precision than $\pm 22.5\,°$, which is obtained by considering only next neighbors.

[1] the diameter $D_{\mathrm{squa.}}$ of the squared wire corresponds to the side-length of the square

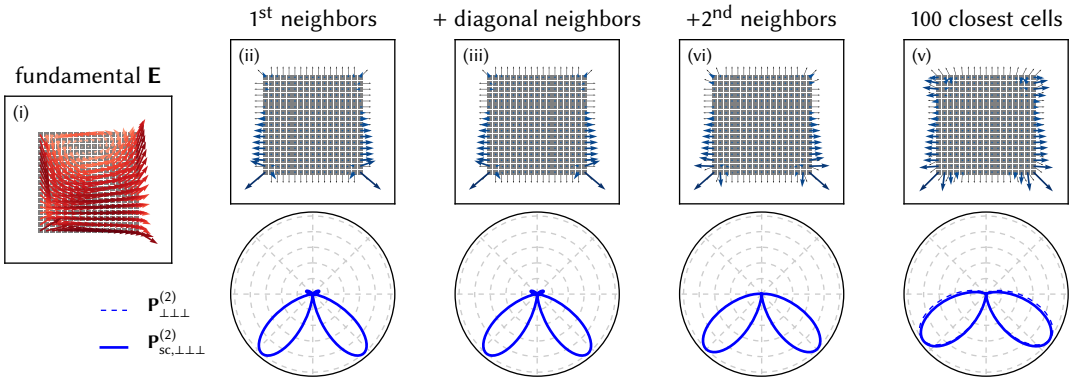

(a) Surface SHG from Squared Silicon Nanowire

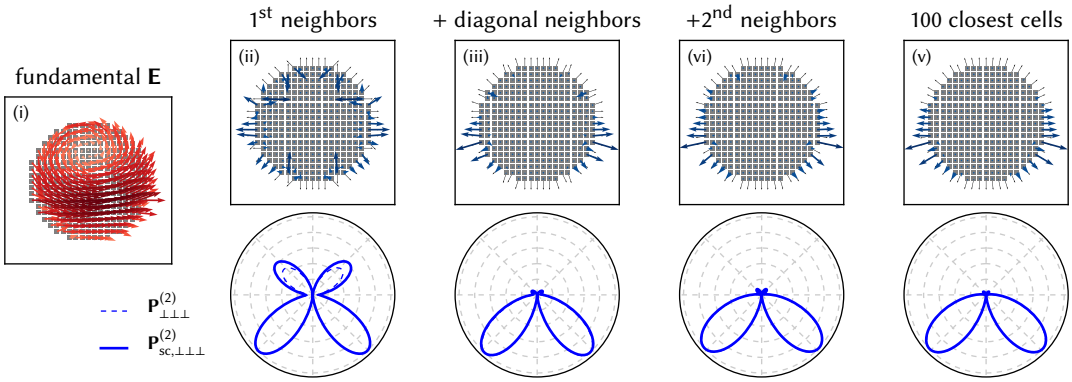

(b) Surface SHG from Cylindrical Silicon Nanowire

Figure 2.17: $\mathbf{P}^{(2)}_{\mathrm{sc},\perp\perp\perp}$ is shown for an infinitely long nanowire (radius 55 nm) of squared crosssection in (a), and for a cylindrical wire (radius 70 nm) in (b). Incidence from the top, linearly polarized along X ($\perp$ wire axis), $\lambda_0 = 800$ nm. From left to right are shown the fundamental field and $\mathbf{P}^{(2)}_{\mathrm{sc},\perp\perp\perp}$, calculated using 4, 8 or 12 next neighbors or all cells in an 11×11 square-steps large area ("100 closest cells"). Below the vector plots, radiation patterns are given for simple ($\mathbf{P}^{(2)}_{\perp\perp\perp}$, dashed) and self-consistent (solid line) SHG calculation.

Finally, we notice that in this example the self-consistent calculation is not absolutely necessary. The farfield radiation patterns are almost identical for the simple and the self-consistent second harmonic calculations.

2.4.4.2 Self-Consistent SHG

As shown in Fig. 2.17 it seems that in most cases the additional numerical effort of self-consistent nonlinear field calculation does not improve the numerical precision significantly.

We will therefore study self-consistent second-harmonic generation in comparison to using the "simple" nonlinear polarization on two more examples.

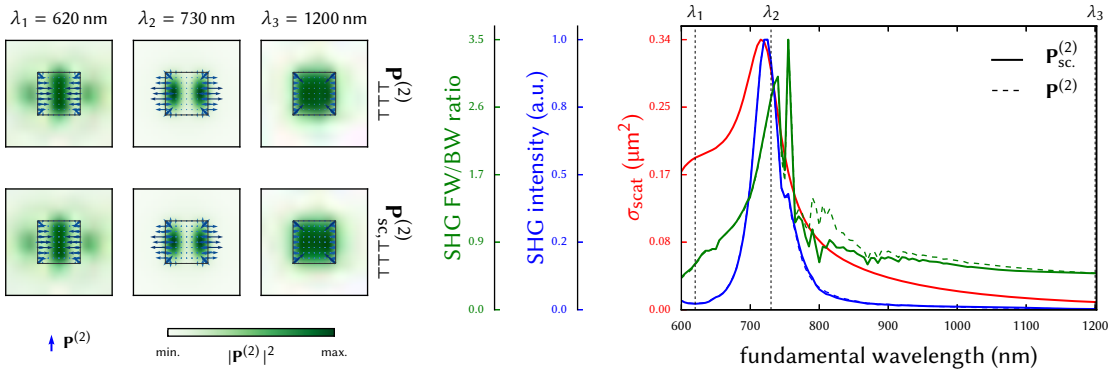

(a) Nearfield (XY-Projections) (b) Farfield

Figure 2.18: $\chi^{(2)}_{\perp\perp\perp}$ contribution to surface second harmonic generation for a $180 \times 180 \times 140\,\mathrm{nm}^3$ silicon nano-block. (a) shows XY-projections of the nearfield in (blue arrows) and 30 nm below the particle, X-polarized planewave incidence in $-Z$ direction. Plotted areas are $400 \times 400\,\mathrm{nm}^2$). In (b) the linear scattering is compared to SHG intensity in the farfield and second harmonic forward/backward emission ratio for simple (dashed) and self-consistent SHG calculation.

Silicon Nano-Cuboid

We start with SHG from a cuboidal silicon nano-block of dimensions $180{\times}180{\times}140\,\mathrm{nm}^3$ ($L{\times}W{\times}H$). In figure 2.18a, the second order nonlinear nearfield distribution is shown for a fundamental wavelength below (λ_1), on (λ_2) and above (λ_3) the TM_{01}-like resonance. Fields in the structure (blue arrows) and the field-intensity on a plane 30 nm below the particle are plotted for $\mathbf{P}^{(2)}_{\perp\perp\perp}$ (top row) and $\mathbf{P}^{(2)}_{\mathrm{sc.},\perp\perp\perp}$ (bottom row). The plots show XY-projections of the 3D structure, a planewave is incident from positive Z-direction, polarized along X. As before, the self-consistent calculation differs only marginally from the nonlinear polarization calculated from the fundamental field.

If we have a look at the farfield in Fig. 2.18b, the similarity between "simple" and self-consistent way of SHG calculation persists (dashed vs. solid blue line). For comparison, the scattering cross section $\sigma_{\mathrm{scat.}}$ is plotted (red line) as well as the forward-to-backward (FW/BW) SHG directionality. Total SHG intensity as well as second harmonic forward scattering have a maximum at the fundamental resonance. The second harmonic resonance has a smaller linewidth compared to the fundamental spectrum, which is in agreement with the second order dependence on the field amplitude. On resonance the FW/BW ratio has a maximum value of ≈ 3 while off resonance, the directionality is more or less uniform.

Gold Nano-Rod

In a second example, we have a closer look on a plasmonic particle, namely a gold nano-rod of $180 \times 180 \times 140\,\mathrm{nm}^3$ ($L \times W \times H$) in size. Like above, the spectral nearfield and farfield response is shown in figure 2.19.

In this particular structure, $\mathbf{P}^{(2)}$- and $\mathbf{P}^{(2)}_{\mathrm{sc.}}$-SHG (dashed and solid lines, respectively, in Fig. 2.19b) deviate significantly within a certain spectral range close to the localized surface plasmon resonance at $\lambda_1 \approx 1000\,\mathrm{nm}$. While the non-self-consistent SHG farfield intensity follows the linear scattering (again with a smaller linewidth), the self-consistent calculation reveals a

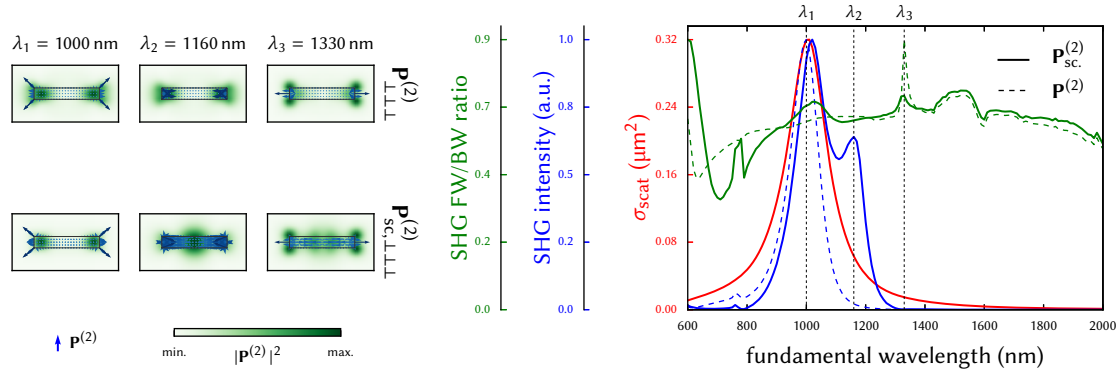

(a) Nearfield (XY-Projections) (b) Farfield

Figure 2.19: $\chi^{(2)}_{\perp\perp\perp}$ contribution to surface second harmonic generation for a $240\times50\times50\,\mathrm{nm}^3$ gold nanorod. (a) shows XY-projections of the nearfield in (blue arrows) and 30 nm below the particle, X-polarized planewave incidence in $-Z$ direction. Plotted areas are $400\times400\,\mathrm{nm}^2$). In (b) the linear scattering is compared to SHG intensity in the farfield and second harmonic forward/backward emission ratio for simple (dashed) and self-consistent SHG calculation

second maximum of the second harmonic around $\lambda_2 = 1160\,\mathrm{nm}$. Interestingly, this has no large influence on the forward-to-backward scattering ratio for SHG.

Having a look at the nearfield distributions at selected wavelengths (Fig. 2.19a), we see that when the excitation hits the plasmon resonance, $\mathbf{P}^{(2)}$ and $\mathbf{P}^{(2)}_{\mathrm{sc.}}$ have a very similar distribution. At the two other considered wavelengths λ_2 and λ_3 however, the self-consistent calculation reveals a significant linear response of the nanorod to the nonlinear polarization, which persists in the farfield and can be detected in the form of a peak of SHG intensity and directionality (for λ_2 and λ_3, respectively). However, the closer examination of this observation lies outside the scope of this thesis.

2.4.4.3 Conclusions

In conclusion we presented a method to calculate and analyze surface second harmonic generation from arbitrary nano-particles of centrosymmetric materials like silicon or gold using the Green Dyadic method.

From several examples we could deduce, that the "simple" nonlinear polarization $\mathbf{P}^{(2)}$ gives usually a good approximation to SHG i.e. it is often not necessary to take into account the presence of the structure at the harmonic frequency. As predicted by the Lorentz reciprocity theorem[1] [173, 313, 314], the optical properties at the harmonic wavelength have a linear influence on the total nonlinear scattering. This "self-consistent" contribution to the second order effects is opposed by a squared dependence on the fundamental field [174, 183, 315]. Hence we conclude that, if a resonance at the fundamental frequency exists, $\mathbf{P}^{(2)}$ does not differ significantly from the self-consistent field $\mathbf{P}^{(2)}_{\mathrm{sc.}}$. The expensive self-consistent computation of the nonlinear polarization is only necessary in particular cases with strong optical response at the harmonic

[1] In electrodynamics, reciprocity states for example that the gain of an antenna is universally describing the capability of reception as well as of emission

frequency. However, it is often difficult to judge in advance whether or not the structure's linear response to its nonlinear polarization is important, and if the self-consistent calculation needs to be performed.

Chapter 3

SHG from Individual Silicon Nanowires

Second harmonic generation (SHG) from silicon is weak from the bulk and in the past has therefore mainly been used for surface characterization [214–217]. More recently it was reported that SHG can be obtained from high field enhancement in silicon photonic crystals [195] or by a strain-induced breaking of the lattice symmetry [208, 209, 221]. Nanostructures, having large surface to volume ratios, can furthermore exhibit resonant modes with high field enhancements. Hence, nanostructures seem to be promising candidates to obtain SHG from silicon, and indeed enhanced SHG was observed on arrays of silicon nanowires (SiNWs) [207].

Due to silicon's non-zero $\chi^{(3)}$ tensor [316], recent research on nonlinear optical effects from silicon nanoparticles focused on third harmonic generation (THG). THG was obtained for example from Fano resonances in metasurfaces [193], individual nanowires [231], nanodiscs [191] or nanodisc oligomers [192].

In this section we investigate in more detail on second harmonic generation from silicon nanowires. In the first part, the linear optical properties will be summarized, before an experimental analysis and a subsequent interpretation of the results is presented.

3.1 Linear Optical Response

Before the discussion of nonlinear optical phenomena in SiNWs, we will start with an overview of their linear optical properties. The response of SiNWs to electromagnetic fields can be analytically treated with the "Lorenz-Mie theory" (usually simply referred to as Mie theory), originally developed for spherical particles [319]. Mie theory can be adapted to infinitely long, homogeneous cylinders using vector cylindrical harmonics for the field expansion series (see e.g. [304]).

3.1.1 Leaky Mode Resonances

It turns out, that optical resonances occur in small cylinders of higher refractive index than the environment. Due to their lossy character they are called "leaky mode resonances" (LMR). In

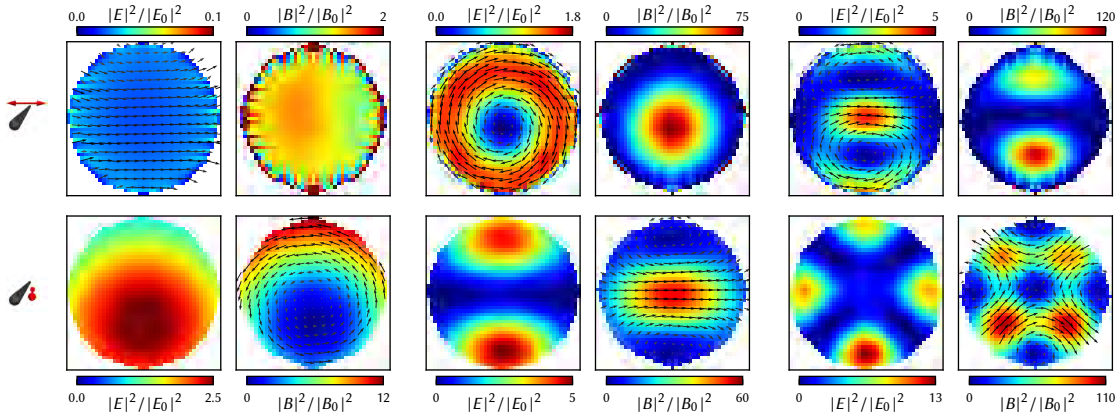

(a) TM_{01} (b) TE_{01} / TM_{11} (c) TE_{11} / TM_{21}

Figure 3.1: GDM-calculated field intensities for leaky mode resonances in silicon nanowires. (a): TM_{01} (NW of $D = 45\,\text{nm}$), (b): TE_{01}/TM_{11} (NW of $D = 115\,\text{nm}$) and (c): TE_{11}/TM_{21} (NW of $D = 175\,\text{nm}$). Electric (left) and magnetic (right) field intensities are shown for TE (top) and TM (bottom) polarized planewave excitation. If in-plane field components exist, the real-part is illustrated by small black arrows. Incident plane wave from top with $\lambda = 600\,\text{nm}$.

an intuitive image, the electric field undergoes multiple reflections inside the particle and the leaky mode resonance occurs if these reflective "round-trips" constructively interfere (for an illustrative support of this explanation, see the curled fields at the resonances shown in Fig. 3.1). The spectral positions λ_{LMR} of the LMRs are therefore roughly proportional to the *perimeter* of the nanowire

$$k \cdot \lambda_{\text{LMR}} \propto n \cdot 2R\pi \tag{3.1}$$

where k is an integer number and n the refractive index of the cylinder of radius R.

In figure 3.1 the electric and magnetic field intensity-distributions inside an infinitely long SiNW are shown for planewave excitation at $\lambda = 600\,\text{nm}$, polarized perpendicular (transversal electric, "TE") or parallel (transversal magnetic, "TM") to the wire axis. Diameters are chosen such that the wire is resonantly excited. Diameters are (a) $D = 45\,\text{nm}$, corresponding to a TM_{01} resonance, (b) $D = 115\,\text{nm}$ (TE_{01}/TM_{11}) and (c) $D = 175\,\text{nm}$ (TE_{11}/TM_{21}). The real part of the fields (if non-zero in plane of the NW section) is plotted as small black arrows. Simulations are performed by two-dimensional GDM (see Sec. 2.3).

In the TM_{01} mode (Fig. 3.1a), the fundamental magnetic resonance, a curled magnetic field corresponding to a single oscillating electric dipole along the NW axis occurs. For TE excitation on the other hand, the fields are uniform within the nanowire and can be described by the quasistatic approximation (see section 2.2.3). The electric counterpart is the TE_{01} mode (Fig. 3.1b). This mode is degenerate with the second order magnetic TM_{11} resonance. A double-curled magnetic field is induced in the plane of the NW section, corresponding to two electric dipoles along the wire axis (Fig. 3.1b, bottom). Again, the electric equivalent, the TE_{11} mode (shown in Fig. 3.1c), has a very similar curled electric field distribution and two magnetic dipoles oscillating with opposite phase along the nanowire axis. The latter mode is degenerate with the magnetic TM_{21} resonance, corresponding to four electric dipoles with alternating phase. These dipoles close to the surface can be seen as a result of the multiple reflections at the inner surface of the nanowire. Along

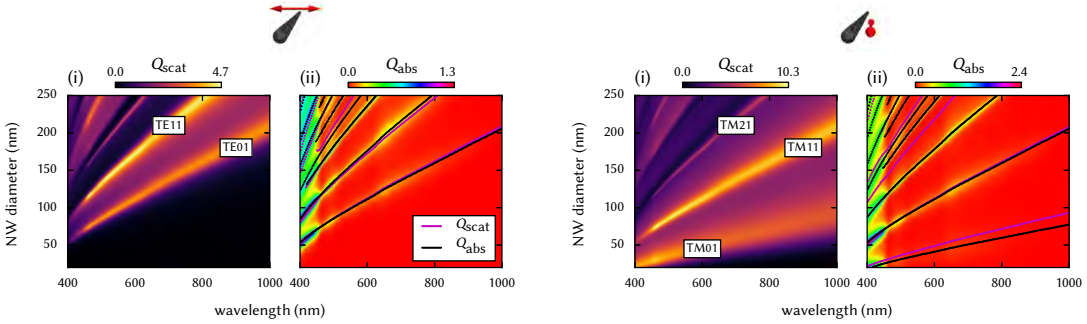

(a) Mie-Theory – TE excitation

(b) Mie-Theory – TM excitation

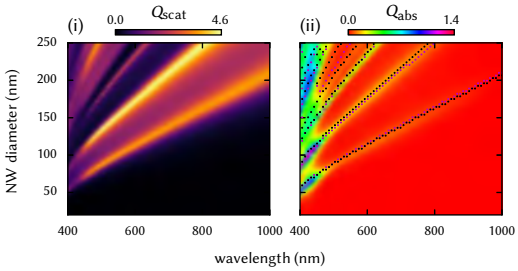

(c) GDM Simulation – TE excitation

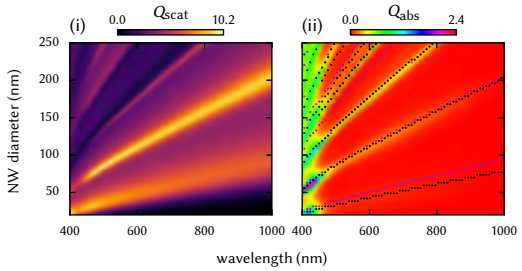

(d) GDM Simulation – TM excitation

Figure 3.2: Comparison between Mie theory (a, b) and GDM simulations (c, d) for scattering (*i*) and absorption (*ii*) efficiencies of infinitely long silicon nanowires. Linearly polarized planewave excitation. (a, c) TE and (b, d) TM. Local maxima of scattering (absorption) are indicated in the plots for Q_{abs} as purple (respectively black) dotted lines.

with these azimuthal modes, higher order radial modes exist (corresponding index j in TE/TM_{ij}). Electric field distributions of some more selected modes are shown in small insets of figure 3.5.

3.1.2 Scattering and Absorption

The LMRs in dielectric nanowires induce – as a consequence of their "leaky" character – resonances in the farfield scattering. As a measure for the ability to scatter light, the scattering efficiency Q_{scat} can be used, which is the ratio of the scattering cross section σ_{scat} over the geometrical cross section[1] σ_{geo}.

$$Q_{scat} = \frac{\sigma_{scat}}{\sigma_{geo}}. \tag{3.2}$$

The same can be done with the absorption cross section σ_{abs} to calculate an absorption efficiency

$$Q_{abs} = \frac{\sigma_{abs}}{\sigma_{geo}}. \tag{3.3}$$

In the case of an infinitely long nanowire (2-dimensional problem), the nanowire diameter is taken as reference size parameter and also σ_{scat} and σ_{abs}, calculated as described in section 2.3.6.3, are of the dimension of a length in this case.

[1] the geometrical cross section corresponds to the "footprint" of an object

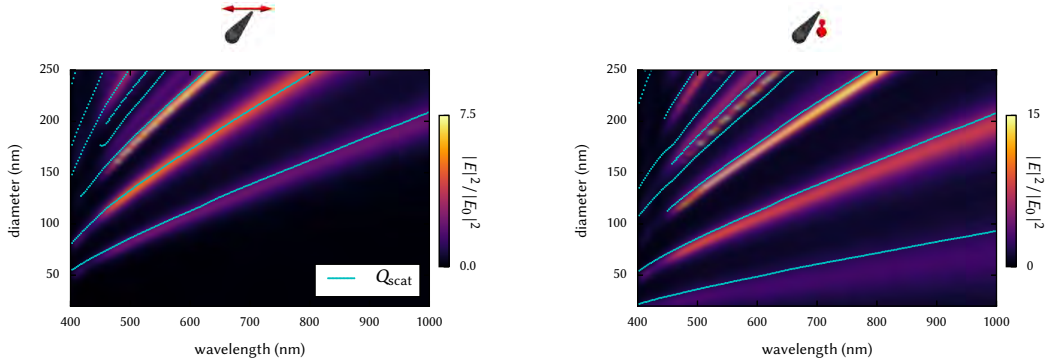

(a) TE excitation

(b) TM excitation

Figure 3.3: Maximum nearfield intensity enhancement inside silicon nanowire for planewave TE (a) and TM (b) excitation. The maxima of the scattering efficiency spectra are indicated with light blue lines for comparison.

Scattering and absorption efficiency spectra of infinitely long SiNWs are plotted as function of the incident wavelength and nanowire diameter in figure 3.2, calculated both, from Mie theory (a, b) and using the GDM (c, d). The incident plane wave is linearly TE (a, c) or TM (b, d) polarized. The numerical simulations are in excellent agreement with the analytical results, justifying the use of the GDM for the description of high-index nano-particles in general. The branches, corresponding to the modes illustrated in figure 3.1 are indicated by labels, where the degeneration of TM_{11}/TE_{01} and TM_{21}/TE_{11} becomes once more obvious, as the scattering branches are at the same positions in the diameter/wavelength plots for the respective incident polarizations.

Finally, we note that for photon energies sufficiently below the direct band-gap of silicon ($\lambda \approx 450\,\text{nm}$), absorption becomes generally very weak. This renders high-index particles like SiNWs very interesting for applications which require low losses and is one of the key differences to plasmonic nanostructures [75, 76, 99, 320].

3.1.3 Nearfield Enhancement

At resonance the electric field inside as well as in the vicinity of the nanowire is enhanced. In figure 3.3, the maximum field intensity enhancement inside a SiNW is plotted against wavelength and diameter for TE (a) and TM (b) polarized plane wave excitation. Light blue lines indicate the maxima of the far-field scattering efficiency. The shift between near- and far-field spectra can be explained by the damping term of a driven oscillator model [321, 322].

A detailed discussion of scattering and absorption as well as of the nearfield enhancement in the vicinity of SiNWs can be found for example in the PhD thesis of Kallel [323].

3.1.4 Directional Scattering

As explained in chapter 1, interferences of fields occurring when simultaneously exciting electric and magnetic resonances in dielectric particles, allow to fulfill the first Kerker condition ($\mu_r = \epsilon_r$, [144]) for nonmagnetic media, leading to purely forward directional scattering [145, 146].[1]

We saw, that in larger nanowires degenerate magnetic / electric LMRs occur, leading to both, strong electric and magnetic field enhancement. As a consequence, anisotropic scattering appears, which turns out to be oriented mostly in the forward direction (the same accounts for other high-index nanoparticles, see e.g. [90, 91]). The ratios of forward to backward (FW/BW) and backward to forward (BW/FW) scattering are plotted in figure 3.4 for TE (a) and TM (b) excitation. The maxima of the total scattered intensity are indicated with red and blue lines. In agreement with the not fulfilled Kerker condition, no directionality is obtained for the non-degenerate, purely magnetic TM_{01}-mode.

Some scattered fields around SiNWs and corresponding far-field radiation patterns are shown in figure 3.4c-f. For TE polarization, an excitation of the forward- (c) and backward-scattering (d) branch is shown (slightly below and above the TE_{01}-resonance in terms of NW diameter, respectively). A transition of forward- to mainly backward scattering takes place. For an incident plane wave polarized along the axis, scattering under excitation of the TM_{01} (e) and the TM_{11} (f) mode is shown. While unidirectional scattering occurs at the fundamental magnetic mode, almost pure forward scattering is obtained at the TM_{11} resonance.

3.1.5 Influence of Different Geometrical Cross Sections

From a numerical point of view, round surfaces such as the whole interface of a cylindrical Mie-nanowire, are technically demanding to be treated and often cause numerical artifacts. Under bad conditions, this can even lead to significant convergence problems and distort the simulation results (see for example Fig. 2.5). In a cubic discretization scheme it is therefore favorable to use flat surfaces.

Furthermore, lithographically defined nanowires are of square or rectangular cross section which raises the question, how the optical response changes if the cross section differs from a circle or hexagonal shape of VLS grown nanowires (see section 3.2.1).

In figure 3.5, scattering from infinitely long nanowires of different cross sectional shape is plotted. Circular (a,b), hexagonal (c,d), square (e,f) and triangular (g,h) sections are compared for TE (left) and TM (right) excitation. Obviously, apart from a slight spectral shift, low order cylinder LMRs are relatively insensitive to a change of the 2-dimensional section (see also [64]). However, deviations occur for higher order modes, which is obvious when square and circular wires are compared. Scattering efficiencies from hexagonal wires seem to stay close to the behavior of their circular counterparts for higher order modes. Also the field distributions at the resonant modes (see insets in Figs. 3.5) are in good qualitative agreement. Modes from triangular wires finally are shifted to larger diameters and longer wavelengths, which can be attributed to the lower amount of material per size parameter. Interestingly, the degeneracy of the TM_{11} and the TE_{01} mode seems to be relaxed in triangular wires, the TE_{01} mode is occurring for larger triangular sections

[1] We note, that the second Kerker condition under which pure backward scattering occurs (when the first order magnetic and electric Mie coefficients are equally large and of opposite sign: $a_1 = -b_1$) requires spherical particles [145].

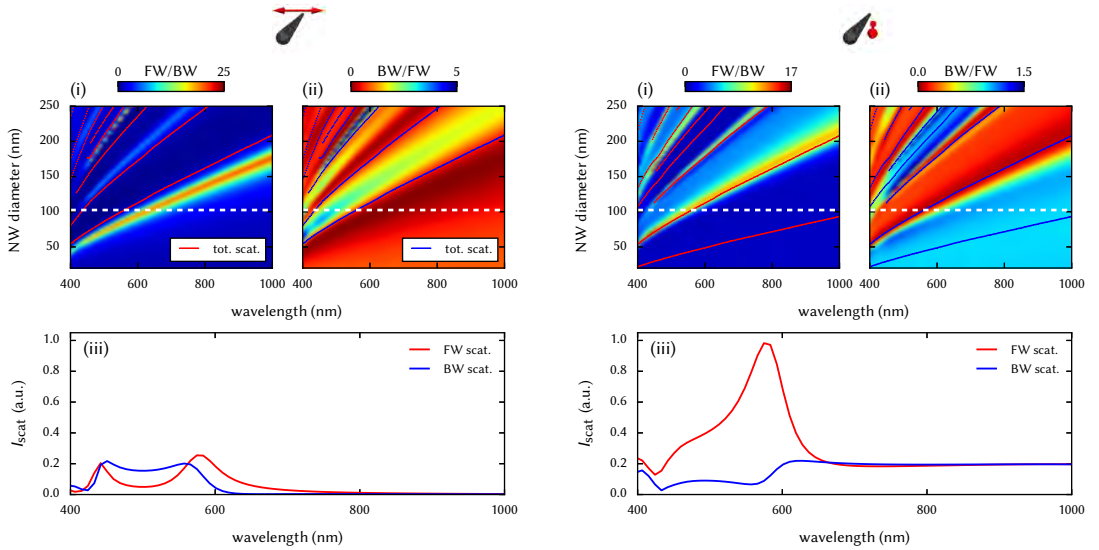

(a) TE excitation

(b) TM excitation

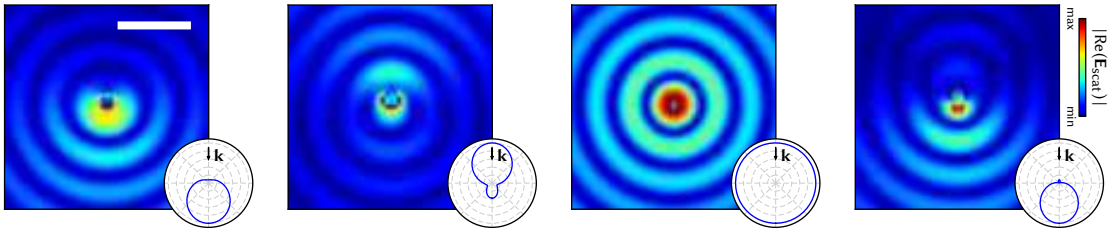

(c) $D <$ TE01

(d) $D >$ TE01

(e) TM01

(f) TM11

Figure 3.4: Ratio of forward to backward scattering (*i*: FW/BW, *ii*: BW/FW) for a silicon nanowire, illuminated by a TE (a) and TM (b) polarized planewave. (*iii*) FW (red) and BW (blue) scattering spectra for a SiNW with diameter $d = 100\,\mathrm{nm}$, indicated by a dashed line in (*i*) and (*ii*). Local maxima of the corresponding total scattering efficiency spectra (Fig. 3.2) are indicated in the plots by dotted lines. (c-f) show the absolute amplitude of the scattered electric field ($|\,\mathrm{Re}(\mathbf{E}_{scat})|$) in the vicinity of the nanowire for different modes. Scalebar corresponds to λ_0. In the insets the normalized radiation patterns for the farfield ($|\mathbf{E}_{scat}|^2$) are shown. Incidence from the top, the NW axis is in the center of each plot and is pointing towards the reader.

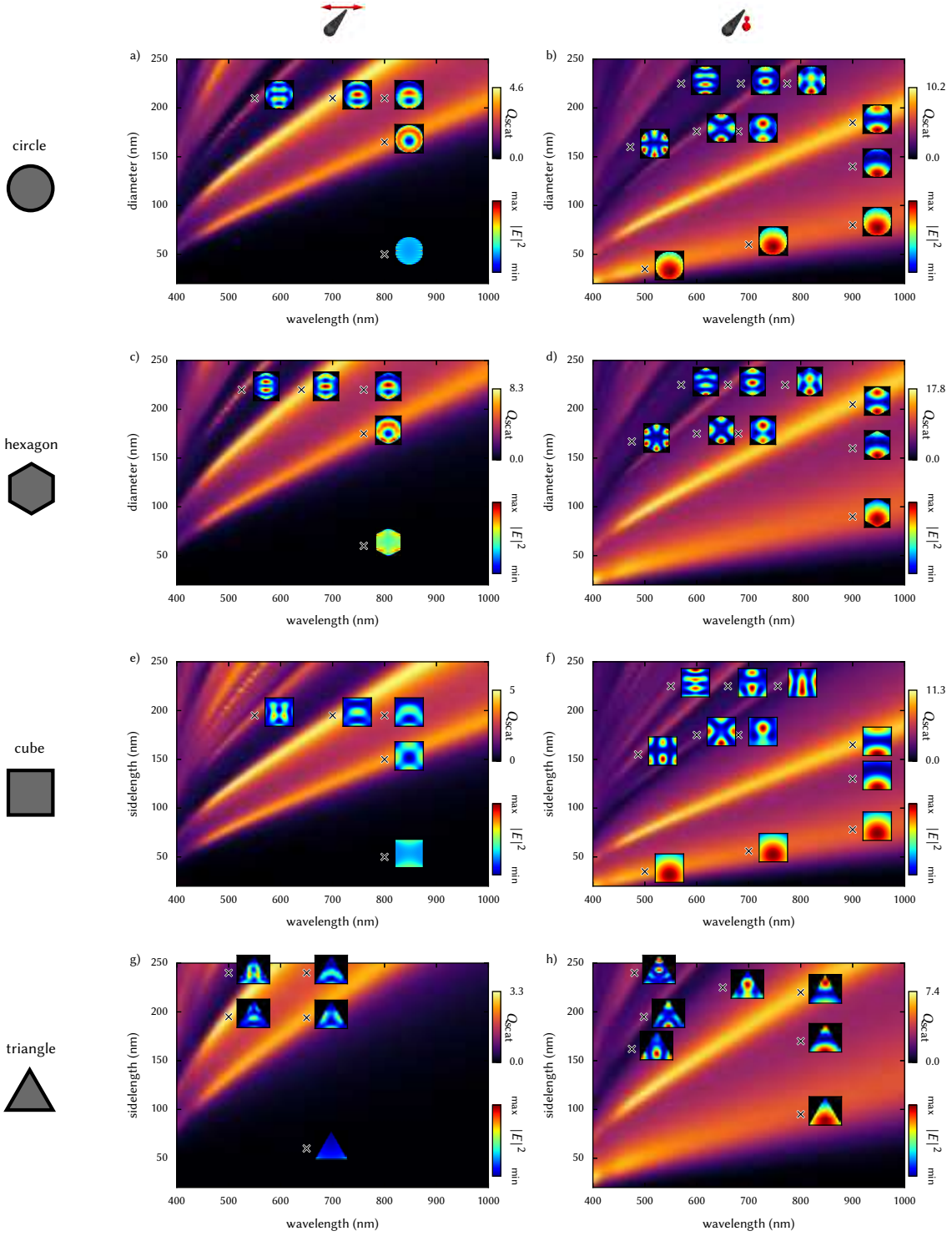

Figure 3.5: Scattering efficiency of infinitely long wires with various different cross sections under (a,c,e,g) TE and (b,d,f,h) TM polarized planewave illumination. Incidence from top. Nanowire cross section geometries are (a,b) circle, (c,d) regular hexagon, (e,f) square and (g,h) regular triangle. The field-intensity distribution inside the wire is shown for selected modes in insets (indicated by small crosses).

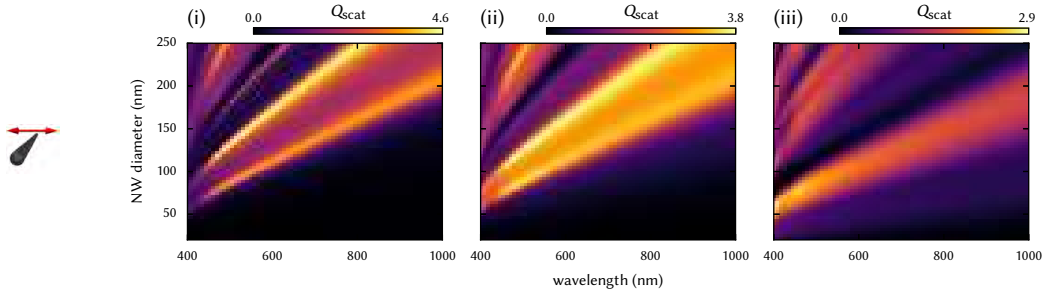

(a) TE excitation. (*i*) no, (*ii*) $n = 1.5$ and (*iii*) $n = 3.5$ substrate

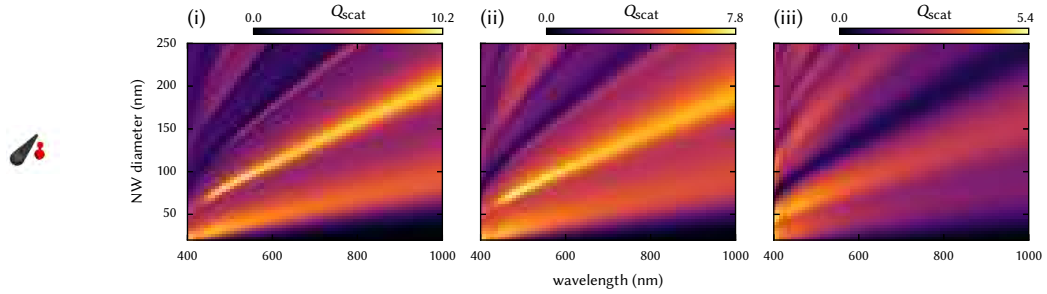

(b) TM excitation. (*i*) no, (*ii*) $n = 1.5$ and (*iii*) $n = 3.5$ substrate

Figure 3.6: Influence of a substrate on the scattering efficiency from SiNW for planewave TE (a) and TM (b) excitation. The case of no substrate (*i*) is compared with substrates of refractive index $n = 1.5$ (*ii*) and $n = 3.5$ (*iii*). $\mathrm{Im}(n) = 0$.

compared to the TM_{11} resonance. However, spatial field distributions are very resembling for all geometries and similar modal patterns are found in all cases.

We conclude, that a circular wire can be modeled in good approximation using a hexagonal or square section. In the following we will use square nanowires which have proven to provide the best numerical stability. As a final remark we note, that VLS grown SiNWs are in fact of hexagonal shape, so inversely we can deduce that Mie theory is a good approximation for such nanowires but a small shift of the resonances has to be kept in mind if comparing experimental spectra with simulations.

3.1.6 Influence of a Substrate

It is difficult to perform experiments on nanostructures in a homogeneous environment, since nanostructures are usually lying on a substrate. The presence of a substrate should therefore be taken into account in numerical modeling. This cannot be done in analytical Mie theory but is easily possible within the GDM (see section 2.3.2.1). To get an idea of the impact of a substrate on farfield scattering, scattering efficiency spectra are plotted as function of the cylindrical NW diameter in figure 3.6 for SiNWs in vacuum (*i*), on a $n = 1.5$ (*ii*) and on a $n = 3.5$ substrate. While a substrate of low refractive index (e.g. SiO_2 has $n \approx 1.45$ in the visible spectral range [324]) has only a minor influence on the spectral response of a silicon nanowire, a severe impact on the optical behavior is observed when the refractive index of both the NW and the substrate are

nearly equal (such as for SiNW on Si). The damping and broadening of the resonances might be explained by an increased "leaking" of the optical field at the interface to the substrate due to the refractive index matching, which consequently lowers the reflectivity at the interface between wire and environment.

We conclude that a low-index substrate will only weakly modify the analytical solution from a homogeneous environment and interpretations of results from nanowires on glass substrates can be done in good approximation using Mie theory.

3.1.7 Nanowires of Finite Length

In finite length cylinders the Mie resonances become hybridized with guided modes [69]. It has been shown, that the LMR contribution to the resonant behavior is dominant for nanowires with large aspect ratios (aspect ratio $L/D \gtrsim 10$) [70, 323].

3.2 Sample and Experimental Setup

After having discussed the linear optical properties of silicon nanowires, we will investigate on the nonlinear optical response in more detail. At first, we briefly present the samples and the experimental setup.

3.2.1 VLS Grown Silicon Nanowires

In the following we show results obtained from vapor-liquid-solid (VLS) grown crystalline silicon nanowires (growth along the [111] direction). The nanowire growth is performed at LTM Grenoble, in the group of Dr. Thierry Baron [326]. The VLS process is a chemical vapor phase epitaxial technique in which nanowires are grown from a precursor gas on a substrate, mediated by catalytic nanodroplets (usually gold). It allows for an accurate control of the diameter by adapting the size of the gold nanoparticles used as catalyst [131]. After the removal of the gold catalyst on top of the grown wires, the NWs are dispersed in solution by leaving the as-grown sample in an ultra-sonic bath for about 30 s. We deposited nanowires of three different diameters on transparent glass substrates (refractive index $n \approx 1.5$). The nanowires can then be characterized using scanning electron microscopy (SEM), atomic force microscopy (AFM) or darkfield microscopy (DF) and comparison with Mie theory. Illustrative results are shown in Figs. 3.7a,b,c. The range of NW sizes in the three selected samples are listed in table 3.1. Lithographic markers on the substrates allowed subsequent measurements on the identical nanowires. Using Raman spectroscopy we also verified that no $\chi^{(2)}$ components are induced by strain [208, 209]. For this,

Table 3.1: Characteristics of investigated VLS grown silicon NWs.

sample name	average diameter of gold droplets d_{VLS} [nm]	measured SiNW diameters d_{SiNW} [nm]
NW50	50	45 – 60
NW100	100	95 – 120
NW200	250	250 – 310

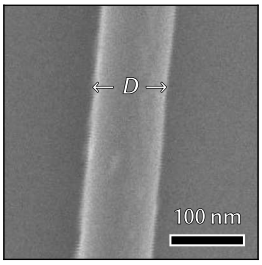

(a) NW100 SEM Image

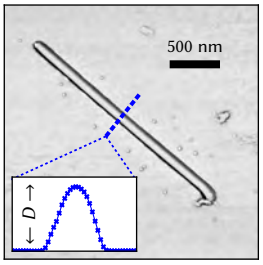

(b) NW100 AFM Image

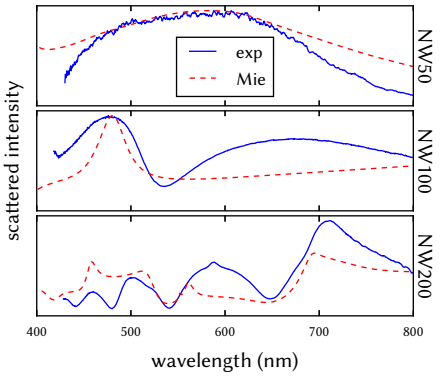

(c) Darkfield Scattering

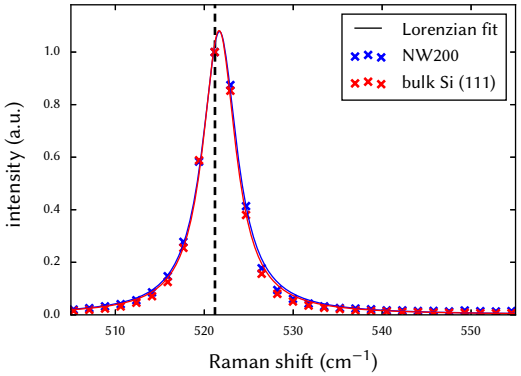

(d) Raman Spectroscopy

Figure 3.7: Characterization of the VLS grown SiNWs by SEM (a) and AFM (b) (scalebars are 200 nm and 500 nm, respectively), as well as optically using darkfield scattering in comparison with Mie theory (c) and Raman spectroscopy (d) In the latter, the dashed black line indicates the silicon Raman line at 521 cm^{-1} [325].

we compared the Raman shift of a NW200 SiNW with a bulk [111]-Si substrate. Lorenzian fits to the data result in an identical Raman shift at the Si-line at 521 cm^{-1} [325], as shown in Fig. 3.7d.

Sizes are chosen such that a single resonance is present in the visible spectrum for the smallest nanowires NW50. This resonance is non-degenerate and only appears under TM excitation. Under TE excitation, there is no mode in the visible spectral range. NW100 have the TM_{01} resonant mode around 700 − 800 nm and a second degenerate mode below 500 nm occurs (TM_{11}/TE_{01}). The large NW200 with diameters > 200 nm finally have multiple resonances. For more details on the linear optical properties, see the previous section 3.1.

3.2.2 Nonlinear Microscopy Setup

The nonlinear experiments were performed on a home-made nonlinear microscopy setup. The heart of the system is a pulsed femtosecond[1] Ti:Sapphire laser (Coherent Chameleon Ultra II), tunable in a range from 680 nm to 1080 nm. At a repetition rate of 80 MHz, the pulse length at $\lambda = 800$ nm is $\tau_{pulse} \approx 150$ fs (see also appendix A.2) and the time-averaged output power is $P_{avg.} \approx 4$ W at this wavelength. Assuming a rectangular pulse shape, this results in a peak laser

[1] 1 fs = 1×10^{-15} s

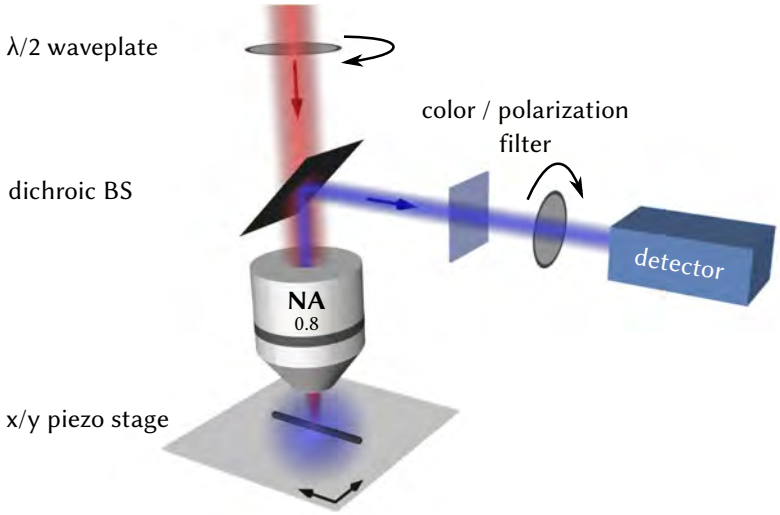

Figure 3.8: Sketch of the nonlinear microscopy experimental setup. A linearly polarized beam is incident from the top (red), its polarization can be controlled via a $\lambda/2$ waveplate. It is focused on the sample, which lies on a x/y piezo stage. The backscattered light (blue) is collected by the focusing optics and separated from the incident beam by a dichroic mirror. Then it is filtered and finally sent on a detector. The blue luminescent "cloud" around the SiNW is an artistic representation of the SHG.

power of $P_{\text{avg.}} \approx 0.33\,\text{GW}$. In the following we will stick to average powers as they can easily be converted to peak powers or energy per pulse.

The linear polarization of the fs-pulsed beam can be rotated by a $\lambda/2$ waveplate and is focused on the sample using a high numerical aperture (NA) microscope objective. If not noted otherwise, we used a $\times 50$, NA 0.8 air objective. To benefit from a larger working distance, some measurements have been performed using a LWD[1] $\times 100$, NA 0.8 air objective. Both objectives have around $90\,\%$ transmittivity at the second harmonic wavelength, slightly decreasing towards the infrared. Lower transmittance at the fundamental frequency when using the $\times 100$ objective is accounted for by increasing the incident laser power accordingly.

The backscattered nonlinear emission is collected by the same microscope objective and separated from the fundamental beam by a dichroic mirror ("Semrock 665 nm edge BrightLine"). Residual laser light is removed using bandpass colorfilters (3 mm Schott BG39) before the signal is directed onto the detection system, for which is used either a photomultiplier tube ("PMT", Hamatsu h7422) coupled to a lock-in amplifier (laser beam mechanically chopped at 6 kHz) or a spectrometer with a high-sensitivity CCD (Andor Shamrock 303 + Andor iDus 401 CCD).

The samples are lying on a x/y piezo stage with a closed-loop feedback positioning controller, allowing for nanometer-precise displacement of the nanostructures. The sample can be moved software-controlled below the focused laser beam in order to perform cartographic raster-scan acquisitions (see also Fig. 3.15b). In such map-scan experiments, the (nonlinear) signal is recorded at each position of the x/y stage, allowing to draw a 2-dimensional intensity map of the nonlinear signal.

[1] Long working distance

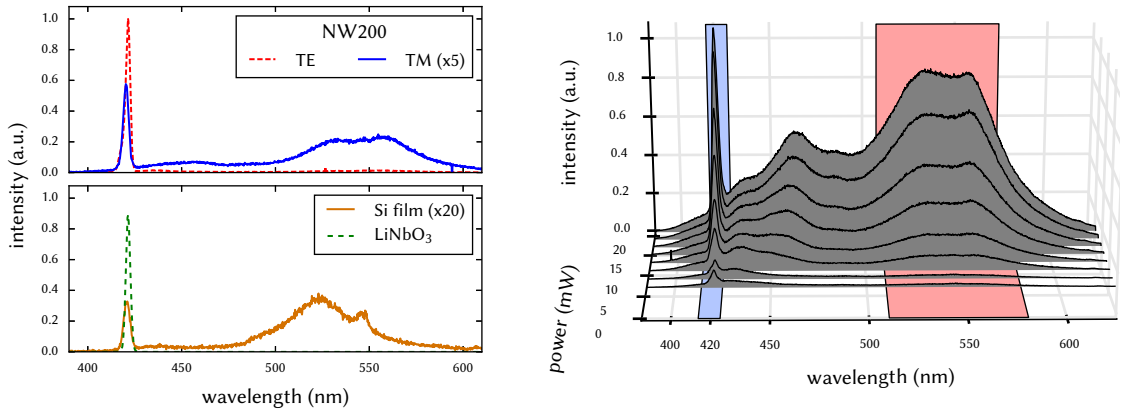

(a) Comparison of Spectra

(b) NW200, TM: Spectra vs. Incident Power

Figure 3.9: (a) shows a spectral comparison of the nonlinear emission from TE/TM excited NW200 (top) to a 200 nm thick Si-on-Quartz film ([100] surface orientation) and a bulk $LiNbO_3$ nonlinear crystal (bottom). In (b), spectra for NW200 are shown with increasing excitation power (average power). Power-law plots of the highlighted zones are shown in Fig. 3.12a.

3.3 Enhanced Nonlinear Optical Response

3.3.1 Spectrum of Nonlinear Response

In a first step, the nonlinear signal from a crystalline silicon nanowire (NW200) was spectrally analyzed and compared to reference samples, namely to a silicon-on-Quartz (SOQ) film of 200 nm thickness and a $LiNbO_3$ single-crystal with high $\chi^{(2)}$ for a pure second order nonlinear response [165, 327]. A BG39 colorfilter was inserted prior the spectrometer to remove residual fundamental laser light from the detection path and avoid damage of the sensitive CCD.

Measured spectra are shown in Fig. 3.9a for an excitation at $\lambda_0 = 840$ nm. The silicon samples were excited with an average power of $3.8\,\mathrm{mW}/\mu\mathrm{m}^2$, the $LiNbO_3$ crystal with $0.9\,\mathrm{mW}/\mu\mathrm{m}^2$. While the $LiNbO_3$ shows a purely second harmonic spectral response (sharp peak at $\lambda_0/2$), the silicon samples feature an additional large multi-photon photoluminescence (MPPL) band, covering the full spectral range between the SH peak and the cutoff of the BG39 colorfilter at around 600 nm. Interestingly, the MPPL band is much stronger in case of TM excitation than for a TE polarized incident beam. We can attribute this to the stronger field enhancement inside the NW for the TM case (see also Fig. 3.3).

3.3.2 Involved Nonlinear Effects

We found that the nonlinear response of individual SiNWs consists of different contributions: Second harmonic generation and a spectrally broad nonlinear luminescence, which we call multi-photon photoluminescence (MPPL). In the following we will therefore study these different spectral bands in more detail. We will find that the observed peak at $\lambda_0/2$ is very easily attributed to SHG. The analysis of the MPPL band, however, is not as unambiguous as it is concerning SHG, therefore we will use different characterization methods to corroborate our interpretation.

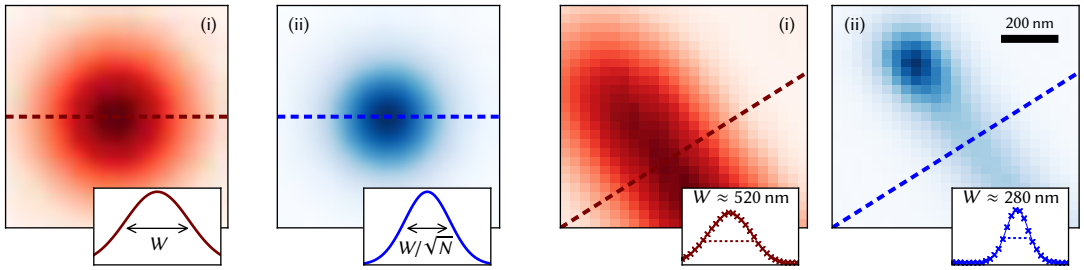

(a) Sketch: Width of Nonlinear Response

(b) Elastic and Nonlinear Scan of SiNW

Figure 3.10: (a) shows a sketch of the nonlinear response of order N (*ii*) to a diffraction limited gaussian profile (*i*). In (b) an experimental SiNW raster-scan map is shown. (*i*) elastic scattering and (*ii*) nonlinear signal.

3.3.2.1 Profile Width of Line-Scans

In order to gain a first insight about the order of the nonlinearity responsible for the measured signal, raster-scan measurements were performed on the NW200 sample. An illustration of the raster-scan type of measurements is shown in Fig. 3.15b. From the widths of the intensity profiles, we draw conclusions on the order of the nonlinearity at the origin of the luminescence. To estimate the spatial extension of a diffraction limited nonlinear response of order N to a Gaussian profile, we compare a Gaussian and the Nth power of a Gaussian

$$f(x) = \exp\left(\frac{-x^2}{2w_{\text{elastic}}^2}\right) \quad \longleftrightarrow \quad f(x)^N = \exp\left(N\,\frac{-x^2}{2w_{\text{elastic}}^2}\right) \tag{3.4}$$

where w_{elastic} is the diffraction limited spotsize of the focused laser beam. Comparison of the left- and right-hand side in Eq. (3.4) yields for the width of the nonlinear Gaussian

$$w_{\text{order } N} = \frac{w_{\text{elastic}}}{\sqrt{N}} \tag{3.5}$$

which is illustrated in figure 3.10a (*i* [red] linear, *ii* [blue] nonlinear response). This means for a second and third order nonlinear response:

$$\begin{aligned} w_{\text{2nd Order}} &= \frac{1}{\sqrt{2}} \cdot w_{\text{elastic}} \approx \frac{1}{1.414} \cdot w_{\text{elastic}} \\ w_{\text{3rd Order}} &= \frac{1}{\sqrt{3}} \cdot w_{\text{elastic}} \approx \frac{1}{1.732} \cdot w_{\text{elastic}} \\ &= \frac{2}{\sqrt{6}} \cdot w_{\text{2nd Order}} \approx \frac{1}{1.225} \cdot w_{\text{2nd Order}} \end{aligned} \tag{3.6}$$

A nonlinear intensity map of NW200 is shown in Fig. 3.10b(*ii*), the corresponding elastic scattering is shown in (*i*). The former was acquired with a BG39 filter, the latter without BG39 filter and strongly reduced laser power. We observe that the width of the nonlinear signal is too small to be caused by a second order nonlinear response, hence the observed nonlinear emission is *not* a consequence of SHG. To study this observation in more detail, we used a homemade

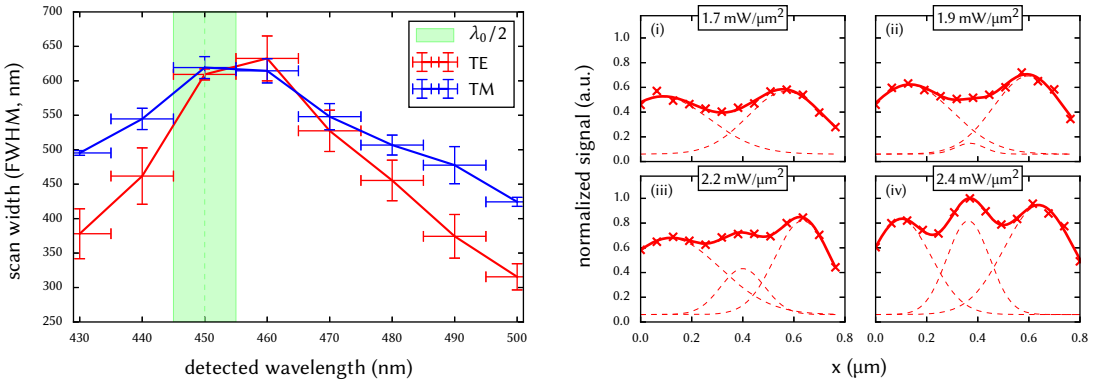

(a) Scan Width vs. Detected λ, NW200

(b) Scan Profiles for Several $P_{\text{exc.}}$, NW200

Figure 3.11: (a) shows a the scan width of the nonlinear emission of NW200 as function of the detection wavelength (like indicated by dashed lines in Figs. 3.10). Excitation at $\lambda_0 = 900\,\text{nm}$ ($\lambda_{\text{SHG}} = \lambda_0/2$ is highlighted green). Precision of the monochromator is $\pm 5\,\text{nm}$ (horizontal errorbars). In (b) profiles of the luminescence at the harmonic wavelength are shown across the NW for increasing excitation power. A fit to the data using three superposed Gaussians is shown as well as the individual Gaussian contributions to the fit. (*i*): lowest to (*vi*): highest average incident power. TM excitation of NW200.

monochromator setup, which we characterized with a calibrated white lamp and an Ocean Optics USB2000+ spectrometer. An investigation on the smaller nanowires NW50 and NW100 yielded good agreement with a second order nonlinear response at the SHG wavelength and a third order nonlinear scaling for the broad MPPL. The results are summarized in table 3.2.

The width of the nonlinear raster-scan across a SiNW (NW200) is shown as function of the detected wavelength in Fig. 3.11a. The spectral transmission window was $\approx 10\,\text{nm}$ large, indicated by horizontal errorbars. The vertical errorbars are standard deviations from the Gaussian fit to the linescan perpendicular to the NW axis. Interestingly, the width for detection at the SHG wavelength is about as large as we would assume for the scattering of the fundamental wavelength of $\lambda_0 = 900\,\text{nm}$. On the other hand, far from the SHG wavelength the measured profile widths across the wire correspond to a third order nonlinear response, in agreement with the smaller NWs.

In Fig. 3.11b profiles across the NW from a detection at the SHG wavelength ($\pm 5\,\text{nm}$) are shown for different excitation powers. In these plots we can observe two features with different

Table 3.2: Comparison of measured widths (all data from TM excitation) of several profiles to the nonlinear signal of SiNWs, filtered at SHG or MPPL. All widths indicate the FWHM. Physical diameters from comparison of Mie theory to linear scattering spectra.

NW	D_{physical} [nm]	w_{elastic} [nm]	w_{SHG} [nm]	w_{Broad} [nm]	$\frac{w_{\text{elastic}}}{w_{\text{SHG}}}$	$\frac{w_{\text{elastic}}}{w_{\text{Broad}}}$	$\frac{w_{\text{SHG}}}{w_{\text{Broad}}}$
NW50 #1	47	581	363	286	1.60	2.03	1.27
NW50 #2	59	542	359	286	1.51	1.90	1.26
NW50 #3	45	675	410	346	1.65	1.95	1.18
NW100	98	709	520	409	1.36	1.73	1.27

behaviors: On the one hand a signal from the NW borders as well as a second contribution from the NW center on the other hand, whose intensity increases much faster as function of the excitation power compared to the border signal. This can be explained by a strong second order response when the laser is focused on the NW borders, superimposed with a higher order nonlinear contribution which is strongest if the laser beam is focused on the NW center. For lower excitation powers, the higher-order response in the center is then invisible, but it increases more rapidly with rising incident power, such that it becomes dominant at a certain excitation strength. A fit to the linescans of Fig. 3.11b using a superposition of three Gaussians reveals indeed a convolution of two Gaussians of larger width at the borders and one more narrow Gaussian placed in between. The large values for the scan-width around $\lambda_0/2$ in Fig. 3.11a are the result of of the superposition of several nonlinear sources and can therefore not be used to estimate the order of the nonlinear effect.

We conclude that the NW200 are large enough to have a nonlinear optical response with several distinct features, resolvable by (nonlinear) optical microscopy. In consequence, Eq. (3.5) cannot be applied, because it is based on the assumption of a diffraction limited signal.

3.3.2.2 Power Dependence

In order to verify the finding of SHG at $\lambda_0/2$ and a third order broad luminescence, we performed a spectrally resolved series of measurements using increasing excitation powers, which is shown in Fig. 3.9b. The corresponding peak intensities as function of the excitation power are shown in Fig. 3.12a on a logarithmic scale (log-log plot). Power-law lines for $N = 2$ (blue) and $N = 3$ (red) are plotted as guide-to-the-eye and confirm a second order for the peak at the second harmonic wavelength as well as the hypothesis of a third order nonlinear process responsible for the MPPL.

3.3.2.3 Autocorrelation Measurements

Finally we performed a third series of measurements, to confirm the orders of nonlinear processes: We did autocorrelation measurements using two excitation beam paths with variable time-delay, controllable via a servomotor driven delay stage. The two beams are unified by a beam splitter before being focused on the sample by the same microscope objective. For the fits to the autocorrelation data, a chirp-free, Fourier limited Gaussian wave packet was assumed. The pulse-width of the laser at the fundamental wavelength τ_{pulse} was determined by a fit to autocorrelation data from a reference $LiNbO_3$ crystal, having a pure second order response, and was found to be $\tau_{\text{pulse}} \approx 150\,\text{fs}$. Experiments were carried out with excitation at $\lambda_0 = 810\,\text{nm}$ using

Table 3.3: Results for fits to autocorrelation measurements on a SiNW "NW200", filtered using color filters at the SHG wavelength $\lambda_{\text{SHG}} = 405\,\text{nm}$ and at the large multi-photon luminescence $435\,\text{nm} \lesssim \lambda_{\text{MPPL}} \lesssim 600\,\text{nm}$. Excitation on the NW tip at $\lambda_0 = 810\,\text{nm}$. Corresponding autocorrelation plots are shown in Fig. 3.12b.

λ_{det} (nm)	Order of Nonlinearity TE	TM
405 (SH)	1.9 ± 0.1	1.9 ± 0.1
> 435	2.6 ± 0.1	2.8 ± 0.1

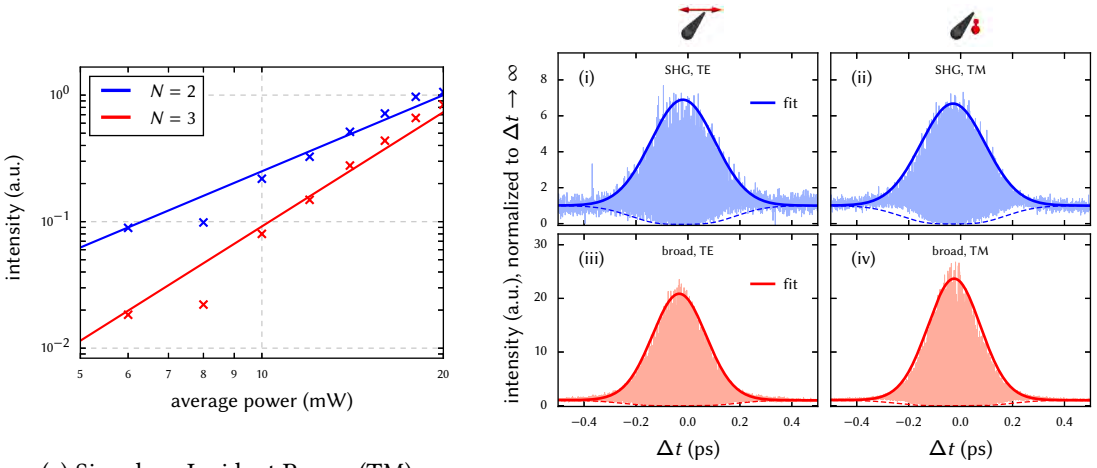

(a) Signal vs. Incident Power (TM)

(b) Autocorrelation

Figure 3.12: Investigation on the order of the nonlinear processes in silicon NWs. (a) powerlaw plot of the nonlinear signal filtered at the SHG wavelength (blue) and around the MPPL (red), as indicated in Fig. 3.9b. Power-law functions x^N for $N = 2$ and $N = 3$ are plotted as guides to the eye. In (b) interferometric autocorrelation measurements are shown for TE (*i, iii*) and TM (*ii, iv*) excited NW200. Colorfilters for SHG (*i, ii*) and the spectrally broad MPPL (*iii, iv*) were added prior detection. Autocorrelation fits to the envelope are plotted as solid lines, results are given in table 3.3.

Table 3.4: Results for fits to autocorrelation measurements at several detection wavelengths using a monochromator setup for wavelength range selection (transmitting a spectral window of $\lambda_{\text{filter}} \pm 5\,\text{nm}$). Excitation at $\lambda_0 = 840\,\text{nm}$.

	NW200 #1				**NW200 #2**			
λ_{det} (nm)	TE Tip	TE Center	TM Tip	TM Center	TE Tip	TE Center	TM Tip	TM Center
410	1.7	1.8	1.9	1.7	-	-	2.2	-
420 (SH)	1.7	1.8	1.8	1.8	1.9	1.8	1.9	1.7
450	2.1	-	2.2	2.5	-	-	2.3	-
480	-	-	3.1	2.7	-	-	2.7	-
510	-	-	3.1	2.8	-	-	2.8	3.4
540	-	-	2.9	2.7	-	-	2.8	2.7
540	-	-	-	-	-	-	2.8	3.2

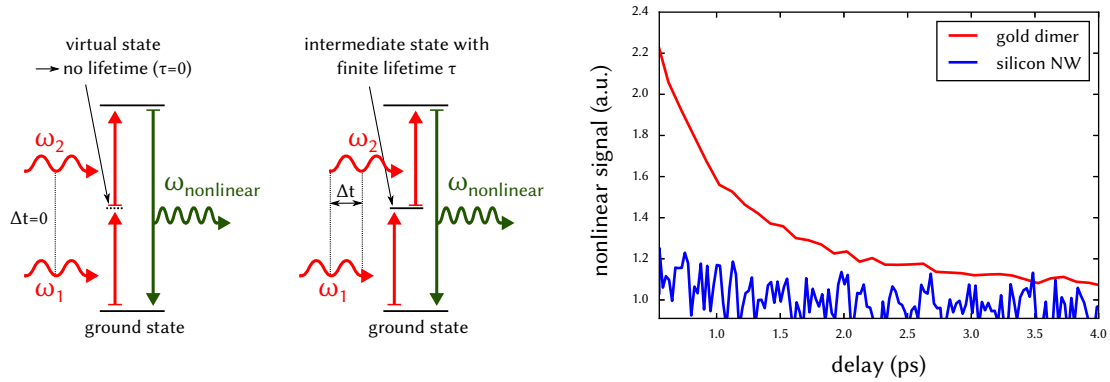

(a) Coherent Process (b) Incoherent Process (c) Two-Pump Experiment

Figure 3.13: (a) and (b) show schemes of a coherent and incoherent second order nonlinear process, respectively. In (c) two-pump time-delay measurements are shown comparing TPL from a gold nano-dimer and a silicon nanowire (NW200). Data is normalized to the intensity at large time-delay. No additional color-filter was added apart from a BG39 filter for residual fundamental light. The gold data (red) is in agreement with results published by Biagioni et al. [167]. No finite lifetime could be probed for SiNWs.

bandpass filters (405 ± 5 nm for SHG and > 435 nm for MPPL), as well as using the monochromator setup at an excitation wavelength of $\lambda_0 = 840$ nm. The results are listed in tables 3.3 and 3.4, respectively, confirming the second order nonlinear scaling for SHG as well as a third order response for the MPPL.

For a detailed description of the autocorrelation measurement technique, the theoretical modelling and fitting, the two-pump optical setup as well as for results of the reference measurements, see appendix A.2.

3.3.2.4 Coherent and Incoherent Nonlinear Processes

Finally we want to analyse if the observed MPPL in the silicon nanowires is of coherent nature. Coherent nonlinear effects are excited instantaneously with no intermediate states involved. Often, the concept of a *virtual state* is used: This state (which in reality doesn't exist!) is populated by a first photon and instantaneously further excited by a simultaneous second photon, as shown in figure 3.13a. The particularity of such a *coherent* nonlinear process is that – as the name suggests – the phase of the incident light is conserved. An *incoherent* nonlinear process on the other hand involves real intermediate states with finite lifetimes (Fig. 3.13b). In the latter case, the process can still be observed if the incident photons have a certain time-delay in the order of the intermediate state's lifetime, but their phase information is lost.

Using two time-delayed incident coherent beams (usually from a beamsplitted pulsed laser, equivalent to the autocorrelation measurement setup, see appendix A.2), intermediate states can be probed when measuring the nonlinear signal vs. time delay between the two beams. Attention has to be payed on the autocorrelation signal, which has to be cropped entirely. Such measurements revealed no detectable finite lifetime for the case of SiNWs, while the lifetime of gold nanoparticles, previously reported by Biagioni et al. [167] to be in the order of 1 ps, could

be reproduced. We conclude that the MPPL in SiNWs is driven by a coherent excitation process, possibly by THG in the bulk silicon.

3.3.2.5 Conclusions on Involved Nonlinear Processes

In summary, we conclude that the peak at $\lambda_0/2$, observed in nonlinear spectra from fs-pulse excited SiNWs, is indeed due to second harmonic generation and that the spectrally broad MPPL is a coherently excited third-order nonlinear process, probably a three-photon-induced photoluminescence[1].

Silicon has a large bulk $\chi^{(3)}$, and consequently third order processes are relatively efficient [191, 231, 282, 316]. The large luminescence could be a three photon absorption induced photoluminescence (3PPL) from the silicon. Direct PL from silicon lies in the spectral range between 450 nm and 600 nm [328], which corresponds to the observed wavelength range of the third order MPPL. It has also been reported that silicon nanowires can enhance luminescence from oxygen defects in SiO_2 [329]. Hence, the large luminescent band could be from the nanowire's thin shell of native silicon-oxide or from the glass substrate [330], excited e.g. by THG from the SiNW[2]. Further investigations e.g. with SiNWs deposited on different substrates should be performed to clarify the origin of the spectrally large luminescence.

3.3.3 Second Harmonic Generation Microscopy

We now leave aside the third order nonlinear photoluminescence and focus in the following section on second harmonic generation from individual SiNWs as function of their size.

3.3.3.1 SHG Line-Scans along SiNWs

In Fig. 3.14a, typical raster-scan maps of a NW200 are shown, excited at $\lambda_0 = 810\,\text{nm}$ and filtered at the second harmonic wavelength ($\lambda_{\text{SHG}} = 405\,\text{nm}$). In (*i*) the incident polarization was perpendicular to the NW axis (TE) and in (*ii*) parallel to the wire (TM). SHG intensity profiles along the SiNW are shown for both incident polarizations in (*iii*). While a homogeneous second harmonic signal is detected along the axis under TE excitation, a strong anisotropy occurs in the TM case, where the SHG intensity has a distinct maximum at the NW tips.

This effect can be explained by simple considerations on the continuity conditions at the interface of two dielectric media, which is described by the dielectric contrast i.e. by the difference of the relative permittivity. For a dielectric medium of permittivity ϵ_r placed in vacuum (ϵ_0), we get [294] (see also appendix 6.4.4)

$$E_{\parallel} = E_{0,\parallel} \tag{3.7}$$

$$E_{\perp} = E_{0,\perp}\frac{2\epsilon_0}{\epsilon_0 + \epsilon_r} \tag{3.8}$$

[1] Comparable to two-photon photoluminescence (TPL) in gold, which however is an incoherently excited process, since Au lacks a bandgap and real electronic states exist

[2] For excitation wavelengths of $800\,\text{nm} \lesssim \lambda_0 \lesssim 900\,\text{nm}$, THG lies in the UV. We cannot detect the corresponding light directly due to the limited sensitivity of the detectors

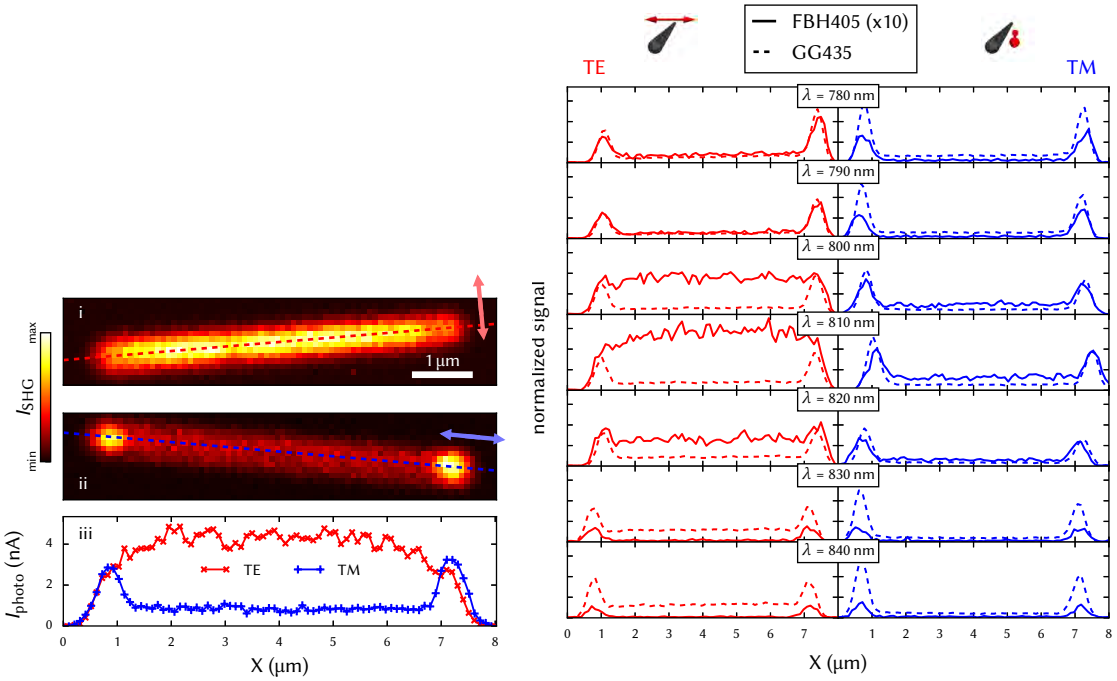

(a) NW200 SHG Rasterscan Maps

(b) NW200, TM: Spectra vs. Incident Power

Figure 3.14: Linescans along SiNW axis. (a) shows SHG-filtered 2D rasterscan of NW200 for TE (*i*) and TM (*ii*) excitation. Profiles extracted along the wire axis are shown in (*iii*). In (b), profiles along the NW200 axis are shown for different excitation wavelengths, filtered at $\lambda_{\text{filter}} = 405 \pm 5\,\text{nm}$ (solid lines) and at $435\,\text{nm} \lesssim \lambda_{\text{filter}} \lesssim 600\,\text{nm}$ (dashed lines). TE (blue) and TM (green) excitation are shown in the left and the right column, respectively.

where $E_{\parallel}$ and $E_{\perp}$ are the tangential and normal field components and E_0 is the incident field amplitude. The parallel field component is continuous over the interface, while the normal component is scaled by the dielectric contrast. This, together with the fact that $\chi^{(2)}_{\perp\perp\perp}$ ($\mathbf{P}^{(2)}_{\perp\perp\perp} \propto E^2_{\perp}$) is supposed to be the largest component of the second order susceptibility tensor for silicon [300], can explain the anisotropy of the SH intensity distribution in the TM case: The normal field component discontinuity occurs only at the tips, not along the NW where all field components are purely tangential.

Interestingly, this qualitative anisotropy appears only for SHG. When the third order MPPL is mapped, also for TE incidence the nonlinear signal increases under excitation on the NW tips compared to the signal intensity when focusing the laser along the NW. This is a further indication for the predominant role of $\chi^{(2)}_{\perp\perp\perp}$ and shown in Fig. 3.14b, where the fundamental wavelength is varied between $780\,\text{nm} \lesssim \lambda_0 \lesssim 840\,\text{nm}$, while the detection is fixed using color-filters at $\lambda_{\text{det.}} = 405 \pm 5\,\text{nm}$ (solid lines) or $\lambda_{\text{det.}} \gtrsim 435\,\text{nm}$ (dashed lines). Only when the second harmonic wavelength matches the color-filter's transmission line at $\lambda_{\text{det.}} = 405\,\text{nm}$, the intensity peaks at the NW edges disappear, outshined by the more intense second harmonic light.

As noted above, this behavior can be explained by the dominating $\chi^{(2)}_{\perp\perp\perp}$ component for second harmonic generation, boosting the signal from the perpendicular field components along the NW

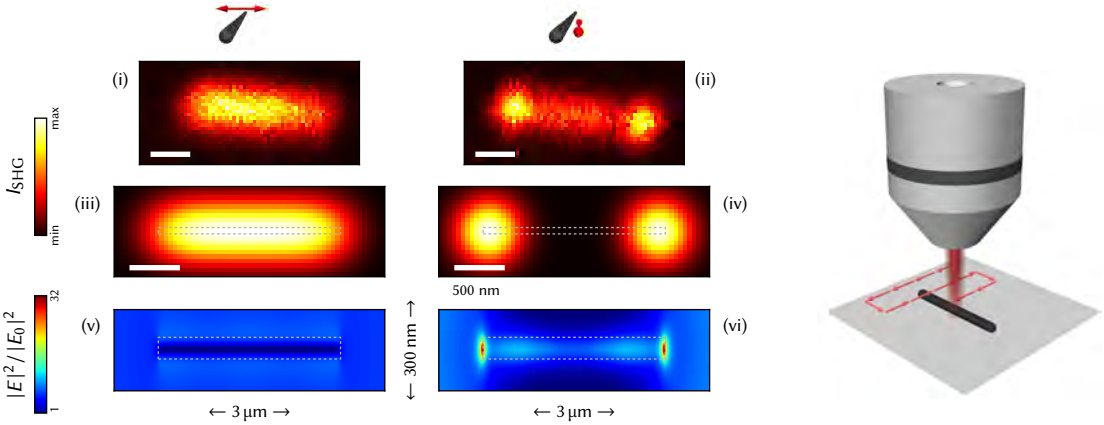

(a) Comparison Exp. / Sim.

(b) Sketch Rasterscan

Figure 3.15: In (a) the TE (*i*) and TM (*ii*) SHG mapping from experiment on a NW100 are compared to GDM rasterscan simulations using $\mathbf{P}^{(2)}_{\perp\perp\perp}$ (*iii*, *iv*) and the GDM-simulated fundamental nearfield on a plane 20 nm below the NW (*v*, *vi*). (b) shows an illustration of the rasterscans, performed in experiment and GDM simulations (*i-iv*).

axis under TE illumination. For the case of the $\chi^{(3)}$-induced MPPL this anisotropic contribution of certain field components to the nonlinear emission does no longer take place and the signal along the axis decreases strongly. The general enhancement of MPPL from the tips is a result of the dielectric contrast and probably further enhanced by guided light coupled into the wire, increasing the local density of photonic states (LDOS)[1].

This hypothesis is in agreement with the intensity evolution of the $\lambda_{\text{det.}} = 405\,\text{nm}$-filtered TE signal in Fig. 3.14b. Similar SHG anisotropies due to the contribution of only specific field components have also been reported from NWs of other materials like ZnSe [331] and gold [176].

3.3.3.2 Nearfield and SHG Rasterscan Simulations

To confirm that a $\chi^{(2)}_{\perp\perp\perp}$ induced SHG in SiNWs results in the observed polarization-dependent anisotropy of the raster-scan maps, we performed GDM simulations of the fundamental nearfield distribution and of a farfield raster-scan using only $\mathbf{P}^{(2)}_{\perp\perp\perp}$. The fundamental wavelength was set to $\lambda_0 = 810\,\text{nm}$, a focused planewave (see section 2.3.3.2) of diffraction limited diameter after the Rayleigh criterion ($d_{\text{spot}} \approx 1.22\lambda_0/\text{NA}$) is used for the raster-scan simulations, a plane wave for the near-field distributions which are calculated 20 nm below the NW. The structure model was a 2 µm long silicon nanowire of rectangular section with diameter $D = 100\,\text{nm}$. A square section is a valid approximation to cylindrical nanowires, as we showed in section 3.1.5: At lower order modes a rectangular wire behaves equivalently to a Mie nanowire, except for a small shift in the spectral positions of the resonances. The results of GDM rasterscan simulations are shown in figure 3.15a (*iii* and *iv* for TE and TM incidence, respectively) and compared to measurements on a similarly long nanowire NW100 for TE (*i*) and TM (*ii*) incident polarization. Maps of the

[1] The contribution of guided modes in crystalline NWs is further supported by recent measurements on lithographic wires (etched surfaces): Far less pronounced SHG and MPPL from the tips was observed in this case, which we attribute to imperfect surfaces, hindering the efficient coupling of light in the NW.

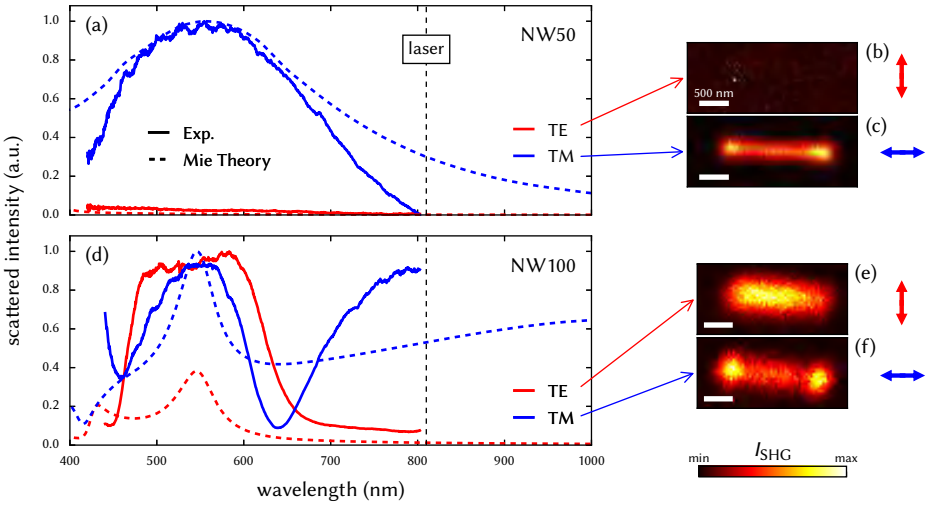

Figure 3.16: Left: Polarization filtered darkfield spectra of NW50 (a) and NW100 (d), measured (solid) and calcuated by Mie theory (dashed) for TE (red) and TM (blue) excitation. SHG-filtered raster-scan maps are shown at the right for TE (TM) excited NW50 (b, respectively c) and NW100 (e: TE, f: TM). Scalebars correspond to 500 nm.

nearfield intensity distribution are shown for the corresponding polarizations in (*v*) and (*vi*). A sketch illustrating the principle of the raster-scans is shown in Fig. 3.15b.

The SHG simulations using only perpendicular surface field components reproduce with good qualitative agreement the homogeneous SHG along the wire for TE excitation as well as the enhanced SHG from the NW tips for TM polarized illumination. In the latter case, no SHG is generated from the wire center, because only field components parallel to the wire surface exist. Finally, a comparison to the nearfield closely below the nanowire reveals an interesting analogy between the farfield SHG mappings and the nearfield distribution: While the field intensity is homogeneous along the wire for TE polarized incidence, in the TM case a strong field enhancement at the NW tips occurs. This is in agreement with reported experimental characterization of the optical nearfield in the vicinity of SiNWs [66].

3.3.3.3 SHG and Resonant Modes

In the following we explore the influence of resonant modes on the second harmonic generation. Therefore we focus on the smaller nanowires NW50 and NW100, featuring a limited number of resonant optical modes in the visible spectral range. NW50 has one, respectively no optical resonance under TM and TE excitation. NW100 has one resonance for TE incidence and supports two modes for TM illumination (see also Fig. 3.7c). In figure 3.16, typical results of NW50 and NW100 are shown. (a) for NW50 and (d) for NW100 show polarization filtered elastic scattering spectra (solid lines) compared to Mie theory (dashed lines) for TE (red) and TM (blue) polarization. Individually normalized SHG raster-scan measurements on the exact same SiNWs are shown in (b-c) for NW50 and (e-f) for NW100, excited at $\lambda_0 = 810\,\text{nm}$ with corresponding polarizations (indicated by small arrows).

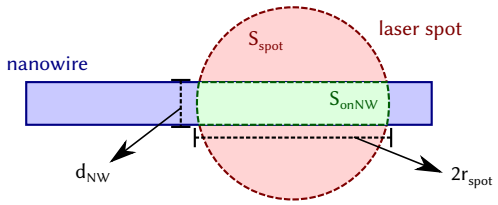

Figure 3.17: Scheme illustrating the renormalization of the SHG signal: Spotsize with respect to the illuminated NW area. $K_{\text{spot}} = S_{\text{onNW}}/S_{\text{spot}}$.

While always SHG was measured if a Mie mode was close to the fundamental wavelength (NW100 and TM excited NW50), no detectable second harmonic light was obtained from NW50 under TE excitation. From the corresponding scattering spectrum we see that there is no interaction of the nanowire with the exciting field. A comparison with Fig. 3.3a shows furthermore that the electric field inside the nanowire is close to zero, which explains the lack of SHG in the absence of a resonance. This is in agreement with nonlinear scattering theory, predicting highest SHG for a maximum spatial overlap of resonant modes at both, fundamental (squared proportionality) and harmonic wavelength (linear proportionality) [173, 332, 333] (see also Sec. 2.4.3.3). Hence, particularly in the absence of a resonance at the excitation wavelength, SHG is supposed to be very weak. The results in figure 3.16 are individually normalized, corresponding absolute values are given in table 3.5 where the results of NW50 and NW100 are furthermore compared to values from NW200 as well as to a bare glass substrate, a silicon substrate and a $LiNbO_3$ reference crystal ($\chi^{(2)}_{\text{bulk}} \neq 0$, excitation power reduced by a factor of 10).

3.3.3.4 Comparison of SHG from SiNWs to bulk Materials

In the experiment the diffraction limited minimal spot radius $r_{\text{spot}} \approx 0.61\lambda_0/\text{NA} \approx 620\,\text{nm}$[1] (for $\lambda_0 = 810\,\text{nm}$) is always significantly larger than the radius of the SiNW. We therefore calculate a scaling coefficient using the ratio between the illuminated area of the nanowire and the (nonlinear) area of the focused laser spot

$$K_{\text{spot}} = \frac{S_{\text{onNW}}}{S_{\text{spot, NL}}} \tag{3.9}$$

with the area governed by the second order nonlinear response to the focused laser spot (taking into account the quadratic intensity-scaling of the SH nonlinear response by the factor $1/\sqrt{2}$)

$$S_{\text{spot, NL}} = \pi(r_{\text{spot}}/\sqrt{2})^2 \tag{3.10}$$

and the intersection of spot and NW surface

$$S_{\text{onNW}} = d_{\text{NW}} \cdot \frac{2r_{\text{spot}}}{\sqrt{2}}. \tag{3.11}$$

To obtain the normalized SHG yield, we divide the photocurrent by the scaling coefficient K_{spot}, which then allows a comparison of the SHG signal from nanowires and bulk samples. Corre-

[1] Assuming the Rayleigh criterion is a good approximation.

sponding values are given in the rightmost column of table 3.5. We observe that the strongest SHG per illuminated area is obtained from NW100, being more than two orders of magnitude stronger than SHG from a bulk silicon crystal.

3.3.4 Conclusions

In conclusion, we found that the nonlinear response of silicon nanowires in the visible spectral range under femtosecond pulsed excitation in the near infrared consists of two main contributions: Second harmonic generation (SHG) on the one hand and a spectrally broad multi-photon induced photoluminescence (MPPL) on the other hand. While we could confirm the peak at $\lambda_0/2$ to be SHG, the latter contribution was found to be the result of a third order nonlinear effect, possibly a third harmonic induced luminescence. As for the SHG, we observed a polarization dependent anisotropy in raster-scan mappings. For an incident light linearly polarized normal to the wire axis, a homogeneous SHG all along the NW was observed, while for a polarization parallel to the axis, an enhancement of the SHG on the nanowire tips occured. We could track this behavior down to a mainly $\chi^{(2)}_{\perp\perp\perp}$-induced surface SHG in the SiNWs which we confirmed by numerical raster-scan simulations. Finally we observed a dependence of the SHG on the presence of resonant modes. In the absence of any resonance at the fundamental frequency, no SHG was observed. On the other hand, if Mie modes exist in the spectral vicinity of the fundamental wavelength, a SHG enhancement of more than two orders of magnitude can be obtained compared to bulk Si. In this context, further work with NWs of several different diameters, supporting resonances at either fundamental or harmonic frequency, as well as at both frequencies, should be

Table 3.5: Comparison of SHG signals for different samples and different experimental conditions. In the last column, the photocurrent is normalized to the illuminated area of the sample (K_{spot}, see Fig. 3.17). Laser power and wavelength were fixed at 3.15 mW/µm^2 and 810 nm, respectively (except 0.315 mW/µm^2 for $LiNbO_3$). The scattering efficiency $Q_{\text{scat.}}$ at 810 nm is calculated using Mie theory.

Sample	Laser Pos.	Polarization	$Q_{\text{scat.}}$	K_{spot}	I_{photo} (nA)	$\frac{I_{\text{photo}}}{K_{\text{spot}}}$ (nA)
$LiNbO_3$	–	–	–	1	55	55
Glass substrate	–	–	–		0.015	0.015
Si bulk (001)	–	–	–		0.19	0.19
200 nm Si (001) on Quartz	–	–	–		0.22	0.22
NW50	Tip	TE	0.014	0.073	0.015	0.20
	Center				0.015	0.20
	Tip	TM	3.32		2.5	34.2
	Center				1.6	21.9
NW100	Tip	TE	0.061	0.116	0.30	2.6
	Center				0.30	2.6
	Tip	TM	6.34		4.8	41.4
	Center				4.4	37.9
NW200	Tip	TE	0.60	0.436	3.3	7.6
	Center				3.8	8.7
	Tip	TM	1.61		5.6	12.8
	Center				1.6	3.7

very interesting. As SHG from silicon is normally forbidden in the dipole approximation (see section 2.4.2.2), the enhanced SHG renders SiNWs interesting for second order nonlinear photonic applications compatible to state-of-the-art CMOS technology. Furthermore, the possibility to tailor a polarization controlled on/off-switching behavior by the presence or absence of resonant modes might be exploited in various ways.

3.4 Origin of Second Harmonic Generation

As shown in section 2.4.2, SHG from centrosymmetric materials can be due to different processes. In this context, the source of the largest contribution to SHG has led to controversial conclusions. Often, second order effects in centrosymmetric nanostructures are modeled assuming the $\chi^{(2)}_{\perp\perp\perp}$ surface contribution from field components normal to the surface to be most significant, neglecting other possible sources (e.g. [176, 178, 300]). In the previous section we found, that the $\chi^{(2)}_{\perp\perp\perp}$ component can describe SHG also from SiNWs in a first, qualitative approximation. Nevertheless, we will see in the following that several phenomena we observed cannot be explained by $\chi^{(2)}_{\perp\perp\perp}$-SHG and we will find that, depending on the NW diameter and excitation conditions, contributions from tangential fields at the surface as well as from strong field gradients in the bulk have to be considered.

3.4.1 Introduction: Contributions to Surface SHG

Studies on the magnitude of other contributions have been performed on homogeneous surfaces [302, 307] as well as on metal nanoparticles like nanospheres [179, 201]. A geometrical study on the selection rules for local surface and non-local bulk contributions to SHG from metal nano-tips under planewave excitation pointed out a purely surface-like SHG in collinear measurements [297]. Nonlocal bulk contributions to SHG (Sec. 2.4.2.3) can be induced by field gradients due to resonant modes or tightly focused laser beams. For instance, the consequence of strong field gradients from focused excitation has been theoretically described for low-index spherical nanoparticles and a characteristic signature in the far-field emission pattern has been predicted [206]. A study on arrays of small Si spheres excited under tight focus found comparably strong bulk and surface contributions to SHG, and a scheme using polarization analysis of the harmonic emission was suggested to separate and identify those contributions [296]. Motivated by those publications, we will try in this section to understand the origin of SHG from SiNWs.

3.4.2 Experimental Results

Following the suggestion of a polarization analysis to separate SHG contributions [296], we filter the linear polarization state of SHG prior detection. Apart from this, we use the same experimental setup as in the preceding section (see Sec. 3.2.2 and Fig. 3.8). In figure 3.18 typical experimental results for representative nanowires of (a) NW50, (b) NW100 and (c) NW200 are shown. On the left of each subplot, second harmonic raster-scan maps along the NWs are shown. On the right, SH polar plots (farfield) are shown, recorded under excitation on the nanowire centers. Polar fits to the intensity of (partially) polarized light are shown as well, using the formula for the intensity of a superposition of two perpendicular, linearly polarized fields

$$I(\varphi) = A\sin^2(\varphi - \theta) + B\cos^2(\varphi - \theta) \tag{3.12}$$

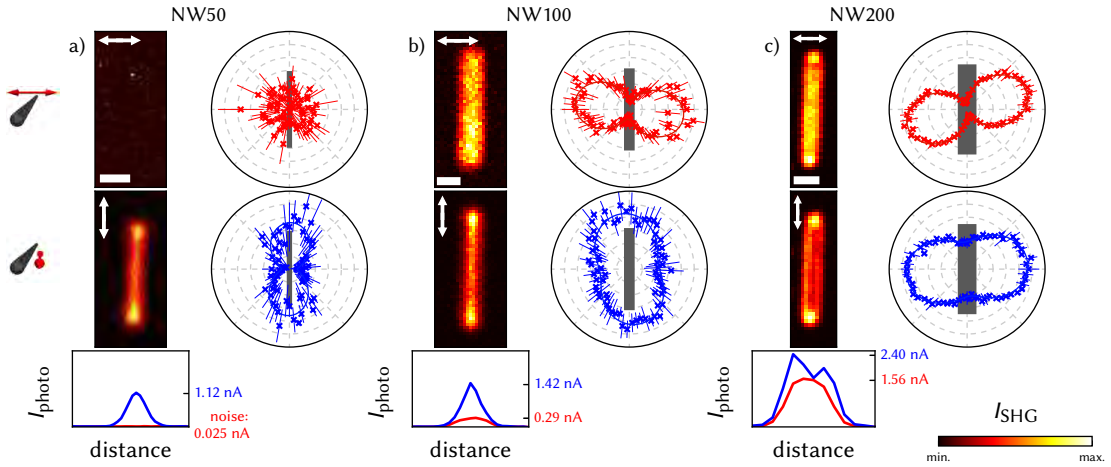

Figure 3.18: Left columns: Experimental second harmonic maps (no pol. filter), individually normalized to maximum intensity for (a) NW50, (b) NW100 and (c) NW200. Right columns: SH farfield polar plots (excitation on NW center; solid lines are fits to the data). Bottom row: Intensity profiles measured at the center across the NW for TE (red) and TM (blue) incidence. Scalebars are 0.5 µm.

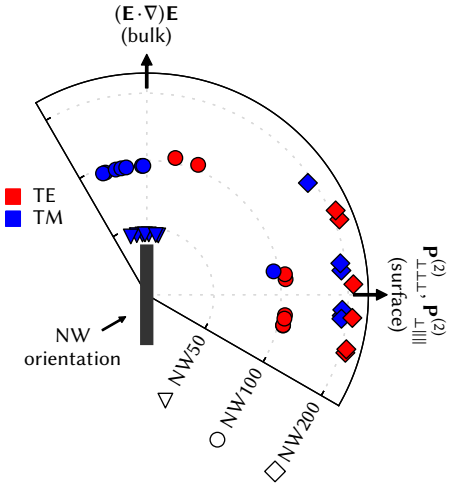

Figure 3.19: SH polarization angles of NW50 (triangles), NW100 (circles) and NW200 (diamonds) for TE (red) and TM (blue) excitation, focused on the NW center. Angles are obtained by fits to polar plots of the farfield SHG polarization like shown in Fig. 3.18. The results are grouped by NW diameter per radial coordinate. The arrows indicate the orientation of the far field second harmonic polarization of the nonvanishing contributions.

where φ corresponds to the angle of the polarization filter and θ is the angle of the second harmonic light's linear polarization, obtained from the fit.

The laser spot radius is about 620 nm at a wavelength of $\lambda_0 = 810$ nm. As we already observed in the previous section, TE excitation produces a homogeneous SHG along the NW axis and TM excitation leads to enhanced SHG from the NW tips, however with a significant remaining signal when the laser is focused on the nanowire axis.

As can be seen in the SH polarization polar plots of Fig. 3.18, a 90° flip of the polarization direction occurs in the TM configuration. Under TE excitation on the other hand, the SH light is always polarized perpendicularly to the nanowire axis, following the incident polarization. This general trend of SH polarization was confirmed by investigating over 20 different SiNWs. The polarization angles from fits using Eq. (3.12) to the data are shown in Fig. 3.19. Few NWs of the NW100 group showed atypical polarization behavior, which was possibly caused by partial illumination of one of the NW tips due to their relatively shorter length $L \approx 2\,\mu$m.

3.4.3 Theoretical Considerations

To interpret the experimental observation of a size-dependent flip of SHG polarization under TM excitation, we carry out some theoretical considerations on SHG from sub-wavelength small cylinders of centrosymmetric material.

3.4.3.1 Local Surface Contributions

Second order electric polarization in centrosymmetric materials can be written as a superposition of surface and bulk polarizations [169] (see also Sec. 2.4.2)

$$\mathbf{P}^{(2)}_{\mathrm{cs}} = \mathbf{P}^{(2)}_{\mathrm{sf}} + \mathbf{P}^{(2)}_{\mathrm{bulk}} \tag{3.13}$$

where for homogeneous and isotropic surfaces, $\mathbf{P}^{(2)}_{\mathrm{sf}}$ is a superposition of three independent non-zero components:

$$\mathbf{P}^{(2)}_{\perp\perp\perp} = \chi^{(2)}_{\perp\perp\perp} \left[E^2_{\perp}\right] \widehat{\mathbf{e}}_{\perp} \tag{3.14a}$$

$$\mathbf{P}^{(2)}_{\perp\parallel\parallel} = \chi^{(2)}_{\perp\parallel\parallel} \left[E^2_{\parallel}\right] \widehat{\mathbf{e}}_{\perp} \tag{3.14b}$$

$$\mathbf{P}^{(2)}_{\parallel\parallel\perp} = \chi^{(2)}_{\parallel\parallel\perp} \left[E_{\perp} E_{\parallel}\right] \widehat{\mathbf{e}}_{\parallel} \tag{3.14c}$$

where E is the field amplitude at the fundamental frequency ω, $\parallel$ and $\perp$ denote the directions parallel and perpendicular to the local NW surface and for simplicity we set $\epsilon_0 = 1$. Let us consider the case of an infinite cylinder. For an incident field normal to the cylinder axis (TE), it turns out that the three surface terms lead to a nonlinear polarization perpendicular to the nanowire axis. This is obvious for equations (3.14a) and (3.14b). In addition, as for TE polarization $\widehat{\mathbf{e}}_{\parallel}$ in Eq. (3.14c) corresponds to $\widehat{\mathbf{e}}_{\varphi}$ in the cylindrical coordinate system of the wire, it is as well perpendicular to the NW axis. If the incident field is parallel to the axis (TM case), no field component $E_{\perp}$ normal to the infinite cylinder surface exists, so that both $\mathbf{P}^{(2)}_{\perp\perp\perp}$ and $\mathbf{P}^{(2)}_{\parallel\parallel\perp}$ vanish (see also appendix B.3 for a numerical confirmation). As a consequence, equation (3.14b) alone describes the surface SHG in the TM case, which is polarized along $\widehat{\mathbf{e}}_{\perp}$, thus perpendicularly to the nanowire. This leads to the insight, that under excitation far from the NW tips, surface SH

polarization under either TE or TM excitation should always be perpendicular to the NW axis – a finding that is in contradiction with the TM polar plots shown in Fig 3.18a-b, where both SH and fundamental light polarizations are parallel to the NW axis (see also NW50 and NW100 in Fig. 3.19).

3.4.3.2 Non-Local Bulk Contributions

Let us therefore inspect the nonlinear bulk polarization, induced by field gradients in the material. Due to both, the presence of leaky mode resonances and a tightly focused laser beam, we presume that strong field gradients may exist in the SiNWs, so that bulk effects can not be neglected from the start. In first non-vanishing order, the bulk polarization consists of three terms [169]

$$\begin{aligned}\mathbf{P}^{(2)}_{\text{bulk}} = \gamma\, \nabla \left[\mathbf{E}^2\right] + \\ \beta\, \mathbf{E} \left[\nabla \cdot \mathbf{E}\right] + \\ \delta\, \left[\mathbf{E} \cdot \nabla\right] \mathbf{E}\end{aligned} \tag{3.15}$$

Note that we omitted the ζ-term proportional to $E_i \nabla_i E_i$ (Eq. (2.95)), whose susceptibility equals zero for homogeneous media [206]. It has been shown that the γ-term can be included in equations (3.14a) and (3.14b) using effective susceptibilities [204, 334]

$$\chi^{(2,\text{eff})}_{\perp\perp\perp} = \chi^{(2)}_{\perp\perp\perp} - \frac{\gamma}{\epsilon_r(\omega) \cdot \epsilon_r(2\omega)} \tag{3.16}$$

and

$$\chi^{(2,\text{eff})}_{\perp\parallel\parallel} = \chi^{(2)}_{\perp\parallel\parallel} - \frac{\gamma}{\epsilon_r(2\omega)}. \tag{3.17}$$

Thanks to its surface-like behavior, it is often referred to as the non-separable bulk contribution, which becomes small for high-index semiconductors (large ϵ_r) due to the electric permittivity in the denominator of the additional terms in the $\chi^{(2,\text{eff})}$. We can also neglect the β-term in Eq. (3.15), as $\nabla \cdot \mathbf{E}$ vanishes in the bulk of a homogeneous medium [302, 307].

Concerning the δ-term in Eq. (3.15), we find that under TE polarization strong field gradients appear only for large diameters because no field component exists along the axis[1], and the in-plane fields normal to the axis can be considered constant for diameters below the appearance of the first resonant mode[2]. At $\lambda_0 = 810\,\text{nm}$ this is valid for $D \lesssim 150\,\text{nm}$ (see Fig. 3.3). In consequence, the last term in Eq. (3.15) is supposed to vanish for sufficiently small NWs in the TE configuration. Under TM illumination, field components normal to the cylinder axis are zero and the bulk polarization reduces to

$$\mathbf{P}^{(2)}_{\text{bulk,TM}} = \delta \left(E_z \frac{\partial E_z}{\partial z}\right) \widehat{\mathbf{e}}_z \tag{3.18}$$

where z denotes the axial direction. This means that for TM incidence, the δ-bulk contribution is the sole SH source able to generate a nonlinear polarization along the NW axis. We consequently

[1] Note that field gradients along the axis in the case of a TE excited incidence cancel in the scalar product $(\mathbf{E} \cdot \nabla)$, because $E_z = 0$ ($Z \parallel$ NW axis).

[2] Corresponding to the quasistatic approximation for small NWs. Furthermore, the first resonance is a non-degenerate TM-mode, hence does not exist under TE illumination

assume that SHG under TM excitation on the center of NW50 and NW100 (figures 3.18a, 3.18b and 3.19) can be attributed to the $(\mathbf{E}\cdot\nabla)\mathbf{E}$ bulk contribution. For larger NWs the surface term $\mathbf{P}^{(2)}_{\perp\parallel\parallel}$ seems to become more significant, leading to the observed flip of the polarization (figures 3.18c and 3.19).

3.4.3.3 Conclusions

In summary, three contributions to SHG remain under consideration to explain our experimental results: The surface terms $\mathbf{P}^{(2)}_{\perp\perp\perp}$ and $\mathbf{P}^{(2)}_{\perp\parallel\parallel}$, resulting in a nonlinear polarization perpendicular to the NW axis, and the $(\mathbf{E}\cdot\nabla)\mathbf{E}$ bulk source ("δ"), creating a polarization along the NW axis. We also found that for a cylindrical geometry, the latter contribution only exists in the TM case.

In the case of silicon $\chi^{(2)}_{\perp\perp\perp}$ is considered to dominate SHG (see also Sec.3.3), while the weaker surface terms ($\chi^{(2)}_{\perp\parallel\parallel}$, $\chi^{(2)}_{\parallel\parallel\perp}$) and the separable bulk susceptibilities are supposed to be of comparable magnitude [300]. In the following, we will therefore examine the different contributions in more detail. This will be done using electro-dynamical simulations with the Green Dyadic Method (GDM).

3.4.4 Simulations

3.4.4.1 Simulation Method and Model

We model SHG using the GDM, as explained in detail in section 2.4. The incident field at wavelength $\lambda_0 = 810\,\mathrm{nm}$ is modeled as a focused planewave with a diffraction limited spot-size corresponding to NA 0.8 used in the experiments (see section 2.3.3.2). The δ-bulk contribution is calculated using central differences to approximate the gradients in Eq. (3.15). Finally, each meshpoint is considered as an emitter at $\lambda_0/2 = 405\,\mathrm{nm}$ and the radiation of the ensemble to the far-field is calculated using a propagator taking into account the presence of the substrate (see Sec. 2.3.6.4). The harmonic far-field intensity is integrated over the collecting solid angle of the NA 0.8, and optionally analyzed for its linear polarization state.

In order to simplify the numerical work and reduce numerical artifacts from round surfaces in cubic discretization, all 3-dimensional simulations have been performed using wires of rectangular cross section. We have shown in section 3.1.5 that for lower order modes, the difference between cylindrical and square sections is only a spectral shift of the resonances, while the resonance number and qualitative field distribution is conserved (see also [146]). The validity of this assumption is verified when comparing Mie theory for an infinite cylinder to simulated elastic scattering spectra of our square-wire 3D-model (Fig. 3.20a,*i*). Finally, we have shown in section 2.4.4.1, that the numerical SHG calculation is less error-prone using flat surfaces. To allow comparison with Mie theory, the simulated wires were chosen to be long compared to the spot size of the incident beam ($L > 2\,\mu\mathrm{m}$, see also section 3.1.7).

Throughout this section we stick to the "simple" SHG description, neglecting the influence of the presence of the structure on the harmonic field. A comparison of self-consistent and "simple" SHG calculus on SiNWs can be found in appendix B.3.

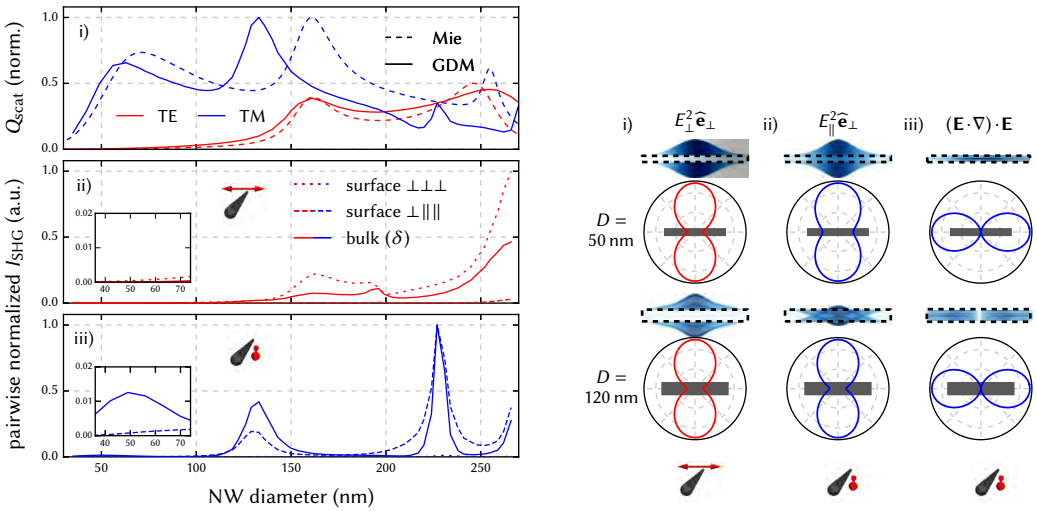

(a) SHG vs. NW Diameter

(b) SHG Farfield Polarization

Figure 3.20: All data for an incident wavelength of $\lambda_0 = 810\,\text{nm}$. (b, *i*): Elastic scattering intensities from Mie theory (dashed) and GDM simulations (solid) for TE (red) and TM (blue) excitation. GDM simulated SHG far-field intensities are plotted in (*ii*) for TE and (*iii*) for TM excitation. Surface (pointed: ⊥⊥⊥, dashed: ⊥||||) and bulk SHG (δ-term, solid lines) are pairwise normalized to their overall (TE / TM) maximum. The insets show zooms on the region of small diameters. In (b) are shown the nonlinear polarizations $\mathbf{P}^{(2)}$ (real parts, dense vector plots in blue color) and SH far-field polarizations (polar plots) for (*i*) TE excited ⊥⊥⊥, (*ii*) TM excited ⊥||| and (*iii*) TM excited bulk (δ) for a $D = 50\,\text{nm}$ and a $D = 120\,\text{nm}$ NW (top and bottom respectively).

3.4.4.2 $\mathbf{P}^{(2)}_{\perp\perp\perp}$ Surface contribution

In Fig. 3.15, a SHG raster-scan 3D-simulation considering only the $\mathbf{P}^{(2)}_{\perp\perp\perp}$ surface term, is shown for a NW of diameter $d = 100\,\text{nm}$. We observed from comparison with experimental data, that the global trend of homogeneous SHG for TE and tip-enhanced SHG for TM can be reproduced using only the normal surface contribution. Similar results are obtained for simulations using both, smaller and larger diameters. However, as pointed out above, two experimental phenomena can not be explained by only Eq. (3.14a): (1) TM-excited SHG from illumination of the NW center and (2) SH light polarized along the NW axis.

3.4.4.3 Diameter-dependence of SHG contributions

In order to verify the hypothesis of mainly $\mathbf{P}^{(2)}_{\perp\perp\perp}$ generated-SH in the TE case on the one hand and mixed ⊥|||-surface / δ-bulk SH for the TM case on the other hand, we carried out diameter-dependent SHG simulations, shown in figure 3.20. To include the bulk-contribution in our investigation, it was necessary to perform 3D GDM simulations using a focused incident beam which induces field gradients due to the Gaussian intensity distribution. As discussed earlier, nanowires of square section were used for these simulations.

A focused (NA 0.8) incident beam at $\lambda_0 = 810\,\text{nm}$, either polarized TE (Fig. 3.20a,*ii*) or TM (Fig. 3.20a,*iii*) was set on the center of a NW model, whose diameter was progressively increased.

SH intensities in the far-field were calculated for the $\mathbf{P}^{(2)}_{\perp\perp\perp}$ and $\mathbf{P}^{(2)}_{\perp\parallel\parallel}$ surface terms, as well as for the δ-bulk contribution. Each contribution is normalized to the highest intensity value within both incident polarizations. Note that absolute comparison of SH intensities is only possible within simulations of each contribution, and not between separate components, because we set the susceptibility components individually = 1.

The $\perp\perp\perp$-surface contribution under TE excitation exceeds the case of TM incidence on the entire diameter range by several orders of magnitude. As $\chi^{(2)}_{\perp\perp\perp}$ is supposed to surpass the other second order susceptibility components (see section 3.3, [300]), we conclude that SHG under TE excitation is dominated by the normal surface component, whereas under TM excitation the $\perp\perp\perp$-surface contribution seems to be negligible over the whole simulated range, which is in agreement with the theoretical prediction.

While the normal surface term vanishes for incident fields along the axis, $\perp\parallel\parallel$-surface and δ-bulk contributions are radiated more efficiently than in the TE case. We also see in Fig. 3.20a,*iii* that the surface term grows more rapidly with increasing diameters when compared relatively to the bulk term. This supports our assumption that SHG from TM illumination on the NW center is due to $\mathbf{P}^{(2)}_{\perp\parallel\parallel}$ and/or δ-bulk contributions, depending on the diameter range. We show in Fig. 3.20b simulated $\mathbf{P}^{(2)}$ near-fields (top row) and their polarization patterns after radiation to the far-field (bottom row) for $D = 50\,\text{nm}$ and $D = 120\,\text{nm}$. The behavior of the SH polarization is identical for all sizes of simulated wires. The $\mathbf{P}^{(2)}_{\perp\perp\perp}$ case under TE excitation shown in Fig. 3.20b,*i* is in agreement with the experimental results. $\mathbf{P}^{(2)}_{\perp\parallel\parallel}$ and the δ-bulk term under TM excitation are shown in Fig. 3.20b,*ii* and Fig. 3.20b,*iii*, respectively. These simulations show the $90\,^\circ$ flip of the far-field polarization pattern with respect to the NW axis. This is in agreement with the experimental plots of Fig. 3.18 and confirms ultimately the axis-parallel polarization emitted by the δ-bulk term, which is hence the main contribution to SHG from NW50.

3.4.4.4 Maps of SHG Farfield Intensity Distribution

The maps shown in Fig. 3.21 are calculated from a NW with diameter $d = 100\,\text{nm}$, but results for different NW diameters are qualitatively similar. Like above, the exciting beam is tightly focused on the NW center. The total intensity on the detector in the experiment corresponds to the integrated intensity over the area delimited by the NA of the microscope objective (indicated by dashed circles). As expected due to the symmetry of the system, the intensity in the center of the maps is zero. The data is normalized to the global maximum of each contribution, which reveals the polarization direction of the total collected harmonic emission.

While both, the TE excited $\mathbf{P}^{(2)}_{\perp\perp\perp}$ contribution and the TM excited $\mathbf{P}^{(2)}_{\perp\parallel\parallel}$ surface contribution result in mainly "TE" polarized SHG (perpendicular to the NW axis), the TM excited $\mathbf{P}^{(2)}_{\delta\text{-bulk}}$ has a nonlinear emission mainly polarized along the NW axis ("TM" polarized), confirming our earlier considerations. Furthermore, the residual TM-filtered SHG in the surface contributions show, that the figure-of-eight patterns in the polar plots can be more or less open also for a single contribution, as can be seen in the polar plots in Fig. 3.20b. This can explain relatively "open" measured polar plots, as shown for instance in Fig. 3.18. The SH intensity distribution in the far-field also shows that reducing the objective NA can enhance the detection of the δ-bulk contribution with respect to the surface components (surface SHG emits more to the "sides").

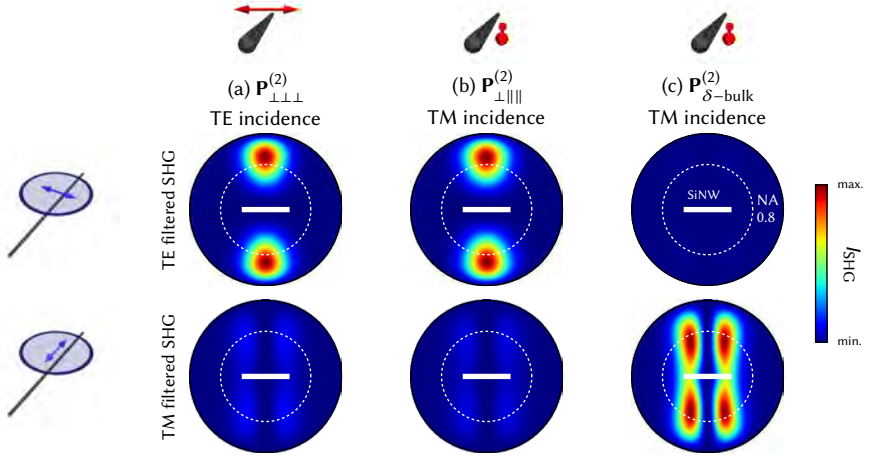

Figure 3.21: GDM simulation of the angular resolved farfield intensity distribution of SHG from a $d = 100$ nm SiNW. (a) $\mathbf{P}^{(2)}_{\perp\perp\perp}$-response under TE excitation, (b) $\mathbf{P}^{(2)}_{\perp\parallel\parallel}$-response under TM excitation and (c) $\mathbf{P}^{(2)}_{\delta\text{-bulk}}$-response under TM excitation, for each contribution the same colorscaling was used. In the upper plots TE-polarization (perpendicular to the NW axis) filtered SH emission pattern is shown and TM (along NW axis) filtered SH is given in the lower plots. The polar angle corresponding to NA 0.8 is indicated by dashed circles. The orientation of the nanowire with respect to the polar angle is indicated by a bar in the center of the polar plots. The incident polarization and analyzed polarization direction are indicated by small sketches at the figure borders.

3.4.4.5 Efficiency of SHG Epi-Collection

It may appear rather counterintuitive that SHG in small diameter nanowires occurs due to the δ-bulk contribution, while the surface sources increase with increasing diameter – hence for *decreasing* surface over volume ratio. Resonant optical modes have an influence on the relative weight of the nonlinear contributions, as can be seen in figure 3.20a, by a comparison to the linear Mie modes. A second important factor on the efficiency of the SH radiation to the far-field can be microscopic symmetries of the nonlinear polarization. Actually, strong silencing of farfield SHG is expected due to the high symmetry of the nanowires [176, 297]. By analyzing the nonlinear polarization vectors (see figures 3.20b), we indeed find a strong microscopic cancellation for the surface contributions while retardation among the more distant bulk polarization vectors circumvents the cancellation of oppositely radiating dipoles to the far-field.

To give an illustrative explanation for the observation of bulk effects dominating for small nanowires while surface effects occur only for larger structures, we consider in a simplified scenario two oppositely oscillating "effective" dipoles for the nonlinear polarizations $\mathbf{P}^{(2)}_{\perp\perp\perp}$, $\mathbf{P}^{(2)}_{\perp\parallel\parallel}$ and $\mathbf{P}^{(2)}_{\delta}$. The far-field radiation intensity through solid angles corresponding to different numerical apertures is plotted as a function of the inter-dipole distance between "dp1" and "dp2" in figure 3.22b. While for small distances cancellation is almost perfect, the radiation becomes observable in the far-field only for distances corresponding to a major fraction of the wavelength. In contrast to the local surface nonlinear polarization, the bulk contribution is mainly induced by the field gradient from tight focusing. Hence the average distance of dipoles oscillating with opposite phase will mainly be determined by the focal spot size which is of constant value.

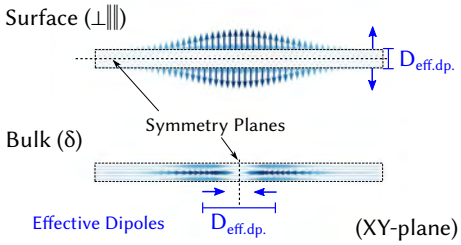

(a) Sketch Illustrating Distance of Effective Nonlinear Dipoles

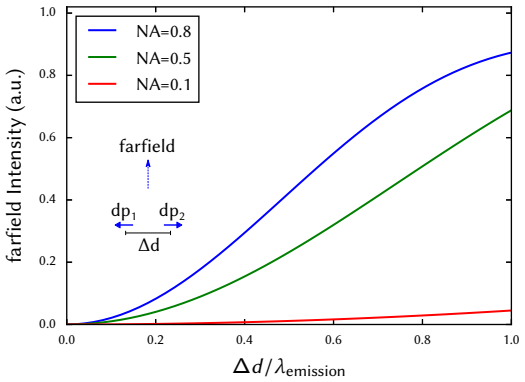

(b) Opposite Phase Dipoles Farfield Intensity

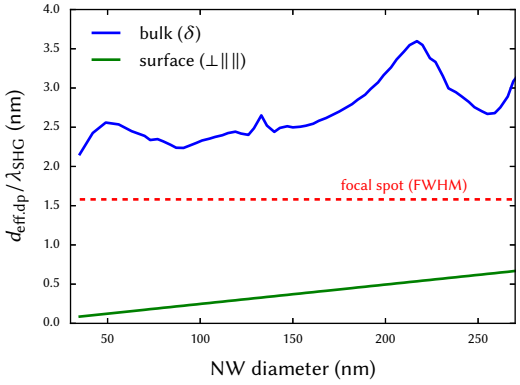

(c) Distance of Eff. $\mathbf{P}^{(2)}$ Dipoles in SiNWs

Figure 3.22: (a) Sketch illustrating the data analysis. The nonlinear polarization is separated in two areas with respect to a symmetry plane. In each area, an average dipole is calculated, neglecting retardation effects. The detecting optics are placed in direction towards the reader. (b) Farfield intensity of two coherently radiating dipoles of equal amplitude and opposite phase in normal direction to their polarization vector as function of the distance between the two dipoles. The intensity is integrated over different solid angles where NA 0.8 corresponds to the objective used in the experiments. The inset shows a sketch of the considered geometry. (c) Distance of two "effective" dipoles for surface (blue) and bulk (green) nonlinear polarization under TM excitation, calculated from the simulation data. The dips observed for the bulk dipole-distance correspond to the resonance positions (see Fig. 3.20).

In order to verify that this assumption is valid for the cases of $\mathbf{P}^{(2)}_{\perp\parallel\parallel}$ and $\mathbf{P}^{(2)}_{\delta}$ in TM excited nanowires, we reduce the nonlinear polarization to two effective dipoles, oscillating with opposite phase. We define their positions using the weighted averages

$$\mathbf{r}_{\text{eff.}} = \frac{\sum_i \mathbf{r}_i |\mathbf{P}^{(2)}_i|}{\sum_i |\mathbf{P}^{(2)}_i|} \tag{3.19}$$

of all dipoles $\mathbf{P}^{(2)}_i$ at $\mathbf{r}_i$ in two symmetric fractions of the structure as illustrated in figure 3.22a. In this rough approximation we neglect retardation effects in the summation by taking the modulus of each complex polarization vector. The distance between the two effective dipoles is plotted in figure 3.22c as a function of the nanowire diameter.

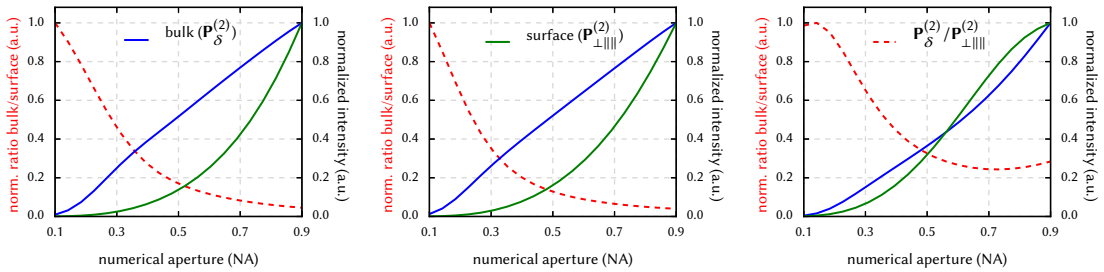

(a) NW50 ($D = 50\,\text{nm}$) (b) NW100 ($D = 100\,\text{nm}$) (c) NW200 ($D = 250\,\text{nm}$)

Figure 3.23: Normalized ratio of detected bulk and surface farfield-SHG (red dashed line) for SiNWs of different diameter as function of the collecting numerical aperture. Normalized δ-bulk and $\mathbf{P}^{(2)}_{\perp\parallel\parallel}$-surface contributions (blue and green lines, respectively) are plotted for comparison. Focused TM-excitation on the NW center at $\lambda_0 = 810\,\text{nm}$.

We observe that the surface polarization has always an effective spacing corresponding to the nanowire diameter. The δ-bulk nonlinear polarization on the other hand is found to be characterized by two effective dipoles with a separating distance always larger than the focal spot size. This behavior is in agreement with our initial hypothesis and can explain the observation of surface effects exclusive to large NW diameters, while bulk SHG is observed for small nanowires. We note that this effect is further reducing SHG in small NWs from $\mathbf{P}^{(2)}_{\perp\perp\perp}$ under TE excitation. Together with the lack of an optical resonance, farfield SHG due to $\chi^{(2)}_{\perp\perp\perp}$ is then entirely suppressed.

In figure 3.23 we plot the (normalized) ratio of bulk vs. surface SHG (under TM excitation) as function of the collecting numerical aperture at the example of diameters $D = 50\,\text{nm}$ (a), $D = 100\,\text{nm}$ (b) and $D = 250\,\text{nm}$ (c). We see that generally, a higher sensitivity to the δ-bulk contribution is obtained when the collecting solid angle is decreased. This is due to the more sidewards radiation of surface-SHG compared to the bulk-term (see Fig. 3.21). On the other hand, the total collected intensity decreases for lower NAs. In consequence for very low collection angles, neither surface nor bulk contributions would be detected. Finally, we observe that the surface contribution is detected more efficiently for smaller NA in the case of large nanowires (see Fig. 3.23c), which further supports the transition from bulk to surface second harmonic generation for increasing NW sizes, eventually resulting in the flip of the polarization.

We note that the nonlinear polarization is calculated from an excitation with a fixed NA 0.8. In backscattering geometry, the excitation is done with the same microscope objective as the collection, which might have an additional impact on the ratio between bulk and surface SHG.

3.4.5 Conclusions

In conclusion, our study of SHG from individual SiNWs showed that $\mathbf{P}^{(2)}_{\perp\perp\perp}$ dominates SHG for TE polarized excitation, resulting in a SH polarization normal to the NW axis, which is in agreement with former observations of $\chi^{(2)}_{\perp\perp\perp}$ as leading source of second-order susceptibility [300]. For TM excitation on the other hand, $\mathbf{P}^{(2)}_{\perp\perp\perp}$ vanishes as soon as the laser spot leaves the NW tips, giving the opportunity to examine the $\mathbf{P}^{(2)}_{\perp\parallel\parallel}$ surface source and the δ-bulk contribution in more detail. A diameter-dependent flip of the SH polarization was observed in this case, which we studied using

numerical simulations. The latter confirmed a changeover in the leading contribution from bulk ($(\mathbf{E}\cdot\nabla)\mathbf{E}$) SHG for small NWs to surface ($\mathbf{P}^{(2)}_{\perp\parallel\parallel}$) SHG for larger NWs with diameters $\gtrsim 150\,\mathrm{nm}$. We concluded that radiation from both $\mathbf{P}^{(2)}_{\perp\parallel\parallel}$ and $\mathbf{P}^{(2)}_{\delta}$ is of comparable magnitude and can be individually addressed by simply adjusting the diameter of the nanowire, which is particularly interesting as the δ-bulk contribution is supposed to be difficult to isolate from the other SHG terms from planar surfaces [302, 306, 307].

We showed that, because of their geometry and optical properties, SiNWs provide a highly promising research platform to gain insight in the relations between surface and bulk contributions of SHG from centrosymmetric materials in general. This allow to separate different contributing $\chi^{(2)}$ terms also for other materials, though accurate quantification of the $\chi^{(2)}$ elements is a difficult task, due to strong silencing of the nanoscopic nonlinear polarization because of the high symmetry of the NWs and many other influences like the collection efficiency for detection parallel to the excitation direction.

Chapter 4

Design of Photonic Nanostructures by Evolutionary Optimization

In the following chapter the focus will move towards the specific tailoring of optical properties in photonic nanoparticles. The rational design of photonic nanostructures usually consists in anticipating their optical response from simple models or as variations of reference systems, which are then studied systematically. This strategy, however, is often limited by the capabilities of the initially chosen geometry and even more demanding when different objectives are simultaneously targeted. In consequence, it is difficult to find the optimum geometry for specific optical functionalities and usually trade-offs between design simplicity and performance have to be made.

4.1 Design of Nanostructures as Optimization Problem

As it comes to applications, a more convenient approach is to define the requested optical properties and design a nanostructure that optimally exhibits the desired features. For the latter approach, a structure model has to be developed, which, based on a certain set of parameters, can describe in a generic way a large variety of particle geometries. However, this leads to huge parameter spaces which usually cannot be explored systematically within reasonable time. Also trial-and-error is normally not an efficient search strategy.

Root-finding or maximization algorithms seem promising at a first thought, however it is difficult to describe nanoparticle geometries by analytical, continuous and differentiable models, required e.g. by derivatives of Newton's method. Additionally, it is likely to obtain a function-landscape with countless local extrema (see Fig. 4.1a-b), which further restricts the applicability of classical optimization algorithms, since they get stuck in local extreme points and in consequence fail to converge to the global optimum, as illustrated in figure 4.1a at the example of a one-dimensional minimization problem.

4.1.1 Evolutionary Optimization

More promising techniques are evolutionary optimization (EO) strategies which, by mimicking natural selection, are able to find fittest parameter sets to a complex non-analytical problem [335].

In the field of nanophotonics, evolutionary algorithms have been applied to the maximization of field enhancement [336–340], scattering from plasmonic particles [341–343], or the design of hybrid plasmonic/dielectric antennas [344]. Such methods were also successfully used for more technological applications like electron-beam field emission sources [345], waveguide couplers

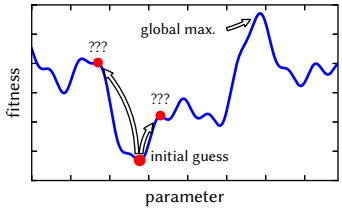

(a) Local Optimization

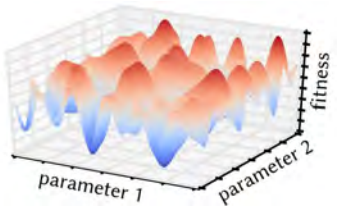

(b) Local Extrema: 2D Function

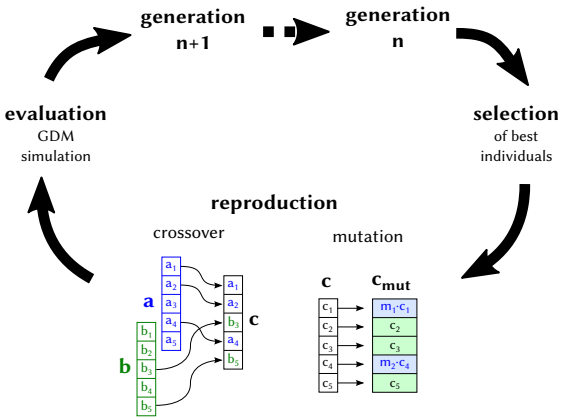

(c) Illustration of Evolutionary Optimization

Figure 4.1: Illustration of evolutionary optimization. (a) Dilemma of classical local optimization algorithms: If local extrema exist, the minimization gets stuck and does not converge to the global minimum (same holds for maximization). (b) Case of two input parameters, where the optimization problem becomes drastically more complex. (c) Illustration of the iteration cycle in evolutionary optimization algorithms.

[346], thermophotovoltaic solar cells [347] or core-shell nanoparticles for optically induced local heat-treatment in medicine [54]. EO techniques are furthermore applied in the analysis of complex, multi-dimensional spectroscopic data from optical experiments [348].

Figure 4.1c gives an illustration of how evolutionary optimization mimics the process of natural selection. A population of individuals is defined ("generation n" in Fig. 4.1c), where each individual is in our case a set of parameters describing an antenna morphology. This population undergoes an evaluation and selection procedure in which weak solutions are eliminated and the fittest candidates (*i.e.* the parameter-sets yielding the best target values) are chosen to "mate" with each other. The target value of the optimization is also called the *fitness*. The following process of reproduction usually consists of a step called *crossover*, where the parameters are exchanged and mixed – just like DNA in nature – and a *mutation* step, in which some randomly selected parameters are multiplied by or replaced with random numbers (see figure 4.1c, step "reproduction"). Like this, a new population of individuals is generated, the generation "$n + 1$". This process of selection, reproduction and evaluation is repeated until some stop-criterion is met, like a time limit, a maximum number of iterations or a maximum number of consecutive generations without further improvement.

4.2 Maximization of SHG from Si Nanoparticles

Since the previous part was focused on SHG from silicon nanowires, in our first example we will try to find silicon nanostructures for a maximum second harmonic emission. We will verify the outcome of the algorithm by measurements on samples, fabricated following the design of the evolutionary optimization.

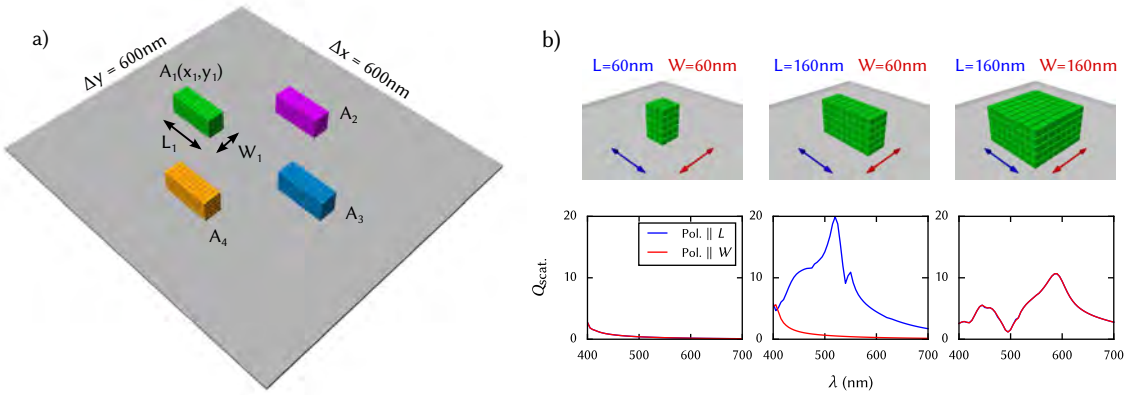

Figure 4.2: Structure model for EO. a) Example of silicon block arrangement forming a pixel. b) Scattering efficiencies calculated for individual silicon blocks of the minimum allowed size (left), minimum width and maximum length (center), and maximum possible size (right). The constraints are $L_{\text{min.}} = W_{\text{min.}} = 60\,\text{nm}$ and $L_{\text{max.}} = W_{\text{max.}} = 160\,\text{nm}$, the height is fixed to $H = 100\,\text{nm}$.

4.2.1 Numerical and Experimental Methods

4.2.1.1 Structure Model

The "population" of particle morphologies to be considered in the computation must be diverse enough to explore, after several generations, a significant fraction of possible solutions. However, this requires a very large number of parameters, significantly slowing down convergence. Furthermore, the optimized geometries must remain within the limits of fabrication capabilities and have neither too many nor too small features. For these reasons we use a very simple model, based on four individual silicon elements with variable dimensions and positions, placed on a SiO_2 substrate ($n \approx 1.5$) within a limited area. A sketch of the model is shown in Fig. 4.2a.

Both, the x- and y-dimension of each antenna is allowed to vary between 60 nm and 160 nm, in steps of 20 nm, corresponding to the precision of a state-of-the-art electron-beam lithographic system. The height H is fixed to 100 nm, equal to the silicon overlayer thickness of our silicon-on-insulator (SOI) substrate. The antenna is placed within an area of $600 \times 600\,\text{nm}^2$. This constrained area limits the accessible parameter-range to reduce complexity and facilitate convergence. Furthermore it ensures that the whole particle is illuminated by the incident field.

Exemplary spectra of single silicon-cuboids with dimensions corresponding to the size-limits used in our optimizations are shown in figure 4.2b. For simplicity, the positions are discretized in steps of 20 nm. In order to validate this large stepsize, we calculated spectra for the same structures using different discretization stepsizes, which yielded comparable results (see figure 4.11a). Overlapping antennas are allowed, corresponding antennas are fused together accordingly. The number of possible parameter combinations in this model is larger than 1×10^{15}. We conclude that using the simple model described above, it is already inconceivable to use a brute-force strategy (evaluation of all possible combinations). We will therefore employ an EO algorithm, namely a self-adaptive variant of differential evolution, "jDE" [349], implemented in the parallel EO toobox "PaGMO/PyGMO" [350].

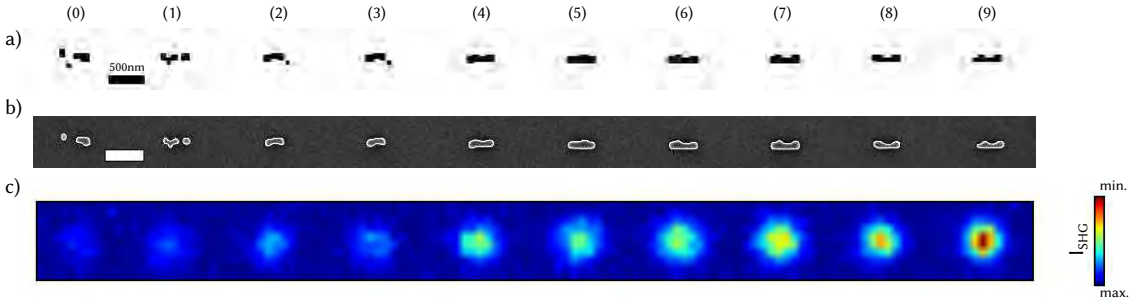

Figure 4.3: Evolutionary optimization of Si nanostructure for $\chi^{(2)}_{\perp\perp\perp}$ SHG. (a) Mask with fittest structures of consecutive iterations of the evolutionary optimization. (b) SEM images of the corresponding sample fabricated on SOI. (c) SHG raster-scan measurement of the sample. Fundamental wavelength is $\lambda_0 = 810\,\text{nm}$, linearly polarized along the horizontal axis (X-direction).

4.2.1.2 E-Beam Lithography on SOI

Samples were fabricated in cooperation with LAAS-CNRS in Toulouse by Dr. Guilhem Larrieu and Dr. Aurélie Lecestre. In a top-down approach, Electron Beam Lithography (EBL) was coupled with anisotropic plasma etching. This was used to pattern the designed nanostructures [351, 352] on a commercial silicon-on-insulator (SOI) wafer as substrate (Si: 95 nm, BOX: 145 nm). The EBL was carried out with a RAITH 150 writer at an energy of 30 keV on a thin (60nm) negative-tone resist layer, namely hydrogen silsesquioxane (HSQ). After exposure, HSQ was developed by immersion in 25 % tetramethylammonium hydroxide (TMAH) for 1 min. HSQ patterns were subsequently transferred to the silicon top layer by reactive ion etching in a SF6/C4F8 plasma based chemistry down to the buried oxide layer.

In the EMO runs, the minimum feature size was set to 60 nm to avoid removing small features of the structures during lift-off. The structures were discretized and placed on a grid by steps of 20 nm to match the precision of the EBL. SEM images and corresponding mask layouts are shown in Fig. 4.3a-b.

4.2.1.3 SHG Modeling and Measurement

The particles are excited with a NA 0.8 air objective and SHG is detected in backscattering by the same microscope objective. A more detailed description of the setup and measurement procedure can be found section 3.2.2 (see also Fig. 3.8). The numerical modeling for SHG is the "simple" method for SHG modeling, i.e. using $\mathbf{P}^{(2)}$ without the self-consistent correction. It is described in detail and used in the previous sections (see Sec. 2.4) and, by considering the NA 0.8 numerical aperture for both excitation and collection, reflects the experimental procedure.

4.2.2 Results and Discussion

SHG raster-scan measurements, like shown in figure 4.3c, were performed on structures, corresponding to fittest candidates from consecutive generations of the evolutionary optimization. Three copies of identical particles were measured, with quantitatively reproducible results. The average experimental results (blue, errorbars: standard deviation) are compared to the calculated fitness (red), which is shown in figure 4.4. Both datasets are normalized to their maximum values.

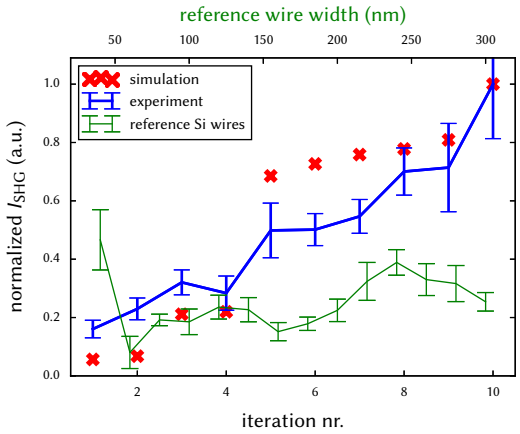

Figure 4.4: Fitness vs. measured SHG intensity for consecutive generations of evolutionary optimization. Measured intensity from three copies of identical structures on the sample, errorbars indicate the standard deviation obtained from the sum of the five highest intensity values from raster-scan measurements on three copies of each nanoparticle (see raster-scan in Fig. 4.3c). Simulation and measured data from the optimized structures (red and blue, respectively) refer to the bottom x-scale. Reference measurements of SHG on rectangular silicon nanowires of different widths are shown in green color (top x-scale). Heights are constant with $H = 95\,\text{nm}$ (simulations: $H = 100\,\text{nm}$) for all structures, corresponding to the silicon layer thickness of the SOI substrate.

A good agreement of experiment and prediction can be observed. Furthermore a comparison to rod-like reference structures on the same substrate of variable width and fixed length $L = 2\,\mu\text{m}$), shows an increase by a factor $\gtrsim 2$ in SHG emission. Corresponding data is shown in green in Fig. 4.4, scaled equally to the SHG intensity measured from the optimized particles. When the data is normalized considering the intersection of the exciting beam and the structures' geometrical cross section, the enhancement factor compared to the best wire-structure is even as high as ≈ 5 (for the normalization procedure, see also section 3.3.3.4).

4.3 Optimization of Plasmonic Antennas: Directional Scattering

A great advantage of the GDM is, that it can be adapted to different media in a straightforward way: It is sufficient to use the corresponding dielectric function for the description of an arbitrary material. In contrast to time-domain methods, no analytical model for the electric permittivity is required and tabulated data can be used.

Our nano-photonic evolutionary optimization approach is based on the Green Dyadic Method and inherits therefore all conveniences of this technique. In order to demonstrate the versatility of this tool, we will employ EO on a model describing a plasmonic nanoantenna made from gold – in contrast to the previously optimized silicon nanoparticle. EO has manifold potential applications, constrained only by possible limitations of the numerical method for the electrodynamical simulations. We will therefore also target a different optimization objective than SHG and try to design a nano-antenna for directional scattering in the following section.

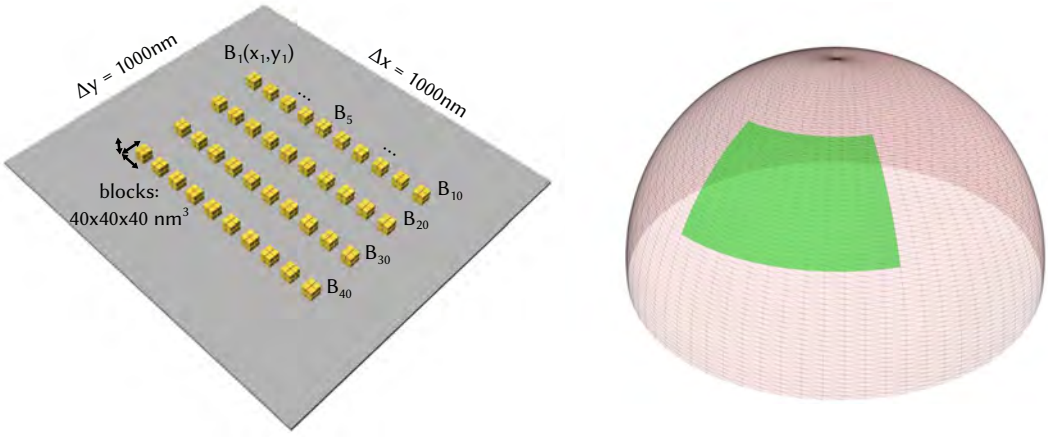

(a) Plasmonic Structure Model

(b) Directional Scattering Problem

Figure 4.5: (a) Structure model for EO of directional scattering from a plasmonic antenna. 40 gold-blocks ("B_i"), each $40 \times 40 \times 40\,\mathrm{nm}^3$ large are placed on an area of $1 \times 1\,\mu\mathrm{m}^2$. (b) Sketch of the directionality problem: Maximize the ratio of scattering through a small window (green) with respect to the remaining solid angle (red). Target scattering direction is chosen to be in X direction and centered at a polar angle of $45\,^\circ$. Polar and azimuthal widths are $30\,^\circ$ and $45\,^\circ$, respectively.

4.3.1 Problem and Model

4.3.1.1 Model: Cubic Gold Blocks on Substrate

A scheme of the model for a plasmonic nano-antenna is shown in Fig. 4.5a. 40 gold blocks named B_i, each $40 \times 40 \times 40\,\mathrm{nm}^3$ in size, are placed on a substrate ($n = 1.5$). Each of the blocks are modeled by $2 \times 2 \times 2$ dipoles with a stepsize of $d = 20\,\mathrm{nm}$. The free parameters are the positions (x_i, y_i) of the blocks, which are bound to an area of $1 \times 1\,\mu\mathrm{m}^2$, in order to limit the numerical complexity. Additionally, the positions of the blocks have to lie on a grid with steps of 40 nm in order to avoid problems from partly overlapping bricks. Fully overlapping blocks are treated as a single block, hence the material of the antenna is not necessarily fixed.

4.3.1.2 Problem: Directional Scattering

The goal of the optimization is to find a plasmonic antenna with strongly directional scattering at a certain wavelength. A linearly X-polarized planewave is incident from the top and the scattering from the nanostructure is calculated as described in section 2.3.6.4. The radiated intensity is separated in two parts: First the intensity I_{direct}, scattered through a solid angle of polar and azimuthal dimensions $\Delta\varphi = 30\,^\circ$ and $\Delta\theta = 45\,^\circ$, centered at $\varphi = 45\,^\circ$ in X-direction (green window in Fig. 4.5b). And second, the intensity I_{rest}, scattered through the rest of the semi-sphere (indicated red in Fig. 4.5b). The ratio of directional and scattering through the rest of the solid angle

$$R_{\mathrm{direct}} = \frac{I_{\mathrm{direct}}}{I_{\mathrm{rest}}} \tag{4.1}$$

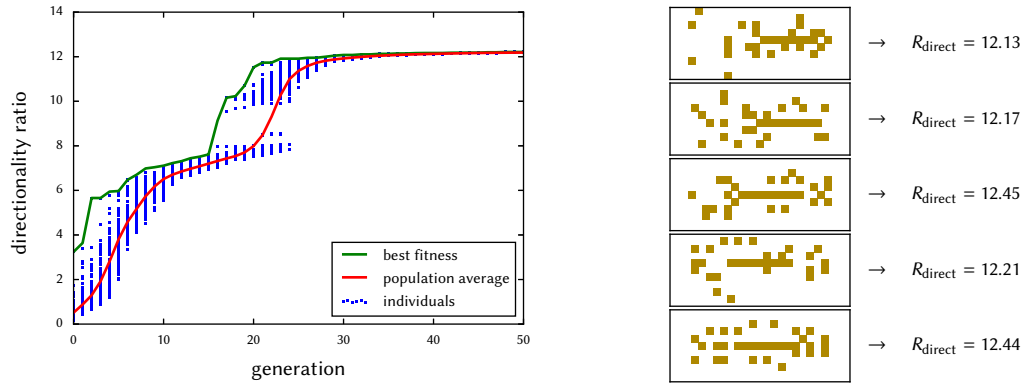

(a) Evolution of Antenna-Population (b) Reproducibility

Figure 4.6: (a) Fitnesses of the individuals (blue dots) of a large population vs. generation number. Best (green line) and population average fitness (red line) are indicated as well. (b) Demonstration of reproducibility: Antenna designs and directivity ratios from 5 independent runs of the optimization.

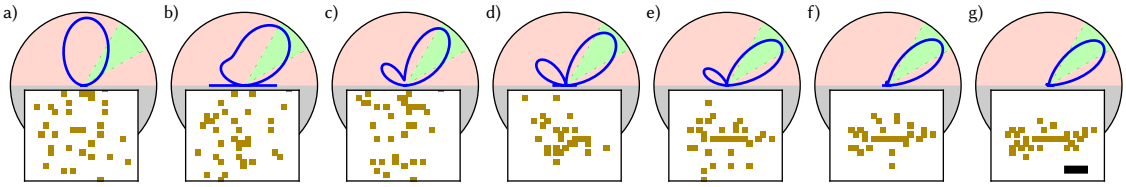

Figure 4.7: Selected iterations of evolutionary optimization of directional scattering. Radiation pattern in XZ-plane is shown in the top panels by blue lines, where a green segment indicates the optimization target region. Scalebar is 200 nm The corresponding plasmonic structures, composed of gold cubes, is shown in the bottom panels (lying on a $n = 1.5$ substrate in the XY plane). (a) Randomly initialized structure. (b-f) Fittest candidate of intermediate generations during evolution. (g) Best individual in final population.

is the target of maximization via EO. Like in the previous section, we use the self-adaptive differential evolution algorithm "jDE" for this purpose. Because we have as much as 80 free parameters, a large population is necessary to assure a diverse gene pool. Therefore we make use of the so-called "generalized island model" [353], provided by the PaGMO toolkit: Several independent populations are in parallel evolved on different "islands", to make use of the multiple CPU cores in modern computers. After the reproduction of a new generation, DNA is exchanged between the islands in order to guarantee a high diversity of the total population.

4.3.2 Results and Discussion

4.3.2.1 Analysis of Evolution

The full population in our case consists of 10×50 individuals, distributed over 10 "islands". We observed that for smaller populations, the optimization does not always converge to the best directionality of $R_{\text{direct}} \approx 12$. It seems, in the case of a small population the diversity may decrease too rapidly until it gets eventually stuck in a sub-optimal branch of the evolution (which *almost*

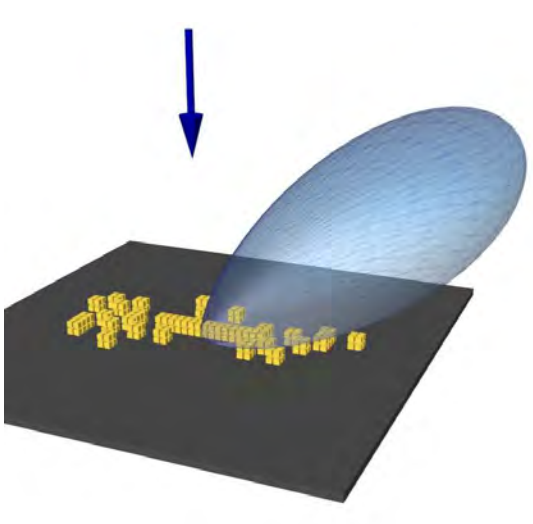

(a) Fittest Antenna of Final Population

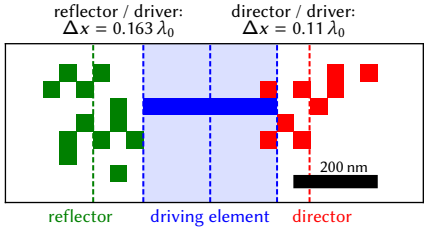

(b) Functional Constituents

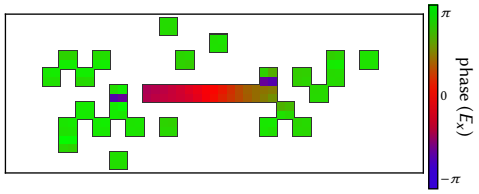

(c) Phase of the **E**-Field

Figure 4.8: Analysis of fittest evolutionary optimized directional antenna. (a) Sketch of the evolutionary optimized gold antenna with highest directionality. 3D radiation pattern is shown in light blue. Planewave incidence from the top, indicated by blue arrow. $\lambda_0 = 800\,\text{nm}$, polarized along X (direction of scattering). (b) The antenna can be divided into three functional constituents: A main driving element in the center (blue) as well as a reflector (green, on the left) and a director (red, right). The centers of gravity are indicated by dashed lines of the corresponding colors and the distance to the driving element edges are given at the top. Scalebar is 200 nm. (c) Color-plot of the relative phase of the E_x component of the electric field, with respect to the driving element's center. The horizontal direction corresponds to the X-axis. Same scaling as (b).

happens around gen. 20 in Fig. 4.6a). The evolution of a sufficiently large population during 50 generations is shown in figure 4.6a. The optimization was stopped after 50 cycles. Each blue dot corresponds to the fitness of an individual, the green and red lines indicate the best and average fitness, respectively. The fittest candidates from selected generations and their far-field patterns of scattered light are shown in Fig. 4.7. (a-f) are individuals from the first 20 iterations and (g) shows the best solution, taken from the 50^{th} generation.

To verify the reproducibility of the method, we performed the same optimization multiple times. For sufficiently large populations ($\gtrsim 10 \times 40$ individuals), the EO yields always similarly high directionality ratios of $R_{\text{direct}} \approx 12$ and also the antenna morphologies are always similar, as can be seen in figure 4.6b.

4.3.2.2 Analysis of Optimum Antenna

A sketch of the fittest candidate from the last generation is shown in figure 4.8a together with a 3D representation of the radiation pattern of scattered light, where the incident planewave's wave vector is indicated by a blue arrow. The directionality of the scattering is obvious from the cone of radiation (see also Fig. 4.7). Interestingly, the result of the optimization visually resembles much the well-known Yagi-Uda antenna design [354], an antenna geometry which is famous for its capability of directional emission and reception.

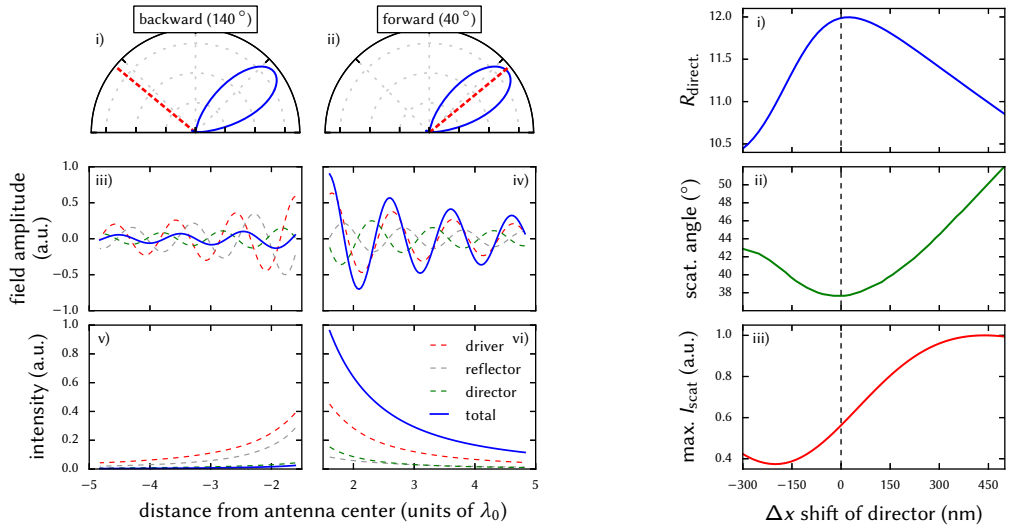

(a) Scattering of Antenna Components

(b) Analysis Director Position

Figure 4.9: Analysis of directional antenna found by EO (see Fig. 4.8). (a) Scattering in backward (left column) and forward (right column) direction. (*i-ii*): Scattering radiation pattern, indicating the analyzed profile-path by a dashed red line (along angles of $140°$ and $40°$, respectively). (*iii-iv*): Electric field amplitude E_x and (*v-vi*): Total intensity as function of distance from the nano-antenna in backward, respectively forward direction. (b) Directionality ratio R_{direct} (*i*), maximum scattering angle (*ii*) and maximum scattered intensity (*iii*) as function of an x-displacement of the antenna's director element (red part in Fig. 4.8b).

By a closer look on the nano-antenna, three main functional constituents can be differentiated, as shown in figure 4.8b: A driving element in the center (blue), a reflector on the left (green) as well as a director element on the right end of the antenna (red). The distances of the centers of gravity of reflector $\Delta x_{\text{refl.}} \approx 0.16\lambda_0$ and director $\Delta x_{\text{dir.}} \approx 0.11\lambda_0$ to the driving dipole correspond to typical suggestions in literature with $\Delta x_{\text{refl.}} > \Delta x_{\text{dir.}}$. Finally, an analysis of the phase of the electric field's x-component E_x reveals a difference of π between the driving element and the director / reflector parts, as shown in Fig. 4.8c. This phase difference persists in the propagating fields away from the antenna, resulting in cancellation of the electric field in backward direction and in a constructive interference of the contributions in forward direction (see Fig. 4.9a). This is in agreement with the Yagi-Uda antenna design template, where interference of phase-shifted fields yields a strongly anisotropic scattering [354].

We note in this context, that Novotny [11] showed that it is possible to scale antennas to optical frequencies by using an effective wavelength scaling, which considers the electron-plasma occurring in small metal particles. Following this principle, nano Yagi-Uda antennas have been fabricated and their directional emission was confirmed [30].

Finally we analyzed the antenna performance as function of the position of the director element (red in Fig. 4.8b), shown in figure 4.9b. The evolutionary algorithm could maximize indeed the directionality ratio as far as the director position is concerned. We also find, that dependent on the director position, the scattering angle can be tuned by around $15°$. Finally we observe that the scattered intensity might be enhanced by a factor of ≈ 2, simply by repositioning the director component. The reason for this finding is, that the presented optimization targeted the

directionality *ratio* of forward scattering with respect to uniformly scattered light – no interest was placed on the intensity of the scattering. In future work, the above results could be compared with an EO of the *absolute* scattered intensity towards a certain solid angle.

4.3.3 Conclusions

In the design of radio frequency antennas, evolutionary optimization is actually common practice [355], although in corresponding applications the global design of the antenna is normally imposed. The free parameters describe then usually minor variations of a given antenna system. In our approach on the other hand, initially the design of the structure is completely free, within the limits of possible geometries built by 40 equal metal blocks. In conclusion, it is remarkable that an antenna design is found – fully automatically and with very good reproducibility – which corresponds to well known design-principles from radio-frequency antennas. We deduce, that from the results of such optimizations, general design principles can be derived for the optimum geometries with respect to the target properties. In our case, we could verify that common design rules from directional radio-frequency antennas apply also in plasmonic nano-antennas at optical wavelengths. We want to note that the working principle of the EO antenna is also identical to nano Yagi-Uda antennas discussed in a former study on directional plasmonic antennas [356].

4.4 Multi-Objective Optimization of High-Index Dielectric Particles

In the last section of this chapter, we want to go even one step further. Most studies using evolutionary optimization in the context of nano-optics were limited to the maximization of one target property at a specific wavelength and polarization. Such single-objective scenarios represent the simplest case of an optimization problem, while a structure that concurrently matches multiple objectives will be in general more difficult to design. Evolutionary multi-objective optimization (EMO) strategies [357, 358] are a promising approach to tackle such problems. They are used for example for the optimization of trajectories of space-crafts in order to deliver a maximum possible load to some location in space within reasonable traveling time [359], for the design of radio-frequency antennas [355] or for the design of telescope objectives [360]. In a recent work, genetic multi-objective optimization was used on plasmonic waveguides. A figure of merit describing the waveguide and its robustness against geometrical variations were maximized simultaneously [361].

EMO could lead to considerable improvements in the design of wavelength dependent (multi-) directional scattering, multiresonant antennas or polarization dependent tailored optical behavior. Nanoantennas possessing multiple resonances, for instance at the fundamental and harmonic frequencies, may also be optimized by EMO to enhance nonlinear effects.

In the following, we present a combination of EMO with the Green Dyadic Method (GDM) for self-consistent full-field electro-dynamical simulations (see chapter 2). We apply the EMO-GDM technique to design dielectric (silicon) nanoantennas that concurrently maximize the scattering at different wavelengths, dependent on the polarization of the incident light. With the computed EMO design, Si nanostructures are then fabricated on a SOI substrate and their optical response is measured by confocal dark-field scattering microscopy. These experiments show that the scattering properties are in excellent agreement with the optimization predictions.

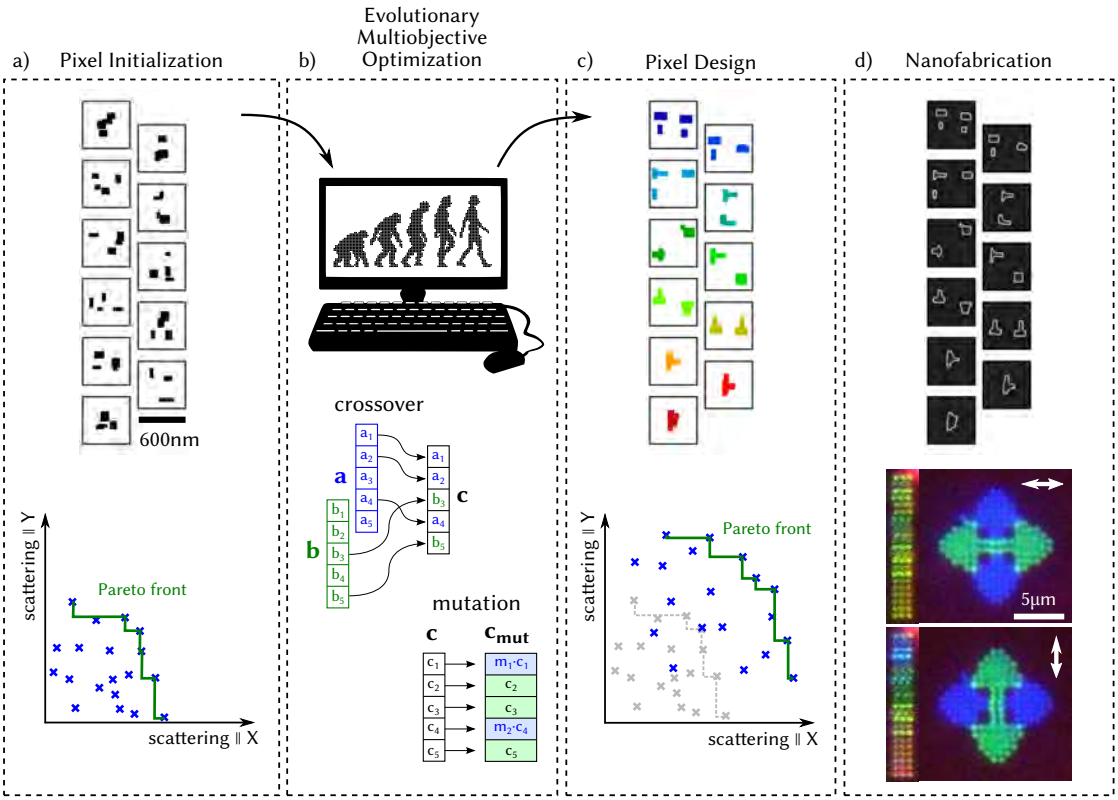

Figure 4.10: Illustration of evolutionary multi-objective optimization (EMO). a) Initialization step of pixel-populations for the EMO algorithm. b) Evolution of the pixel-population (see also Fig. 4.1c). c) Optimum pixel-population at the end of the evolution. d) Nanofabrication and characterization of the polarization dependent color-pixels.

4.4.1 Optimization Problem and Techniques

4.4.1.1 Optimizing the Scattering Efficiency from Nanostructures

We illustrate the EMO-GDM technique with the scattering efficiency Q_{scat} as target property. Q_{scat} is defined as the ratio between the scattering cross-section σ_{scat} and the geometrical cross-section σ_{geom} (the "footprint"). Our goal is to maximize the scattering efficiency at a wavelength λ_X, for an incident linear polarization along the X-axis, and simultaneously at a second wavelength λ_Y, for polarization along the Y-axis.

While this problem is mainly chosen for practical reasons – scattering and polarization are easily accessible values in the experiment – applications exist like holographic color-filters [105] or color rendering and printing close to the diffraction limit. The latter has been demonstrated either using plasmonics [15, 17, 362] or dielectric nanostructures [63]. Polarization dependent, dual-color pixels have been recently reported using plasmonic nanoapertures [363]. The advantage of plasmonic nanoantennas is the capability to provide widely tunable single mode responses using simple geometries (pillars in ref. [15], bent stripes in ref. [17], cuboids in ref. [362] and crosses in ref. [363]). Dielectric nanostructures on the contrary often support high order and degenerate

modes, occurring in a narrow spectral range. Therefore an EMO scheme is of particular interest for the design of multiresonant dielectric nanostructures.

4.4.1.2 Evolutionary Multi-Objective Optimization

In an optimization with a single objective, the initial population is evolved until eventually the parameter-set that yields the best fitness is considered the optimum solution (see also section 4.1.1 and Fig. 4.1c). In multi-objective problems however, the parameters describe not a single objective alone, but yield several target values that are all in parallel subject of the optimization. In our case, the target values are the scattering efficiencies at λ_X and λ_Y. During the EMO evolution, this fitness-vector is therefore stored in an archive and remembered for comparison during the optimization. Once the evolution finished, the final solution is not trivially determined neither: A whole M-dimensional set of *non-dominated solutions* exists, with $M = (\text{Nr. of objectives} - 1)$. This final set of individuals is called the *Pareto-front*, which is the set of solutions that cannot be further optimized in one of the objectives, without worsening at least one other target value. There is no guarantee that the final solution converged to the absolute optimum but, due to the complexity of many problems, EMO is often the best possible approach. An illustration of EMO at the example of nano-scatterer optimization is shown in Figure 4.10.

4.4.1.3 EMO-GDM Interfacing

We use the python interface of the parallel evolutionary multi-objective optimization toolkit paGMO/pyGMO [350] and in particular its implementation of the "SMS-EMOA" algorithm [364]. A comprehensive introduction to evolutionary multi-objective optimization can be found in reference [357].

For the electro-dynamical simulations, we use the Green Dyadic method, a volume integral technique in the frequency domain, described in detail in Chap. 2. It is implemented in fortran to yield high computational speed. All interfacing between the EMO and the electro-dynamical full-field solver is implemented in python.

4.4.1.4 Structure Model

Since it has proven to be compatible with electron-lithographic fabrication on SOI, we will use the same model as initially in this chapter for the maximization of SHG. For details, see Sec. 4.2.1.1. Fabrication of the structures is done on SOI substrates by EBL, like explained in Sec. 4.2.1.2. SEM images of individual structures are shown and are compared to the mask-layout in Figs. 4.12b, 4.15a and c as well as in 4.13b.

4.4.1.5 Measurements by Confocal Dark-Field Microscopy

Confocal optical dark-field microscopy was performed on a conventional spectrometer (Horiba XploRA). A spectrally broad white lamp was focused on the sample by a $\times 50$, NA 0.45 dark-field objective, backscattered, polarization filtered and dispersed by a 300 grooves per mm grating onto an Andor iDus 401 CCD. The intensity distribution of the lamp as well as the spectral response of the optical components was accounted for by subtracting the background measured on bare SOI and normalizing the measured spectra to a white reference sample.

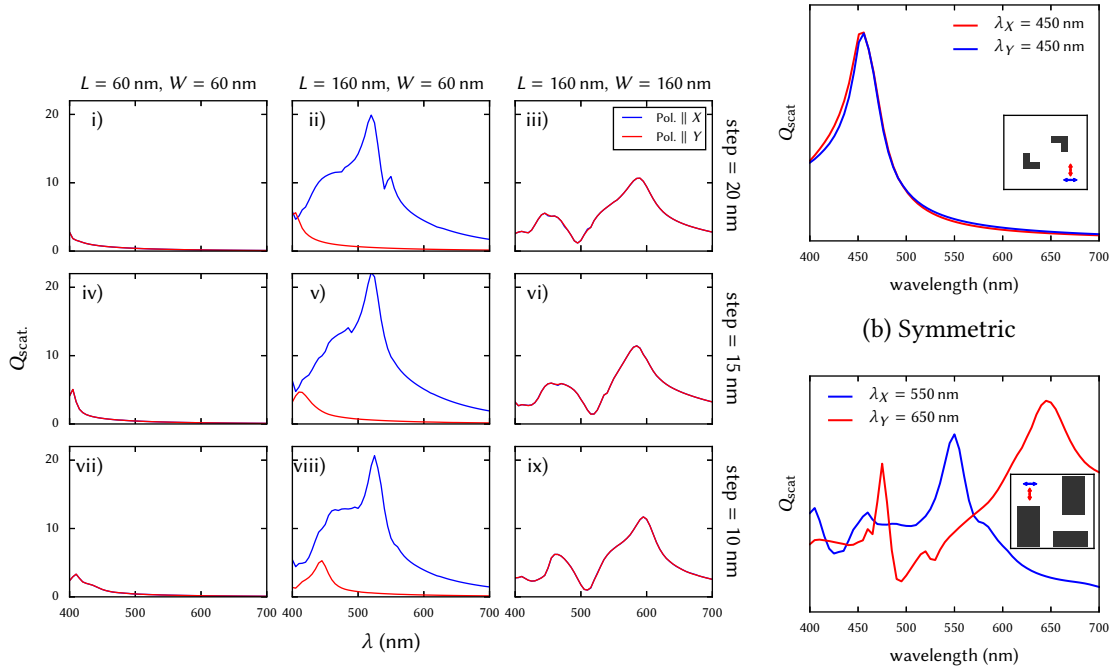

(a) Different Discretization Step-Sizes

(b) Symmetric

(c) Larger Sub-Blocks

Figure 4.11: (a) Spectra for cuboidal silicon blocks of height $H = 100\,\text{nm}$ and width / length combinations corresponding to the minimal and maximal allowed dimensions. Simulations were performed with different discretization step-sizes $S = 20\,\text{nm}$ (*i-iii*), $S = 15\,\text{nm}$ (*iv-vi*) and $S = 10\,\text{nm}$ (*vii-ix*). (b) Spectra for X- (blue) and Y-polarization (red) of EMO with $\lambda_X = \lambda_Y = 450\,\text{nm}$. (c) Spectra for X- (blue) and Y-polarization (red) of EMO with $\lambda_X = 550\,\text{nm}$ and $\lambda_Y = 450\,\text{nm}$ with more available material to the algorithm. Insets: Sketch of structure (shown areas: $600 \times 600\,\text{nm}^2$ in b and $700 \times 700\,\text{nm}^2$ in c).

4.4.2 Results and Discussion

4.4.2.1 Proof of Principle: $\lambda_X = \lambda_Y = 630\,\text{nm}$

In a first step, we test the EMO-GDM technique on a simple problem. A single target wavelength $\lambda_{\text{max.}} = 630\,\text{nm}$ is selected, at which σ_{scat} is maximized simultaneously for X and Y polarization. The structures of the final population and the corresponding Pareto-front after an evolution over 200 generations are shown in Fig. 4.12a and 4.12c. In figure 4.12a the geometries of the initial population (top) are furthermore compared to those on the Pareto-front (bottom).

The geometries found by evolutionary optimization are also transformed into a lithographic mask, which we use to produce the silicon nanostructures on a SOI substrate (see Methods). Fig. 4.12b shows a comparison of the design with SEM images of the sample. Simulated (Fig. 4.12e-f) and experimental spectra (Fig. 4.12g-h) are in very good agreement. The good agreement is also demonstrated by a comparison of simulated (lines) and measured (crosses) scattering efficiencies, shown in Fig. 4.12d.

The outermost individuals on the Pareto-front (particles (1) and (40)) correspond to equivalent results of a single-objective optimization using one target wavelength and polarization. We observe in these cases, that all four sub-antennas are combined during the evolution to form a single

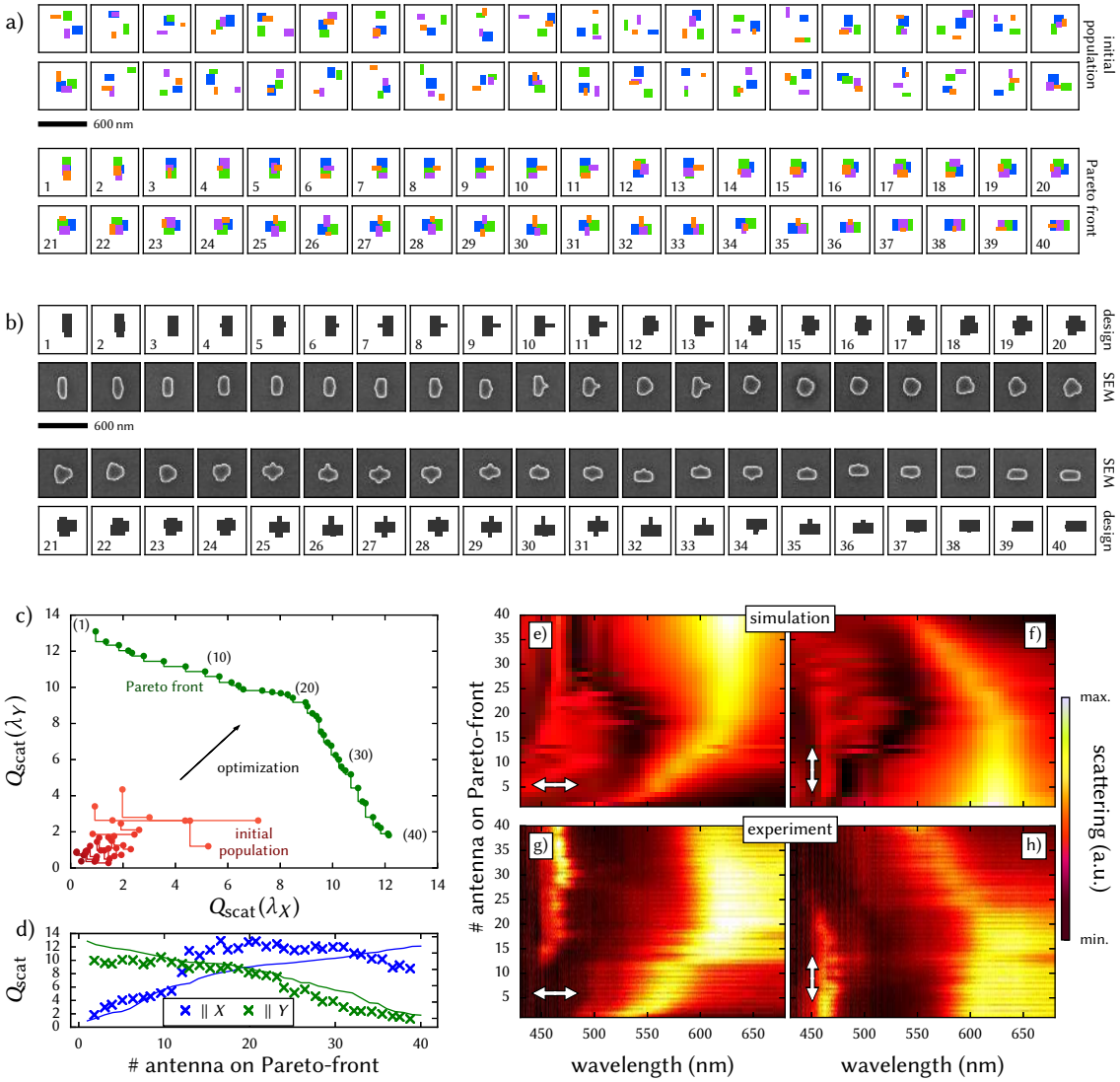

Figure 4.12: Results of EMO-GDM for identical target wavelengths $\lambda_X = \lambda_Y = 630\,\text{nm}$. (a) Structures of the randomized initial population (top) compared to the optimized Pareto-set of solutions (bottom). (b) Structures of the Pareto-front and corresponding SEM images. Blue, green, purple and orange dots are used to highlight the positions of the sub-blocks the structures consist of. All fields in (a) and (b) are $600 \times 600\,\text{nm}^2$ large. (c) Pareto-front (green) and randomized initial population (red). (d) Comparison of scattering from simulation (lines) and experiment (markers). (e-h) Scattering spectra for X (left) and Y polarization (right). Simulated and experimental spectra are shown in the top and bottom rows, respectively.

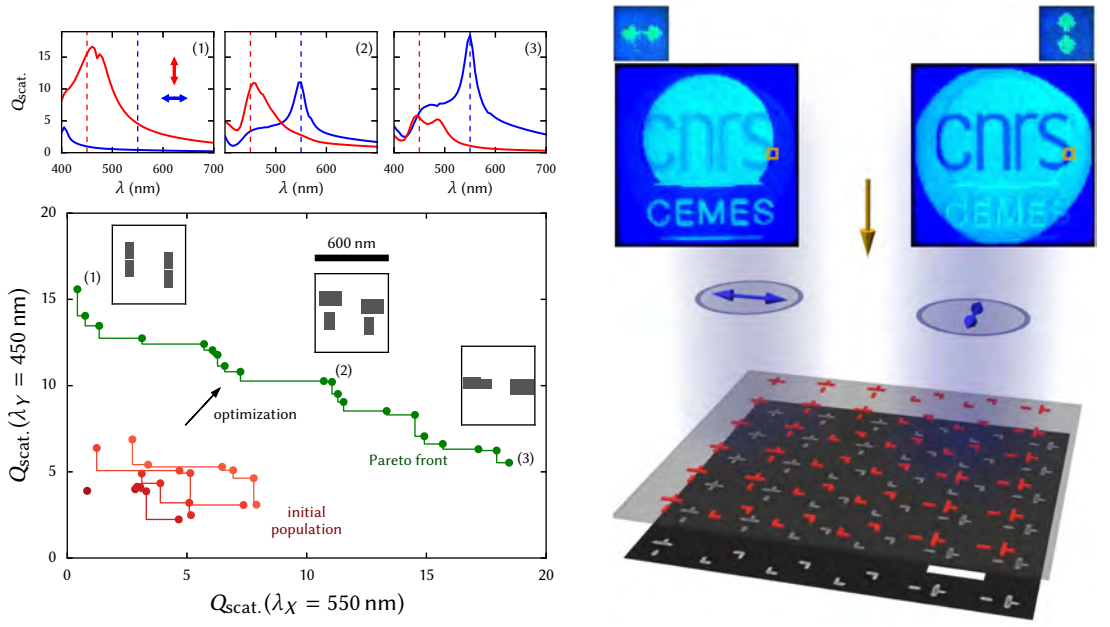

(a) Pareto-Front: $\lambda_X = 550\,\text{nm}$, $\lambda_Y = 450\,\text{nm}$

(b) Polarization Filtered DF Images

Figure 4.13: (a) Pareto-front example of an optimization run with $\lambda_X = 550\,\text{nm}$ and $\lambda_Y = 450\,\text{nm}$. Top: Spectra of selected antennas (indicated by numbers on Pareto front), where either a single wavelength is optimized (1 and 3) or both resonance wavelengths are scattered approximately equally (2). X (Y) polarized illumination is plotted with blue (red) color. The selected structures are sketched in the insets, showing areas of $600 \times 600\,\text{nm}^2$. (b) Polarization-filtered dark-field images of micrometer scale EMO-based pictures. Micrometer scale pictures composed of 24×24 (arrows) and 100×100 (logos) EMO-GDM designed particles. A linear polarization filter is added before the camera, oriented along X (top, left) and along Y (top, right). Arrow images are $15 \times 15\,\mu\text{m}^2$, logos $60 \times 60\,\mu\text{m}^2$ large. Bottom image: Zoom into the logo-picture. SEM image in grey (scalebar is 500 nm) and sketch of the lithographic mask in red, highlighted by small yellow squares in the dark-field images. The yellow arrow and blue emission indicate the incident and scattered light, respectively.

rod-like antenna along the target polarization direction. In agreement with literature, this yields an optimum scattering efficiency with respect to the considered polarization direction ("1": Y, "40": X) – at the expense of a very low scattering for the respective perpendicular polarization [69]. To obtain comparably high scattering efficiencies for both polarizations (particle "20" and neighbors), the evolution produces cross-like antennas.

We note, that the convergence and reproducibility of the EMO of silicon nano-scatterers have been carefully checked by repeatedly running the same optimization with different randomized initial populations, which always yielded similar results (test case was $\lambda_X = \lambda_Y = 630\,\text{nm}$). By monitoring the Pareto-front during the evolution, we found convergence usually after less than 100 generations. In order assure convergence in all cases, the optimizations were run for as much 200 iterations.

4.4.2.2 Doubly Resonant Nanostructures by EMO-GDM

In a next step we study the maximization of Q_{scat} at two different wavelengths $\lambda_X = 550\,\text{nm}$ and $\lambda_Y = 450\,\text{nm}$ for mutually crossed polarizations. The randomly initialized population of 20 individuals at the beginning of the evolution (red), the Pareto-front (green) and selected structure designs as well as corresponding spectra are shown in figure 4.13a. The individuals at the Pareto-front borders, labeled (1) and (3), correspond to single-objective optimizations for λ_Y and λ_X, respectively. Inspecting the three selected structures in more detail leads to the following observations.

Obviously twin structures like (1) and (2) seem to be preferred, because they result in an increase of the overall scattering efficiency. Indeed, structures (1) and (2) both consist of two dimer antennas that, if taken individually, have about 30 %, respectively 10 %, lower Q_{scat} at the target wavelength of $\lambda_Y = 450\,\text{nm}$ compared to the twin structure. Furthermore, the peak positions in the scattering spectra are slightly shifted and match the target wavelengths only in the combined antenna.

We point out that the rather symmetric relative positioning of the two dimers is crucial for an optimum scattering efficiency. The configuration found by the evolutionary optimization is very close to the ideal positions. A marginally stronger scattering can be obtained for both structures (1) and (2), when the dimers are placed on the same horizontal axis but the possible gain is as low as about 3 % and 1 %, respectively. Figs 4.14a for structure (1) and in Fig. 4.14b for structure (2).

At last, particle (3) in Fig. 4.13a consists only of a single dimer structure, which we attribute to the constrained maximum antenna size in our model. The maximization of the scattering at the longer target wavelength ($\lambda_X = 550\,\text{nm}$) requires a larger amount of material compared to shorter wavelength λ_Y. We carried out EMO simulations allowing the algorithm to use larger constituents and found that the scattering efficiency can be further improved and indeed is limited by the constrained amount of silicon.

4.4.2.3 Polarization Encoded Micro Images

To illustrate the previous results we produced small images, only few micrometers large, composed of EMO-optimized antennas. The absolute scattering cross section σ_{scat} was used as the optimization target. An additional spacing of 250 nm is used between the individual particles, which results in pixel sizes of $850 \times 850\,\text{nm}^2$ (≈ 30000 dpi), close to the diffraction limit.

Polarization-filtered dark field images are shown in figure 4.13b. Depending on the orientation of the polarization filter (left: X, right: Y), one single arrow is visible, pointing in the corresponding direction while the second arrow vanishes in a blue background. Furthermore, the logos of the CNRS and CEMES laboratory are nested into one image, encoded in perpendicular polarizations. A scheme of the lithographic mask (red) and a SEM image (grey) of a zoom into the logos, indicated by small yellow squares, is shown at the bottom. We attribute the slightly reminiscent signatures of the hidden motifs to intensity-variations due to the arrangement of the antennas in grating-like 2D-arrays.

4.4.2.4 Tuning the Resonances of Silicon Nanoantennas

For a further illustration of the EMO-GDM technique, we perform several multi-objective optimizations for different combinations of target wavelengths. The wavelength $\lambda_X = 550\,\text{nm}$ is

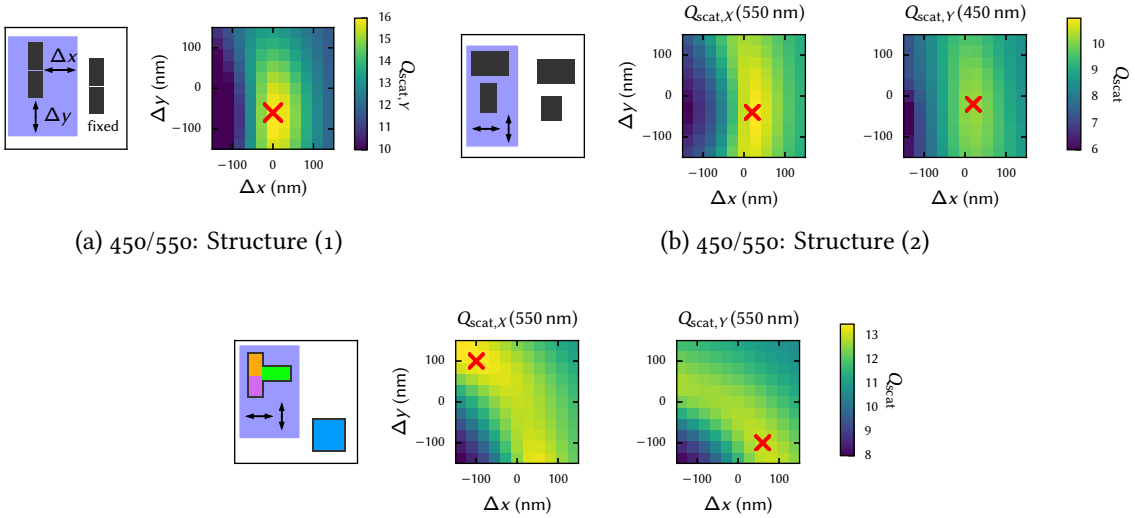

(a) 450/550: Structure (1)

(b) 450/550: Structure (2)

(c) 550/550

Figure 4.14: Blue highlighted parts in the structure sketches (right sides, areas are $600 \times 600\,\mathrm{nm}^2$) are shifted in X- and Y-direction. Zero-shift coresponds to the positioning as found by EMO. The scattering efficiency of the shifted structure is shown on the right sides for the target wavelengths. The maximum is indicated by a red cross. (a) Single objective optimization at $\lambda_Y = 450\,\mathrm{nm}$ ("1" in Fig. 4.13a). (b) Optimization at $\lambda_X = 550\,\mathrm{nm}$ and $\lambda_Y = 450\,\mathrm{nm}$ ("2" in Fig. 4.13a). (c) Optimization at $\lambda_X = \lambda_Y = 550\,\mathrm{nm}$ (see Fig. 4.15).

fixed, while the other (λ_Y) is varied from $450\,\mathrm{nm}$ to $650\,\mathrm{nm}$ in steps of $10\,\mathrm{nm}$. Each simulation consists of an initial population of 20 random individuals, which is evolved for 200 generations. At the end of the evolution, the structure with the most similar $Q_{\mathrm{scat}}(\lambda_X)$ and $Q_{\mathrm{scat}}(\lambda_Y)$ is chosen from each simulation (like structure (2) in Fig. 4.13a).

In Figure 4.15, we show the resulting structures (a) and their GDM-simulated spectra for X- and Y-polarized incidence (b). The different λ_Y are indicated by a color coding from blue ($\lambda_Y = 450\,\mathrm{nm}$) to red ($\lambda_Y = 650\,\mathrm{nm}$). As explained in the previous subsection, for increasing wavelengths, the four sub-antennas tend to combine in only two structures (instead of more constituents for the shortest wavelengths), which is due to the limited amount of allowed material. For the same reason, at wavelengths above $600\,\mathrm{nm}$ all sub-antennas are even merged into one single structure, and for the longest wavelengths the available material is not sufficient to yield a satisfactory maximization. Indeed, if more material is allowed for the algorithm to be used, a distinct peak in the scattering spectra can be obtained also for larger wavelengths, as shown in Fig. 4.11c for an optimization using $\lambda_X = 550\,\mathrm{nm}$ and $\lambda_Y = 550\,\mathrm{nm}$.

For an experimental verification, we fabricated Si-structures corresponding to the optimized color-tuned nanoantennas. SEM images (Fig. 4.15c) and polarization filtered dark-field spectra (Fig. 4.15d, top: filter along X, bottom: along Y) are shown in figure 4.15. Polarization filtered dark-field images (Fig. 4.10d and insets in Fig. 4.15d) of color-switching pictograms, composed of the optimized structures, demonstrate the polarization dependence of the scattered wavelengths.

By a closer look on the individual structures, we observe that the "symmetric" optimization with $\lambda_X = \lambda_Y = 550\,\mathrm{nm}$ results in a non-symmetric particle. We would intuitively expect a point-symmetric antenna (*i.e.* of S_2 symmetry group) to be ideally suited for equally strong scattering

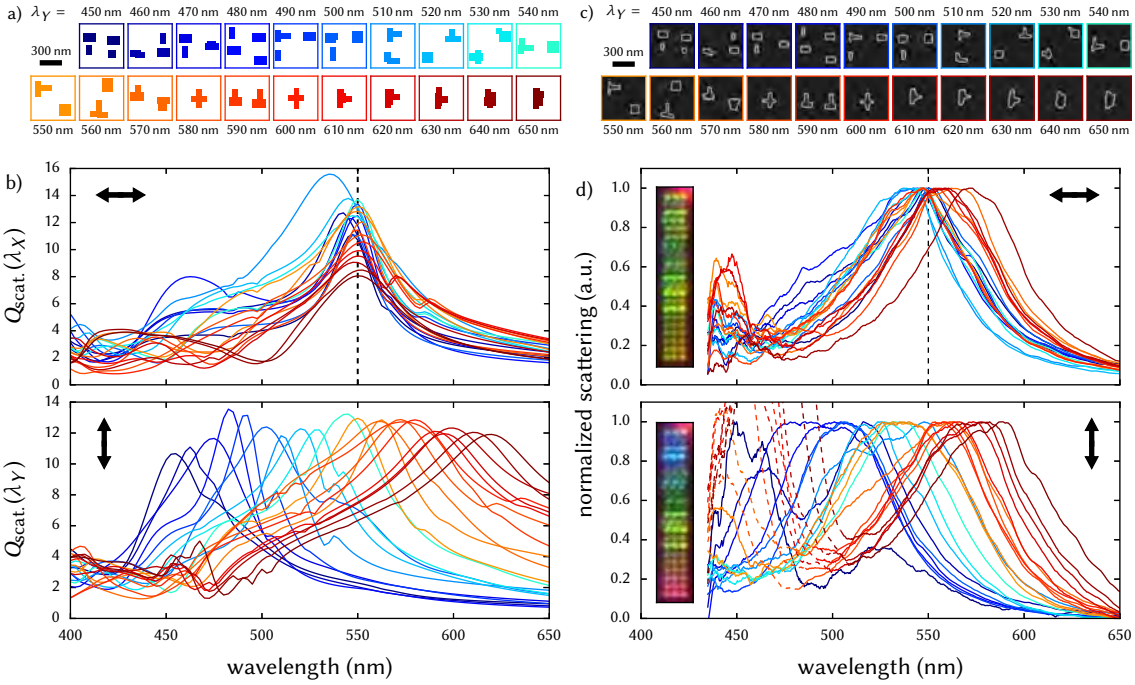

Figure 4.15: Experimental demonstration of several dual-resonant Si structures based on EMO-GDM simulations. (a) EMO design of multi-resonant dielectric particles and (b) simulated scattering spectra for $\lambda_X = 550\,\text{nm}$ (indicated by a black dashed line) and various λ_Y. (c) SEM images and (d) polarization filtered scattering spectra of the corresponding nanofabricated sample. Insets in (d) show polarization filtered dark-field microscopy images of the full set of structures ($4 \times 20\,\mu\text{m}^2$) Areas in (a) and (c) are $600 \times 600\,\text{nm}^2$.

under both, X- and Y-polarization. The evolutionary optimization, being a non-analytic routine, should at least result in some "quasi"-symmetric structures, which is however not the case here. As before, this can be explained by the finite amount of material available in our structure model. Because the T-shaped part of the antenna already consists of three of the four sub-antennas, the fourth sub-antenna is added as a square block of maximum allowed dimension, and it is impossible for the algorithm to generate a symmetric structure within the given constraints. A simulation with $\lambda_X = \lambda_Y = 450\,\text{nm}$ results in quasi-symmetric structures, like intuitively expected (see Fig. 4.11c).

Again, for $\lambda_X = \lambda_Y = 550\,\text{nm}$, interference between both parts of the antenna results in an optimum scattering efficiency at the target wavelength and therefore exact positioning of the constituents is crucial: We find from a look at the scattering efficiency as function of the X/Y-shift of the T-shaped sub-antenna (shown in Fig. 4.14c), that the relative positioning is indeed the ideal solution, as a displacement in any direction results in a decrease of either $Q_{\text{scat},X}$ or $Q_{\text{scat},Y}$. A change of the spacing between the T-shaped and squared sub-structures by $\Delta x = 100\,\text{nm}$ for example, already results in a decrease of more than 5 % in scattering efficiency for at least one polarization.

4.4.3 Conclusions

In summary, we emphasize that despite the simplicity of the designs generated by the EMO, all the parameters (sizes, positions, distances) were nearly perfectly optimized by the evolutionary algorithm. The EMO-GDM technique is able to find ideal nanostructures even within narrow constraints on parameters like the size, the available amount of material or discrete step-sizes for compatibility with nanofabrication technology. We applied the method on silicon nanostructures which are are of great interest as alternatives to plasmonic particles. Due to their multi-modal optical behavior it is often difficult to find appropriate geometries. For this problem, we successfully applied an evolutionary optimization scheme and finally verified the results experimentally with very good agreement to the predictions.

4.5 Conclusions

In conclusion, evolutionary (multi-objective) optimization coupled to full-field electro-dynamical simulations is very promising for the automatic design of many different kinds of photonic nanostructures. We successfully applied the method for the optimization of SHG from silicon nanoparticles, on a plasmonic antenna for directional scattering and for the design of polarization-dependent dual-resonant silicon nano-pixels. We demonstrated that an evolutionary optimization approach is able to realize complex photonic characteristics like dual-resonant behavior even within a very simple and strongly constrained structure-model. For a maximum compatibility with fabrication methods, technological limitations were included as boundary conditions in the model. Due to these technological considerations, we were able to produce samples on SOI substrate using the outcome of the optimizations for a lithographic mask. With SHG measurements and polarization filtered dark-field microscopy we finally confirmed the agreement between samples and simulations.

A great advantage of EO/EMO coupled to GDM is its flexibility and the ability to self-adapt to arbitrary limitations. Additional constraints can easily be implemented because no analytical treatment of the input model needs to be performed. Inadequate structures, inconsistent with the constraint functions, are being discarded automatically during the evolution and only technologically convenient designs are generated. The method can also be easily extended for the rigorous design of metasurfaces, where interference between the unit cells needs to be considered. Periodic boundary conditions can be included in the GDM by means of an appropriate Green's Dyad (see section 2.3.2.2). In this way, the distance between substructures on the metasurface may also be included as a free parameter in the optimization. Evolutionary (multi-objective) optimization of photonic nanostructures has a tremendous potential for many kinds of possible applications both, in near- and far-field nano-optics for example in the design of multiresonant or broadband particles for light harvesting, or of nonlinear nanostructures.

Chapter 5

Conclusion

Plasmonic particles, made of noble metals, suffer from dissipative losses due to a large imaginary part in the dielectric function. High index dielectric materials have recently attracted attention as possible low-loss alternatives. The advantages and complementary characteristics of the two material platforms were subject of a detailed review in chapter 1 and motivated further investigations on silicon-based nanostructures, particularly with regard to non-linear optical phenomena.

In chapter 2, a brief introduction to classical electrodynamics was given before particular focus was set on the numerical description of light-matter interaction at a sub-wavelength scale. The Green Dyadic Method was presented as versatile numerical framework, applicable to both, plasmonic and high-index dielectric nanoobjects. Furthermore, after an introduction to nonlinear optics and in particular to surface second harmonic generation, an expansion of the GDM for the self-consistent description of nonlinear effects was described and applied to selected examples.

In the following, the optical response of high-index dielectric nanostructures in the visible and near-infrared spectral range was studied at the example of silicon nanowires in chapter 3. At first, the linear optical properties were summarized and the appearance of resonant optical modes was explained. In this context, we compared Mie Theory to GDM simulations in order to justify the further excessive use of GDM simulations for the interpretation of the measurement results. We studied in particular the influence of the geometrical section of silicon nanowires on their modal response and found that circular, hexagonal and squared cross sections provide a very similar resonant behavior for lower-order modes (up to orders of about 3 or 4), before more severe deviations occur at higher order resonances. Subsequently, the nonlinear optical response of SiNWs in the spectral region of visible wavelengths was studied in great detail. We found a multi-photon induced photoluminescence as well as second harmonic generation, which we showed is dependent on the existence of resonant modes and can be enhanced by more than two orders of magnitude, compared to SHG from a bulk silicon surface. In agreement with literature, we deduced from experimental observations, that $\chi^{(2)}_{\perp\perp\perp}$ leads to the strongest contribution to SHG – similar to other centrosymmetric materials like gold. However, dependent on the nanowire size and the incident polarization, SHG in SiNWs was found to contain several different contributions and is either due to surface SHG or as a consequence of strong field gradients in the bulk-core of the nanowires. In conclusion, due to their geometry nanowires offer an interesting platform for the distinction of different contributions to surface SHG. This is of particular interest since on planar surfaces, the bulk contribution is difficult to isolate from the surface terms, which can be achieved more easily using nanowires.

In the last chapter (Chap. 4), we pursue an alternative approach for the tailoring of optical properties in plasmonic and dielectric nanostructures. Commonly, a reference system is studied

e.g. by small variations of its design, in order to tailor the optical properties. This, however, is an inherently limited approach since the optical properties are more or less imposed by the initial choice of the particle geometry. In order to overcome these limitations, we employ evolutionary optimization algorithms, coupled to the GDM, on a generic structure model. We showed on different examples the remarkable potentials of such methods. By including technological constraints, we finally succeeded to actually fabricate the structures, designed by evolutionary optimization and verify the outcomes of the algorithm.

Evolutionary optimization clearly has tremendous potentials for direct applications, since any possible kind of constraint like technological limitations can be included in optimizations of many different possible problems. However, evolutionary strategies might also be exploited to design particular platforms for more fundamental investigations. For example the maximization of SHG originating from individual $\chi^{(2)}$ elements might be helpful in the quantification of the components of nonlinear susceptibility tensors. Another possible application could be the evolutionary design of efficient magnetic field enhancement with a concurrently suppressed electric field amplitude in nanometer small cavities. Such system would be an interesting platform for research on magnetic-field driven phenomena. In conclusion, countless possible applications of EO exist which are limited only by the capacities of the numerical method for the description of the optimization target.

Chapter 6

French Summary / Résumé Français

Par la suite un résumé de la thèse sera donné, chapitre par chapitre, en langue française.

Propriétés Optiques Linéaires et Non-Linéaires de Nanostructures Diélectriques à Haut Indice de Réfraction

6.1 Introduction et Motivation

Seulement des éléments de la bibliographie du chapitre 1 seront ici donnés. Pour une liste exhaustive des références, le lecteur est renvoyé au chapitre entier en langue anglaise.

La nano-optique est un domaine de recherche qui attire de plus en plus l'attention des chercheurs du monde entier. En général, la nano-optique traite les effets qui se produisent à l'interaction de la lumière avec la matière à des dimensions inférieures à la longueur d'onde. Ainsi – pour la lumière du visible et du proche infrarouge – nous nous trouvons à l'échelle du nanomètre. Dans ce chapitre, un aperçu des systèmes de différents matériaux sera donné et le progrès de la recherche actuelle sur les nano-structures photoniques et de leurs applications sera résumé. Une comparaison entre les structures plasmoniques et celles aux diélectriques à haut indice de réfraction motivera des investigations plus approfondies sur ce dernier système de matériel. Enfin, nous allons donner un bref aperçu des effets non-linéaires et de leurs applications dans la nano-optique.

6.1.1 Diélectriques à Haut Indice vs. Plasmonique

6.1.1.1 Plasmonique

La principale force motrice en nano-optique est probablement le domaine de la "plasmonique" [2, 3]. L'interaction des ondes électromagnétiques avec des métaux peut lancer des oscillations collectives des électrons libres. La constante diélectrique des métaux est négatif et par conséquence les vecteurs d'onde à leur intérieur sont imaginaires. Les champs sont donc évanescents et confinés dans une petite région à la surface, ce qui s'appelle "l'effet de peau" [4]. En conséquence, les oscillations du collectif des électrons se propagent le long de la surface, ce qui s'appelle polariton-plasmons de surface (Anglais: Surface plasmon polaritons, "SPP") [5–8]. En outre, dans de petites particules de métal, la propagation des SPP est entravée à cause du confinement spatial et des modes localisés apparaissent, nommés en Anglais "localized surface plasmon (LSP) resonances". Ces LSPs permettent de serrer la lumière en volumes de taille nettement plus petite que la longueur d'onde, et loin en dessous de la limite de diffraction. En plus des fortes exaltations du champ locale apparaissent [9]. Dans le domaine spectral visible les tailles caractéristiques

se trouvent entre plusieurs 10 nm et quelques 100 nm. Grâce à leur forte réponse aux champs électromagnétiques du visible, les particules plasmoniques sont souvent appelées "antennes optiques" qui, par des variations de géométrie, peuvent être taillées sur mesure pour répondre aux besoins variés (Anglais: "tailoring" of optical properties) [10–13]. Pour une introduction approfondie sur la plasmonique, nous renvoyons le lecteur à la référence [2].

6.1.1.2 Nanostructures de Diélectriques à Haut Indice

Toutefois, l'attention de ce travail sera principalement fixée sur un autre type de nanostructures: Des particules composées de diélectriques à haut indice de réfraction. En règle générale, ces dernières comprennent des matériaux semi-conducteurs tels que le germanium ou le silicium (indice de réfraction du Si dans le visible: $n \approx 3.5 - 4$). En conséquence, la différence décisive en comparaison avec la plasmonique est l'absence de charges libres. Il en résulte une partie réelle de la fonction diélectrique qui – contrairement aux métaux – est positive ce qui signifie que la lumière peut se propager efficacement à l'intérieur du matériau. Irradié par des champs électromagnétiques, le matériau est polarisé à cause d'un déplacement des électrons *liés* par rapport à leurs atomes. Cette polarisation électrique est proportionnelle au contraste diélectrique avec l'environnement (voir aussi annexe 6.4.4).

Par ailleurs, dans des structures avec des dimensions inférieures ou comparable à la longueur d'onde de la lumière incidente, des fortes résonances optiques apparaissent [63, 64], comparable aux résonances plasmons, décrites précédemment. Figure 6.1a démontre une image de microscopie en champ sombre des nanofils de silicium de différente largeur. Le changement de couleur est due aux résonances optiques qui varient spectralement en fonction de la taille du nano-objet.

6.1.1.3 Comparaison des Plates-Formes

Comparons maintenant les différences entre les nano-particules plasmoniques et diélectriques afin d'exposer les points forts et les désavantages des deux systèmes de matériels.

Exaltation du champ électrique La spectroscopie à champ exalté est l'une des applications principales des particules plasmoniques. Afin de stimuler les signaux faibles de quelques ou même d'une unique molécule(s), une exaltation élevée de champ électrique est indispensable. Pour l'essentiel, l'exaltation du champ électrique au voisinage de particules de haut indice de réfraction est proportionnelle au contraste diélectrique entre la particule ($\epsilon_{r,1}$) et son environnement ($\epsilon_{r,0}$). Ceci est le résultat des conditions de continuité à des interfaces diélectriques (voir annexe A.1)

$$E_{\parallel,0} = E_{\parallel,1} \qquad \epsilon_{r,0}\, E_{\perp,0} = \epsilon_{r,1}\, E_{\perp,1}. \tag{6.1}$$

La composante normale (indice $\perp$) du champ électrique à la proximité de la particule est exaltée par le rapport des permittivités[1] et éventuellement encore amplifiée si des modes de résonance existent. Une exaltation de l'intensité de champ dans l'ordre de ≈ 100 est possible [66, 76, 98].

Ceci est néanmoins nettement inférieur au cas de la plasmonique, où trois ordres de grandeur peuvent facilement être atteints pour l'exaltation des intensités de champ [75]. En fin de compte, alors que dans la plasmonique l'exaltation des champs est généralement beaucoup plus forte, les particules diélectriques offrent de plus grands volumes d'extension du champ [98]. En ce qui

[1] la composante tangentielle (indice $\parallel$) par contre est constante.

(a) Image en Champs Sombre des Nanofils de Silicium

(b) Résonances Magnétiques: Au vs. Si

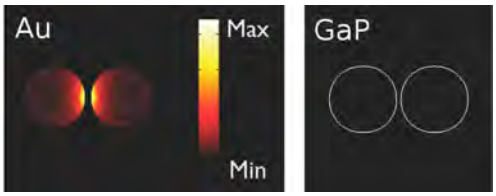

(c) Dissipation de Chaleur: Au vs. GaP

Figure 6.1: (a): Image en champs sombre des nanofils de silicium d'une longueur de 5 µm, gravés dans SOI. Les largeurs augmentent de 30 nm à gauche jusqu'à 400 nm à droite. (b) illustration de la génération des champs magnétiques dans des anneaus brisés plasmoniques (gauche) et des nanosphères diélectriques (droite), reproduction de Kuznetsov et al. [72]. Copyright (2012) CC BY. (c) comparaison de la dissipation de chaleur dans des dimères d'Or (gauche) et de phosphure de gallium (droit). Adapté avec permission de Albella et al. [75]. Copyright (2014) American Chemical Society.

concerne les antennes plasmoniques, l'extension de l'exaltation du champ la plus intense est de l'ordre de ≈ 1 nm. Quant aux nano-particules diélectriques, il est possible d'atteindre ≈ 10 nm.

Exaltation du champ magnétique En outre, une différence notable est l'occurrence des fortes résonances magnétiques dans des nano-particules diélectriques, ce qui est difficile à obtenir avec des antennes plasmoniques [72, 137–140]. Des résonances dipolaires magnétiques dans des dimères diélectriques peuvent exalter l'intensité du champ magnétique dans le visible par un facteur $\approx$ 100 [76]. En résultat, l'amplitude du champ magnétique peut devenir comparable ou même dépasser le champ électrique. Des interférences entres des résonances électriques et magnétiques peuvent ainsi provoquer des phénomènes surprenants comme une diffusion de la lumière fortement anisotrope [91, 145–147].

En plasmonique, des performances comparables sont possibles uniquement avec des compositions de particules complexes et asymétriques [141] ou alors dans l'infrarouge, en utilisant des résonateurs de forme d'anneaux brisés [142] (voir aussi la figure 6.1b). Toutefois, des structures plasmoniques souffrent généralement de fortes pertes quant à l'exaltation du champ magnétique dans le visible [72].

Pertes Un désavantage majeur des nano-structures plasmoniques, ce sont les pertes importantes liées à la partie réelle négative et à la partie imaginaire large de la permittivité diélectrique des métaux. Ces pertes sont responsables de dissipation importante. Il en résulte une forte production de chaleur qui peut être mortelle par exemple pour des biomolécules fragiles en spectroscopie à champ exalté. Bien que les diélectriques à haut indice donnent des exaltations de champ

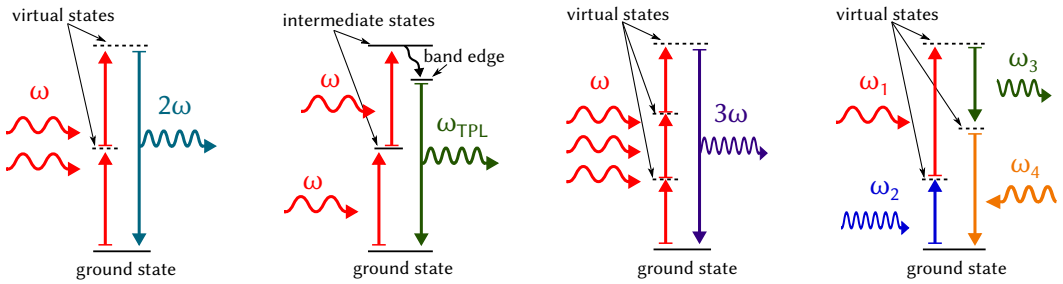

(a) SHG (b) TPL (c) THG (d) FWM

Figure 6.2: Illustrations de (a) génération de seconde harmonique (SHG), (b) photoluminescence induit par deux photons (TPL), (c) génération de troisième harmonique (THG) et (d) possibilité d'interaction dans un mélange à quatre ondes (FWM).

inférieures, les pertes associées sont même de plusieurs ordres de grandeur plus faibles. Pour le cas de structures plasmoniques et diélectriques qui possèdent d'une exaltation du champ comparable, la différence de la hausse de température entre les particules plasmoniques et diélectriques peut atteindre plusieurs 100 °C [75, 99] (voir la figure 6.1c).

Les très faibles pertes sont un avantage-clé des matériaux diélectriques quant à des applications comme la spectroscopie à champ exalté. Cependant, la dissipation dans les antennes plasmoniques peut être utilisé de manière constructive pour la production de chaleur localisée à une échelle nanométrique [134]. D'autre part, ce chauffage local n'est pas possible avec des nanostructures diélectriques.

6.1.2 Effets Non-Linéaires

Toutes les propriétés et les applications des nano-particules photoniques décrites précédemment sont basées sur une réponse optique linéaire. Par contre, si l'amplitude d'un champ électromagnétique excitant est assez élevée, des effets optiques *non-linéaires* se produisent, qui peuvent offrir une large gamme de fonctionnalités uniques au-delà de l'optique linéaire. L'effet optique non-linéaire le plus populaire probablement est la génération d'harmoniques [164]. Parmi cela, les exemples les plus marquants sont la génération de seconde harmonique (Anglais: Second harmonic generation, "SHG", illustré sur la figure 6.2a) et la génération de troisième harmonique (Anglais: Third harmonic generation, "THG", figure 6.2c): Deux (ou trois) photons d'une longueur d'onde fondamentale (λ_0) sont convertis de manière cohérente[1] à un seul photon avec $\lambda_{SHG} = \lambda_0/2$ (ou $\lambda_{THG} = \lambda_0/3$).

Outre la génération d'harmoniques, une multitude d'autres phénomènes non-linéaires existe, parmi eux le mélange à quatre ondes (Anglais: Four-wave mixing, "FWM", figure 6.2d), utilisé par exemple dans les oscillateurs et amplificateurs paramétriques optiques [165, 166], ou la photoluminescence induite par deux photons (Anglais: Two photon induced photo-luminescence, "TPL", voir figure 6.2b). Ce dernier est une conversion incohérente de deux photons incidents à un photon de longueur d'onde plus courte (avec $\lambda_0 > \lambda_{TPL} > \lambda_0/2$), impliquant des états intermédiaires réels avec des durées de vie limitées [167, 168].

[1] le processus se produit instantanément, il n'y a pas d'états intermédiaires

Le lien entre l'optique non-linéaire et les nano-structures est la nécessité de fortes amplitudes des champs pour provoquer des effets non-linéaires et la possibilité d'exalter fortement les champs électriques par des nano-particules photoniques. Par conséquent, les nano-structures photoniques semblent être des candidats idéaux pour évoquer des effets non-linéaires. Ceci est la raison pour l'intérêt croissant de la communauté nano-optique dans les effets non-linéaires à l'échelle sub longueur d'onde.

6.1.2.1 Effets Non-Linéaires dans des Nano-Structures Diélectriques

En conséquence des très faibles pertes et d'autres avantages comme la compatibilité avec CMOS (pour le cas du silicium), des structures diélectriques à haut indice sont des alternatives prometteuses au structures plasmoniques (voir revue sur plasmonique non-linéaire [186]), qui néanmoins souffrent particulièrement par des pertes importantes aux courtes longueurs d'ondes, impliquées par les effets non-linéaires [188]. Par conséquence, depuis peu de temps des nano-structures photoniques – et en particulier sur la plate-forme de silicium – attirent l'intérêt de la recherche en nano-optique sur les effets non-linéaires. Un des buts est de mettre en œuvre un traitement de signaux tout-optique, compatible avec des dispositifs micro-électroniques [189]. Des effets non-linéaires de troisième ordre sont très prometteurs dans ce contexte, comme le silicium possède d'un $\chi^{(3)}$ élevé. Bien que les exaltations du champ sont généralement plus faibles par rapport à la plasmonique, le grand $\chi^{(3)}$ et les pertes réduites permettent de renforcer la génération de troisième harmonique dans les nano-structures de silicium. Par rapport à un cristal massif de Si, la THG pouvait être exalté par des facteurs allant jusqu'à 10^5 en utilisant des cristaux photoniques [190] ou des nano-antennes diélectriques [191–194]. La lumière harmonique produite, peut même être assez intense pour être visible à l'œil humain nu [195].

En conclusion, l'étude des effets non-linéaires dans les structures diélectriques est très prometteuse afin de trouver des alternatives pour des antennes plasmoniques en ce qui concerne les effets optiques non-linéaires.

6.2 Simulations Numériques de Phénomènes Nano-Optiques

Les ondes électromagnétiques dans une gamme de longueur d'onde de l'ultraviolet à l'infrarouge lointain (d'environ 10 nm à plusieurs 10 µm) sont généralement appelées *lumière*, y compris la lumière visible d'environ 400 nm à 700 nm. Dans le chapitre 2, des effets ainsi que leur modélisation sont discutés qui se produisent à l'interaction de la lumière avec des particules plus petites que la longueur d'onde.

6.2.1 Description de la Réponse Linéaire

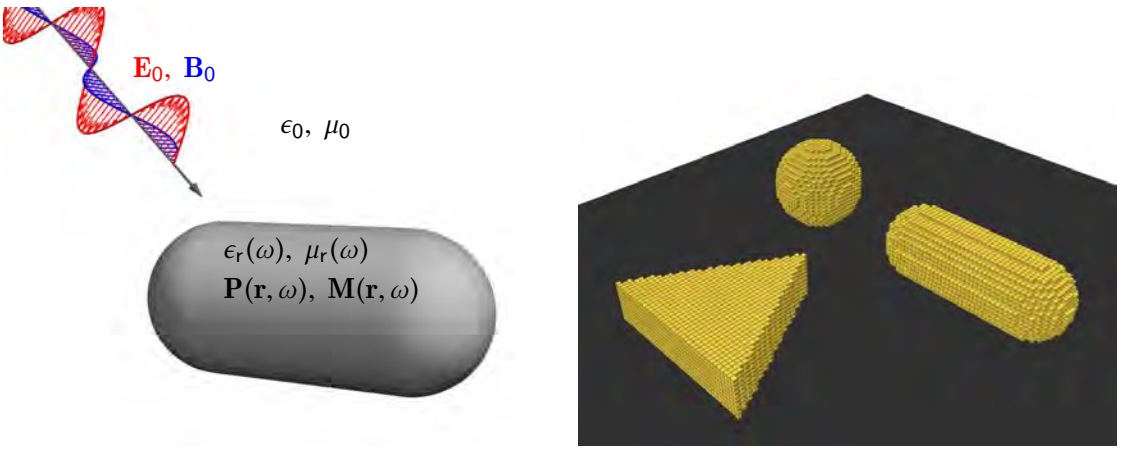

(a) Objet dans le Vide (b) Discrétisation de Volume

Figure 6.3: (a) Structure aléatoire dans le vide, caractérisée par ϵ_r et μ_r. Sa réponse à un champ électromagnétique incident $\mathbf{E}_0$, $\mathbf{B}_0$ peut être décrite par sa polarisation $\mathbf{P}$ et sa magnétisation $\mathbf{M}$. (b) Illustration de discrétisation du volume en maillage cubique d'une structure aléatoire.

6.2.1.1 Définition du Problème

En règle générale, l'objectif en nano-optique est de trouver le champ électrique (et / ou magnétique) dans une nano-structure donnée sous excitation externe, comme illustré dans la figure 6.3a. La nano-structure est normalement placée dans un milieu homogène et se trouve souvent au-dessus d'un substrat. La réponse d'une nanoparticule à un éclairement est obtenue en résolvant les équations de Maxwell (voir équations (6.2)) pour le système donné. Dans la première partie de ce chapitre, nous présentons une approche pour la résolution numérique des équations de Maxwell par intégrales de volume. Elle est basée sur des fonctions dyadiques de Green, pour cette raison appelée "méthode dyadique de Green" (Anglais: Green Dyadic Method, "GDM"). Dans la deuxième partie, nous donnerons une introduction à l'optique non-linéaire et nous présenterons une extension du modèle numérique pour la description de la génération de seconde harmonique.

6.2.1.2 Méthode Dyadique de Green

À partir des équations de Maxwell transformées en espace Fourier

$$\mathrm{div}\mathbf{D}(\mathbf{r},\omega) = \rho(\mathbf{r},\omega) \tag{6.2a}$$
$$\mathrm{rot}\mathbf{E}(\mathbf{r},\omega) = \mathrm{i}\omega\mathbf{B}(\mathbf{r},\omega) \tag{6.2b}$$
$$\mathrm{div}\mathbf{B}(\mathbf{r},\omega) = 0 \tag{6.2c}$$
$$\mathrm{rot}\mathbf{H}(\mathbf{r},\omega) = -\mathrm{i}\omega\mathbf{D}(\mathbf{r},\omega) + \mathbf{j}(\mathbf{r},\omega) \tag{6.2d}$$

il est possible d'en déduire une équation d'onde pour le champ électrique

$$(\Delta + k^2)\mathbf{E} = -\frac{1}{\epsilon_0\epsilon_r}\left(k^2 + \nabla\nabla\right)\mathbf{P} \tag{6.3}$$

qui finalement conduit à une équation "Lippmann-Schwinger" optique

$$\mathbf{E}(\mathbf{r},\omega) = \mathbf{E}_0(\mathbf{r},\omega) + \int \mathbf{G}_0(\mathbf{r},\mathbf{r}',\omega)\cdot\chi\mathbf{E}(\mathbf{r}',\omega)\mathrm{d}\mathbf{r}'. \tag{6.4}$$

Cela relie le champ électrique incident ($\mathbf{E}_0$) et la réponse de la structure ($\mathbf{E}$) de manière auto-cohérente et peut être résolue par la méthode des fonctions de Green (voir par exemple [244, chapitre 6.4]). Pour décrire des champs en espace 3D, des tenseurs de Green équivalents aux vecteurs sont définis, appelés fonctions *dyadiques* de Green ($\mathbf{G}_0$ dans éq. (6.4)).

Pour une résolution numérique du problème, la nanoparticule cible est discrétisée sur un maillage cubique en N points de volume d^3. Pour chacun d'eux une réponse dipolaire est supposée. Cette approche conduit finalement à un système de $3N$ équations couplées qui relie le champ électrique incident $\mathbf{E}_0$ au champ dans la particule $\mathbf{E}$ en réponse à l'excitation:

$$\mathbf{E}_0 = \mathbf{M}\cdot\mathbf{E}. \tag{6.5}$$

Le champ dans la structure peut alors être obtenu par une inversion de la matrice $\mathbf{M}$ qui est composée de sous-matrices de rang 3×3

$$\mathbf{M}_{ij} = \delta_{ij}\mathbf{I} - \chi_i(\omega)V_i\,\mathbf{G}(\mathbf{r}_i,\mathbf{r}_j,\omega). \tag{6.6}$$

Ici, $\mathbf{I}$ est le tenseur unitaire cartésien, δ_{ij} le symbole de Kronecker et χ la susceptibilité électrique relative à l'environnement. V_i est le volume de chaque cellule, donc dans notre cas $V_i = d^3$.

Un grand avantage de la GDM est que la présence d'un substrat peut être prise en compte par une fonction dyadique de Green appropriée, et donc à presque aucun coût de calcul supplémentaire. $\mathbf{G}_0$ dans l'équation (6.4) est simplement remplacé par une dyade $\mathbf{G}$ plus générale, qui est composée d'un terme de vide et d'un terme de surface

$$\mathbf{G}(\mathbf{r}_i,\mathbf{r}_j,\omega) = \mathbf{G}_0(\mathbf{r}_i,\mathbf{r}_j,\omega) + \mathbf{G}_{\mathrm{surf}}(\mathbf{r}_i,\mathbf{r}_j,\omega). \tag{6.7}$$

Pour une expression analytique, voir par exemple [250]. Pour tenir compte de la divergence de la fonction de Green à $\mathbf{r}_i = \mathbf{r}_j$, un système de normalisation

$$\mathbf{G}_0(\mathbf{r}_i,\mathbf{r}_i,\omega) = \mathbf{I}\,C(\omega) \tag{6.8}$$

est introduit. Pour un maillage cubique cela donne

$$C(\omega) = \frac{-1}{3\epsilon_{\text{env.}}(\omega)V_i} \tag{6.9}$$

ce qui doit être adapté en même temps que le volume de la cellule, si un maillage différent est utilisé, comme par exemple un maillage hexagonal compact [250]. Enfin, l'inversion de la matrice est fait par des techniques standards comme la décomposition LU [266, chapitre 2.3].

6.2.1.3 Traitement des Résultats

À partir du champ $\mathbf{E}$ à l'intérieur de la particule, une multitude de valeurs physiques peut être calculée. Par exemple les rendements de diffusion et absorption [280], le champ électrique (à travers équation (6.4)) ou magnétique [279] à l'extérieur de la particule, le diagramme de rayonnement de la diffusion [281] ou les dissipations de chaleur [134].

6.2.2 Optique Non-Linéaire

Tant que les champs considérés sont faibles par rapport au potentiel du réseau cristallin des médias, les phénomènes optiques peuvent être expliqués par une réponse linéaire. Dans le régime linéaire, la force de rappel agissant sur les électrons qui oscillent autour de leurs noyaux (l'oscillation est à la fréquence ω d'éclairage, voir la figure 6.4a) est une fonction linéaire du déplacement des charges relatives à leur noyau. Le noyau, ayant une masse importante par rapport aux électrons, est considéré statique. Cela peut être décrit par un potentiel harmonique.

Toutefois, en réalité le potentiel n'est pas harmonique et l'approximation linéaire échoue dès que les taux de photons sont vivement élevés. Par conséquent, si un médium est excité par un champ électromagnétique de très forte amplitude, les oscillations d'électrons deviennent sensibles à la non-linéarité du potentiel et des nouveaux phénomènes se produisent. Dans le cadre d'une approche perturbative, ce genre d'effets *non-linéaires* peut être décrit par une expansion de type "Taylor" de la polarisation électrique:

$$\mathbf{P}_{\text{tot.}} = \underbrace{\epsilon_0\chi^{(1)}\,\mathbf{E}}_{\text{Linear, } =\mathbf{P}^{(1)}} + \underbrace{\epsilon_0\chi^{(2)}\,\mathbf{E}^2}_{\text{2. Order, } =\mathbf{P}^{(2)}} + \underbrace{\epsilon_0\chi^{(3)}\,\mathbf{E}^3}_{\text{3. Order, } =\mathbf{P}^{(3)}} + \dots \tag{6.10}$$

où les susceptibilités $\chi^{(n)}$ sont des tenseurs du rang $n+1$ (n est l'ordre de la non-linéarité).

6.2.2.1 Génération de Seconde Harmonique de Surface

Pour des raisons de symétrie, les termes d'ordre pair dans l'équation (6.10) disparaissent dans des potentiels symétriques. La figure 6.4b démontre les spectres en domaine fréquentiel d'une oscillation dans des potentiels anharmoniques. Nous constatons que l'oscillation dans un potentiel symétrique ne contient que des fréquences harmoniques d'ordre impair. En conséquence, des effets non-linéaires d'ordre pair sont interdits dans des cristaux centrosymétriques. Seuls les effets d'ordre impair se produisent, comme par exemple la génération de troisième harmonique (THG, voir figure 6.2c). Des effets non-linéaires d'ordre pair (comme la SHG, voir figure 6.2a) nécessitent un potentiel d'énergie asymétrique et par conséquent ne se produisent que dans des

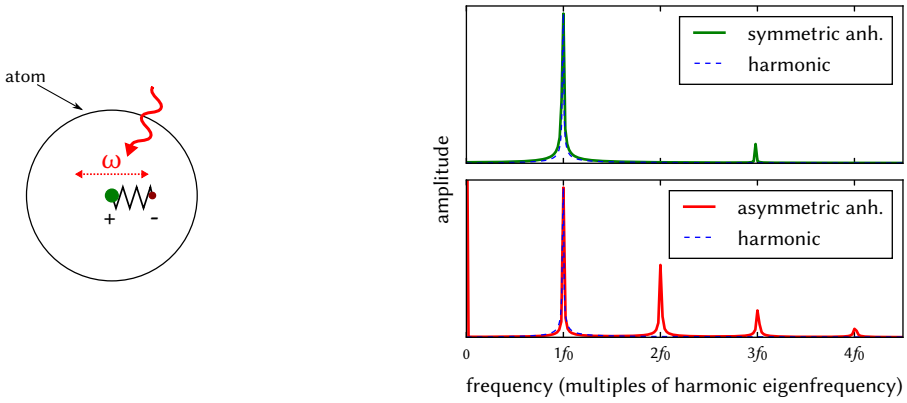

(a) Polarisation Électrique

(b) Spectre de Fourier

Figure 6.4: (a) Schéma de l'oscillation des électrons autour de leur noyau, pilotée par un champ électromagnétique externe. (b) Spectre de Fourier correspondant à une oscillation piloté dans un potentiel anharmonique symétrique (haut) et asymétrique (bas) en comparaison avec une oscillation dans un potentiel harmonique (ligne bleu pointillée).

réseaux cristallins non symétriques. Cela se trouve par exemple dans des semiconducteurs III-V (GaAs, GaP, InP, ...) ou dans d'autres matériaux composés, tels que $LiNbO_3$.

Cependant, il est possible d'obtenir de la SHG depuis des cristaux centrosymétriques (comme le silicium) à partir des ruptures locales de la symétrie du réseau. Ceci peut être réalisé par exemple au niveau des surfaces, ou en raison de forts gradients de champ. La polarisation électrique de deuxième ordre de surface se compose de trois éléments indépendants [169]:

$$\mathbf{P}^{(2)}_{\mathrm{sf}} = \mathbf{P}^{(2)}_{\perp\perp\perp} + \mathbf{P}^{(2)}_{\perp\parallel\parallel} + \mathbf{P}^{(2)}_{\parallel\parallel\perp} \tag{6.11}$$

qui sont

$$\mathbf{P}^{(2)}_{\perp\perp\perp} = \chi^{(2)}_{\perp\perp\perp}[E^2_{\perp}]\widehat{\mathbf{e}}_{\perp} \tag{6.12a}$$

$$\mathbf{P}^{(2)}_{\perp\parallel\parallel} = \chi^{(2)}_{\perp\parallel\parallel}[E^2_{\parallel}]\widehat{\mathbf{e}}_{\perp} \tag{6.12b}$$

$$\mathbf{P}^{(2)}_{\parallel\parallel\perp} = \chi^{(2)}_{\parallel\parallel\perp}[E_{\parallel}E_{\perp}]\widehat{\mathbf{e}}_{\parallel}. \tag{6.12c}$$

Les indices $\parallel$ et $\perp$ désignent les directions parallèles et perpendiculaires à l'élément de surface locale avec des vecteurs unitaires $\widehat{\mathbf{e}}_{\parallel}$ et $\widehat{\mathbf{e}}_{\perp}$.

Le premier ordre non-nul des contributions par gradients de champ (appelées "contributions du volume"), comprend quatre termes sources [290, 303]:

$$\mathbf{P}^{(2)}_{\mathrm{sf,bulk}} = \mathbf{P}^{(2)}_{\gamma} + \mathbf{P}^{(2)}_{\beta} + \mathbf{P}^{(2)}_{\delta} + \mathbf{P}^{(2)}_{\zeta} \tag{6.13}$$

où

$$\mathbf{P}^{(2)}_{\gamma} = \gamma\ \nabla[\mathbf{E}^2] \tag{6.14a}$$

$$\mathbf{P}^{(2)}_{\beta} = \beta\ \mathbf{E}[\nabla \cdot \mathbf{E}] \tag{6.14b}$$

$$\mathbf{P}^{(2)}_{\delta} = \delta\ [\mathbf{E} \cdot \nabla]\mathbf{E} \tag{6.14c}$$

$$\mathbf{P}^{(2)}_{\zeta,i} = \zeta\ E_i \nabla_i E_i. \tag{6.14d}$$

γ, β, δ et ζ sont des coefficients phénoménologiques qui peuvent être exprimés en termes d'éléments de $\chi^{(2)}$ [169, section 2.5].

6.2.2.2 SHG avec la GDM

SHG de Surface Pour la description de la SHG de surface, dans un premier pas les vecteurs unitaires parallèles et normaux à la surface sont calculés numériquement à chaque élément de surface. Avec ceci, les composantes correspondantes du champ s'écrivent

$$\begin{aligned} E_{\perp} &= \mathbf{E} \cdot \widehat{\mathbf{e}}_{\perp} \\ E_{\parallel} &= \mathbf{E} \cdot \widehat{\mathbf{e}}_{\parallel}. \end{aligned} \tag{6.15}$$

et qui, d'après équations (6.12), permettent de calculer directement la polarisation de surface de second ordre.

Or, l'influence de la présence de la nanoparticule à la fréquence harmonique doit être prise en compte: Nous devons calculer le champ auto-cohérent induit dans la nanostructure par la polarisation non-linéaire. Dans une première étape, nous considérons les polarisations non-linéaires $\mathbf{P}^{(2)}(\mathbf{r}, 2\omega)$ comme la source d'un "champ incident effectif" à la fréquence harmonique. A l'exemple de $\chi^{(2)}_{\perp\perp\perp}$ cela donne

$$\mathbf{E}^{(2)}_{0,\perp\perp\perp}(\mathbf{r}, 2\omega) = \frac{1}{\epsilon_0} \int_V \mathbf{G}_0(\mathbf{r}, \mathbf{r}', 2\omega)\mathbf{P}^{(2)}_{\perp\perp\perp}(\mathbf{r}, 2\omega)\mathrm{d}\mathbf{r}' \tag{6.16}$$

avec le tenseur de Green $\mathbf{G}_0$ à la fréquence *harmonique*.

Nous supposons qu'il n'y a pas de champ incident externe $\mathbf{E}_0(2\omega)$ à la longueur d'onde harmonique et donc que $\mathbf{E}^{(2)}_{0,\perp\perp\perp}$ est le seul champ à 2ω. Dans une deuxième étape, nous propageons le "champ incident effectif" à l'intérieur de la particule – à la fréquence harmonique – comme décrit ci-dessus

$$\mathbf{E}^{(2)}_{\mathrm{sc},\perp\perp\perp}(\mathbf{r}, 2\omega) = \int_V \mathbf{M}^{-1}(\mathbf{r}, \mathbf{r}', 2\omega)\mathbf{E}^{(2)}_{0,\perp\perp\perp}(\mathbf{r}', 2\omega)\mathrm{d}\mathbf{r}'. \tag{6.17}$$

$\mathbf{M}^{-1}$ est l'inverse de la matrice définie par équation (6.6). L'indice "sc" signifie qu'il s'agit du champ auto-cohérent (Anglais: "self-consistent"). Enfin, nous obtenons la *polarisation non-linéaire auto-cohérente* par une multiplication avec la susceptibilité électrique *linéaire*, à la fréquence harmonique

$$\mathbf{P}^{(2)}_{\mathrm{sc},\perp\perp\perp}(\mathbf{r}, 2\omega) = \chi(2\omega) \cdot \mathbf{E}^{(2)}_{\mathrm{sc},\perp\perp\perp}(\mathbf{r}, 2\omega) \tag{6.18}$$

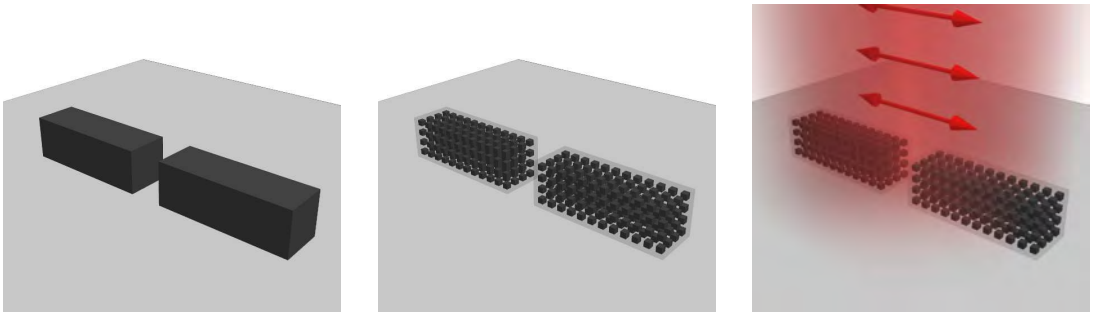

(a) Structure (b) Discrétisation (c) Champ Incident

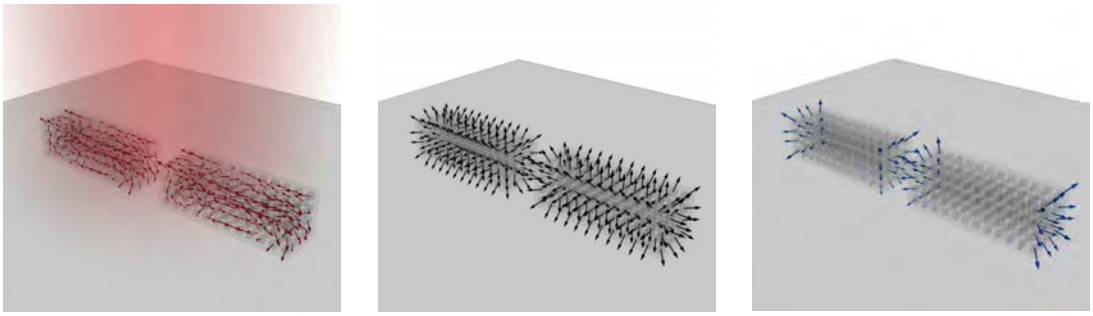

(d) Champ à l'Intérieur (e) Vecteurs $\perp$ de Surface (f) Polarisation nonlin. $\mathbf{P}^{(2)}$

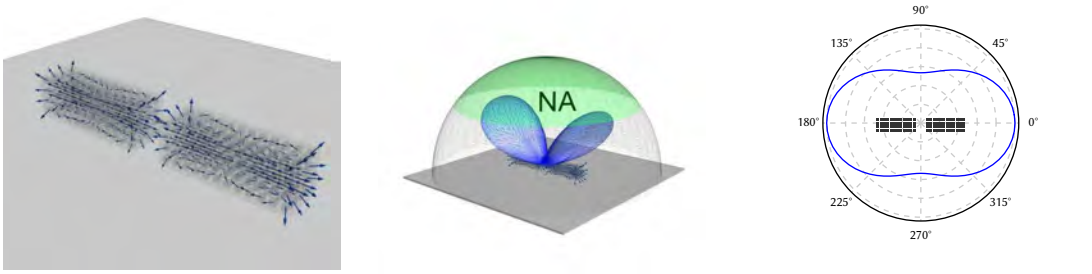

(g) $\mathbf{P}^{(2)}_{\text{sc}}$ Auto-Cohérent (h) Propa. Champ Lointain (i) Polar. Champ Lointain

Figure 6.5: Illustration de la procédure de simulation de SHG par GDM à l'exemple d'un dimère de silicium de dimensions $2 \times 250 \times 100 \times 100\,\text{nm}^3$ ($2 \times L \times W \times H$) séparé par un gap de $G = 75\,\text{nm}$. La particule (a) est discrétisée (b) et le champ induit par un faisceau incident est calculé par GDM (c-d). Depuis cette réponse linéaire, la polarisation non-linéaire de surface ($\mathbf{P}^{(2)}_{\perp\perp\perp}$ dans cet exemple) est calculée. Cela est fait par la sélection des point de maillage sur la surface dans un premier pas et puis par la détermination des vecteurs localement normaux à la surface (e). Avec ces vecteurs, la polarisation non-linéaire peut-être calculée depuis le champ fondamental au même endroit pour chaque point de surface (f). Cette polarisation non-linéaire est ensuite re-propagée de façon auto-cohérente en utilisant la susceptibilité du champ à la fréquence harmonique (g). Enfin, la polarisation non-linéaire de second ordre peut être propagée vers le champ lointain (h) afin de calculer par exemple des plots polaires de la SHG (i) capturée par une certaine aperture numérique (l'angle solide en vert dans (h) correspond à une NA 0.8). L'inset dans (i) est un schéma illustrant l'orientation du dimère de silicium par rapport au plot polaire.

Une illustration du calcul de SHG par GDM est donnée, étape par étape, dans la figure 6.5 à l'exemple de $\mathbf{P}^{(2)}_{\perp\perp\perp}$.

Contributions du Volume Pour être applicable dans la manière la plus générale possible, les contributions du volume à la SHG de surface sont calculées numériquement en utilisant des dérivés par différences finies. Nous utilisons notamment le *différentiel central* [266, chapter 5.7]:

$$\frac{\partial f(x)}{\partial x} = \lim_{\epsilon \to 0} \frac{f(x+\epsilon) - f(x-\epsilon)}{2\epsilon} \approx \frac{f(x+\Delta x) - f(x-\Delta x)}{2\Delta x} \tag{6.19}$$

Dans le cas de la GDM Δx sera généralement égal à la taille du pas de discrétisation.

6.3 Réponse Optique Non-Linéaire de Nanofils de Silicium

Dans le chapitre 3 nous étudions en détail la réponse optique non-linéaire de nanofils individuels de silicium. Particulièrement la génération de seconde harmonique est détaillée. Puisque la SHG est interdite dans le volume du silicium, la surface est la seule source de seconde harmonique. Il se trouve que les nanofils sont des candidats prometteurs pour renforcer cet effet, car le rapport superficie/volume élevé ainsi que des champs fortement exaltés par des résonances optiques sont en faveur de la SHG de surface.

6.3.1 Réponse Linéaire

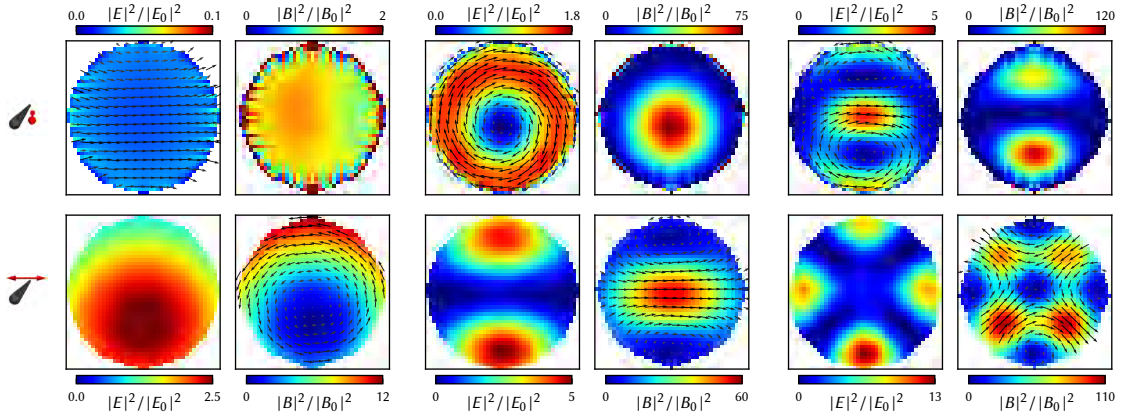

(a) TM_{01} (b) TE_{01} / TM_{11} (c) TE_{11} / TM_{21}

Figure 6.6: Intensités de champ pour les premières résonances de Mie dans un nanofil de silicium (résonances de mode "Leaky"), calculées par GDM: (a): TM_{01}, (b): TE_{01}/TM_{11} et (c): TE_{11}/TM_{21}. Intensités de champ électrique (à gauche) et magnétique (à droite) après excitation en onde plane, polarisée TE (en haut) et TM (en bas). Si des composantes du champ dans le plan existent, la partie réelle est indiquée par des petites flèches en couleur noire. Incidence par en haut.

Avant d'étudier en détail les phénomènes optiques non-linéaires dans les nanofils de Si, nous élaborons leurs propriétés linéaires. La réponse de nanofils aux champs électromagnétiques est traité analytiquement dans le cadre de la "théorie de Lorenz-Mie" (ou simplement la théorie de Mie) développée à l'origine pour des particules sphériques [319]. La Théorie de Mie peut être adaptée aux cylindres (de longueur infinie) en utilisant des harmoniques cylindriques vectorielles pour la série d'expansion du champ (voir par exemple [304]).

Il se trouve que des résonances optiques se produisent dans de petits cylindres d'indice de réfraction supérieur à celui de l'environnement. En Anglais ces résonances sont appelées "leaky mode resonances" (LMR). Dans une image intuitive, le champ électrique subit des réflexions multiples à l'intérieur de la particule et des résonances se produisent quand ces "circulations de lumière" interfèrent de manière constructive. Pour un support illustratif de cette explication, voir les champs bouclés dans la figure 6.6. Par conséquent, les positions spectrales λ_{LMR} des LMRs sont à peu près proportionnelles au *périmètre* du nanofil

$$k \cdot \lambda_{\mathrm{LMR}} \propto n \cdot 2R\pi \tag{6.20}$$

où k est un numéro entier et n l'indice de réfraction du cylindre de radius R.

Dans la figure 6.6, les intensités des champs électriques et magnétiques à l'intérieur d'un nanofil de longueur infinie sont présentés pour les LMRs des trois premiers ordres. L'excitation par ondes planes à $\lambda = 600\,\text{nm}$ est polarisée perpendiculairement (transversal électrique, "TE") ou parallèlement (transversal magnétique, "TM") à l'axe du fil. On peut voir à partir des échelles de couleurs, qu'en résonance le champ électrique à l'intérieur du nanofil est fortement exalté[1].

Le rapport de superficie/volume élevé, aussi que l'exaltation du champ proche, peuvent stimuler la réponse non-linéaire de nanofils de silicium. À cause de ces conditions favorables, nous allons étudier de façon plus détaillée les effets non-linéaires depuis des nanofils de silicium.

6.3.2 Réponse Non-Linéaire

6.3.2.1 Échantillons: Nanofils crû par VLS

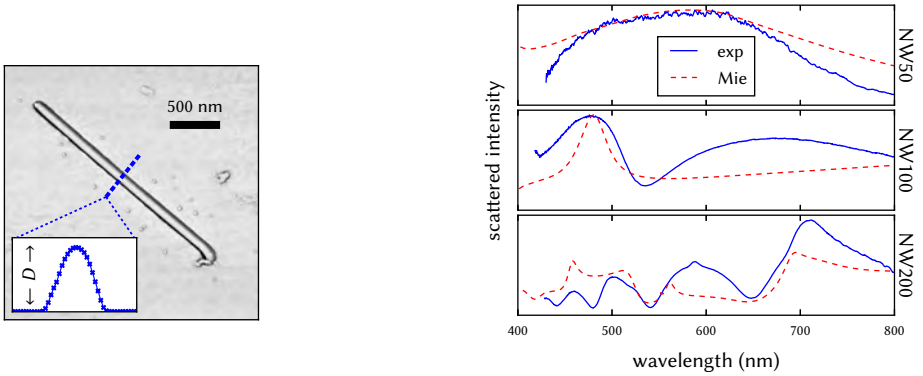

(a) Microscopie à Force Atomique (NW100) (b) Spectres de Diffusion Champ Sombre

Figure 6.7: Characterisation des nanofils VLS de silicium par microscopie à force atomique (a) (barre est 500 nm), et en microscopie optique champ sombre en comparaison avec la théorie de Mie (b).

Tous les résultats ont été obtenus sur des nanofils de silicium cristallin, crû par la méthode "vapeur-liquide-solide" (VLS) (croissance selon la direction [111]). La méthode VLS est une technique chimique de croissance en phase vapeur, dans laquelle les nanofils sont crû sur un substrat à partir d'un gaz précurseur, médiée par les gouttes catalytiques (habituellement de l'or) de taille nanométrique [131]. Les nanofils peuvent ensuite être caractérisées par exemple par microscopie à force atomique (Anglais: Atomic force microscopy, "AFM") ou par spectroscopie en champ sombre (Anglais: Dark field, "DF") en comparaison avec la théorie de Mie. Voir figure 6.7 pour des exemples.

Par la suite, trois groupes de nanofils seront étudiés. Les dimensions pour les plus petits nanofils sont choisies telle qu'une seule résonance est présente dans le visible "NW50". Cette résonance est non dégénérée et apparaît seulement sous excitation "TM", i.e. en polarisation parallèle à l'axe du fil. En "TE" (polarisation perpendiculaire au nanofil), il n'y a aucun mode dans la gamme spectrale du visible. Le deuxième groupe étudié, "NW100", a une résonance TM_{01} autour de $700 - 800\,\text{nm}$ et un second mode dégénéré (TM_{11} / TE_{01}) au-dessous de $500\,\text{nm}$. Enfin, un

[1] d'ailleurs ainsi que à leur voisinage

troisième groupe de très grands nanofils “NW200”, avec des diamètres $> 200\,\text{nm}$, est caractérise, qui produit plusieurs résonances à travers le visible. Des spectres typiques des nanofils étudiés sont présentés dans la figure 6.7b.

6.3.2.2 Dispositif du Microscope Non-Linéaire

Le dispositif expérimental est composé d’un laser Ti:Sa accordable, émettant avec une largeur d’impulsion d’environ $150\,\text{femtosecondes}$ (fs) et un taux de répétition de $80\,\text{MHz}$. Le faisceau du laser est focalisé sur l’échantillon par une ouverture numérique NA 0.8 (Anglais: Numerical aperture, “NA”). Il est utilisé à des longueurs d’onde autour de $\lambda_0 = 800\,\text{nm}$. La puissance moyenne à l’arrière de l’objectif est dans l’ordre de $10\,\text{mW}$. En utilisant une lame demi-onde, la polarisation linéaire de la lumière incidente peut être contrôlée. Étant déposé sur une table piézo, l’échantillon est positionné avec une précision de $\approx 1\,\text{nm}$. L’émission non-linéaire est collecté en rétro-diffusion et finalement réfléchie vers le détecteur par une lame séparatrice dichroïque. Le détecteur est soit un photomultiplicateur connecté à un amplificateur synchrone, ou un spectromètre avec un capteur CCD de haute sensibilité. Filtres de couleur à bande étroite sont introduits devant le détecteur afin de sélectionner des parties particulières d’émission non-linéaire (par exemple la SHG).

6.3.2.3 Spectres de l’Émission Non-Linéaire

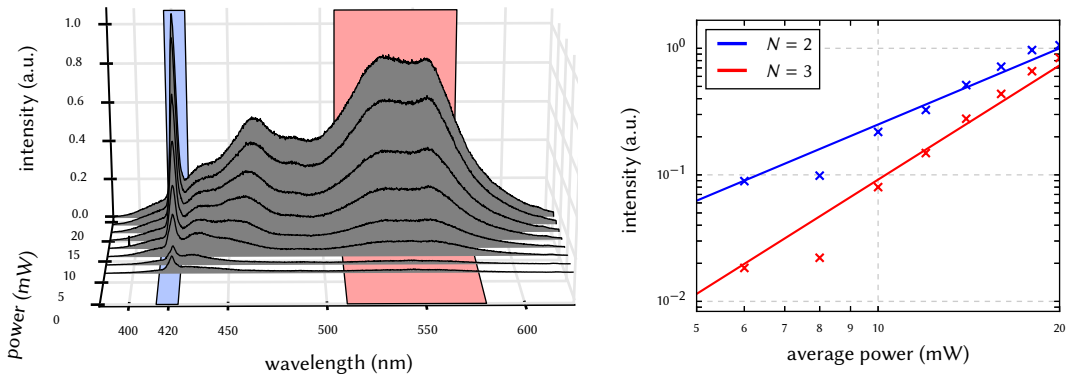

(a) NW200, TM: Spectres vs. Puissance Laser

(b) Signaux Non-Linéaires vs. Puissance

Figure 6.8: (a) Spectres obtenus depuis NW200 pour différentes puissances de l’excitation (puissance moyenne du laser pulsé). (b) Plot double-logarithmique pour les intensités dans les zones indiquées par couleur bleue (SHG) et rouge (bande large). Des Lois de puissance en ordres $N = 2$ et $N = 3$ sont indiquées comme “guide pour l’œil”.

Dans une première étape, le spectre du signal non-linéaire d’un nanofil de silicium (NW200) est analysé. Sur la figure 6.8a, des spectres expérimentaux sont tracés pour différentes puissances du laser. L’excitation est à $\lambda_0 = 840\,\text{nm}$ et polarisée en TM. Les intensités correspondantes aux zones rouge et bleu sont tracées en fonction de la puissance d’excitation dans la figure 6.8b sur une échelle logarithmique (échelle log-log). Des lois de puissances sont indiquées comme “guide pour l’œil” pour $N = 2$ (bleu) et $N = 3$ (rouge). Les résultats confirment un ordre 2 pour le signal

à la longueur d'onde de la SHG ($\lambda_0/2$) tout comme un processus non-linéaire du troisième ordre responsable de la luminescence large. Par conséquent, cette dernière bande est probablement une photoluminescence induite à trois photons, soit du silicium lui-même, soit de la coquille de SiO_2 autour du fil [328–330].

6.3.2.4 Dépendance de SHG sur Résonances Optiques

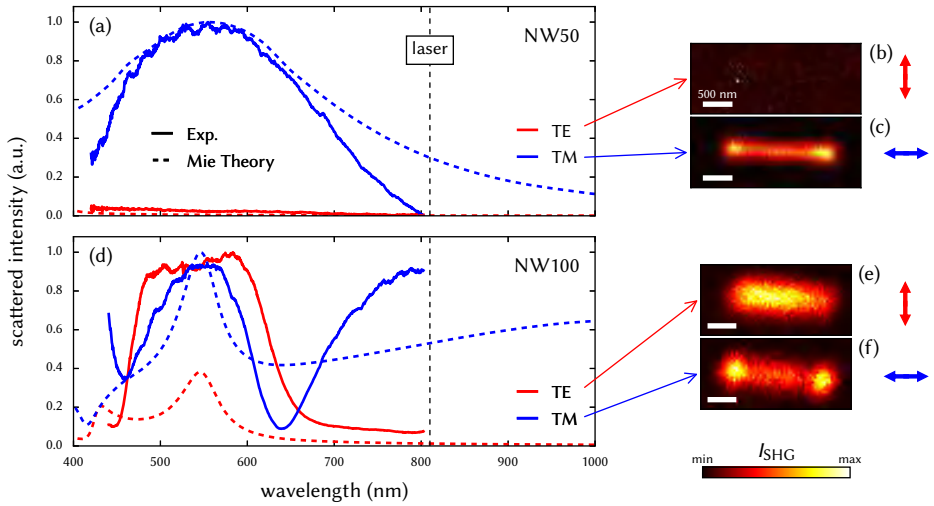

Figure 6.9: Gauche: Spectres de diffusion mesurés en champs sombre et filtrés en polarisation (lignes solides) depuis NW50 (a) et NW100 (d), comparés avec la théorie de Mie (pointillé) pour une excitation TE (rouge) et TM (bleu). À droite, des cartes de balayage filtrées pour SHG depuis NW50 (b et c) et NW100 (e et f). Barres correspondent à 500 nm.

Nous étudions également l'influence des résonances optiques sur la génération de seconde harmonique sur les petits nanofils NW50 et NW100. Sous excitation TM, ces fils disposent d'un et de deux modes respectivement. Pour un incidence polarisé TE, aucune, respectivement une seule résonance de Mie se produit dans les nanofils NW50 et NW100 (voir aussi la figure 6.7b). Dans la figure 6.9a et d, des spectres filtrés en polarisation sont présentés et comparés à des cartes de balayage de SHG.

Bien que de la SHG ait été toujours mesurée si un mode de Mie existait proche de la longueur d'onde fondamentale (NW100 et NW50 excité en TM), aucune lumière de seconde harmonique ne pouvait être obtenue depuis NW50 sous excitation polarisée TE, en l'absence de toute résonance. Des simulations GDM montrent en outre que le champ électrique à l'intérieur du nanofil est quasiment nul dans ce dernier cas. Cela explique le manque de SHG en absence de résonances optiques. Les résultats montrés dans la figure 6.9 sont normalisés individuellement sur les valeurs maximales. Une comparaison des valeurs absolues a montré qu'une exaltation de la SHG par plus que deux ordres de grandeur est obtenue par rapport à un cristal de silicium en vrac. La SHG la plus forte est observée pour les nanofils NW100, où des résonances paraissent à la longueur d'onde fondamentale ainsi qu'à la harmonique.

Enfin, on observe que la SHG est exaltée aux bouts des nanofils sous excitation "TM" alors que, en cas de TE, l'intensité de la SHG est homogène tout le long de l'axe du fil. Ce comporte-

ment peut être expliqué par le composant $\chi^{(2)}_{\perp\perp\perp}$, étant l'élément dominant dans le tenseur de la susceptibilité non-linéaire.

6.3.2.5 Origine de la SHG

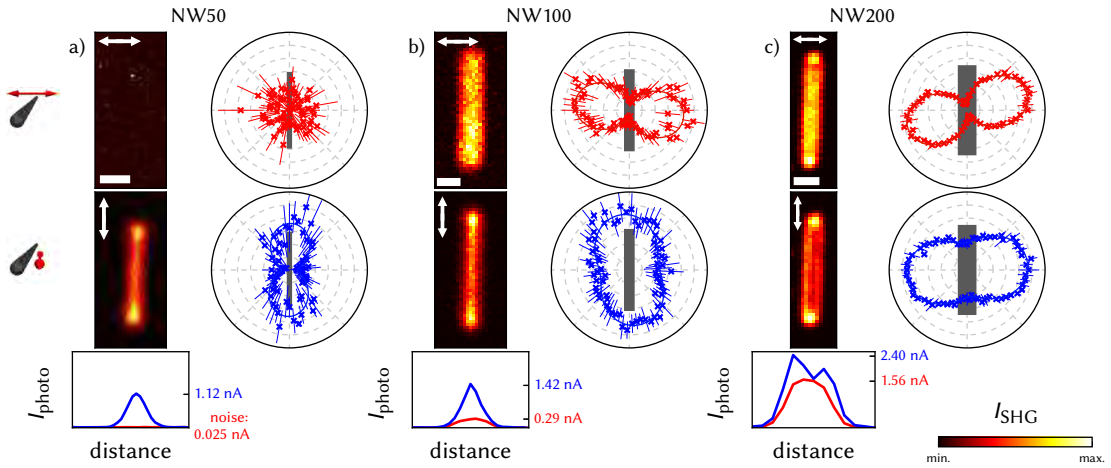

Figure 6.10: (a) NW50, (b) NW100 et (c) NW200. Excitation TE en rouge, TM en bleu. Colonnes à gauche: Cartes en balayage de SHG (pas de filtre de polarisation). Toutes cartes sont normalisées à leur valeur maximale (voir profiles à travers les fils en bas). Barres sont 0.5 µm. Colonnes à droite: Polarisation de SHG au champ lointain, après excitation au centre du nanofil. Lignes solides sont des régressions de courbe sur les données.

Suite à la suggestion d'analyser la polarisation de SHG pour séparer les contributions à son origine [296], nous effectuons des mesures de génération de seconde harmonique filtrées en polarisation linéaire. Des résultats sont présentés dans la figure 6.10, où nous pouvons observer que la direction de polarisation de la SHG se retourne par 90°. Ce phénomène se produit sous excitation TM en augmentant la taille du nanofil. Au cas d'excitation TE d'autre part, la lumière SHG est toujours polarisée perpendiculairement à l'axe du nanofil, suivant la polarisation incidente. Des considérations théoriques permettent d'expliquer ce comportement par une transition de contribution principale à la SHG. Dans les petits nanofils, la SHG est à l'origine de la contribution δ du volume (voir éq. (6.14)), induite par les gradients du champ du à la forte focalisation du faisceau laser. En augmentant la taille, la contribution de surface $P^{(2)}_{\perp\parallel\parallel}$ s'augmente et finalement domine la SHG totale. D'autre part, sous éclairage TE, ou, si les extrémités des nanofils sont éclairées, $\mathbf{P}^{(2)}_{\perp\perp\perp}$ est toujours la contribution principale à la SHG. Ce comportement est en outre confirmé par des simulations numériques.

En résumé, la SHG dans les nanofils de petits diamètres est due à une contribution de volume, tandis que les sources de surface augmentent avec un diamètre croissant – donc pour une *diminution* du rapport superficie/volume. Malgré le fait que ceci est plutôt contre-intuitif, le phénomène peut être expliqué par une annulation microscopique de la polarisation non-linéaire,

à cause d'une phase localement opposée [176, 297]. En effet, en analysant les vecteurs de la polarisation non-linéaire, on constate une forte annulation microscopique pour les contributions de surface. Cette annulation s'affaiblit quand le diamètre du nanofil augmente. Quant à la contribution δ du volume par contre, des effets de retard contournent partiellement l'annulation du rayonnement vers le champ lointain.

6.4 Optimisation Évolutionniste de Nano-Structures Photoniques

Dans le chapitre 4 nous nous éloignons des propriétés optiques fondamentales et l'accent est mis sur la conception et l'adaptation d'attributs optiques de nanoparticules. La conception de nanostructures photoniques consiste habituellement à anticiper leur réponse optique à partir de modèles simples ou par des variations de systèmes de référence. Ces systèmes sont ensuite étudiés systématiquement. Cette stratégie est limitée par les capacités de la géométrie choisie initialement. En outre, si différents objectifs sont simultanément ciblés, le problème devient encore plus compliqué (voir aussi figure 6.11c).

6.4.1 Algorithmes d'Optimisation Évolutionniste

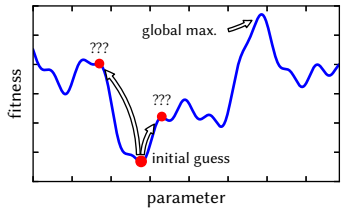

(a) Optimisation Locale

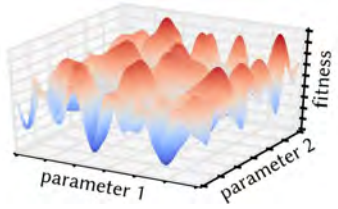

(b) Points Extrêmes en 2D

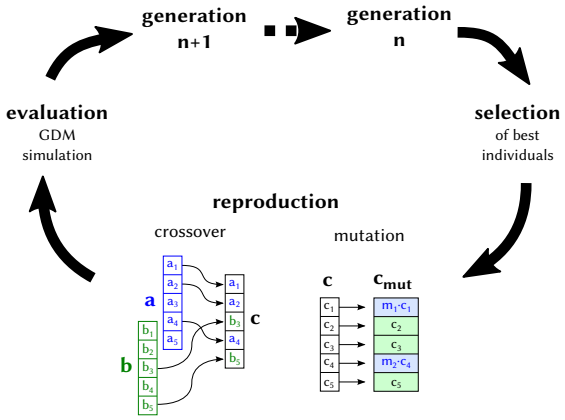

(c) Schéma Optimisation Évolutionniste

Figure 6.11: Schéma du principe d'optimisation évolutionniste. (a) Dilemme des algorithmes d'optimisation locales "classiques": Si des points extrêmes locaux existent, la minimisation reste coincé et ne converge pas vers le minimum global. (b) Illustration d'un problème complexe en deux dimensions. (c) Illustration du cycle de reproduction parcourue par un algorithme d'optimisation évolutionniste.

Quant à des applications, une approche plus pratique est de d'abord définir les propriétés optiques requises et de concevoir une nanostructure qui présente les caractéristiques souhaitées de manière optimale. Les algorithmes classiques de maximisation ou de recherche d'un zéro d'une fonction semblent prometteurs de prime abord. Cependant, il est difficile de décrire les géométries de nanoparticules par des fonctions analytiques, nécessaires par exemple pour des dérivés quant à la méthode de Newton. De plus, il est fort probable que la fonction de l'objectif possède d'innombrables points extrêmes locaux (voir la figure 6.11a-b.). Cela limite encore plus l'applicabilité des algorithmes d'optimisation classiques, car ils se coincent dans les points extrêmes locaux. Par conséquent la solution ne convergera pas vers l'optimum global, comme illustré dans la figure 6.11a à l'exemple d'un problème de minimisation en une dimension.

Des techniques plus prometteuses sont des stratégies d'optimisation évolutionniste (Anglais: Evolutionary optimization, "EO"). Ces méthodes, imitant la sélection naturelle, sont en mesure

de trouver les plus aptes ensembles de paramètres face à un problème complexe [335] (voir la figure 6.11c). Dans le domaine de la nano-optique, les algorithmes évolutionnistes ont été appliqués afin de maximiser l'exaltation de champ proche [336–340] ou la diffusion de lumière depuis des particules plasmoniques [341–343], ainsi qu'à la conception d'antennes hybrides plasmoniques/diélectriques [344], pour citer quelques exemples.

Dans l'EO, une population d'individus est définie ("génération n" dans la figure 6.11c), où chaque individu constitue un ensemble de paramètres pour la fonction de l'objectif. Dans notre cas, les ensembles de paramètres décrivent des morphologies d'antenne nano-photonique. Cette population subit une procédure d'évaluation et de sélection dans laquelle les solutions faibles sont éliminées. Ensuite, les candidats les plus aptes (*i.e.* les ensembles de paramètres donnant les meilleures valeurs cibles) sont choisis pour la reproduction. Ce dernier processus consiste en une étape appelée *croisement* (Anglais: Crossover), où les paramètres sont échangés et mélangés[1], et une étape de *mutation*, dans laquelle certains paramètres choisis au hasard sont remplacés par des nombres aléatoires (voir figure 6.11c, étape "reproduction"). De cette manière, une nouvelle population d'individus est générée. Ce processus de sélection, de reproduction et d'évaluation est répété jusqu'à ce qu'un critère d'arrêt soit satisfait.

6.4.2 Optimisation de Nano-Antenne Directionnelle

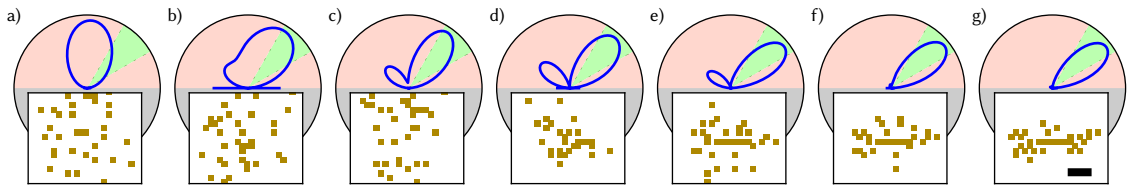

Figure 6.12: Itérations sélectionnées de l'évolution d'une antenne plasmonique directionnelle. Le diagramme de rayonnement en plan XZ est démontré en haut, où un segment vert indique l'angle solide de l'objectif. Les structures plasmoniques correspondantes aux diagrammes de rayonnement sont démontrées en bas (en plan XY). (a) Structure initiale aléatoire. (b-f) Meilleurs candidats depuis des générations intermédiaires. (g) Meilleur candidat de la population final. La barre est de 200 nm.

Afin de démontrer l'optimisation évolutionniste en nano-photonique, nous employons l'EO sur un modèle de nano-antenne plasmonique, fabriqué avec de l'or. Avec ceci, nous voulons concevoir une nano-antenne pour la diffusion directionnelle de la lumière. Les candidats les plus aptes au cours de l'optimisation sont présentés dans la figure 6.12 ainsi que les diagrammes de rayonnement de la diffusion élastique. La lumière incidente est réalisée par une onde plane de $\lambda_0 = 800\,\text{nm}$, polarisée linéairement selon la direction de diffusion souhaitée. (a-f) montrent des itérations au cours des premières 20 générations, et (g) montre la solution finale, trouvée après 50 itérations.

L'antenne finale montre une diffusion fortement directionnelle et son principe de fonctionnement est égal au fonctionnement des antennes directionnelles utilisées pour les fréquences radio. Sachant qu'initialement la conception de la structure est complètement libre, il est remarquable qu'une disposition d'antenne ait été trouvée – tout à fait automatiquement et avec

[1] comme les gènes dans la nature

une très bonne reproductibilité – qui correspond aux principes de fonctionnement bien connus provenant d'antennes des fréquences radio.

6.4.3 Optimisation de Pixels Double-Résonants

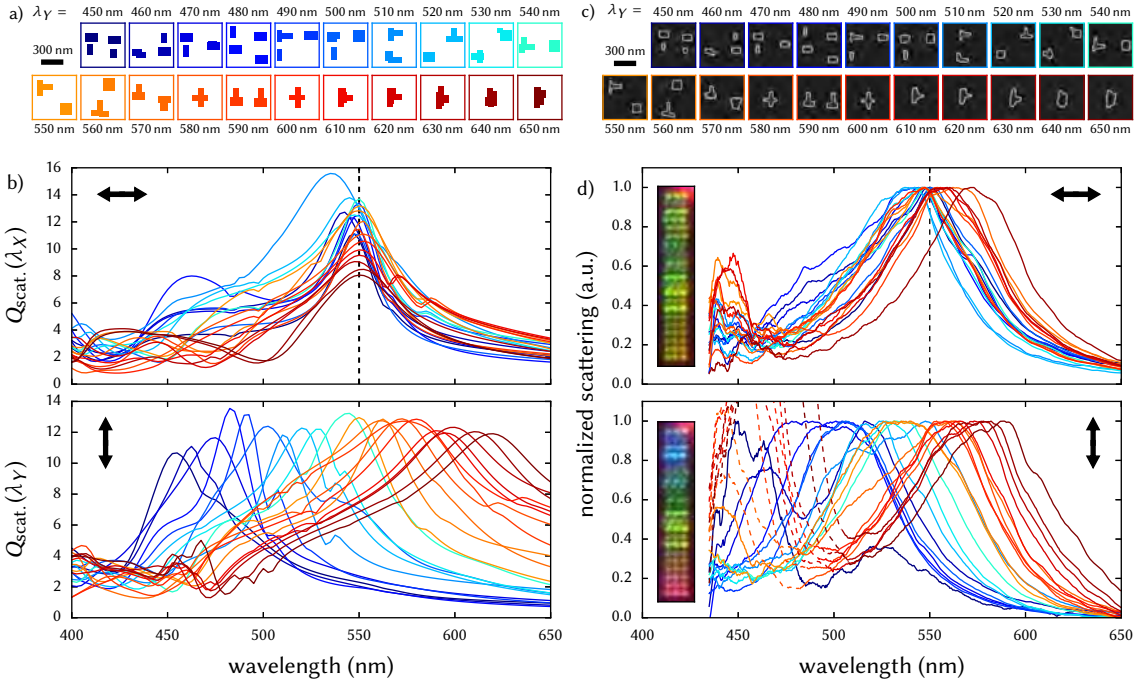

Figure 6.13: Démonstration expérimentale des structures double-résonnantes, trouvées par optimisation évolutionniste. (a) Modèle de structure EMO des particules diélectriques double-résonnantes et (b) spectres de diffusion correspondantes avec $\lambda_X = 550\,\text{nm}$ (indiqué par ligne noire pointillée) et différents λ_Y. (c) Images SEM des structures nano-fabriquées et (d) spectres correspondantes mesurées en champ sombre et filtrés en polarisation. Les insets dans (d) démontrent des images du set des structures, obtenues par microscopie en champ sombre filtré en polarisation ($4 \times 20\,\mu\text{m}^2$). Les zones dans (a) et (c) sont de $600 \times 600\,\text{nm}^2$.

Dans la dernière partie, nous voulons aller encore plus loin. La plupart des études appliquant l'optimisation évolutionniste dans le contexte de la nano-optique ont été limitées à la maximisation d'une seule propriété cible et cela à une longueur d'onde et à polarisation bien spécifique. De tels scénarios à objectif unique représentent le cas le plus simple d'un problème d'optimisation. Une structure qui remplit simultanément plusieurs objectifs sera en général plus difficile à concevoir. Des stratégies d'optimisation évolutionniste à objectifs multiples (Anglais: Evolutionary multi-objective optimization, "EMO") [357, 358] sont une approche prometteuse pour contrer ces problèmes. Dans cette partie, nous présentons une combinaison de EMO avec la GDM que nous appliquons à la conception de structures diélectriques multi-résonantes. Notre objectif est de maximiser l'efficacité de la diffusion Q_{scat} à une longueur d'onde λ_X pour une polarisation incidente linéaire le long de la direction X, et en même temps de maximiser la diffusion à une deuxième longueur d'onde λ_Y, polarisée en Y.

Nous effectuons plusieurs optimisations à objectifs multiples pour de différentes combinaisons de longueurs d'onde cibles. La longueur d'onde $\lambda_X = 550\,\text{nm}$ reste fixe, tandis que l'autre objectif (λ_Y) varie de $450\,\text{nm}$ à $650\,\text{nm}$ en incréments de $10\,\text{nm}$. Chaque simulation est constituée d'une population de 20 individus, initialisée aléatoirement et subséquemment évoluée pendant 200 générations. À la fin de chaque évolution, la structure avec les plus proches $Q_{\text{scat}}(\lambda_X)$ et $Q_{\text{scat}}(\lambda_Y)$ est choisie.

Dans la figure 6.13, nous montrons les structures résultantes (a) et leurs spectres simulés par GDM pour illumination polarisée le long des directions X et Y (b). Les différents λ_Y sont indiqués par un code couleur allant du bleu ($\lambda_Y = 450\,\text{nm}$) au rouge ($\lambda_Y = 650\,\text{nm}$). Pour une vérification expérimentale, nous avons fabriqué des structures de silicium correspondantes aux nano-antennes EMO. Des images de microscopie électronique à balayage (figure 6.13c) et des spectres de diffusion, filtrés en polarisation (figure 6.13d, en haut: filtré X, en bas: filtré Y) sont présentés à gauche de figure 6.13. Dans les insets, des images des structures optimisées, obtenues par microscopie optique en champ sombre, filtrée en polarisation, démontrent le changement de couleurs en fonction de la polarisation de la lumière.

6.4.4 Conclusions

En conclusion, l'optimisation évolutionniste reliée aux simulations électro-dynamiques est très prometteuse pour la conception automatique de divers types de nano-structures photoniques. Nous avons démontré qu'une approche d'optimisation évolutionniste est en mesure de réaliser des objectifs photoniques complexes comme des résonances multiples, même au sein d'un modèle très simple et fortement restreint. Pour une bonne compatibilité avec des méthodes de fabrication, les limitations technologiques peuvent être incluses dans l'algorithme. Grâce à de tels considérations technologiques, nous avons pu produire des échantillons sur substrat SOI en utilisant les résultats des optimisations évolutionnistes. Avec la microscopie en champ sombre, filtrée en polarisation, nous avons finalement pu confirmer l'accord entre les propriétés optiques des échantillons et les simulations.

L'optimisation évolutionniste de nano-structures photoniques a un potentiel énorme pour de nombreux types d'applications dans la nano-optique du champ proche et du champ lointain. Des exemples imaginables se trouvent dans la conception des particules multi-résonantes ou à large bande pour des capteurs de lumière ou quant aux nano-structures pour l'optique non-linéaire.

Appendix A

Dielectric Interfaces

A.1 Continuity Conditions

To calculate the continuity conditions at the interface between two dielectric materials, we start with the Maxwell equations for homogeneous, isotropic and constant media:

$$\text{div}\mathbf{D} = \rho \qquad \text{rot}\mathbf{E} = 0 \tag{A.1}$$

$$\text{div}\mathbf{B} = 0 \qquad \text{rot}\mathbf{H} = \mathbf{j} \tag{A.2}$$

with $\mathbf{D} = \epsilon_0\epsilon_r\mathbf{E}$ and $\mathbf{B} = \mu_0\mu_r\mathbf{H}$.

Furthermore, we will use Gauss' integral theorem for vector fields $\mathbf{V}$

$$\int_{\Delta V} \mathrm{d}r^3 \cdot \text{div}\mathbf{V} = \int_{S(\Delta V)} \mathrm{d}\mathbf{f} \cdot \mathbf{V} \tag{A.3}$$

where $S(\Delta V)$ is the surface around the volume ΔV, as well as Stokes' integral theorem:

$$\int_{S} \mathrm{d}\mathbf{f} \cdot \text{rot}\mathbf{V} = \int_{\partial F} \mathrm{d}\mathbf{r} \cdot \mathbf{V} \tag{A.4}$$

with ∂F the path around the area S.

To find the continuity conditions for the $\mathbf{E}$-field component normal to the interface, we integrate the Maxwell equation for the divergence of the electric field over a cuboid around the interface between two dielectric media ϵ_{r0} and ϵ_{r1} (see fig. A.1a). With Gauss' integral theorem (A.3), we get

$$\int_{V} \mathrm{d}r^3 \cdot \text{div}\mathbf{D} = \int_{\Delta F} \mathrm{d}\mathbf{f} \cdot \mathbf{D} \quad \xrightarrow{\Delta x \to 0} \quad 2\Delta F \cdot \mathbf{n} \cdot (\mathbf{D}_1 - \mathbf{D}_0) \tag{A.5}$$

and

$$\int_{V} \mathrm{d}r^3 \cdot \text{div}\mathbf{D} = \int_{V} \mathrm{d}r^3 \cdot \rho = \sigma \cdot 2\Delta F = 0 \tag{A.6}$$

with σ the surface charge at the interface which we assume to be zero. From eq. (A.5) and (A.6) we get:

$$\mathbf{n} \cdot (\mathbf{D}_1 - \mathbf{D}_0) = 0 \tag{A.7}$$

To find the tangential component's continuity condition, we integrate over an area around the

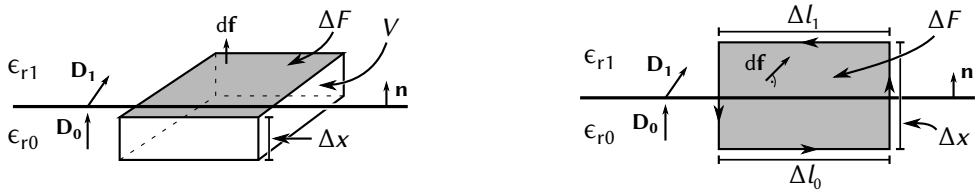

(a) Gauss' cuboid

(b) Stokes' area

Figure A.1: At the interface between two dielectrics, integrating over an infinitely small cuboid leads to the continuity condition for the **E**-field normal component a, while by integrating over an infinitely small area the tangential component's continuity condition is found b.

interface using Stokes' theorem (A.4):

$$0 = \int_{\Delta F} \mathrm{d}\mathbf{f} \cdot \mathrm{rot}\mathbf{E} = \int_{\partial(\Delta F)} \mathrm{d}\mathbf{r} \cdot \mathbf{E} \quad \xrightarrow{\Delta x \to 0} \quad \Delta l \cdot (\mathbf{n}_{\Delta F} \times \mathbf{n}) \cdot (\mathbf{E}_1 - \mathbf{E}_0) \tag{A.8}$$

with $\Delta l_1 \cdot \hat{\mathbf{e}}_{l1} = -\Delta l_0 \cdot \hat{\mathbf{e}}_{l0} = \Delta l \cdot (\mathbf{n}_{\Delta F} \times \mathbf{n})$ where the notation from figure A.1b is used and $\hat{\mathbf{e}}_{li}$ are unitary vectors in path direction. Analogously, the Maxwell equations of the magnetic field (A.2) can be integrated to obtain the corresponding continuity conditions.

Finally we have four continuity conditions, for the normal ((A.9), (A.10)) and parallel ((A.11), (A.12)) components of the electric and the magnetic field respectively:

$$\mathbf{n} \cdot (\mathbf{D}_1 - \mathbf{D}_0) = 0 \tag{A.9}$$
$$\mathbf{n} \cdot (\mathbf{B}_1 - \mathbf{B}_0) = 0 \tag{A.10}$$
$$\mathbf{n} \times (\mathbf{E}_1 - \mathbf{E}_0) = 0 \tag{A.11}$$
$$\mathbf{n} \times (\mathbf{H}_1 - \mathbf{H}_0) = 0 \tag{A.12}$$

We see, that the normal component of the electric displacement field **D** as well as the electric field **E**'s tangential component are continuous over the interface. Analogously, the magnetic and the demagnetizing fields' (**B** and **H**) normal and tangential components are conserved.

A.2 Reflected Field Amplitudes

From the above derived continuity conditions, the reflectivity and transmittance coefficients at the interface can be calculated. Again, we assume normal incidence ($\mathbf{n} \perp \mathbf{E} \perp \mathbf{B}$), so equations (A.9) and (A.10) are already fulfilled. Furthermore, the vector products of the fields in equations (A.11) and (A.12) can be replaced by scalar products of the field amplitudes. The electric field in the material with index "0" can be written as a superposition of a forward (E_0) and a backward ($E_{0,r}$) traveling component (see fig. A.2). With

$$\mathbf{B} = \mu_r \cdot \mathbf{H} = \frac{\mathbf{k}}{\omega} \times \mathbf{E} \tag{A.13}$$

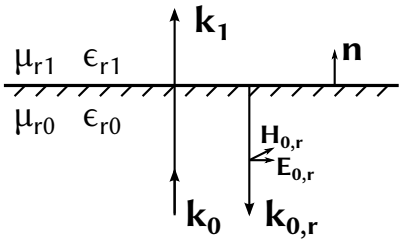

Figure A.2: Normal reflection at an interface between two dielectric media.

equation (A.12) can be written as

$$\frac{k_1 E_1}{\mu_{r1}} - \frac{k_0 E_0 + k_{0,r} E_{0,r}}{\mu_{r0}} = 0 \tag{A.14}$$

We know that

$$k = \frac{\omega}{c} n = \frac{2\pi}{\lambda} \sqrt{\epsilon_r \mu_r} \tag{A.15}$$

with the refractive index $n = \sqrt{\epsilon_r \mu_r}$. We see, that for normal incidence $k_{0,r} = -k_0$. By inserting (A.15) in equation (A.14), we obtain

$$E_1 \cdot \left(\sqrt{\frac{\epsilon_{r1}}{\mu_{r1}}} \right) = (E_0 - E_{0,r}) \cdot \left(\sqrt{\frac{\epsilon_{r0}}{\mu_{r0}}} \right) \tag{A.16}$$

For non-magnetic media ($\mu_r = 1 \rightarrow n = \sqrt{\epsilon_r}$), we can now calculate the reflectance and the transmittance at the interface by taking equation (A.11) into account ($E_1 = E_0 + E_{0,r}$):

$$r_{0,1} = \frac{E_{0,r}}{E_0} = \frac{n_0 - n_1}{n_0 + n_1} \tag{A.17}$$

$$t_{0,1} = \frac{E_1}{E_0} = \frac{2n_0}{n_0 + n_1} \tag{A.18}$$

The deduction of the reflectivity for the general case of non-normal incidence is analogue to the calculation above and can be found in literature (e.g. [365]). Finally we note that an addition-rule for the reflectivities of several successive layers can be derived using a substitution of the form $r = \tanh s$ [366]. In analogy to quantum mechanics transfer-matrix methods can be used alternatively, to obtain the reflectivity of or field amplitudes in multi-layer systems [367, 368].

Appendix B

Autocorrelation Measurements

Interferometric autocorrelation (IAC) measurements can be used to obtain the order of the nonlinear response. In order to perform a fit to the IAC measurements, we need to describe the signal mathematically.

B.1 Model Assuming Unchirped Gaussian Wave Packets

Remark: The pulse widths are given as the Gaussian's width w of the pulse envelope, i.e. the duration during which the amplitude is larger than $E \cdot 1/e$, with E the maximum field amplitude and e Euler's number. To obtain the width of the pulse's intensity, the width of the electric field has to be divided by $\sqrt{2}$ (because $I = E^2$). Finally, from the Gaussian width w, the full width at half maximum is found by FWHM $= w \cdot 2\sqrt{2 \ln 2}$.

We assume a Gaussian shape for the envelope of the traveling wave packets, sent by the pulsed laser

$$A(x,t) = A_0 \cdot \exp\left(-2\frac{(x - v_g t)^2}{(\tau_{\text{pulse}} \cdot c)^2}\right) \tag{B.1}$$

where τ_{pulse} is the Gaussian width of the pulse in time domain and v_g its group velocity. The time and space-dependent field amplitude of the pulse is the product of $A(x,t)$ with a plane wave $u(x,t)$

$$u(x,t) = u_0 \cdot \exp\left(\pm i(kx - kct)\right) \tag{B.2}$$

($k = \omega/c,\ \omega = 2\pi f = 2\pi c/\lambda$) and writes

$$E(x,t) = E_0 \cdot u(x,t) \cdot A(x,t) \tag{B.3}$$

as illustrated in Fig. B.1a,*i*. For a description in time domain, the space coordinate x of the field can be substituted by $x = t \cdot c$ (for more details on wave packets, see e.g. [365, chapter 4.3]).

Now we assume two coherent Gaussian wave packet-like pulses (E_{p1} and E_{p2}) with a time delay δ between each other (illustrated in Fig. B.1a,*iii*). For a given delay, the experimentally accessible value, the intensity of the fields, is obtained by integrating both pulses over the entire time-range

$$I_{\text{meas.}}(\delta) = \int_{-\infty}^{\infty} \left[E_{\text{p1}}(t) + E_{\text{p2}}(t - \delta)\right]^2 \mathrm{d}t. \tag{B.4}$$

If a signal from an interaction of the two pulses with a nonlinear medium is acquired, the inte-

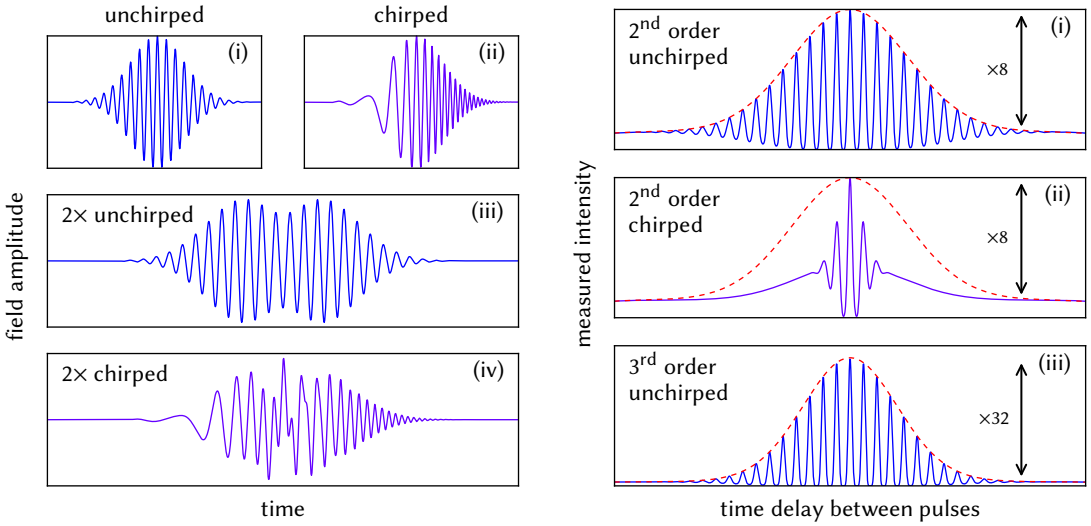

(a) Gaussian Wave Packets

(b) Interferometric Autocorrelation

Figure B.1: (a) illustration of an unchirped (*i*) and a chirped (*ii*) pulse, as well as a partial temporal superposition of two such pulses ((*iii*) and (*iv*), respectively). (b) interferometric autocorrelation of two unchirped pulses from second (*i*) and third order (*iii*) nonlinear response, as well as a second order chirped autocorrelation figure (*ii*). Red dashed lines show the (unchirped) envelope to the IAC plots. The intensity enhancement factors between infinite and zero time-delay are indicated at the right.

grand has to be taken to the power of N, where N is the order of the nonlinearity

$$I_{\text{meas., NL}}(\delta) = \int_{-\infty}^{\infty} \left| \left[E_{\text{p1}}(t) + E_{\text{p2}}(t-\delta) \right]^2 \right|^N \mathrm{d}t. \tag{B.5}$$

In experiment, the signal $I_{\text{meas., NL}}(\delta)$ can be measured as a function of the time-delay δ going from negative to positive values. Usually, a crystal with significant nonlinear susceptibility is used as reference sample, hence the order N is known.

For a numerical calculation of the autocorrelation signal, we replace the integral and the differential $\mathrm{d}t$ by a sum over small time-steps Δt:

$$\int f(t)\mathrm{d}t \quad \rightarrow \quad \sum f(t)\Delta t \tag{B.6}$$

In order for Eq. B.5 to be a valid approximation, several assumptions have to be made:

1. a Gaussian wave packet is a good approximation for the laser-pulse
2. both beams have equal width and amplitude
3. all observed light is generated due to the same physical effect ⇒ the same order of nonlinear response can be assumed for the minimum as well as the maximum occuring field amplitudes

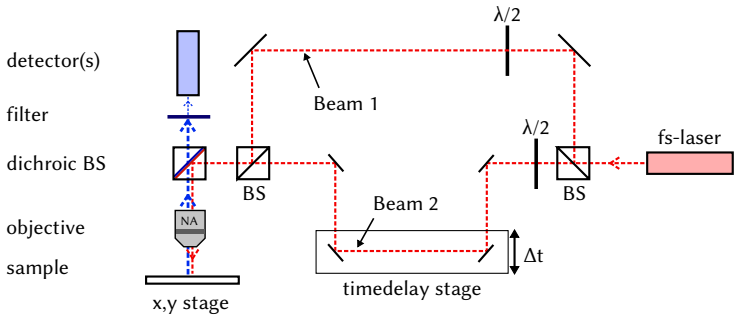

Figure B.2: Experimental setup for interferometric autocorrelation measurements.

4. the laser-pulse has only a negligible chirp, although it is very likely that there is some amount of chirp (Chirped pulse, see Fig. B.1a,*ii*. For the influence of a chirp on the autocorrelation signal, see below)

Assuming these conditions are met, the measured intensity can be written as a function of the pulse width τ_{pulse}, the pulse amplitude E_0 and the order of (nonlinear) response N. For fitting the numercially obtained autocorrelation function, an additional delay-offset $\Delta\delta$ is included to take account of the zero delay position in experiment. The function for the interferometric autocorrelation intensity

$$I_{\text{meas.}}(\delta) = I_{\text{meas.}}(\delta, E_0, \tau_{\text{pulse}}, N, \Delta\delta) \tag{B.7}$$

can be used to simulate the autocorrelation signal. The interferometric autocorrelation is calculated by using

$$E(x,t) = E_0 \cdot u(x,t) \cdot A(x,t) \tag{B.8}$$

as shown in Fig. B.1b (solid lines), whereas the envelope to this signal is obtained using only a Gaussian for the electric field (red dashed lines in Fig. B.1b)

$$E(x,t) = E_0 \cdot A(x,t). \tag{B.9}$$

The latter can be obtained by so-called "intensity autocorrelation" measurements. Fur further details and a broader overview on autocorrelation measurement techniques, we refer to the tutorial on ultrashort pulse shaping by Monmayrant et al. [369].

B.1.1 Influence of Chirp on Gaussian Model

A chirp means, that the wavelength changes with time during a single pulse (see illustration of a chirped pulse in Fig. B.1a,*ii* and scheme of two superposed identical, chirped pulses in Fig. B.1a,*iv*). From intensity and interferometric autocorrelation measurements, the chirp cannot be unambiguously accessed and therefore assumptions on it have to be made. For all fits in the following, a chirp-free pulse has been assumed. The influence of a linear chirp on the autocorrelation signal via a second order nonlinearity is shown in figure B.1b,*ii* in comparison to the envelope of unchirped IAC (using a highly exaggerated chirp). A chirp can make the pulse durations in IAC measurements appearing shorter than they are in reality.

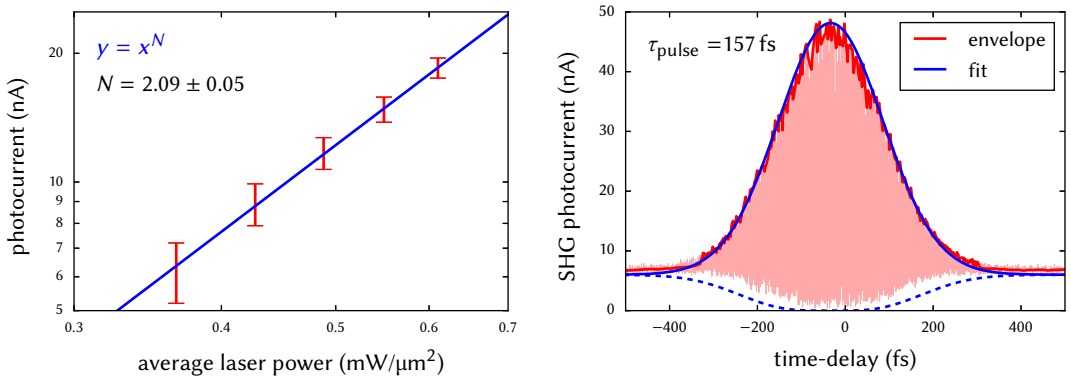

(a) Power Dependence

(b) Interferometric Autocorrelation

Figure B.3: (a) SHG intensity as function of incident laser power and (b) interferometric autocorrelation measurement on a $LiNbO_3$ crystal at $\lambda_0 = 810\,\text{nm}$. In (a) a power-law was fitted to the data, confirming a second order nonlinear response. In (b) a fit to the envelope of the autocorrelation signal was performed in order to obtain the optical pulse width, fixing the order of the nonlinearity to $N = 2$.

B.2 Power Series on $LiNbO_3$

To verify the nonlinearity of the reference $LiNbO_3$ crystal, a measurement of SHG as function of the incident laser power was performed. The data is shown in Fig. B.3a together with a power-law fit. The result of the fit confirms the second-order power-dependence of a $\chi^{(2)}$ nonlinearity.

B.3 Pulse Width Characterization Using $LiNbO_3$ Reference

In order to fit the envelope of the autocorrelation measurements and in this way obtain the order of the response's nonlinearity, we need to determine the laser-pulse width in a reference measurement. Confirmed by the power-dependence measurement, the order of the nonlinear response of the $LiNbO_3$ reference sample is fixed to $N = 2$. Similar pulse widths aorund $\tau_{\text{pulse}} \approx 150\,\text{fs}$ were obtained for the investigated wavelengths $\lambda_0 = 750\,\text{nm}$ (Fig. B.4a), $\lambda_0 = 810\,\text{nm}$ (Fig. B.3b) and $\lambda_0 = 840\,\text{nm}$ (Fig. B.4b).

The experimental setup used for interferometric autocorrelation measurements is shown in figure B.2. The pulses emitted by the fs-laser are split by a beam-splitter, travelling on two equally long optical paths. One of those paths is equipped with a micro-motor controlled time-delay stage, which allows to shorten or enlarge the distance traveled by the photons, thus controlling the time delay between the two optical pulses.

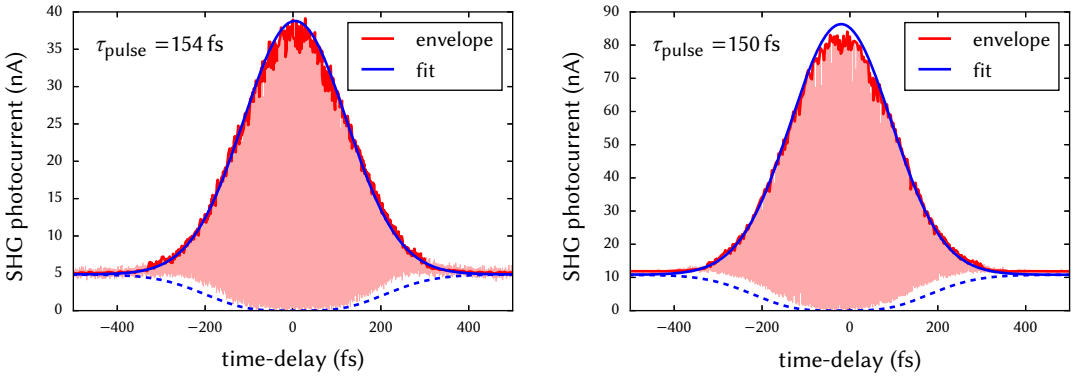

(a) $\lambda_0 = 750\,\text{nm}$ (b) $\lambda_0 = 840\,\text{nm}$

Figure B.4: Interferometric autocorrelation measurements on a $LiNbO_3$ crystal at (a) $\lambda_0 = 750\,\text{nm}$ and (b) $\lambda_0 = 840\,\text{nm}$. For the fit the order of the nonlinearity was fixed to $N = 2$.

Appendix C

SiNW Surface SHG Polarization Dependence

We want to numerically study the polarization dependence of the different contributions to surface SHG from an infinitely long, plane wave illuminated cylindrical[1] nanowire (in vacuum) in more detail, in order to confirm our theoretical considerations from section 3.4.3. The wavelength of the normally incident light is $\lambda_0 = 810\,\mathrm{nm}$, hence $\lambda_{\mathrm{SHG}} = 405\,\mathrm{nm}$.

In Fig. C.1 SHG from "simple" $\mathbf{P}^{(2)}_{\perp\perp\perp}$, $\mathbf{P}^{(2)}_{\perp\parallel\parallel}$, $\mathbf{P}^{(2)}_{\parallel\parallel\perp}$ (top row; blue solid lines) as well as from their self-consistent counterparts (second row; blue dashed lines) is shown as a function of the incident polarization and the NW diameter. A logarithmic color-scale is used to increase the visual contrast. 1D plots for a $D = 100\,\mathrm{nm}$ and a $D = 150\,\mathrm{nm}$ SiNW are shown in (*vii-xii*).

Obviously, for an incidence polarized along the wire axes (transverse magnetic, "TM"), only $\mathbf{P}^{(2)}_{\perp\parallel\parallel}$ is non-zero, confirming our conclusion from section 3.4.3.1. For a polarization normal to the axis ("TE") on the other hand, this component is vanishing (at least for diameters $D \lesssim 230\,\mathrm{nm}$), while the other contributions are non-zero. We can observe, that $\mathbf{P}^{(2)}_{\perp\perp\perp}$ follows perfectly a $\sin^4(\varphi)$, which fits Malus' law for a second order nonlinear response. Also $\mathbf{P}^{(2)}_{\perp\parallel\parallel}$ follows Malus' law for smaller nanowires, but at a diameter $D = 150\,\mathrm{nm}$ first deviations from the plotted $\cos^4(\varphi)$-line occur and it finally becomes non-zero for TE incidence at large diameters[2]. $\mathbf{P}^{(2)}_{\parallel\parallel\perp}$ finally reaches its highest value somewhere between pure TE and pure TM incidence, for a maximum of the product of the perpendicular and parallel field components $E_\parallel \cdot E_\perp$. As a consequence it doesn't obey Malus' law. In the quasistatic approximation, the field inside the particle is proportional to the incident field. For small nanowires, $\mathbf{P}^{(2)}_{\parallel\parallel\perp}$ therefore reaches its maximum at a polarization of $45\,^\circ$ (see $D = 100\,\mathrm{nm}$ in Fig. C.1a, *ix*).

Note that the "simple" as well as a self-consistent SHG calculation give similar results. However, for small nanowire diameters, significant differences can be observed, which can be attributed to the optical coupling of the nonlinear polarization to the modal response of the nanowire. Away from the NW tips, $\mathbf{P}^{(2)}_{\perp\perp\perp}$ and $\mathbf{P}^{(2)}_{\perp\parallel\parallel}$ result in a nonlinear polarization $\perp$ to the NW axis, which hence couple to the TE-response of the nanowire at the harmonic wavelength. For TE however, only a weak optical response exists at the harmonic frequency for small diameters $D \lesssim 50\,\mathrm{nm}$ (see Fig. 3.16 or Fig. 3.2). In consequence, the scattering of the harmonic to the far-field is suppressed for small NWs in the self-consistent calculation.

The suppression of surface-SHG also supports the observation of the bulk contribution for SiNWs of small diameter. In contrast to the "TE-type" surface contributions, a nonlinear bulk polarization with field components along the wire axis can couple efficiently to the far-field via the TM modes at the harmonic wavelength.

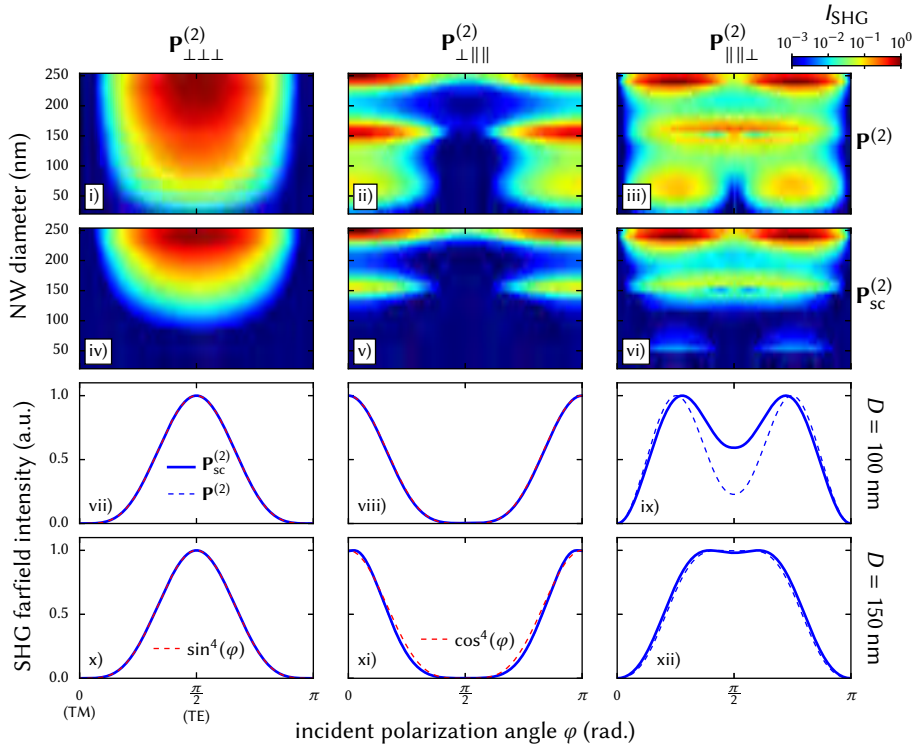

(a) Surface SHG Polarization Dependence (b) Orientation

Figure C.1: Polarization dependence of surface SHG from infinitely long silicon NW. (a) SHG intensity in the farfield (full solid angle) for cylindrical SiNWs. Contributions $\mathbf{P}^{(2)}_{\perp\perp\perp}$, $\mathbf{P}^{(2)}_{\perp\parallel\parallel}$ and $\mathbf{P}^{(2)}_{\parallel\parallel\perp}$ are shown in the left, center and right column, respectively. (*i-iii*) show results of the "simple" SHG calculation ($\mathbf{P}^{(2)}$, solid blue lines in the $1D$-plots), (*iv-vi*) for corresponding self-consistent simulations ($\mathbf{P}^{(2)}_{\mathrm{sc}}$, dashes blue lines in the $1D$-plots). Colormaps are scaled logarithmically. Exemplary 1D plots are shown for diameters $D = 100\,\mathrm{nm}$ (*vii-ix*) and $D = 150\,\mathrm{nm}$ (*x-xii*). $\cos^4(\varphi)$ and $\sin^4(\varphi)$ are plotted for comparison in (*vii, x*) and (*viii, xi*), respectively. Polarization directions for TM (along the wire axis, $\varphi = 0, \pi$) and TE (normal to the wire axis, $\varphi = \pi/2$) with respect to the NW axis are illustrated in (b) by red arrows.

Appendix D

SHG from Lithographic Silicon Wires

We present some preliminary results of SHG from lithographic silicon wires etched in SOI (for details on the fabrication, see Sec. 4.2.1.2). The height of the SOI silicon layer is $H = 95\,\text{nm}$, the length of the lithographic wires is fixed to $L = 3\,\mu\text{m}$ and the width is varied.

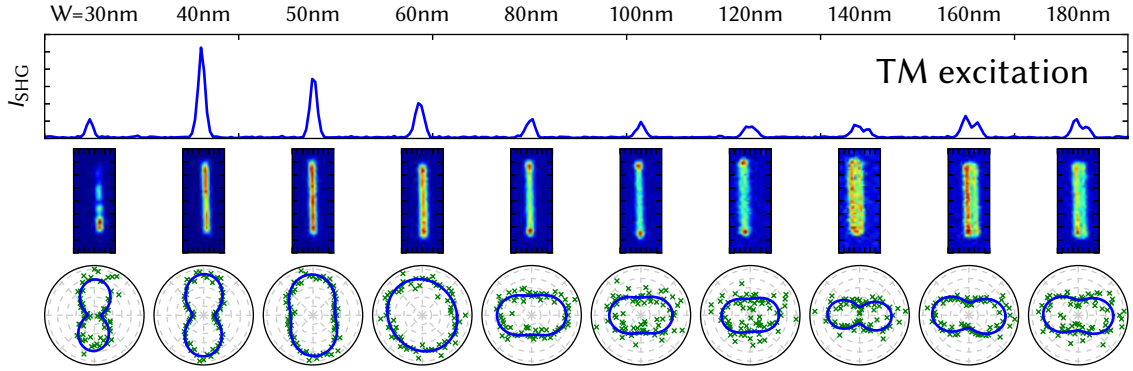

Figure D.1: SHG from TM excited lithographic SiNWs of fixed height ($H = 95\,\text{nm}$) and variable widht W. Top: Intensity profiles across the NW centers. Center: SHG-filtered rasterscan maps. Bottom: SHG farfield polarization from excitation at the NW center.

In figure D.1, SHG results from TM-excited silicon wires are shown (details on the measurement procedure can be found in Sec. 3.2.2). Intensity-profiles across the nanowires are given in the top, the data was acquired in a single measurement, the intensities are therefore directly comparable and a signature of a modal response can clearly be observed. SHG rasterscan mappings are shown in the center, revealing an interesting behavior: For larger rectangular wires, the SHG is strongest under excitation of the wire borders. A similar observation has been already made for VLS grown SiNWs with large diameter (see Sec. 3.4.2). Finally, polar plots, resolving the far-field polarization of the backscattered SHG are shown in the bottom row, where once again the flip in polarization is observed, from perpendicular to parallel with respect to the wire axis. Also rectangular, non-symmetric nanowires seem therefore suitable for a distinction of bulk- and surface contributions to SHG by means of size-variations (see Sec. 3.4.3).

The influence of resonant modes on SHG is demonstrated on the letters “CNRS”, composed of differently large SiNW, shown in Fig. D.2. Wire widths are chosen such that a resonance under TE excitation outweighs the TM response and gives rise to a strong SHG for TE excitation. The widths are $W = 60\,\text{nm}$ (background) and $W = 130\,\text{nm}$ (CNRS letters). This makes the letters appear bright on a dark background for TE incidence (Fig. D.2, top) while under TM excitation SHG from the background is stronger than the nonlinear signal from the letters (Fig. D.2, bottom).

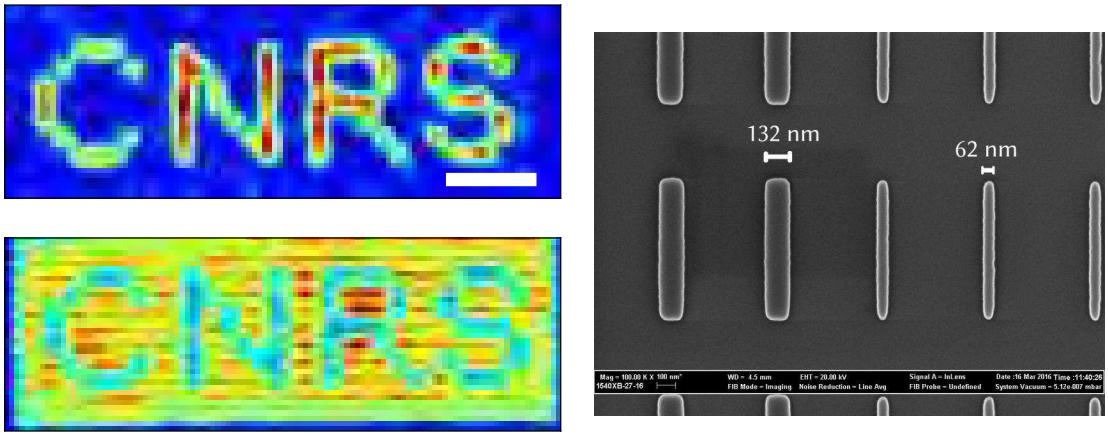

(a) SHG Microscopy (b) SEM

Figure D.2: (a) SHG from TE (top) and TM (bottom) excited CNRS letters, composed of lithographic Si nanowires. Height and length are fixed to $H = 95\,\text{nm}$, respectively $L = 1\,\mu\text{m}$. Widths are $W = 60\,\text{nm}$ (background) and $W = 130\,\text{nm}$ (CNRS letters), scalebar is $5\,\mu\text{m}$. (b) SEM image from the CNRS letters, where both types of wires are shown.

Appendix E

Symbols and Abbreviations

Symbols

a, A	Scalars
$\mathbf{a}, \mathbf{A}$	Vectors (or Tensors, by context)
i	Imaginary unit
∇	Nabla operator
Δ	Laplace operator
G	Green's Function
$\mathbf{G}$	Green's Dyad
(hkl)	Miller indices of crystal lattice
e^-, h^+	Electron, hole
ω	Angular frequency
λ	Wavelength
$\mathbf{k}$	Wave-vector
k	Wave-number ($\lvert\mathbf{k}\rvert$)
ϵ_r	Dielectric permittivity
χ	Electric susceptibility
$\chi^{(N)}$	N^{th} order electric susceptibility
$\mathbf{E}$	Electric field
$\mathbf{D}$	Electric displacement
ρ	Charge density
$\mathbf{j}$	Current density
$\mathbf{P}$	Electric polarization
μ_r	Magnetic permeability
χ_m	Magnetic susceptibility
$\mathbf{B}$	Magnetic field
$\mathbf{H}$	Magnetizing field
$\mathbf{M}$	Magnetization
n	Refractive index

σ_geom	Geometrical cross section
σ_ext	Extinction cross section
σ_scat	Scattering cross section
σ_abs	Absorption cross section
Q_ext	Extinction efficiency
Q_scat	Scattering efficiency
Q_abs	Absorption efficiency
R_direct	Directionality ratio

Constants

c_0	Speed of Light	$2.9979 \times 10^8\ \text{m/s}^2$
ϵ_0	Vacuum Permittivity	$8.8542 \times 10^{-12}\ \text{F/m}$
μ_0	Vacuum Permeability	$4\pi \times 10^{-7}\ \text{N/A}^2$
m_0	Electron Mass	$9.1094 \times 10^{-31}\ \text{kg}$
e	Electron Charge	$1.6022 \times 10^{-19}\ \text{C}$
$\hbar$	Reduced Planck-Constant ($h/2\pi$)	$1.0546 \times 10^{-34}\ \text{J s}$
π	Pi	3.14159265

Abbreviations

AFM	Atomic force microscope
BEM	Boundary element method
CCD	Charge coupled device
CG	Conjugate gradients
CMOS	Complementary metal-oxide-semiconductor technology
CPU	Central processing unit (computer)
DDA	Discrete dipole approximation
(L)DOS	(Local) density of states
EBL	Electron beam lithography
EELS	Electron energy loss spectroscopy
EMO	Evolutionary multiobjective optimization
EO	Evolutionary optimization
FDTD	Finite difference time domain
FW/BW	Forward / Backward
FWHM	Full-width at half-maximum
FWM	Four-wave mixing
GDM	Green Dyadic Method
LMR	Leaky mode resonance
LSP	Localized surface plasmon
(M)IR	(Mid-) infrared
MPPL	Multi-photon induced photoluminescence
NA	Numerical aperture
PL	Photoluminescence
PMT	Photon multiplier tube
QW	Quantum well
SEF	Surface enhanced fluorescence spectroscopy
SEM	Scanning electron microscope
SERS	Surface enhanced Raman spectroscopy
SHG	Second harmonic generation
(Si)NW	(Silicon) Nanowire
SOI	Silicon on insulator
SPP	Surface plasmon-polariton
(s-)SNOM	(Scattering type) scanning near-field optical microscope
THG	Third harmonic generation
TE/TM	Transverse electric / magnetic
TPL	Two-photon induced photoluminescence
UV	Ultraviolet
VLS	Vapor-liquid-solid crystal growth

List of Figures

List of Tables

Index

List of Publications

Peer-Reviewed Publications In the Context of this Thesis

[4] **P. R. Wiecha**, A. Arbouet, C. Girard, A. Lecestre, G. Larrieu, and V. Paillard. "Evolutionary Multi-Objective Optimisation of Colour Pixels based on Dielectric Nano-Antennas". *Nature Nanotechnology* (Oct. 2016), (arxiv preprint).

[3] **P. R. Wiecha**, A. Arbouet, C. Girard, T. Baron, and V. Paillard. "Origin of second-harmonic generation from individual silicon nanowires". *Physical Review B* 93.12 (Mar. 2016), p. 125421.

[2] L.-J. Black, **P. R. Wiecha**, Y. Wang, C. H. de Groot, V. Paillard, C. Girard, O. L. Muskens, and A. Arbouet. "Tailoring Second-Harmonic Generation in Single L-Shaped Plasmonic Nanoantennas from the Capacitive to Conductive Coupling Regime". *ACS Photonics* 2.11 (Nov. 2015), pp. 1592–1601.

[1] **P. R. Wiecha**, A. Arbouet, H. Kallel, P. Periwal, T. Baron, and V. Paillard. "Enhanced nonlinear optical response from individual silicon nanowires". *Physical Review B* 91.12 (Mar. 2015), p. 121416.

Other Peer-Reviewed Publications

[5] J. Treu, M. Bormann, H. Schmeiduch, M. Döblinger, S. Morkötter, S. Matich, **P. Wiecha**, K. Saller, B. Mayer, M. Bichler, M.-C. Amann, J. J. Finley, G. Abstreiter, and G. Koblmüller. "Enhanced Luminescence Properties of InAs–InAsP Core–Shell Nanowires". *Nano Letters* 13.12 (Dec. 2013), pp. 6070–6077.

[4] S. Sprengel, C. Grasse, **P. Wiecha**, A. Andrejew, T. Gruendl, G. Boehm, R. Meyer, and M. Amann. "InP-Based Type-II Quantum-Well Lasers and LEDs". *IEEE Journal of Selected Topics in Quantum Electronics* 19.4 (July 2013), pp. 1900909–1900909.

[3] C. Grasse, T. Gruendl, S. Sprengel, **P. Wiecha**, K. Vizbaras, R. Meyer, and M.-C. Amann. "GaInAs/GaAsSb-based type-II micro-cavity LED with 2–3 μm light emission grown on InP substrate". *Journal of Crystal Growth* 370 (May 2013), pp. 240–243.

[2] C. Grasse, M. Mueller, T. Gruendl, G. Boehm, E. Roenneberg, **P. Wiecha**, J. Rosskopf, M. Ortsiefer, R. Meyer, and M.-C. Amann. "AlGaInAsPSb-based high-speed short-cavity VCSEL with single-mode emission at 1.3 μm grown by MOVPE on InP substrate". *Journal of Crystal Growth* 370 (May 2013), pp. 217–220.

[1] C. Grasse, **P. Wiecha**, T. Gruendl, S. Sprengel, R. Meyer, and M.-C. Amann. "InP-based 2.8–3.5 μm resonant-cavity light emitting diodes based on type-II transitions in GaInAs/GaAsSb heterostructures". *Applied Physics Letters* 101.22 (Nov. 2012), p. 221107.

Conference Proceedings

[1] H. Kallel, **P. Wiecha**, Y. Zhao, A. Arbouet, M. Carrada, G. B. Assayag, P. Periwal, T. Baron, P. Normand, A. Chehaidar, and V. Paillard. "Photoluminescence Enhancement of a Silicon Nanocrystal Plane Positioned in the Near-Field of a Silicon Nanowire (invited)". *ECS Transactions* 61.5 (Mar. 2014), pp. 189–197.

Book Chapters

[1] O. L. Muskens, **P. R. Wiecha**, and A. Arbouet. "Ultrafast Spectroscopy and Nonlinear Control of Single Nanoparticles and Antennas". *Handbook of Metamaterials and Nanophotonics – Nanoplasmonics* (2016, in press). Ed. by J. Aizpurua (general Ed.: S. A. Maier). World Scientific.

Conferences

[17] **P. R. Wiecha**, A. Arbouet, C. Girard, A. Lecestre, G. Larrieu, and V. Paillard. "Evolutionary Multi-Objective Optimization for Multi-Resonant Photonic Nanostructures". *IEEE Nanotechnology Materials and Devices Conference* (Oct. 2016). Toulouse, France, Conference Talk (best oral presentation award).

[16] **P. R. Wiecha**, L.-J. Black, Y. Wang, C. H. de Groot, V. Paillard, C. Girard, O. L. Muskens, and A. Arbouet. "Tuning the linear and non-linear optical response of orthogonal dimer antennas for metasurfaces". *IEEE Nanotechnology Materials and Devices Conference* (Oct. 2016). Toulouse, France, Conference Talk.

[15] **P. R. Wiecha**, A. Arbouet, C. Girard, T. Baron, A. Lecestre, G. Larrieu, and Paillard, Vincent. "Enhanced Second Harmonic Generation from Silicon Nanowires". *IEEE Nanotechnology Materials and Devices Conference* (Oct. 2016). Toulouse, France, Conference Talk.

[14] **P. R. Wiecha**, A. Arbouet, C. Girard, T. Baron, and V. Paillard. "Second Harmonic Generation from Silicon Nanowires". *E-MRS Fall Meeting* (Sept. 2016). Warsaw, Poland, Conference Talk.

[13] **P. R. Wiecha**, A. Arbouet, C. Girard, T. Baron, A. Lecestre, G. Larrieu, and V. Paillard. "Linear and Nonlinear Optical Properties of Individual Silicon Nanowires". *ECS Spring Meeting*. Nanoscale Luminescent Materials (May 2016). San Diego, USA, Invited Talk.

[12] **P. R. Wiecha**, A. Arbouet, T. Baron, C. Girard, and V. Paillard. "Surface and Bulk Contributions to Second Harmonic Generation from Individual Silicon Nanowires". *Nanolight* (Mar. 2016). Benasque, Spain, Poster Presentation.

[11] **P. R. Wiecha**, A. Arbouet, T. Baron, C. Girard, and V. Paillard. "Second Harmonic Generation from Individual Silicon Nanowires". *Nanophotonics Science Camp* (Aug. 2015). London, UK, Poster Presentation.

[10] Black, L.-J., **P. R. Wiecha**, Y. Wang, K. de Groot, O. Muskens, and A. Arbouet. "Tuning the Linear and Non-Linear Optical Response of Orthogonal Dimer Plasmonic Antennas for Metasurfaces". *SPP7* (June 2015). Jerusalem, Israel, Poster Presentation.

[9] **P. R. Wiecha**, A. Arbouet, P. Priyanka, T. Baron, and V. Paillard. "Second Harmonic Generation from individual SiNWs". *MRS Spring Meeting*. Symposium V: Resonant Optics – Fundamentals and Applications (Apr. 2015). San Francisco, USA, Conference Talk.

[8] H. Kallel, **P. R. Wiecha**, M. Carrada, T. Baron, A. Arbouet, and V. Paillard. "Photoluminescence Enhancement of a Silicon Nanocrystal Plane Coupled to a Silicon Nanowire Antenna". *MRS Spring Meeting*. Symposium A: Emerging Silicon Science and Technology (Apr. 2015). San Francisco, USA, Conference Talk.

[7] **P. R. Wiecha**, A. Arbouet, T. Baron, and V. Paillard. "Nonlinear Microscopy on Single Silicon Nanowires using Second Harmonic Generation". *South-West Symposium on Advanced Materials* (Oct. 2014). Toulouse, France, Poster Presentation.

[6] H. Kallel, A. Arbouet, **P. Wiecha**, Z. Yu, M. Carrada, G. Benassayag, P. Periwal, T. Baron, P. Normand, A. Chehaidar, and V. Paillard. "Photoluminescence Enhancement of a Silicon Nanocrystal Plane Positioned in the Near Field of a Silicon Nanowire". *ECS Spring Meeting*. Nanoscale Luminescent Materials (May 2014). Orlando, USA, Invited Talk.

[5] **P. Wiecha**, C. Grasse, S. Sprengel, T. Gruendl, R. Meyer, and M. C. Amann. "InP based type-II resonant cavity LEDs emitting up to 3.5µm". *27. DGKK Workshop* (Dec. 2012). Erlangen, Germany, Conference Talk.

[4] Gruendl, T., C. Grasse, S. Sprengel, **P. Wiecha**, and M. C. Amann. "Type-II Quantum Wells for InP based mid-IR Devices". *MIOMD-11* (Sept. 2012). Chicago/Evanston, USA, Conference Talk.

[3] Grasse, C., T. Gruendl, S. Sprengel, **P. Wiecha**, K. Vizbaras, R. Meyer, and M.-C. Amann. "GaInAs/GaAsSb-based type-II micro-cavity LED with 2–3 µm light emission grown on InP substrate". *16th International Conference on Metalorganic Vapor Phase Epitaxy* (May 2012). Busan, South Korea, Conference Talk.

[2] Grasse, C., M. Mueller, T. Gruendl, G. Boehm, E. Roenneberg, **P. Wiecha**, J. Rosskopf, M. Ortsiefer, R. Meyer, and M.-C. Amann. "AlGaInAsPSb-based high-speed short-cavity VCSEL with single-mode emission at 1.3 µm grown by MOVPE on InP substrate". *16th International Conference on Metalorganic Vapor Phase Epitaxy* (May 2012). Busan, South Korea, Conference Talk.

[1] Grasse, C., S. Sprengel, K. Vizbaras, T. Gruendl, **P. Wiecha**, R. Meyer, and M. C. Amann. "GaInAs/GaAsSb type-II quantum wells for up to 2.8 µm light emission on InP substrate". *26. DGKK Workshop* (Dec. 2011). Stuttgart, Germany, Conference Talk.

Bibliography

[1] J. C. Maxwell. "A Dynamical Theory of the Electromagnetic Field". *Philosophical Transactions of the Royal Society of London* 155 (1865), pp. 459–512.

[2] S. Maier. *Plasmonics: Fundamentals and Applications*. Springer US, 2010. ISBN: 978-1-4419-4113-8.

[3] "Surface plasmon resurrection". *Nature Photonics* 6.11 (Nov. 2012), pp. 707–707.

[4] F. Hubenthal. "1.13 - Noble Metal Nanoparticles: Synthesis and Optical Properties". In: *Comprehensive Nanoscience and Technology*. Ed. by D. L. Andrews, G. D. Scholes, and G. P. Wiederrecht. Amsterdam: Academic Press, 2011, pp. 375–435. ISBN: 978-0-12-374396-1.

[5] W. L. Barnes, A. Dereux, and T. W. Ebbesen. "Surface plasmon subwavelength optics". *Nature* 424.6950 (Aug. 14, 2003), pp. 824–830.

[6] H. Ditlbacher, A. Hohenau, D. Wagner, U. Kreibig, M. Rogers, F. Hofer, F. R. Aussenegg, and J. R. Krenn. "Silver Nanowires as Surface Plasmon Resonators". *Physical Review Letters* 95.25 (Dec. 16, 2005), p. 257403.

[7] S. S. Lo, H. Y. Shi, L. Huang, and G. V. Hartland. "Imaging the extent of plasmon excitation in Au nanowires using pump-probe microscopy". *Optics Letters* 38.8 (Apr. 15, 2013), p. 1265.

[8] J. Jahng, F. T. Ladani, R. M. Khan, X. Li, E. S. Lee, and E. O. Potma. "Visualizing surface plasmon polaritons by their gradient force". *Optics Letters* 40.21 (Nov. 1, 2015), p. 5058.

[9] P. J. Schuck, D. P. Fromm, A. Sundaramurthy, G. S. Kino, and W. E. Moerner. "Improving the Mismatch between Light and Nanoscale Objects with Gold Bowtie Nanoantennas". *Physical Review Letters* 94.1 (Jan. 13, 2005), p. 017402.

[10] K. B. Crozier, A. Sundaramurthy, G. S. Kino, and C. F. Quate. "Optical antennas: Resonators for local field enhancement". *Journal of Applied Physics* 94.7 (Oct. 1, 2003), pp. 4632–4642.

[11] L. Novotny. "Effective Wavelength Scaling for Optical Antennas". *Physical Review Letters* 98.26 (June 27, 2007), p. 266802.

[12] P. Bharadwaj, B. Deutsch, and L. Novotny. "Optical Antennas". *Advances in Optics and Photonics* 1.3 (Nov. 1, 2009), p. 438.

[13] P. Biagioni, J.-S. Huang, and B. Hecht. "Nanoantennas for visible and infrared radiation". *Reports on Progress in Physics* 75.2 (2012), p. 024402.

[14] M. Abb, Y. Wang, P. Albella, C. H. de Groot, J. Aizpurua, and O. L. Muskens. "Interference, Coupling, and Nonlinear Control of High-Order Modes in Single Asymmetric Nanoantennas". *ACS Nano* 6.7 (July 24, 2012), pp. 6462–6470.

[15] S. J. Tan, L. Zhang, D. Zhu, X. M. Goh, Y. M. Wang, K. Kumar, C.-W. Qiu, and J. K. W. Yang. "Plasmonic Color Palettes for Photorealistic Printing with Aluminum Nanostructures". *Nano Letters* 14.7 (July 9, 2014), pp. 4023–4029.

[16] K. Dopf, C. Moosmann, S. W. Kettlitz, P. M. Schwab, K. Ilin, M. Siegel, U. Lemmer, and H.-J. Eisler. "Coupled T-Shaped Optical Antennas with Two Resonances Localized in a Common Nanogap". *ACS Photonics* 2.11 (Nov. 18, 2015), pp. 1644–1651.

[17] L. Duempelmann, D. Casari, A. Luu-Dinh, B. Gallinet, and L. Novotny. "Color Rendering Plasmonic Aluminum Substrates with Angular Symmetry Breaking". *ACS Nano* 9.12 (Dec. 22, 2015), pp. 12383–12391.

[18] G. Wang, X. Chen, S. Liu, C. Wong, and S. Chu. "Mechanical Chameleon through Dynamic Real-Time Plasmonic Tuning". *ACS Nano* 10.2 (Feb. 23, 2016), pp. 1788–1794.

[19] L. Duempelmann, A. Luu-Dinh, B. Gallinet, and L. Novotny. "Four-Fold Color Filter Based on Plasmonic Phase Retarder". *ACS Photonics* 3.2 (Feb. 17, 2016), pp. 190–196.

[20] H. Aouani, H. Šípová, M. Rahmani, M. Navarro-Cia, K. Hegnerová, J. Homola, M. Hong, and S. A. Maier. "Ultrasensitive Broadband Probing of Molecular Vibrational Modes with Multifrequency Optical Antennas". *ACS Nano* 7.1 (Jan. 22, 2013), pp. 669–675.

[21] P. Biagioni, J. S. Huang, L. Duò, M. Finazzi, and B. Hecht. "Cross Resonant Optical Antenna". *Physical Review Letters* 102.25 (June 22, 2009), p. 256801.

[22] Z. Gao and Z.-Y. Wang. "Terahertz Plasmonic Cross Resonant Antenna". *Journal of Electromagnetic Waves and Applications* 25.11 (Jan. 1, 2011), pp. 1730–1739.

[23] J. Yang and J. Zhang. "Nano-polarization-converter based on magnetic plasmon resonance excitation in an L-shaped slot antenna". *Optics Express* 21.7 (Apr. 8, 2013), p. 7934.

[24] L.-J. Black, Y. Wang, C. H. de Groot, A. Arbouet, and O. L. Muskens. "Optimal Polarization Conversion in Coupled Dimer Plasmonic Nanoantennas for Metasurfaces". *ACS Nano* 8.6 (June 24, 2014), pp. 6390–6399.

[25] B. Gallinet and O. J. F. Martin. "Refractive Index Sensing with Subradiant Modes: A Framework To Reduce Losses in Plasmonic Nanostructures". *ACS Nano* 7.8 (Aug. 27, 2013), pp. 6978–6987.

[26] A. G. Curto, T. H. Taminiau, G. Volpe, M. P. Kreuzer, R. Quidant, and N. F. van Hulst. "Multipolar radiation of quantum emitters with nanowire optical antennas". *Nature Communications* 4 (Apr. 23, 2013), p. 1750.

[27] V. K. Valev, J. J. Baumberg, C. Sibilia, and T. Verbiest. "Chirality and Chiroptical Effects in Plasmonic Nanostructures: Fundamentals, Recent Progress, and Outlook". *Advanced Materials* 25.18 (May 14, 2013), pp. 2517–2534.

[28] M. Schnell, P. Sarriugarte, T. Neuman, A. B. Khanikaev, G. Shvets, J. Aizpurua, and R. Hillenbrand. "Real-Space Mapping of the Chiral Near-Field Distributions in Spiral Antennas and Planar Metasurfaces". *Nano Letters* 16.1 (Jan. 13, 2016), pp. 663–670.

[29] V. E. Ferry, M. Hentschel, and A. P. Alivisatos. "Circular Dichroism in Off-Resonantly Coupled Plasmonic Nanosystems". *Nano Letters* 15.12 (Dec. 9, 2015), pp. 8336–8341.

[30] T. Coenen, E. J. R. Vesseur, A. Polman, and A. F. Koenderink. "Directional Emission from Plasmonic Yagi–Uda Antennas Probed by Angle-Resolved Cathodoluminescence Spectroscopy". *Nano Letters* 11.9 (Sept. 14, 2011), pp. 3779–3784.

[31] D. Vercruysse, Y. Sonnefraud, N. Verellen, F. B. Fuchs, G. Di Martino, L. Lagae, V. V. Moshchalkov, S. A. Maier, and P. Van Dorpe. "Unidirectional Side Scattering of Light by a Single-Element Nanoantenna". *Nano Letters* 13.8 (Aug. 14, 2013), pp. 3843–3849.

[32] D. Vercruysse, X. Zheng, Y. Sonnefraud, N. Verellen, G. Di Martino, L. Lagae, G. A. E. Vandenbosch, V. V. Moshchalkov, S. A. Maier, and P. Van Dorpe. "Directional Fluorescence Emission by Individual V-Antennas Explained by Mode Expansion". *ACS Nano* 8.8 (Aug. 26, 2014), pp. 8232–8241.

[33] I. M. Hancu, A. G. Curto, M. Castro-López, M. Kuttge, and N. F. van Hulst. "Multipolar Interference for Directed Light Emission". *Nano Letters* 14.1 (Jan. 8, 2014), pp. 166–171.

[34] K. Lindfors, D. Dregely, M. Lippitz, N. Engheta, M. Totzeck, and H. Giessen. "Imaging and Steering Unidirectional Emission from Nanoantenna Array Metasurfaces". *ACS Photonics* 3.2 (Feb. 17, 2016), pp. 286–292.

[35] R. Verre, M. Svedendahl, N. O. Länk, Z. J. Yang, G. Zengin, T. J. Antosiewicz, and M. Käll. "Directional Light Extinction and Emission in a Metasurface of Tilted Plasmonic Nanopillars". *Nano Letters* 16.1 (Jan. 13, 2016), pp. 98–104.

[36] N. Bonod, A. Devilez, B. Rolly, S. Bidault, and B. Stout. "Ultracompact and unidirectional metallic antennas". *Physical Review B* 82.11 (Sept. 16, 2010), p. 115429.

[37] T. Shegai, S. Chen, V. D. Miljković, G. Zengin, P. Johansson, and M. Käll. "A bimetallic nanoantenna for directional colour routing". *Nature Communications* 2 (Sept. 20, 2011), p. 481.

[38] P. Ghenuche, S. Cherukulappurath, T. H. Taminiau, N. F. van Hulst, and R. Quidant. "Spectroscopic Mode Mapping of Resonant Plasmon Nanoantennas". *Physical Review Letters* 101.11 (Sept. 9, 2008), p. 116805.

[39] S. Viarbitskaya, A. Teulle, A. Cuche, J. Sharma, C. Girard, E. Dujardin, and A. Arbouet. "Morphology-induced redistribution of surface plasmon modes in two-dimensional crystalline gold platelets". *Applied Physics Letters* 103.13 (Sept. 23, 2013), p. 131112.

[40] S. Viarbitskaya, A. Teulle, R. Marty, J. Sharma, C. Girard, A. Arbouet, and E. Dujardin. "Tailoring and imaging the plasmonic local density of states in crystalline nanoprisms". *Nature Materials* 12.5 (May 2013), pp. 426–432.

[41] N. Verellen, D. Denkova, B. D. Clercq, A. V. Silhanek, M. Ameloot, P. V. Dorpe, and V. V. Moshchalkov. "Two-Photon Luminescence of Gold Nanorods Mediated by Higher Order Plasmon Modes". *ACS Photonics* 2.3 (Mar. 18, 2015), pp. 410–416.

[42] D. Rossouw and G. A. Botton. "Plasmonic Response of Bent Silver Nanowires for Nanophotonic Subwavelength Waveguiding". *Physical Review Letters* 110.6 (Feb. 6, 2013), p. 066801.

[43] R. Marty, A. Arbouet, C. Girard, A. Mlayah, V. Paillard, V. K. Lin, S. L. Teo, and S. Tripathy. "Damping of the Acoustic Vibrations of Individual Gold Nanoparticles". *Nano Letters* 11.8 (Aug. 10, 2011), pp. 3301–3306.

[44] F. Della Picca, R. Berte, M. Rahmani, P. Albella, J. M. Bujjamer, M. Poblet, E. Cortés, S. A. Maier, and A. V. Bragas. "Tailored Hypersound Generation in Single Plasmonic Nanoantennas". *Nano Letters* 16.2 (Feb. 10, 2016), pp. 1428–1434.

[45] R. Zia, J. A. Schuller, A. Chandran, and M. L. Brongersma. "Plasmonics: the next chip-scale technology". *Materials Today* 9.7 (July 2006), pp. 20–27.

[46] N. Pleros, E. E. Kriezis, and K. Vyrsokinos. "Optical Interconnects Using Plasmonics and Si-Photonics". *IEEE Photonics Journal* 3.2 (Apr. 2011), pp. 296–301.

[47] B. Pettinger, K. Krischer, and G. Ertl. "Giant raman scattering cross section for an adsorbed dye at ag colloids associated with low EM field enhancement". *Chemical Physics Letters* 151.1 (Oct. 7, 1988), pp. 151–155.

[48] J. N. Farahani, D. W. Pohl, H.-J. Eisler, and B. Hecht. "Single Quantum Dot Coupled to a Scanning Optical Antenna: A Tunable Superemitter". *Physical Review Letters* 95.1 (June 28, 2005), p. 017402.

[49] K. Kneipp, M. Moskovits, and H. Kneipp, eds. *Surface-Enhanced Raman Scattering*. Vol. 103. Topics in Applied Physics. Springer Berlin Heidelberg, 2006. ISBN: 978-3-540-33566-5.

[50] Y. Hong, Y.-M. Huh, D. S. Yoon, J. Yang, Y. Hong, Y.-M. Huh, D. S. Yoon, and J. Yang. "Nanobiosensors Based on Localized Surface Plasmon Resonance for Biomarker Detection, Nanobiosensors Based on Localized Surface Plasmon Resonance for Biomarker Detection". *Journal of Nanomaterials, Journal of Nanomaterials* 2012, 2012 (Oct. 10, 2012), e759830.

[51] S. Kumar. "Plasmonic nanoparticles for imaging intracellular biomarkers". PhD thesis. Biomedical Engineering Department: University of Texas at Austin, USA, June 2007.

[52] P. M. Kosaka, V. Pini, J. J. Ruz, R. A. d. Silva, M. U. González, D. Ramos, M. Calleja, and J. Tamayo. "Detection of cancer biomarkers in serum using a hybrid mechanical and optoplasmonic nanosensor". *Nature Nanotechnology* 9.12 (Dec. 2014), pp. 1047–1053.

[53] S. Lal, S. E. Clare, and N. J. Halas. "Nanoshell-Enabled Photothermal Cancer Therapy: Impending Clinical Impact". *Accounts of Chemical Research* 41.12 (Dec. 16, 2008), pp. 1842–1851.

[54] S. Kessentini, D. Barchiesi, T. Grosges, and M. Lamy de la Chapelle. "Particle swarm optimization and evolutionary methods for plasmonic biomedical applications". In: *2011 IEEE Congress on Evolutionary Computation (CEC)*. June 2011, pp. 2315–2320.

[55] P. Ghosh, G. Han, M. De, C. K. Kim, and V. M. Rotello. "Gold nanoparticles in delivery applications". *Advanced Drug Delivery Reviews*. Inorganic Nanoparticles in Drug Delivery 60.11 (Aug. 17, 2008), pp. 1307–1315.

[56] K. Chen, G. Razinskas, T. Feichtner, S. Grossmann, S. Christiansen, and B. Hecht. "Electromechanically Tunable Suspended Optical Nanoantenna". *Nano Letters* 16.4 (Apr. 13, 2016), pp. 2680–2685.

[57] R. Thijssen, E. Verhagen, T. J. Kippenberg, and A. Polman. "Plasmon Nanomechanical Coupling for Nanoscale Transduction". *Nano Letters* 13.7 (July 10, 2013), pp. 3293–3297.

[58] R. Thijssen, T. J. Kippenberg, A. Polman, and E. Verhagen. “Plasmomechanical Resonators Based on Dimer Nanoantennas”. *Nano Letters* 15.6 (June 10, 2015), pp. 3971–3976.

[59] A. Devilez, X. Zambrana-Puyalto, B. Stout, and N. Bonod. “Mimicking localized surface plasmons with dielectric particles”. *Physical Review B* 92.24 (Dec. 28, 2015), p. 241412.

[60] C. Della Giovampaola and N. Engheta. “Plasmonics without negative dielectrics”. *Physical Review B* 93.19 (May 24, 2016), p. 195152.

[61] G.-H. Ding, C. T. Chan, Z. Q. Zhang, and P. Sheng. “Resonance-enhanced optical annealing of silicon nanowires”. *Physical Review B* 71.20 (May 2, 2005), p. 205302.

[62] L. Cao, B. Nabet, and J. E. Spanier. “Enhanced Raman Scattering from Individual Semiconductor Nanocones and Nanowires”. *Physical Review Letters* 96.15 (Apr. 18, 2006), p. 157402.

[63] L. Cao, P. Fan, E. S. Barnard, A. M. Brown, and M. L. Brongersma. “Tuning the Color of Silicon Nanostructures”. *Nano Letters* 10.7 (July 14, 2010), pp. 2649–2654.

[64] L. Cao, P. Fan, A. P. Vasudev, J. S. White, Z. Yu, W. Cai, J. A. Schuller, S. Fan, and M. L. Brongersma. “Semiconductor Nanowire Optical Antenna Solar Absorbers”. *Nano Letters* 10.2 (Feb. 10, 2010), pp. 439–445.

[65] H. Kallel, A. Arbouet, G. BenAssayag, A. Chehaidar, A. Potié, B. Salem, T. Baron, and V. Paillard. “Tunable enhancement of light absorption and scattering in Si(1-x)Ge(x) nanowires”. *Physical Review B* 86.8 (Aug. 22, 2012), p. 085318.

[66] H. Kallel, A. Arbouet, M. Carrada, G. Ben Assayag, A. Chehaidar, P. Periwal, T. Baron, P. Normand, and V. Paillard. “Photoluminescence enhancement of silicon nanocrystals placed in the near field of a silicon nanowire”. *Physical Review B* 88.8 (Aug. 13, 2013), p. 081302.

[67] R. Paniagua-Domínguez, G. Grzela, J. G. Rivas, and J. A. Sánchez-Gil. “Enhanced and directional emission of semiconductor nanowires tailored through leaky/guided modes”. *Nanoscale* 5.21 (Oct. 10, 2013), pp. 10582–10590.

[68] J. Wang, M. S. Gudiksen, X. Duan, Y. Cui, and C. M. Lieber. “Highly Polarized Photoluminescence and Photodetection from Single Indium Phosphide Nanowires”. *Science* 293.5534 (Aug. 24, 2001), pp. 1455–1457.

[69] D. J. Traviss, M. K. Schmidt, J. Aizpurua, and O. L. Muskens. “Antenna resonances in low aspect ratio semiconductor nanowires”. *Optics Express* 23.17 (Aug. 24, 2015), p. 22771.

[70] H.-S. Ee, J.-H. Kang, M. L. Brongersma, and M.-K. Seo. “Shape-Dependent Light Scattering Properties of Subwavelength Silicon Nanoblocks”. *Nano Letters* 15.3 (2015), pp. 1759–1765.

[71] K. Seo, M. Wober, P. Steinvurzel, E. Schonbrun, Y. Dan, T. Ellenbogen, and K. B. Crozier. “Multicolored Vertical Silicon Nanowires”. *Nano Letters* 11.4 (Apr. 13, 2011), pp. 1851–1856.

[72] A. I. Kuznetsov, A. E. Miroshnichenko, Y. H. Fu, J. Zhang, and B. Luk’yanchuk. “Magnetic light”. *Scientific Reports* 2 (July 4, 2012), p. 492.

[73] T. G. Habteyes, I. Staude, K. E. Chong, J. Dominguez, M. Decker, A. Miroshnichenko, Y. Kivshar, and I. Brener. “Near-Field Mapping of Optical Modes on All-Dielectric Silicon Nanodisks”. *ACS Photonics* 1.9 (Sept. 17, 2014), pp. 794–798.

[74] M. A. van de Haar, J. van de Groep, B. J. Brenny, and A. Polman. "Controlling magnetic and electric dipole modes in hollow silicon nanocylinders". *Optics Express* 24.3 (Feb. 8, 2016), p. 2047.

[75] P. Albella, R. Alcaraz de la Osa, F. Moreno, and S. A. Maier. "Electric and Magnetic Field Enhancement with Ultralow Heat Radiation Dielectric Nanoantennas: Considerations for Surface-Enhanced Spectroscopies". *ACS Photonics* 1.6 (June 18, 2014), pp. 524–529.

[76] R. M. Bakker, D. Permyakov, Y. F. Yu, D. Markovich, R. Paniagua-Domínguez, L. Gonzaga, A. Samusev, Y. Kivshar, B. Luk'yanchuk, and A. I. Kuznetsov. "Magnetic and Electric Hotspots with Silicon Nanodimers". *Nano Letters* 15.3 (Mar. 11, 2015), pp. 2137–2142.

[77] J. van de Groep, T. Coenen, S. A. Mann, and A. Polman. "Direct imaging of hybridized eigenmodes in coupled silicon nanoparticles". *Optica* 3.1 (Jan. 20, 2016), p. 93.

[78] E. C. Regan, Y. Shen, J. J. Lopez, C. W. Hsu, B. Zhen, J. D. Joannopoulos, and M. Soljačić. "Substrate-Independent Light Confinement in Bioinspired All-Dielectric Surface Resonators". *ACS Photonics* 3.4 (Apr. 20, 2016), pp. 532–536.

[79] Y. Yu and L. Cao. "Leaky mode engineering: A general design principle for dielectric optical antenna solar absorbers". *Optics Communications*. Energy efficient nanophotonics: Engineered light–matter interaction in sub-wavelength structures 314 (Mar. 1, 2014), pp. 79–85.

[80] S.-K. Kim, K.-D. Song, T. J. Kempa, R. W. Day, C. M. Lieber, and H.-G. Park. "Design of Nanowire Optical Cavities as Efficient Photon Absorbers". *ACS Nano* 8.4 (Apr. 22, 2014), pp. 3707–3714.

[81] H. Kallel, A. Chehaidar, A. Arbouet, and V. Paillard. "Enhanced absorption of solar light in Ge/Si core-sheath nanowires compared to Si/Ge core-sheath and Si1–xGex nanowires: A theoretical study". *Journal of Applied Physics* 114.22 (Dec. 13, 2013), p. 224312.

[82] L. Tong, J. Lou, and E. Mazur. "Single-mode guiding properties of subwavelength-diameter silica and silicon wire waveguides". *Optics Express* 12.6 (Mar. 22, 2004), pp. 1025–1035.

[83] R. Dubé-Demers, S. LaRochelle, and W. Shi. "Ultrafast pulse-amplitude modulation with a femtojoule silicon photonic modulator". *Optica* 3.6 (June 2016), pp. 622–627.

[84] H. Kim, A. C. Farrell, P. Senanayake, W.-J. Lee, and D. L. Huffaker. "Monolithically Integrated InGaAs Nanowires on 3D Structured Silicon-on-Insulator as a New Platform for Full Optical Links". *Nano Letters* 16.3 (Mar. 9, 2016), pp. 1833–1839.

[85] T. Huber, A. Predojević, M. Khoshnegar, D. Dalacu, P. J. Poole, H. Majedi, and G. Weihs. "Polarization Entangled Photons from Quantum Dots Embedded in Nanowires". *Nano Letters* 14.12 (Dec. 10, 2014), pp. 7107–7114.

[86] R. Röder, T. P. H. Sidiropoulos, C. Tessarek, S. Christiansen, R. F. Oulton, and C. Ronning. "Ultrafast Dynamics of Lasing Semiconductor Nanowires". *Nano Letters* 15.7 (July 8, 2015), pp. 4637–4643.

[87] R. Röder, T. P. H. Sidiropoulos, R. Buschlinger, M. Riediger, U. Peschel, R. F. Oulton, and C. Ronning. "Mode Switching and Filtering in Nanowire Lasers". *Nano Letters* 16.4 (Apr. 13, 2016), pp. 2878–2884.

[88] J. Petersen, J. Volz, and A. Rauschenbeutel. "Chiral nanophotonic waveguide interface based on spin-orbit interaction of light". *Science* (Sept. 4, 2014), p. 1257671.

[89] B. Rolly, B. Stout, and N. Bonod. "Boosting the directivity of optical antennas with magnetic and electric dipolar resonant particles". *Optics Express* 20.18 (Aug. 27, 2012), p. 20376.

[90] I. Staude, A. E. Miroshnichenko, M. Decker, N. T. Fofang, S. Liu, E. Gonzales, J. Dominguez, T. S. Luk, D. N. Neshev, I. Brener, and Y. Kivshar. "Tailoring Directional Scattering through Magnetic and Electric Resonances in Subwavelength Silicon Nanodisks". *ACS Nano* 7.9 (Sept. 24, 2013), pp. 7824–7832.

[91] Y. H. Fu, A. I. Kuznetsov, A. E. Miroshnichenko, Y. F. Yu, and B. Luk'yanchuk. "Directional visible light scattering by silicon nanoparticles". *Nature Communications* 4 (Feb. 26, 2013), p. 1527.

[92] Y. Yang, Q. Li, and M. Qiu. "Controlling the angular radiation of single emitters using dielectric patch nanoantennas". *Applied Physics Letters* 107.3 (July 20, 2015), p. 031109.

[93] P. Albella, T. Shibanuma, and S. A. Maier. "Switchable directional scattering of electromagnetic radiation with subwavelength asymmetric silicon dimers". *Scientific Reports* 5 (Dec. 10, 2015), p. 18322.

[94] M. L. Brongersma, Y. Cui, and S. Fan. "Light management for photovoltaics using high-index nanostructures". *Nature Materials* 13.5 (May 2014), pp. 451–460.

[95] P. Spinelli and A. Polman. "Light Trapping in Thin Crystalline Si Solar Cells Using Surface Mie Scatterers". *IEEE Journal of Photovoltaics* 4.2 (Mar. 2014), pp. 554–559.

[96] F. Priolo, T. Gregorkiewicz, M. Galli, and T. F. Krauss. "Silicon nanostructures for photonics and photovoltaics". *Nature Nanotechnology* 9.1 (Jan. 2014), pp. 19–32.

[97] Y. Li, M. Li, R. Li, P. Fu, L. Chu, and D. Song. "Method to determine the optimal silicon nanowire length for photovoltaic devices". *Applied Physics Letters* 106.9 (Mar. 2, 2015), p. 091908.

[98] S. M. Wells, I. A. Merkulov, I. I. Kravchenko, N. V. Lavrik, and M. J. Sepaniak. "Silicon Nanopillars for Field-Enhanced Surface Spectroscopy". *ACS Nano* 6.4 (Apr. 24, 2012), pp. 2948–2959.

[99] P. Albella, M. A. Poyli, M. K. Schmidt, S. A. Maier, F. Moreno, J. J. Sáenz, and J. Aizpurua. "Low-Loss Electric and Magnetic Field-Enhanced Spectroscopy with Subwavelength Silicon Dimers". *The Journal of Physical Chemistry C* 117.26 (July 3, 2013), pp. 13573–13584.

[100] F. Capolino. *Theory and Phenomena of Metamaterials*. Metamaterials Handbook. CRC Press, 2009. ISBN: 978-1-4200-5426-2.

[101] N. Meinzer, W. L. Barnes, and I. R. Hooper. "Plasmonic meta-atoms and metasurfaces". *Nature Photonics* 8.12 (Dec. 2014), pp. 889–898.

[102] Q. Zhao, J. Zhou, F. Zhang, and D. Lippens. "Mie resonance-based dielectric metamaterials". *Materials Today* 12.12 (Dec. 2009), pp. 60–69.

[103] S. Jahani and Z. Jacob. "All-dielectric metamaterials". *Nature Nanotechnology* 11.1 (Jan. 2016), pp. 23–36.

[104] M. Niraula, J. W. Yoon, and R. Magnusson. "Single-layer optical bandpass filter technology". *Optics Letters* 40.21 (Nov. 1, 2015), p. 5062.

[105] W. Zhao, B. Liu, H. Jiang, J. Song, Y. Pei, and Y. Jiang. "Full-color hologram using spatial multiplexing of dielectric metasurface". *Optics Letters* 41.1 (Jan. 1, 2016), p. 147.

[106] S. J. Kim, J. Park, M. Esfandyarpour, E. F. Pecora, P. G. Kik, and M. L. Brongersma. "Superabsorbing, Artificial Metal Films Constructed from Semiconductor Nanoantennas". *Nano Letters* 16.6 (June 8, 2016), pp. 3801–3808.

[107] J. Xiang, J. Li, H. Li, C. Zhang, Q. Dai, S. Tie, and S. Lan. "Polarization beam splitters, converters and analyzers based on a metasurface composed of regularly arranged silicon nanospheres with controllable coupling strength". *Optics Express* 24.11 (May 30, 2016), p. 11420.

[108] P. Gutruf, C. Zou, W. Withayachumnankul, M. Bhaskaran, S. Sriram, and C. Fumeaux. "Mechanically Tunable Dielectric Resonator Metasurfaces at Visible Frequencies". *ACS Nano* 10.1 (Jan. 26, 2016), pp. 133–141.

[109] Y. Yang, W. Wang, P. Moitra, I. I. Kravchenko, D. P. Briggs, and J. Valentine. "Dielectric Meta-Reflectarray for Broadband Linear Polarization Conversion and Optical Vortex Generation". *Nano Letters* 14.3 (Mar. 12, 2014), pp. 1394–1399.

[110] J. W. Yoon, K. J. Lee, and R. Magnusson. "Ultra-sparse dielectric nanowire grids as wideband reflectors and polarizers". *Optics Express* 23.22 (Nov. 2, 2015), p. 28849.

[111] B. S. Luk'yanchuk, N. V. Voshchinnikov, R. Paniagua-Domínguez, and A. I. Kuznetsov. "Optimum Forward Light Scattering by Spherical and Spheroidal Dielectric Nanoparticles with High Refractive Index". *ACS Photonics* 2.7 (July 15, 2015), pp. 993–999.

[112] Y. F. Yu, A. Y. Zhu, R. Paniagua-Domínguez, Y. H. Fu, B. Luk'yanchuk, and A. I. Kuznetsov. "High-transmission dielectric metasurface with 2pi phase control at visible wavelengths". *Laser & Photonics Reviews* 9.4 (July 1, 2015), pp. 412–418.

[113] Y. Yang, I. I. Kravchenko, D. P. Briggs, and J. Valentine. "All-dielectric metasurface analogue of electromagnetically induced transparency". *Nature Communications* 5 (Dec. 16, 2014), p. 5753.

[114] A. Arbabi, Y. Horie, M. Bagheri, and A. Faraon. "Dielectric metasurfaces for complete control of phase and polarization with subwavelength spatial resolution and high transmission". *Nature Nanotechnology* 10.11 (Nov. 2015), pp. 937–943.

[115] F. Zhang, H. Yu, J. Fang, M. Zhang, S. Chen, J. Wang, A. He, and J. Chen. "Efficient generation and tight focusing of radially polarized beam from linearly polarized beam with all-dielectric metasurface". *Optics Express* 24.6 (Mar. 21, 2016), p. 6656.

[116] R. Paniagua-Domínguez, Y. F. Yu, A. E. Miroshnichenko, L. A. Krivitsky, Y. H. Fu, V. Valuckas, L. Gonzaga, Y. T. Toh, A. Y. S. Kay, B. Luk'yanchuk, and A. I. Kuznetsov. "Generalized Brewster effect in dielectric metasurfaces". *Nature Communications* 7 (Jan. 19, 2016), p. 10362.

[117] H. Huang, H. Li, W. Li, A. Wu, X. Chen, X. Zhu, Z. Sheng, S. Zou, X. Wang, and F. Gan. "High-Efficiency Vertical Light Emission through a Compact Silicon Nanoantenna Array". *ACS Photonics* 3.3 (Mar. 16, 2016), pp. 324–328.

[118] W. Cai, U. K. Chettiar, A. V. Kildishev, and V. M. Shalaev. "Designs for optical cloaking with high-order transformations". *Optics Express* 16.8 (Apr. 14, 2008), p. 5444.

[119] J. B. Pendry, D. Schurig, and D. R. Smith. "Controlling Electromagnetic Fields". *Science* 312.5781 (June 23, 2006), pp. 1780–1782.

[120] F. Monticone and A. Alù. "Invisibility exposed: physical bounds on passive cloaking". *Optica* 3.7 (July 20, 2016), p. 718.

[121] X. Cartoixà, L. Colombo, and R. Rurali. "Thermal Rectification by Design in Telescopic Si Nanowires". *Nano Letters* 15.12 (Dec. 9, 2015), pp. 8255–8259.

[122] J. Lim, H.-T. Wang, J. Tang, S. C. Andrews, H. So, J. Lee, D. H. Lee, T. P. Russell, and P. Yang. "Simultaneous Thermoelectric Property Measurement and Incoherent Phonon Transport in Holey Silicon". *ACS Nano* 10.1 (Jan. 26, 2016), pp. 124–132.

[123] J. D. Christesen, C. W. Pinion, E. M. Grumstrup, J. M. Papanikolas, and J. F. Cahoon. "Synthetically Encoding 10 nm Morphology in Silicon Nanowires". *Nano Letters* 13.12 (Dec. 11, 2013), pp. 6281–6286.

[124] K. M. McPeak, S. V. Jayanti, S. J. P. Kress, S. Meyer, S. Iotti, A. Rossinelli, and D. J. Norris. "Plasmonic Films Can Easily Be Better: Rules and Recipes". *ACS Photonics* 2.3 (Mar. 18, 2015), pp. 326–333.

[125] X. Lu, M. Rycenga, S. E. Skrabalak, B. Wiley, and Y. Xia. "Chemical Synthesis of Novel Plasmonic Nanoparticles". *Annual Review of Physical Chemistry* 60.1 (2009), pp. 167–192.

[126] A. Henkel, O. Schubert, A. Plech, and C. Sönnichsen. "Growth Kinetic of a Rod-Shaped Metal Nanocrystal". *The Journal of Physical Chemistry C* 113.24 (June 18, 2009), pp. 10390–10394.

[127] P. Zijlstra and M. Orrit. "Single metal nanoparticles: optical detection, spectroscopy and applications". *Reports on Progress in Physics* 74.10 (Oct. 1, 2011), p. 106401.

[128] R. Jiang, F. Qin, Y. Liu, X. Y. Ling, J. Guo, M. Tang, S. Cheng, and J. Wang. "Colloidal Gold Nanocups with Orientation-Dependent Plasmonic Properties". *Advanced Materials* (May 1, 2016), n/a–n/a.

[129] F. N. Gür, F. W. Schwarz, J. Ye, S. Diez, and T. L. Schmidt. "Toward Self-Assembled Plasmonic Devices: High-Yield Arrangement of Gold Nanoparticles on DNA Origami Templates". *ACS Nano* 10.5 (May 24, 2016), pp. 5374–5382.

[130] A. Tsargorodska, O. El Zubir, B. Darroch, M. L. Cartron, T. Basova, C. N. Hunter, A. V. Nabok, and G. J. Leggett. "Fast, Simple, Combinatorial Routes to the Fabrication of Reusable, Plasmonically Active Gold Nanostructures by Interferometric Lithography of Self-Assembled Monolayers". *ACS Nano* 8.8 (Aug. 26, 2014), pp. 7858–7869.

[131] Y. Cui, L. J. Lauhon, M. S. Gudiksen, J. Wang, and C. M. Lieber. "Diameter-controlled synthesis of single-crystal silicon nanowires". *Applied Physics Letters* 78.15 (Apr. 9, 2001), pp. 2214–2216.

[132] C. Hu. "SOI (Silicon-On-Insulator) for High Speed Ultra Large Scale Integration". *Japanese Journal of Applied Physics* 33 (Part 1, No. 1B Jan. 30, 1994), pp. 365–369.

[133] M. Bruel, B. Aspar, and A.-J. Auberton-Hervé. "Smart-Cut: A New Silicon On Insulator Material Technology Based on Hydrogen Implantation and Wafer Bonding [*1]". *Japanese Journal of Applied Physics* 36 (Part 1, No. 3B Mar. 30, 1997), pp. 1636–1641.

[134] G. Baffou, R. Quidant, and C. Girard. "Heat generation in plasmonic nanostructures: Influence of morphology". *Applied Physics Letters* 94.15 (Apr. 13, 2009), p. 153109.

[135] A. Devilez, N. Bonod, J. Wenger, D. Gérard, B. Stout, H. Rigneault, and E. Popov. "Three-dimensional subwavelength confinement of light with dielectric microspheres". *Optics Express* 17.4 (Feb. 16, 2009), p. 2089.

[136] D. Gérard, J. Wenger, A. Devilez, D. Gachet, B. Stout, N. Bonod, E. Popov, and H. Rigneault. "Strong electromagnetic confinement near dielectric microspheres to enhance single-molecule fluorescence". *Optics Express* 16.19 (Sept. 15, 2008), p. 15297.

[137] A. García-Etxarri, R. Gómez-Medina, L. S. Froufe-Pérez, C. López, L. Chantada, F. Scheffold, J. Aizpurua, M. Nieto-Vesperinas, and J. J. Sáenz. "Strong magnetic response of submicron Silicon particles in the infrared". *Optics Express* 19.6 (Mar. 14, 2011), p. 4815.

[138] J. C. Ginn, I. Brener, D. W. Peters, J. R. Wendt, J. O. Stevens, P. F. Hines, L. I. Basilio, L. K. Warne, J. F. Ihlefeld, P. G. Clem, and M. B. Sinclair. "Realizing Optical Magnetism from Dielectric Metamaterials". *Physical Review Letters* 108.9 (Feb. 29, 2012), p. 097402.

[139] A. B. Evlyukhin, S. M. Novikov, U. Zywietz, R. L. Eriksen, C. Reinhardt, S. I. Bozhevolnyi, and B. N. Chichkov. "Demonstration of Magnetic Dipole Resonances of Dielectric Nanospheres in the Visible Region". *Nano Letters* 12.7 (July 11, 2012), pp. 3749–3755.

[140] M. K. Schmidt, R. Esteban, J. J. Sáenz, I. Suárez-Lacalle, S. Mackowski, and J. Aizpurua. "Dielectric antennas - a suitable platform for controlling magnetic dipolar emission". *Optics Express* 20.13 (June 18, 2012), p. 13636.

[141] F. Shafiei, F. Monticone, K. Q. Le, X.-X. Liu, T. Hartsfield, A. Alù, and X. Li. "A subwavelength plasmonic metamolecule exhibiting magnetic-based optical Fano resonance". *Nature Nanotechnology* 8.2 (Feb. 2013), pp. 95–99.

[142] C. Enkrich, M. Wegener, S. Linden, S. Burger, L. Zschiedrich, F. Schmidt, J. F. Zhou, T. Koschny, and C. M. Soukoulis. "Magnetic Metamaterials at Telecommunication and Visible Frequencies". *Physical Review Letters* 95.20 (Nov. 7, 2005), p. 203901.

[143] B. Rolly, B. Bebey, S. Bidault, B. Stout, and N. Bonod. "Promoting magnetic dipolar transition in trivalent lanthanide ions with lossless Mie resonances". *Physical Review B* 85.24 (June 18, 2012), p. 245432.

[144] M. Kerker, D.-S. Wang, and C. L. Giles. "Electromagnetic scattering by magnetic spheres". *Journal of the Optical Society of America* 73.6 (June 1, 1983), p. 765.

[145] X. Zambrana-Puyalto, I. Fernandez-Corbaton, M. L. Juan, X. Vidal, and G. Molina-Terriza. "Duality symmetry and Kerker conditions". *Optics Letters* 38.11 (June 1, 2013), p. 1857.

[146] J. van de Groep and A. Polman. "Designing dielectric resonators on substrates: Combining magnetic and electric resonances". *Optics Express* 21.22 (Nov. 4, 2013), pp. 26285–26302.

[147] S. Campione, L. I. Basilio, L. K. Warne, and M. B. Sinclair. "Tailoring dielectric resonator geometries for directional scattering and Huygens' metasurfaces". *Optics Express* 23.3 (Feb. 9, 2015), p. 2293.

[148] G. Boudarham, R. Abdeddaim, and N. Bonod. "Enhancing the magnetic field intensity with a dielectric gap antenna". *Applied Physics Letters* 104.2 (Jan. 13, 2014), p. 021117.

[149] Z. Ma, S. M. Hanham, P. Albella, B. Ng, H. T. Lu, Y. Gong, S. A. Maier, and M. Hong. "Terahertz All-Dielectric Magnetic Mirror Metasurfaces". *ACS Photonics* 3.6 (June 15, 2016), pp. 1010–1018.

[150] Z.-J. Yang, T. J. Antosiewicz, R. Verre, F. J. García de Abajo, S. P. Apell, and M. Käll. "Ultimate Limit of Light Extinction by Nanophotonic Structures". *Nano Letters* 15.11 (Nov. 11, 2015), pp. 7633–7638.

[151] A. B. Evlyukhin and S. I. Bozhevolnyi. "Resonant unidirectional and elastic scattering of surface plasmon polaritons by high refractive index dielectric nanoparticles". *Physical Review B* 92.24 (Dec. 14, 2015), p. 245419.

[152] M. Castro-Lopez, N. de Sousa, A. Garcia-Martin, F. Y. Gardes, and R. Sapienza. "Scattering of a plasmonic nanoantenna embedded in a silicon waveguide". *Optics Express* 23.22 (Nov. 2, 2015), p. 28108.

[153] A. Casadei, E. F. Pecora, J. Trevino, C. Forestiere, D. Rüffer, E. Russo-Averchi, F. Matteini, G. Tutuncuoglu, M. Heiss, A. Fontcuberta i Morral, and L. Dal Negro. "Photonic–Plasmonic Coupling of GaAs Single Nanowires to Optical Nanoantennas". *Nano Letters* 14.5 (May 14, 2014), pp. 2271–2278.

[154] A. Casadei, E. A. Llado, F. Amaduzzi, E. Russo-Averchi, D. Rüffer, M. Heiss, L. D. Negro, and A. F. i. Morral. "Polarization response of nanowires à la carte". *Scientific Reports* 5 (Jan. 7, 2015), p. 7651.

[155] Z. Ruan and S. Fan. "Design of subwavelength superscattering nanospheres". *Applied Physics Letters* 98.4 (Jan. 24, 2011), p. 043101.

[156] Y. Han, J.-A. Huang, X.-Y. Liu, X.-J. Zhang, J.-X. Shi, and C.-C. Yan. "Polarization-independent broadband plasmonic absorber based on a silicon-nanowire array decorated by gold nanoparticles at the optical regime". *Optics Express* 24.9 (May 2, 2016), pp. 9178–9186.

[157] J. Ho, J. Tatebayashi, S. Sergent, C. F. Fong, Y. Ota, S. Iwamoto, and Y. Arakawa. "A Nanowire-Based Plasmonic Quantum Dot Laser". *Nano Letters* 16.4 (Apr. 13, 2016), pp. 2845–2850.

[158] M. Ono, E. Kuramochi, G. Zhang, H. Sumikura, Y. Harada, D. Cox, and M. Notomi. "Nanowire-nanoantenna coupled system fabricated by nanomanipulation". *Optics Express* 24.8 (Apr. 18, 2016), p. 8647.

[159] A. Tuniz and M. A. Schmidt. "Broadband efficient directional coupling to short-range plasmons: towards hybrid fiber nanotips". *Optics Express* 24.7 (Apr. 4, 2016), pp. 7507–7524.

[160] R. Guo, E. Rusak, I. Staude, J. Dominguez, M. Decker, C. Rockstuhl, I. Brener, D. N. Neshev, and Y. S. Kivshar. "Multipolar Coupling in Hybrid Metal–Dielectric Metasurfaces". *ACS Photonics* 3.3 (Mar. 16, 2016), pp. 349–353.

[161] A. Devilez, B. Stout, and N. Bonod. "Compact Metallo-Dielectric Optical Antenna for Ultra Directional and Enhanced Radiative Emission". *ACS Nano* 4.6 (June 22, 2010), pp. 3390–3396.

[162] R. Verre, Z. J. Yang, T. Shegai, and M. Käll. "Optical Magnetism and Plasmonic Fano Resonances in Metal–Insulator–Metal Oligomers". *Nano Letters* 15.3 (Mar. 11, 2015), pp. 1952–1958.

[163] V. K. Narasimhan, T. M. Hymel, R. A. Lai, and Y. Cui. "Hybrid Metal–Semiconductor Nanostructure for Ultrahigh Optical Absorption and Low Electrical Resistance at Optoelectronic Interfaces". *ACS Nano* 9.11 (Nov. 24, 2015), pp. 10590–10597.

[164] P. A. Franken, A. E. Hill, C. W. Peters, and G. Weinreich. "Generation of Optical Harmonics". *Physical Review Letters* 7.4 (Aug. 15, 1961), pp. 118–119.

[165] J. A. Giordmaine and R. C. Miller. "Tunable Coherent Parametric Oscillation in $LiNbO_3$ at Optical Frequencies". *Physical Review Letters* 14.24 (June 14, 1965), pp. 973–976.

[166] J. Hansryd and P. A. Andrekson. "Applications of fiber-based optical parametric amplifiers". In: *All-Optical Networking: Existing and Emerging Architecture and Applications/Dynamic Enablers of Next-Generation Optical Communications Systems/Fast Optical Processing in Optical Transmission/VCSEL and.* 2002, ME3–5–ME3–6.

[167] P. Biagioni, D. Brida, J.-S. Huang, J. Kern, L. Duò, B. Hecht, M. Finazzi, and G. Cerullo. "Dynamics of Four-Photon Photoluminescence in Gold Nanoantennas". *Nano Letters* 12.6 (June 13, 2012), pp. 2941–2947.

[168] X.-F. Jiang, Y. Pan, C. Jiang, T. Zhao, P. Yuan, T. Venkatesan, and Q.-H. Xu. "Excitation Nature of Two-Photon Photoluminescence of Gold Nanorods and Coupled Gold Nanoparticles Studied by Two-Pulse Emission Modulation Spectroscopy". *The Journal of Physical Chemistry Letters* 4.10 (May 16, 2013), pp. 1634–1638.

[169] T. F. Heinz. "Second Order Nonlinear Optical Effects at Surfaces and Interfaces". In: *Nonlinear surface electromagnetic phenomena.* Elsevier. H.E. Ponath and G.I. Stegeman, 1991.

[170] H. Husu, R. Siikanen, J. Mäkitalo, J. Lehtolahti, J. Laukkanen, M. Kuittinen, and M. Kauranen. "Metamaterials with Tailored Nonlinear Optical Response". *Nano Letters* 12.2 (Feb. 8, 2012), pp. 673–677.

[171] H. Aouani, M. Navarro-Cia, M. Rahmani, T. P. H. Sidiropoulos, M. Hong, R. F. Oulton, and S. A. Maier. "Multiresonant Broadband Optical Antennas As Efficient Tunable Nanosources of Second Harmonic Light". *Nano Letters* 12.9 (Sept. 12, 2012), pp. 4997–5002.

[172] K. Thyagarajan, J. Butet, and O. J. F. Martin. "Augmenting Second Harmonic Generation Using Fano Resonances in Plasmonic Systems". *Nano Letters* 13.4 (Apr. 10, 2013), pp. 1847–1851.

[173] K. O'Brien, H. Suchowski, J. Rho, A. Salandrino, B. Kante, X. Yin, and X. Zhang. "Predicting nonlinear properties of metamaterials from the linear response". *Nature Materials* 14.4 (Apr. 2015), pp. 379–383.

[174] M. Celebrano, X. Wu, M. Baselli, S. Großmann, P. Biagioni, A. Locatelli, C. De Angelis, G. Cerullo, R. Osellame, B. Hecht, L. Duò, F. Ciccacci, and M. Finazzi. "Mode matching in multiresonant plasmonic nanoantennas for enhanced second harmonic generation". *Nature Nanotechnology* 10.5 (May 2015), pp. 412–417.

[175] S.-D. Liu, E. S. P. Leong, G.-C. Li, Y. Hou, J. Deng, J. H. Teng, H. C. Ong, and D. Y. Lei. "Polarization-Independent Multiple Fano Resonances in Plasmonic Nonamers for Multimode-Matching Enhanced Multiband Second-Harmonic Generation". *ACS Nano* 10.1 (Jan. 26, 2016), pp. 1442–1453.

[176] J. Berthelot, G. Bachelier, M. Song, P. Rai, G. Colas des Francs, A. Dereux, and A. Bouhelier. "Silencing and enhancement of second-harmonic generation in optical gap antennas". *Optics Express* 20.10 (May 7, 2012), pp. 10498–10508.

[177] L.-J. Black, P. R. Wiecha, Y. Wang, C. H. de Groot, V. Paillard, C. Girard, O. L. Muskens, and A. Arbouet. "Tailoring Second-Harmonic Generation in Single L-Shaped Plasmonic Nanoantennas from the Capacitive to Conductive Coupling Regime". *ACS Photonics* 2.11 (Nov. 18, 2015), pp. 1592–1601.

[178] S. G. Rodrigo, H. Harutyunyan, and L. Novotny. "Coherent Control of Light Scattering from Nanostructured Materials by Second-Harmonic Generation". *Physical Review Letters* 110.17 (Apr. 25, 2013), p. 177405.

[179] G. Bachelier, J. Butet, I. Russier-Antoine, C. Jonin, E. Benichou, and P.-F. Brevet. "Origin of optical second-harmonic generation in spherical gold nanoparticles: Local surface and nonlocal bulk contributions". *Physical Review B* 82.23 (Dec. 1, 2010), p. 235403.

[180] A. Capretti, E. F. Pecora, C. Forestiere, L. Dal Negro, and G. Miano. "Size-dependent second-harmonic generation from gold nanoparticles". *Physical Review B* 89.12 (Mar. 11, 2014), p. 125414.

[181] P. N. Melentiev, A. E. Afanasiev, A. A. Kuzin, A. S. Baturin, and V. I. Balykin. "Giant optical nonlinearity of a single plasmonic nanostructure". *Optics Express* 21.12 (June 17, 2013), p. 13896.

[182] S. Palomba, M. Danckwerts, and L. Novotny. "Nonlinear plasmonics with gold nanoparticle antennas". *Journal of Optics A: Pure and Applied Optics* 11.11 (Nov. 1, 2009), p. 114030.

[183] H. Harutyunyan, G. Volpe, R. Quidant, and L. Novotny. "Enhancing the Nonlinear Optical Response Using Multifrequency Gold-Nanowire Antennas". *Physical Review Letters* 108.21 (May 23, 2012), p. 217403.

[184] K. Imura, T. Nagahara, and H. Okamoto. "Near-Field Two-Photon-Induced Photoluminescence from Single Gold Nanorods and Imaging of Plasmon Modes". *The Journal of Physical Chemistry B* 109.27 (July 1, 2005), pp. 13214–13220.

[185] A. Teulle, R. Marty, S. Viarbitskaya, A. Arbouet, E. Dujardin, C. Girard, and G. Colas des Francs. "Scanning optical microscopy modeling in nanoplasmonics". *Journal of the Optical Society of America B* 29.9 (Aug. 21, 2012), p. 2431.

[186] M. Kauranen and A. V. Zayats. "Nonlinear plasmonics". *Nature Photonics* 6.11 (Nov. 2012), pp. 737–748.

[187] J. Butet, P.-F. Brevet, and O. J. F. Martin. "Optical Second Harmonic Generation in Plasmonic Nanostructures: From Fundamental Principles to Advanced Applications". *ACS Nano* 13.4 (Oct. 16, 2015), pp. 10545–10562.

[188] J. B. Khurgin and G. Sun. "Plasmonic enhancement of the third order nonlinear optical phenomena: Figures of merit". *Optics Express* 21.22 (Nov. 4, 2013), pp. 27460–27480.

[189] J. Leuthold, C. Koos, and W. Freude. "Nonlinear silicon photonics". *Nature Photonics* 4.8 (Aug. 2010), pp. 535–544.

[190] B. Corcoran, C. Monat, C. Grillet, D. J. Moss, B. J. Eggleton, T. P. White, L. O'Faolain, and T. F. Krauss. "Green light emission in silicon through slow-light enhanced third-harmonic generation in photonic-crystal waveguides". *Nature Photonics* 3.4 (Apr. 2009), pp. 206–210.

[191] M. R. Shcherbakov, D. N. Neshev, B. Hopkins, A. S. Shorokhov, I. Staude, E. V. Melik-Gaykazyan, M. Decker, A. A. Ezhov, A. E. Miroshnichenko, I. Brener, A. A. Fedyanin, and Y. S. Kivshar. "Enhanced Third-Harmonic Generation in Silicon Nanoparticles Driven by Magnetic Response". *Nano Letters* 14.11 (Nov. 12, 2014), pp. 6488–6492.

[192] M. R. Shcherbakov, A. S. Shorokhov, D. N. Neshev, B. Hopkins, I. Staude, E. V. Melik-Gaykazyan, A. A. Ezhov, A. E. Miroshnichenko, I. Brener, A. A. Fedyanin, and Y. S. Kivshar. "Nonlinear Interference and Tailorable Third-Harmonic Generation from Dielectric Oligomers". *ACS Photonics* 2.5 (May 20, 2015), pp. 578–582.

[193] Y. Yang, W. Wang, A. Boulesbaa, I. I. Kravchenko, D. P. Briggs, A. Puretzky, D. Geohegan, and J. Valentine. "Nonlinear Fano-Resonant Dielectric Metasurfaces". *Nano Letters* 15.11 (Nov. 11, 2015), pp. 7388–7393.

[194] S. V. Zabotnov, M. M. Kholodov, V. A. Georgobiani, D. E. Presnov, L. A. Golovan, and P. K. Kashkarov. "Photon lifetime correlated increase of Raman scattering and third-harmonic generation in silicon nanowire arrays". *Laser Physics Letters* 13.3 (2016), p. 035902.

[195] M. Galli, D. Gerace, K. Welna, T. F. Krauss, L. O'Faolain, G. Guizzetti, and L. C. Andreani. "Low-power continuous-wave generation of visible harmonics in silicon photonic crystal nanocavities". *Optics Express* 18.25 (Dec. 6, 2010), pp. 26613–26624.

[196] L. Carletti, A. Locatelli, O. Stepanenko, G. Leo, and C. De Angelis. "Enhanced second-harmonic generation from magnetic resonance in AlGaAs nanoantennas". *Optics Express* 23.20 (Oct. 5, 2015), p. 26544.

[197] R. Grange, G. Brönstrup, M. Kiometzis, A. Sergeyev, J. Richter, C. Leiterer, W. Fritzsche, C. Gutsche, A. Lysov, W. Prost, F.-J. Tegude, T. Pertsch, A. Tünnermann, and S. Christiansen. "Far-Field Imaging for Direct Visualization of Light Interferences in GaAs Nanowires". *Nano Letters* 12.10 (Oct. 10, 2012), pp. 5412–5417.

[198] W. Liu, K. Wang, Z. Liu, G. Shen, and P. Lu. "Laterally Emitted Surface Second Harmonic Generation in a Single ZnTe Nanowire". *Nano Letters* 13.9 (Sept. 11, 2013), pp. 4224–4229.

[199] L. Carletti, A. Locatelli, D. Neshev, and C. De Angelis. "Shaping the Radiation Pattern of Second-Harmonic Generation from AlGaAs Dielectric Nanoantennas". *ACS Photonics* Article ASAP (Apr. 26, 2016).

[200] R. Sanatinia, S. Anand, and M. Swillo. "Modal Engineering of Second-Harmonic Generation in Single GaP Nanopillars". *Nano Letters* 14.9 (Sept. 10, 2014), pp. 5376–5381.

[201] J. I. Dadap, J. Shan, K. B. Eisenthal, and T. F. Heinz. "Second-Harmonic Rayleigh Scattering from a Sphere of Centrosymmetric Material". *Physical Review Letters* 83.20 (Nov. 15, 1999), pp. 4045–4048.

[202] J. I. Dadap, J. Shan, and T. F. Heinz. "Theory of optical second-harmonic generation from a sphere of centrosymmetric material: small-particle limit". *Journal of the Optical Society of America B* 21.7 (July 1, 2004), pp. 1328–1347.

[203] M. Finazzi, P. Biagioni, M. Celebrano, and L. Duò. "Selection rules for second-harmonic generation in nanoparticles". *Physical Review B* 76.12 (Sept. 13, 2007), p. 125414.

[204] J. I. Dadap. "Optical second-harmonic scattering from cylindrical particles". *Physical Review B* 78.20 (Nov. 20, 2008), p. 205322.

[205] A. G. F. de Beer, S. Roke, and J. I. Dadap. "Theory of optical second-harmonic and sum-frequency scattering from arbitrarily shaped particles". *Journal of the Optical Society of America B* 28.6 (June 1, 2011), p. 1374.

[206] B. Huo, X. Wang, S. Chang, M. Zeng, and G. Zhao. "Second harmonic generation of individual centrosymmetric sphere excited by a tightly focused beam". *Journal of the Optical Society of America B* 28.11 (Nov. 1, 2011), p. 2702.

[207] M. Khorasaninejad, M. A. Swillam, K. Pillai, and S. S. Saini. "Silicon nanowire arrays with enhanced optical properties". *Optics Letters* 37.20 (Oct. 15, 2012), pp. 4194–4196.

[208] J.-H. Zhao, Q.-D. Chen, Z.-G. Chen, G. Jia, W. Su, Y. Jiang, Z.-X. Yan, T. V. Dolgova, O. A. Aktsipetrov, and H.-B. Sun. "Enhancement of second-harmonic generation from silicon stripes under external cylindrical strain". *Optics Letters* 34.21 (Nov. 1, 2009), pp. 3340–3342.

[209] M. Cazzanelli, F. Bianco, E. Borga, G. Pucker, M. Ghulinyan, E. Degoli, E. Luppi, V. Véniard, S. Ossicini, D. Modotto, S. Wabnitz, R. Pierobon, and L. Pavesi. "Second-harmonic generation in silicon waveguides strained by silicon nitride". *Nature Materials* 11.2 (Feb. 2012), pp. 148–154.

[210] F. De Leonardis, B. Troia, R. A. Soref, and V. M. N. Passaro. "Investigation of mid-infrared second harmonic generation in strained germanium waveguides". *Optics Express* 24.10 (May 16, 2016), p. 11126.

[211] M. Borghi, M. Mancinelli, F. Merget, J. Witzens, M. Bernard, M. Ghulinyan, G. Pucker, and L. Pavesi. "High-frequency electro-optic measurement of strained silicon racetrack resonators". *Optics Letters* 40.22 (Nov. 15, 2015), p. 5287.

[212] H. Aouani, M. Rahmani, M. Navarro-Cía, and S. A. Maier. "Third-harmonic-upconversion enhancement from a single semiconductor nanoparticle coupled to a plasmonic antenna". *Nature Nanotechnology* 9.4 (Apr. 2014), pp. 290–294.

[213] T. J. Duffin, M. P. Nielsen, F. Diaz, S. Palomba, S. A. Maier, and R. F. Oulton. "Degenerate four-wave mixing in silicon hybrid plasmonic waveguides". *Optics Letters* 41.1 (Jan. 1, 2016), p. 155.

[214] T. F. Heinz, M. M. T. Loy, and W. A. Thompson. "Study of Si(111) Surfaces by Optical Second-Harmonic Generation: Reconstruction and Surface Phase Transformation". *Physical Review Letters* 54.1 (Jan. 7, 1985), pp. 63–66.

[215] C. W. van Hasselt, M. A. Verheijen, and T. Rasing. "Vicinal Si(111) surfaces studied by optical second-harmonic generation: Step-induced anisotropy and surface-bulk discrimination". *Physical Review B* 42.14 (Nov. 15, 1990), pp. 9263–9266.

[216] G. Lüpke. "Characterization of semiconductor interfaces by second-harmonic generation". *Surface Science Reports* 35.3 (Nov. 1999), pp. 75–161.

[217] S. Mitchell, M. Mehendale, D. Villeneuve, and R. Boukherroub. “Second harmonic generation spectroscopy of chemically modified Si(1 1 1) surfaces”. *Surface Science* 488.3 (Aug. 10, 2001), pp. 367–378.

[218] A. Rumpel, B. Manschwetus, G. Lilienkamp, H. Schmidt, and W. Daum. “Polarity of space charge fields in second-harmonic generation spectra of Si(100)/SiO_{2} interfaces”. *Physical Review B* 74.8 (Aug. 2, 2006), p. 081303.

[219] J. P. Long, B. S. Simpkins, D. J. Rowenhorst, and P. E. Pehrsson. “Far-field Imaging of Optical Second-Harmonic Generation in Single GaN Nanowires”. *Nano Letters* 7.3 (Mar. 1, 2007), pp. 831–836.

[220] P. Simesen, K. B. Pedersen, and K. Pedersen. “Second-harmonic scanning microscopy of domains in Al wire bonds in IGBT modules”. *Optics Express* 23.26 (Dec. 28, 2015), p. 33466.

[221] R. S. Jacobsen, K. N. Andersen, P. I. Borel, J. Fage-Pedersen, L. H. Frandsen, O. Hansen, M. Kristensen, A. V. Lavrinenko, G. Moulin, H. Ou, C. Peucheret, B. Zsigri, and A. Bjarklev. “Strained silicon as a new electro-optic material”. *Nature* 441.7090 (May 11, 2006), pp. 199–202.

[222] M. R. Shcherbakov, P. P. Vabishchevich, A. S. Shorokhov, K. E. Chong, D.-Y. Choi, I. Staude, A. E. Miroshnichenko, D. N. Neshev, A. A. Fedyanin, and Y. S. Kivshar. “Ultrafast All-Optical Switching with Magnetic Resonances in Nonlinear Dielectric Nanostructures”. *Nano Letters* 15.10 (Oct. 14, 2015), pp. 6985–6990.

[223] G. Di Giuseppe, L. Martin, A. Perez-Leija, R. Keil, F. Dreisow, S. Nolte, A. Szameit, A. F. Abouraddy, D. N. Christodoulides, and B. E. A. Saleh. “Einstein-Podolsky-Rosen Spatial Entanglement in Ordered and Anderson Photonic Lattices”. *Physical Review Letters* 110.15 (Apr. 10, 2013), p. 150503.

[224] M. Tillmann, B. Dakić, R. Heilmann, S. Nolte, A. Szameit, and P. Walther. “Experimental boson sampling”. *Nature Photonics* 7.7 (July 2013), pp. 540–544.

[225] R. Heilmann, M. Gräfe, S. Nolte, and A. Szameit. “Arbitrary photonic wave plate operations on chip: Realizing Hadamard, Pauli-X, and rotation gates for polarisation qubits”. *Scientific Reports* 4 (Feb. 18, 2014).

[226] A. Javadi, I. Söllner, M. Arcari, S. L. Hansen, L. Midolo, S. Mahmoodian, G. Kiršanskė, T. Pregnolato, E. H. Lee, J. D. Song, S. Stobbe, and P. Lodahl. “Single-photon non-linear optics with a quantum dot in a waveguide”. *Nature Communications* 6 (Oct. 23, 2015), p. 8655.

[227] K. Jain and G. W. Pratt Jr. “Optical transistor”. *Applied Physics Letters* 28.12 (June 15, 1976), pp. 719–721.

[228] J. Butet and O. J. F. Martin. “Nonlinear Plasmonic Nanorulers”. *ACS Nano* 8.5 (May 27, 2014), pp. 4931–4939.

[229] M. Mesch, B. Metzger, M. Hentschel, and H. Giessen. “Nonlinear Plasmonic Sensing”. *Nano Letters* 16.5 (May 11, 2016), pp. 3155–3159.

[230] H. Yu, W. Fang, X. Wu, X. Lin, L. Tong, W. Liu, A. Wang, and Y. R. Shen. “Single Nanowire Optical Correlator”. *Nano Letters* 14.6 (June 11, 2014), pp. 3487–3490.

[231] Y. Jung, L. Tong, A. Tanaudommongkon, J.-X. Cheng, and C. Yang. "In Vitro and In Vivo Nonlinear Optical Imaging of Silicon Nanowires". *Nano Letters* 9.6 (June 10, 2009), pp. 2440–2444.

[232] F. J. G. de Abajo. "Optical excitations in electron microscopy". *Reviews of Modern Physics* 82.1 (Feb. 3, 2010), pp. 209–275. arXiv: 0903.1669.

[233] A. Arbouet, A. Mlayah, C. Girard, and G. C. d. Francs. "Electron energy losses and cathodoluminescence from complex plasmonic nanostructures: spectra, maps and radiation patterns from a generalized field propagator". *New Journal of Physics* 16.11 (2014), p. 113012.

[234] D. Griffiths. *Introduction to Electrodynamics*. Prentice-Hall International, 1989. ISBN: 978-0-13-481615-9.

[235] L. Novotny. *Principles of nano-optics*. In collab. with B. Hecht. Cambridge ; New York: Cambridge University Press, 2006. 539 pp. ISBN: 0-521-83224-1.

[236] P. B. Johnson and R. W. Christy. "Optical Constants of the Noble Metals". *Physical Review B* 6.12 (Dec. 15, 1972), pp. 4370–4379.

[237] P. Drude. "Zur Elektronentheorie der Metalle". *Annalen der Physik* 306.3 (Jan. 1, 1900), pp. 566–613.

[238] N. Ashcroft and N. Mermin. *Solid State Physics*. Cengage Learning, 2011. ISBN: 978-81-315-0052-1.

[239] D. F. Edwards. "Silicon (Si)*". In: *Handbook of Optical Constants of Solids*. Ed. by E. D. Palik. Burlington: Academic Press, 1997, pp. 547–569. ISBN: 978-0-12-544415-6.

[240] A. Deinega, I. Valuev, B. Potapkin, and Y. Lozovik. "Minimizing light reflection from dielectric textured surfaces". *Journal of the Optical Society of America A* 28.5 (May 1, 2011), p. 770.

[241] A. Deinega and S. John. "Effective optical response of silicon to sunlight in the finite-difference time-domain method". *Optics Letters* 37.1 (Jan. 1, 2012), p. 112.

[242] A. J. Cox, A. J. DeWeerd, and J. Linden. "An experiment to measure Mie and Rayleigh total scattering cross sections". *American Journal of Physics* 70.6 (June 1, 2002), pp. 620–625.

[243] J. Shan, J. I. Dadap, I. Stiopkin, G. A. Reider, and T. F. Heinz. "Experimental study of optical second-harmonic scattering from spherical nanoparticles". *Physical Review A* 73.2 (Feb. 23, 2006), p. 023819.

[244] J. D. Jackson. *Classical Electrodynamics*. 3rd ed. Wiley, 1999.

[245] E. N. Economou. *Green's Functions in Quantum Physics*. 2nd ed. Springer, 1983. ISBN: 978-3-540-12266-1.

[246] C. Girard. "Near fields in nanostructures". *Reports on Progress in Physics* 68.8 (Aug. 1, 2005), pp. 1883–1933.

[247] M. Hazewinkel. *Encyclopaedia of mathematics: an updated and annotated translation of the Soviet "Mathematical encyclopaedia"*. Encyclopaedia of Mathematics: An Updated and Annotated Translation of the Soviet "Mathematical Encyclopaedia". Reidel, 1994. ISBN: 978-1-55608-010-4.

[248] M. Spiegel. *Mathematical handbook of formulas and tables*. Schaum's outline series. McGraw-Hill, 1968.

[249] G. Colas des Francs. "Optique sub-longueur d'onde et fluorescence moléculaire perturbée". PhD thesis. CEMES: Université Paul Sabatier Toulouse, 2002.

[250] C. Girard, E. Dujardin, G. Baffou, and R. Quidant. "Shaping and manipulation of light fields with bottom-up plasmonic structures". *New Journal of Physics* 10.10 (Oct. 1, 2008), p. 105016.

[251] W. Cai and T. Yu. "Fast Calculations of Dyadic Green's Functions for Electromagnetic Scattering in a Multilayered Medium". *Journal of Computational Physics* 165.1 (Nov. 2000), pp. 1–21.

[252] M. Paulus, P. Gay-Balmaz, and O. J. F. Martin. "Accurate and efficient computation of the Green's tensor for stratified media". *Physical Review E* 62.4 (Oct. 1, 2000), pp. 5797–5807.

[253] A. M. Attiya. "Dyadic Green's function of an elementary point source above a periodically-defected-grounded dielectric slab". *Progress In Electromagnetics Research B* 4 (2008), pp. 127–145.

[254] B. Gallinet and O. J. F. Martin. "Electromagnetic Scattering of Finite and Infinite 3D Lattices in Polarizable Backgrounds". *Theoretical And Computational Nanophotonics (Tacona-Photonics 2009)* 1176 (2009), pp. 63–65.

[255] C. Craeye, X. Radu, F. Capolino, and A. G. Schuchinsky. "Fundamentals of Method of Moments for Artificial Materials". In: *Modeling Principles of Metamaterials*. CRC Press. Vol. II. VII vols. Theory and Phenomena of Metamaterials. Filippo Capolino, 2009. ISBN: 978-1-4200-5425-5.

[256] P. C. Chaumet and A. Sentenac. "Simulation of light scattering by multilayer crossgratings with the coupled dipole method". *Journal of Quantitative Spectroscopy and Radiative Transfer* 110.6 (Apr. 2009), pp. 409–414.

[257] J. Kottmann and O. Martin. "Accurate solution of the volume integral equation for high-permittivity scatterers". *IEEE Transactions on Antennas and Propagation* 48.11 (Nov. 2000), pp. 1719–1726.

[258] M. Paulus and O. J. F. Martin. "Green's tensor technique for scattering in two-dimensional stratified media". *Physical Review E* 63.6 (May 29, 2001), p. 066615.

[259] G. Colas des Francs, J. Grandidier, S. Massenot, A. Bouhelier, J.-C. Weeber, and A. Dereux. "Integrated plasmonic waveguides: A mode solver based on density of states formulation". *Physical Review B* 80.11 (Sept. 17, 2009), p. 115419.

[260] O. J. F. Martin, C. Girard, and A. Dereux. "Generalized Field Propagator for Electromagnetic Scattering and Light Confinement". *Physical Review Letters* 74.4 (Jan. 23, 1995), pp. 526–529.

[261] A. Yaghjian. "Electric dyadic Green's functions in the source region". *Proceedings of the IEEE* 68.2 (Feb. 1980), pp. 248–263.

[262] C. Girard and A. Dereux. "Near-field optics theories". *Reports on Progress in Physics* 59.5 (1996), p. 657.

[263] R. W. Boyd. "Intuitive explanation of the phase anomaly of focused light beams". *Journal of the Optical Society of America* 70.7 (July 1, 1980), p. 877.

[264] R. Quidant, J.-C. Weeber, A. Dereux, D. Peyrade, Y. Chen, and C. Girard. "Near-field observation of evanescent light wave coupling in subwavelength optical waveguides". *Europhysics Letters (EPL)* 57.2 (Jan. 2002), pp. 191–197.

[265] L. Jiang, T. Yin, Z. Dong, M. Liao, S. J. Tan, X. M. Goh, D. Allioux, H. Hu, X. Li, J. K. W. Yang, and Z. Shen. "Accurate Modeling of Dark-Field Scattering Spectra of Plasmonic Nanostructures". *ACS Nano* 9.10 (Oct. 27, 2015), pp. 10039–10046.

[266] W. Press. *Numerical Recipes 3rd Edition: The Art of Scientific Computing*. Cambridge University Press, 2007. ISBN: 978-0-521-88068-8.

[267] J. W. Demmel, S. C. Eisenstat, J. R. Gilbert, X. S. Li, and J. W. H. Liu. "A supernodal approach to sparse partial pivoting". *SIAM J. Matrix Analysis and Applications* 20.3 (1999), pp. 720–755.

[268] X. S. Li. "An Overview of SuperLU: Algorithms, Implementation, and User Interface". *ACM Transactions on Mathematical Software* 31.3 (2005), pp. 302–325.

[269] P. Joly and G. Meurant. "Complex conjugate gradient methods". *Numerical Algorithms* 4.3 (Oct. 1993), pp. 379–406.

[270] X. S. Li and M. Shao. "A Supernodal Approach to Incomplete LU Factorization with Partial Pivoting". *ACM Transactions Mathematical Software* 37.4 (2011), p. 43.

[271] B. T. Draine and P. J. Flatau. "Discrete-dipole approximation for scattering calculations". *Journal of the Optical Society of America A* 11.4 (Apr. 1, 1994), p. 1491.

[272] J. J. Goodman, B. T. Draine, and P. J. Flatau. "Application of fast-Fourier-transform techniques to the discrete-dipole approximation". *Optics Letters* 16.15 (Aug. 1, 1991), p. 1198.

[273] F. J. García de Abajo and A. Howie. "Retarded field calculation of electron energy loss in inhomogeneous dielectrics". *Physical Review B* 65.11 (Mar. 8, 2002), p. 115418.

[274] U. Hohenester and A. Trügler. "MNPBEM – A Matlab toolbox for the simulation of plasmonic nanoparticles". *Computer Physics Communications* 183.2 (Feb. 2012), pp. 370–381.

[275] A. F. Oskooi, D. Roundy, M. Ibanescu, P. Bermel, J. D. Joannopoulos, and S. G. Johnson. "MEEP: A flexible free-software package for electromagnetic simulations by the FDTD method". *Computer Physics Communications* 181 (Jan. 2010), pp. 687–702.

[276] J. Smajic, C. Hafner, L. Raguin, K. Tavzarashvili, and M. Mishrikey. "Comparison of Numerical Methods for the Analysis of Plasmonic Structures". *Journal of Computational and Theoretical Nanoscience* 6.3 (Mar. 1, 2009), pp. 763–774.

[277] J.-J. Greffet and R. Carminati. "Image formation in near-field optics". *Progress in Surface Science* 56.3 (Nov. 1, 1997), pp. 133–237.

[278] J. A. Porto, R. Carminati, and J.-J. Greffet. "Theory of electromagnetic field imaging and spectroscopy in scanning near-field optical microscopy". *Journal of Applied Physics* 88.8 (Oct. 15, 2000), pp. 4845–4850.

[279] C. Girard, J.-C. Weeber, A. Dereux, O. J. F. Martin, and J.-P. Goudonnet. "Optical magnetic near-field intensities around nanometer-scale surface structures". *Physical Review B* 55.24 (June 15, 1997), pp. 16487–16497.

[280] B. T. Draine. “The Discrete-Dipole Approximation and its Application to Interstellar Graphite Grains”. *Astrophysical Journal* 333 (1988), pp. 848–872.

[281] L. Novotny. “Allowed and forbidden light in near-field optics. II. Interacting dipolar particles”. *Journal of the Optical Society of America A* 14.1 (Jan. 1, 1997), pp. 105–113.

[282] R. W. Boyd. *Nonlinear optics*. 3rd ed. Amsterdam ; Boston: Academic Press, 2008. 613 pp. ISBN: 978-0-12-369470-6.

[283] J. A. Giordmaine. “Mixing of Light Beams in Crystals”. *Physical Review Letters* 8.1 (Jan. 1, 1962), pp. 19–20.

[284] C. Schriever, C. Bohley, and R. B. Wehrspohn. “Strain dependence of second-harmonic generation in silicon”. *Optics Letters* 35.3 (Feb. 1, 2010), pp. 273–275.

[285] R. W. Terhune, P. D. Maker, and C. M. Savage. “Optical Harmonic Generation in Calcite”. *Physical Review Letters* 8.10 (May 15, 1962), pp. 404–406.

[286] D. Guidotti, T. A. Driscoll, and H. J. Gerritsen. “Second harmonic generation in centrosymmetric semiconductors”. *Solid State Communications* 46.4 (Apr. 1, 1983), pp. 337–340.

[287] H. W. K. Tom, T. F. Heinz, and Y. R. Shen. “Second-Harmonic Reflection from Silicon Surfaces and Its Relation to Structural Symmetry”. *Physical Review Letters* 51.21 (Nov. 21, 1983), pp. 1983–1986.

[288] G. L. Richmond, J. M. Robinson, and V. L. Shannon. “Second harmonic generation studies of interfacial structure and dynamics”. *Progress in Surface Science* 28.1 (Jan. 1, 1988), pp. 1–70.

[289] P. Guyot-Sionnest, W. Chen, and Y. R. Shen. “General considerations on optical second-harmonic generation from surfaces and interfaces”. *Physical Review B* 33.12 (June 15, 1986), pp. 8254–8263.

[290] P. Guyot-Sionnest and Y. R. Shen. “Local and nonlocal surface nonlinearities for surface optical second-harmonic generation”. *Physical Review B* 35.9 (Mar. 15, 1987), pp. 4420–4426.

[291] B. Koopmans, F. van der Woude, and G. A. Sawatzky. “Surface symmetry resolution of nonlinear optical techniques”. *Physical Review B* 46.19 (Nov. 15, 1992), pp. 12780–12783.

[292] C. Ciracì, E. Poutrina, M. Scalora, and D. R. Smith. “Second-harmonic generation in metallic nanoparticles: Clarification of the role of the surface”. *Physical Review B* 86.11 (Sept. 27, 2012), p. 115451.

[293] H. E. Ruda and A. Shik. “Nonlinear optical phenomena in nanowires”. *Journal of Applied Physics* 101.3 (Feb. 12, 2007), p. 034312.

[294] R. Cisek, V. Barzda, H. E. Ruda, and A. Shik. “Nonlinear Optical Properties of Semiconductor Nanowires”. *IEEE Journal of Selected Topics in Quantum Electronics* 17.4 (July 2011), pp. 915–921.

[295] V. L. Brudny, B. S. Mendoza, and W. Luis Mochán. “Second-harmonic generation from spherical particles”. *Physical Review B* 62.16 (Oct. 15, 2000), pp. 11152–11162.

[296] W. L. Mochán, J. A. Maytorena, B. S. Mendoza, and V. L. Brudny. “Second-harmonic generation in arrays of spherical particles”. *Physical Review B* 68.8 (Aug. 19, 2003), p. 085318.

[297] C. C. Neacsu, G. A. Reider, and M. B. Raschke. "Second-harmonic generation from nanoscopic metal tips: Symmetry selection rules for single asymmetric nanostructures". *Physical Review B* 71.20 (May 31, 2005), p. 201402.

[298] C. I. Valencia, E. R. Méndez, and B. S. Mendoza. "Second-harmonic generation in the scattering of light by an infinite cylinder". *Journal of the Optical Society of America B* 21.1 (Jan. 1, 2004), pp. 36–44.

[299] A. Capretti, C. Forestiere, L. D. Negro, and G. Miano. "Full-Wave Analytical Solution of Second-Harmonic Generation in Metal Nanospheres". *Plasmonics* 9.1 (Sept. 18, 2013), pp. 151–166.

[300] M. Falasconi, L. C. Andreani, A. M. Malvezzi, M. Patrini, V. Mulloni, and L. Pavesi. "Bulk and surface contributions to second-order susceptibility in crystalline and porous silicon by second-harmonic generation". *Surface Science* 481.1 (June 10, 2001), pp. 105–112.

[301] D. Krause, C. W. Teplin, and C. T. Rogers. "Optical surface second harmonic measurements of isotropic thin-film metals: Gold, silver, copper, aluminum, and tantalum". *Journal of Applied Physics* 96.7 (Oct. 1, 2004), pp. 3626–3634.

[302] F. X. Wang, F. J. Rodríguez, W. M. Albers, R. Ahorinta, J. E. Sipe, and M. Kauranen. "Surface and bulk contributions to the second-order nonlinear optical response of a gold film". *Physical Review B* 80.23 (Dec. 8, 2009), p. 233402.

[303] J. E. Sipe, D. J. Moss, and H. M. van Driel. "Phenomenological theory of optical second- and third-harmonic generation from cubic centrosymmetric crystals". *Physical Review B* 35.3 (Jan. 15, 1987), pp. 1129–1141.

[304] C. F. Bohren and D. R. Huffman. *Absorption and scattering of light by small particles*. Wiley, 1998.

[305] Y. Zeng, W. Hoyer, J. Liu, S. W. Koch, and J. V. Moloney. "Classical theory for second-harmonic generation from metallic nanoparticles". *Physical Review B* 79.23 (June 4, 2009), p. 235109.

[306] K. Koskinen, R. Czaplicki, T. Kaplas, and M. Kauranen. "Recognition of multipolar second-order nonlinearities in thin-film samples". *Optics Express* 24.5 (Mar. 7, 2016), p. 4972.

[307] S. Cattaneo and M. Kauranen. "Polarization-based identification of bulk contributions in surface nonlinear optics". *Physical Review B* 72.3 (July 22, 2005), p. 033412.

[308] S. Maneewongvatana and D. M. Mount. "Analysis of approximate nearest neighbor searching with clustered point sets". *arXiv:cs/9901013* (Jan. 26, 1999). arXiv: cs/9901013.

[309] S. I. Bozhevolnyi and V. Z. Lozovski. "Self-consistent model for second-harmonic near-field microscopy". *Physical Review B* 61.16 (Apr. 15, 2000), pp. 11139–11150.

[310] V. Lozovski and S. Bozhevolnyi. "Second harmonic imaging of individual semiconductor nanostructures for scanning far field microscopy". *Physica E: Low-dimensional Systems and Nanostructures* 15.4 (Dec. 2002), pp. 229–237.

[311] V. Z. Lozovski, J. Beermann, and S. I. Bozhevolnyi. "Modeling of second-harmonic scanning optical microscopy of molecular quasi-one-dimensional aggregates". *Physical Review B* 75.4 (Jan. 31, 2007), p. 045438.

[312] J. Sun, X. Wang, S. Chang, M. Zeng, S. Shen, and N. Zhang. "Far-field radiation patterns of second harmonic generation from gold nanoparticles under tightly focused illumination". *Optics Express* 24.7 (Apr. 4, 2016), p. 7477.

[313] J. R. Carson. "A Generalization of the Reciprocal Theorem". *Bell System Technical Journal* 3.3 (July 1, 1924), pp. 393–399.

[314] R. Carminati, M. Nieto-Vesperinas, and J.-J. Greffet. "Reciprocity of evanescent electromagnetic waves". *Journal of the Optical Society of America A* 15.3 (Mar. 1, 1998), p. 706.

[315] L. Sánchez-García, C. Tserkezis, M. O. Ramírez, P. Molina, J. J. Carvajal, M. Aguiló, F. Díaz, J. Aizpurua, and L. E. Bausá. "Plasmonic enhancement of second harmonic generation from nonlinear RbTiOPO_4 crystals by aggregates of silver nanostructures". *Optics Express* 24.8 (Apr. 18, 2016), p. 8491.

[316] N. Bloembergen, W. K. Burns, and M. Matsuoka. "Reflected third harmonic generated by picosecond laser pulses". *Optics Communications* 1.4 (Sept. 1969), pp. 195–198.

[317] P. R. Wiecha, A. Arbouet, H. Kallel, P. Periwal, T. Baron, and V. Paillard. "Enhanced nonlinear optical response from individual silicon nanowires". *Physical Review B* 91.12 (Mar. 31, 2015), p. 121416.

[318] P. R. Wiecha, A. Arbouet, C. Girard, T. Baron, and V. Paillard. "Origin of second-harmonic generation from individual silicon nanowires". *Physical Review B* 93.12 (Mar. 17, 2016), p. 125421. arXiv: 1510.05409.

[319] G. Mie. "Beiträge zur Optik trüber Medien, speziell kolloidaler Metallösungen". *Annalen der Physik* 330.3 (Jan. 1, 1908), pp. 377–445.

[320] U. Zywietz, M. K. Schmidt, A. B. Evlyukhin, C. Reinhardt, J. Aizpurua, and B. N. Chichkov. "Electromagnetic Resonances of Silicon Nanoparticle Dimers in the Visible". *ACS Photonics* 2.7 (July 15, 2015), pp. 913–920.

[321] J. Zuloaga and P. Nordlander. "On the Energy Shift between Near-Field and Far-Field Peak Intensities in Localized Plasmon Systems". *Nano Letters* 11.3 (Mar. 9, 2011), pp. 1280–1283.

[322] P. Alonso-González, P. Albella, F. Neubrech, C. Huck, J. Chen, F. Golmar, F. Casanova, L. E. Hueso, A. Pucci, J. Aizpurua, and R. Hillenbrand. "Experimental Verification of the Spectral Shift between Near- and Far-Field Peak Intensities of Plasmonic Infrared Nanoantennas". *Physical Review Letters* 110.20 (May 14, 2013), p. 203902.

[323] H. Kallel. "Study of optical properties of individual nanowires of Si, Ge and their alloys and SiGe heterostructures for the control of the light absorption and scattering". PhD thesis. CEMES: Université Paul Sabatier Toulouse, June 2014.

[324] I. H. Malitson. "Interspecimen Comparison of the Refractive Index of Fused Silica". *Journal of the Optical Society of America* 55.10 (1965), p. 1205.

[325] J. H. Parker, D. W. Feldman, and M. Ashkin. "Raman Scattering by Silicon and Germanium". *Physical Review* 155.3 (Mar. 15, 1967), pp. 712–714.

[326] T. Baron, F. Dhalluin, S. Bassem, B. Salhi, H. Abed, A. Potie, M. Panabière, S. Decossas, M. Kogelschatz, L. Montès, F. Oehler, P. Gentile, N. Pauc, M. D. Hertog, J.-L. Rouvière, P. Noe, and P. Ferret. "Study of Si Nanowires Growth by CVD-VLS and Physical Properties". *Meeting Abstracts* MA2009-02.34 (July 20, 2009), pp. 2646–2646.

[327] L. Arizmendi. “Photonic applications of lithium niobate crystals”. *physica status solidi (a)* 201.2 (Jan. 1, 2004), pp. 253–283.

[328] J. Qi, A. M. Belcher, and J. M. White. “Spectroscopy of individual silicon nanowires”. *Applied Physics Letters* 82.16 (Apr. 21, 2003), pp. 2616–2618.

[329] P. Noé, J. Guignard, P. Gentile, E. Delamadeleine, V. Calvo, P. Ferret, F. Dhalluin, and T. Baron. “Enhancement of the photoluminescence of silicon oxide defect states by combining silicon oxide with silicon nanowires”. *Journal of Applied Physics* 102.1 (July 1, 2007), p. 016103.

[330] M. Guzzi, M. Martini, M. Mattaini, F. Pio, and G. Spinolo. “Luminescence of fused silica: Observation of the O2- emission band”. *Physical Review B* 35.17 (June 15, 1987), pp. 9407–9409.

[331] V. Barzda, R. Cisek, T. L. Spencer, U. Philipose, H. E. Ruda, and A. Shik. “Giant anisotropy of second harmonic generation for a single ZnSe nanowire”. *Applied Physics Letters* 92.11 (Mar. 17, 2008), p. 113111.

[332] R. C. Miller. “Optical Second Harmonic Generation in Piezoelectric Crystals”. *Applied Physics Letters* 5.1 (July 1, 1964), pp. 17–19.

[333] C. Hubert, L. Billot, P.-M. Adam, R. Bachelot, P. Royer, J. Grand, D. Gindre, K. D. Dorkenoo, and A. Fort. “Role of surface plasmon in second harmonic generation from gold nanorods”. *Applied Physics Letters* 90.18 (Apr. 30, 2007), p. 181105.

[334] P. Guyot-Sionnest and Y. R. Shen. “Bulk contribution in surface second-harmonic generation”. *Physical Review B* 38.12 (Oct. 15, 1988), pp. 7985–7989.

[335] S. Sivanandam and S. Deepa. *Introduction to Genetic Algorithms*. Heidelberg: Springer, 2008. ISBN: 978-3-540-73189-4.

[336] C. Forestiere, M. Donelli, G. F. Walsh, E. Zeni, G. Miano, and L. Dal Negro. “Particle-swarm optimization of broadband nanoplasmonic arrays”. *Optics Letters* 35.2 (Jan. 15, 2010), p. 133.

[337] T. Feichtner, O. Selig, M. Kiunke, and B. Hecht. “Evolutionary Optimization of Optical Antennas”. *Physical Review Letters* 109.12 (Sept. 19, 2012), p. 127701.

[338] C. Forestiere, A. J. Pasquale, A. Capretti, G. Miano, A. Tamburrino, S. Y. Lee, B. M. Reinhard, and L. Dal Negro. “Genetically Engineered Plasmonic Nanoarrays”. *Nano Letters* 12.4 (Apr. 11, 2012), pp. 2037–2044.

[339] T. Feichtner, O. Selig, and B. Hecht. “Plasmonic nanoantenna design and fabrication based on evolutionary optimization”. *arXiv:1511.05438 [cond-mat, physics:physics]* (Nov. 17, 2015). arXiv: 1511.05438.

[340] C. Forestiere, Y. He, R. Wang, R. M. Kirby, and L. Dal Negro. “Inverse Design of Metal Nanoparticles’ Morphology”. *ACS Photonics* 3.1 (Jan. 20, 2016), pp. 68–78.

[341] P. Ginzburg, N. Berkovitch, A. Nevet, I. Shor, and M. Orenstein. “Resonances On-Demand for Plasmonic Nano-Particles”. *Nano Letters* 11.6 (June 8, 2011), pp. 2329–2333.

[342] A. Tassadit, D. Macías, J. A. Sánchez-Gil, P. .-.-M. Adam, and R. Rodriguez-Oliveros. "Metal nanostars: Stochastic optimization of resonant scattering properties". *Superlattices and Microstructures*. Special issue: Proceedings of the 10th International Conference on the Physics of Light–Matter Coupling in Nanostructures, PLMCN 2010 (Cuernavaca, Mexico), 12–16 April, 2010 49.3 (Mar. 2011), pp. 288–293.

[343] D. Macías, P.-M. Adam, V. Ruíz-Cortés, R. Rodríguez-Oliveros, and J. A. Sánchez-Gil. "Heuristic optimization for the design of plasmonic nanowires with specific resonant and scattering properties". *Optics Express* 20.12 (June 4, 2012), p. 13146.

[344] F. Bigourdan, F. Marquier, J.-P. Hugonin, and J.-J. Greffet. "Design of highly efficient metallo-dielectric patch antennas for single-photon emission". *Optics Express* 22.3 (Feb. 10, 2014), p. 2337.

[345] P. Y. Chen, C. H. Chen, J. S. Wu, H. C. Wen, and W. P. Wang. "Optimal design of integrally gated CNT field-emission devices using a genetic algorithm". *Nanotechnology* 18.39 (Oct. 3, 2007), p. 395203.

[346] Mengyu Wang, Aytac Alparslan, Sascha M. Schnepp, and Christian Hafner. "Optimization of a Plasmon-Assisted Waveguide Coupler Using FEM and MMP". *Progress In Electromagnetics Research B* 59 (2014), pp. 219–229.

[347] Y. K. Zhong, S. M. Fu, N. P. Ju, P. Y. Chen, and A. Lin. "Experimentally-implemented genetic algorithm (Exp-GA): toward fully optimal photovoltaics". *Optics Express* 23.19 (Sept. 21, 2015), A1324.

[348] M. N. Kholodtsova, C. Daul, V. B. Loschenov, and W. C. P. M. Blondel. "Spatially and spectrally resolved particle swarm optimization for precise optical property estimation using diffuse-reflectance spectroscopy". *Optics Express* 24.12 (June 13, 2016), p. 12682.

[349] J. Brest, V. Zumer, and M. S. Maucec. "Self-Adaptive Differential Evolution Algorithm in Constrained Real-Parameter Optimization". In: *IEEE International Conference on Evolutionary Computation*. 2006, pp. 215–222.

[350] F. Biscani, D. Izzo, and C. H. Yam. "A Global Optimisation Toolbox for Massively Parallel Engineering Optimisation". *arXiv:1004.3824 [cs, math]* (Apr. 21, 2010). arXiv: 1004.3824.

[351] X.-L. Han, G. Larrieu, P.-F. Fazzini, and E. Dubois. "Realization of ultra dense arrays of vertical silicon nanowires with defect free surface and perfect anisotropy using a top-down approach". *Microelectronic Engineering*. Proceedings of the 36th International Conference on Micro- and Nano-Engineering (MNE) 88.8 (Aug. 2011), pp. 2622–2624.

[352] Y. Guerfi, F. Carcenac, and G. Larrieu. "High resolution HSQ nanopillar arrays with low energy electron beam lithography". *Microelectronic Engineering* 110 (Oct. 2013), pp. 173–176.

[353] D. Izzo, M. Ruciński, and F. Biscani. "The Generalized Island Model". In: *Parallel Architectures and Bioinspired Algorithms*. Ed. by F. F. d. Vega, J. I. H. Pérez, and J. Lanchares. Studies in Computational Intelligence 415. Springer Berlin Heidelberg, 2012, pp. 151–169. ISBN: 978-3-642-28788-6.

[354] H. Yagi. "Beam Transmission of Ultra Short Waves". *Proceedings of the Institute of Radio Engineers* 16.6 (June 1928), pp. 715–740.

[355] U. Singh, M. Rattan, N. Singh, and M. S. Patterh. "Design of a Yagi-Uda antenna by simulated annealing for gain, impedance and FBR". In: *IET-UK International Conference on Information and Communication Technology in Electrical Sciences (ICTES 2007), 2007. ICTES.* Dec. 2007, pp. 974–979.

[356] H. F. Hofmann, T. Kosako, and Y. Kadoya. "Design parameters for a nano-optical Yagi–Uda antenna". *New Journal of Physics* 9.7 (2007), p. 217.

[357] K. Deb. *Multi-objective optimization using evolutionary algorithms*. Vol. 16. Wiley, 2001.

[358] G. M. Sacha and P. Varona. "Artificial intelligence in nanotechnology". *Nanotechnology* 24.45 (Nov. 15, 2013), p. 452002.

[359] V. Coverstone-Carroll, J. W. Hartmann, and W. J. Mason. "Optimal multi-objective low-thrust spacecraft trajectories". *Computer Methods in Applied Mechanics and Engineering* 186.2 (June 9, 2000), pp. 387–402.

[360] B. F. Carneiro de Albuquerque, F. Luis de Sousa, and A. S. Montes. "Multi-objective approach for the automatic design of optical systems". *Optics Express* 24.6 (Mar. 21, 2016), p. 6619.

[361] J. Jung. "Robust Design of Plasmonic Waveguide Using Gradient Index and Multiobjective Optimization". *IEEE Photonics Technology Letters* 28.7 (Apr. 2016), pp. 756–758.

[362] X. M. Goh, R. J. H. Ng, S. Wang, S. J. Tan, and J. K. Yang. "Comparative Study of Plasmonic Colors from All-Metal Structures of Posts and Pits". *ACS Photonics* 3.6 (June 15, 2016), pp. 1000–1009.

[363] Z. Li, A. W. Clark, and J. M. Cooper. "Dual Color Plasmonic Pixels Create a Polarization Controlled Nano Color Palette". *ACS Nano* 10.1 (Jan. 26, 2016), pp. 492–498.

[364] N. Beume, B. Naujoks, and M. Emmerich. "SMS-EMOA: Multiobjective selection based on dominated hypervolume". *European Journal of Operational Research* 181.3 (Sept. 16, 2007), pp. 1653–1669.

[365] W. Nolting. *Elektrodynamik*. Grundkurs theoretische Physik. Springer, 2004. ISBN: 3-540-20509-8.

[366] S. Corzine, R. Yan, and L. Coldren. "A tanh substitution technique for the analysis of abrupt and graded interface multilayer dielectric stacks". *IEEE Journal of Quantum Electronics* 27.9 (Sept. 1991), pp. 2086–2090.

[367] P. Voisin, G. Bastard, and M. Voos. "Optical selection rules in superlattices in the envelope-function approximation". *Physical Review B* 29.2 (Jan. 15, 1984), pp. 935–941.

[368] B. Jonsson and S. T. Eng. "Solving the Schrodinger equation in arbitrary quantum-well potential profiles using the transfer matrix method". *IEEE Journal of Quantum Electronics* 26.11 (Nov. 1990), pp. 2025–2035.

[369] A. Monmayrant, S. Weber, and B. Chatel. "A newcomer's guide to ultrashort pulse shaping and characterization". *Journal of Physics B: Atomic, Molecular and Optical Physics* 43.10 (May 28, 2010), p. 103001.